Novel ImmunoPET Tracers for Noninvasive Imaging of $CD4^+$ Cell Distribution in Cancer Mouse Models

Dissertation

der Mathematisch-Naturwissenschaftlichen Fakultät
der Eberhard Karls Universität Tübingen
zur Erlangung des Grades eines
Doktors der Naturwissenschaften
(Dr. rer. nat.)

vorgelegt von
MSc, Stefania Pezzana
aus Novara, Italien

Tübingen
2025

Gedruckt mit Genehmigung der Mathematisch-Naturwissenschaftlichen Fakultät der Eberhard Karls Universität Tübingen.

Tag der mündlichen Qualifikation:	02.03.2026
Dekan:	Prof. Dr. Thilo Stehle
1. Berichterstatter/-in:	PD. Dr. Manfred Kneilling
2. Berichterstatter/-in:	Prof. Dr. Ulrich Rothbauer
3. Berichterstatter/-in:	Prof. Dr. Dorothee Kretschmer

Table of content

I. Summary

Increasing evidence highlights the crucial role of $CD4^+$ cells in orchestrating cancer immunity, suggesting their potential as biomarkers for disease classification and for monitoring responses to a wide range of immunotherapies. However, there is currently no established noninvasive diagnostic procedure to determine the $CD4^+$ cell content in diseased tissue. Molecular imaging of $CD4^+$ cells could offer novel insights into their migration dynamics during immunotherapies and better define patient-specific therapeutic approaches. Additionally, a noninvasive, repetitive method to detect $CD4^+$ cells throughout the entire body would enable clinicians to track disease progression and therapeutic effects, thus providing guidance for personalized treatments.

The aim of this thesis was to validate novel scFv-CH3 (minibody, Mb)-based and VHH single domain antibody (nanobody, Nb)-based PET tracers for noninvasive *in vivo* imaging of human $CD4^+$ cells. Aiming for subsequent clinical translation, we thoroughly evaluated their ability to visualize, spatially localize, and distinguish clinically relevant changes in endogenous $CD4^+$ immune cell infiltrates in preclinical cancer models.

The simultaneous development of radiolabeled murine and human Mbs (^{89}Zr-mCD4-Mb and ^{89}Zr-hCD4-Mb, respectively) for PET imaging enabled noninvasive monitoring and visualization of whole-body endogenous $CD4^+$ cell distributions in experimental models of cancer immunotherapy (CIT) in human CD4 receptor knock-in (hCD4-KI) and wild-type (WT) mice, as well as the prediction of CIT response. Furthermore, our newly developed ^{64}Cu radiolabeled CD4 specific Nb (^{64}Cu-CD4-Nb1) allowed for the highly sensitivedetection and spatial localization of little alterations in $CD4^+$ cell densities in different experimental cancer models.

One of the main differences between the two imaging probes is their molecular weight, which influenced their pharmacokinetic properties, making them suitable for different imaging purposes. The development of these probes targeting the hCD4 antigen and the evidence that neither format alters T-cell proliferation or function make them promising candidates for clinical translation across a wide range of tumors and cancer immunotherapy applications.

II. Zusammenfassung

CD4⁺-Zellen spielen eine entscheidende Rolle bei der Steuerung der Krebsimmunität und sind daher vielversprechende Biomarker für die Klassifizierung von Erkrankungen sowie für die Überwachung von Immuntherapien. Allerdings existiert derzeit kein etabliertes nichtinvasives Diagnoseverfahren zur Bestimmung des CD4⁺ Zellgehalts im erkrankten Gewebe. Die molekulare Bildgebung von CD4⁺ Zellen könnte neue Einblicke in deren Migrationsdynamik während Immuntherapien bieten und personalisierte Therapieansätze ermöglichen. Darüber hinaus eröffnet die longitudinale, nichtinvasive Ganzkörper-Bildgebung von CD4⁺ Zellen klinisch die Möglichkeit, Krankheitsverlauf und Therapieeffekt sowohl bei Tumorerkrankungen als auch bei entzündlichen Erkrankungen zu verfolgen.

Ziel dieser Arbeit war es, verschiedene für die Immunzellbildgebung bevorzugte Antikörperfragmente wie scFv-CH3-Antikörper (Minibodies, Mbs) und VHH-Einzeldomänen-Antikörper (Nanobodies, Nbs) für die ImmunoPET-Bildgebung zu validieren, um humane CD4⁺ Zellen nichtinvasiv detektieren zu können. Ihre Fähigkeit, endogene CD4⁺ Immunzell-Infiltrate sichtbar zu machen, räumlich zu lokalisieren und klinisch relevante Veränderungen differenzieren zu können, wurde in präklinischen Krebsmodellen im Hinblick auf klinische Umsetzbarkeit untersucht.

Die gleichzeitige Entwicklung von radioaktiv markierten murinen und humanen Minibodies (^{89}Zr-mCD4-Mb bzw. ^{89}Zr-hCD4-Mb) für die PET-Bildgebung ermöglichte die nichtinvasive Überwachung und Visualisierung der körpereigenen CD4⁺-Zellverteilungen in Krebsimmuntherapie-Modellen in humanen CD4-Rezeptor-Knock-in- und Wildtyp-Mäusen, die auch eine Vorhersage des Therapieansprechens ermöglichte. Darüber hinaus erlaubte ein neu entwickelter ^{64}Cu-markierter CD4-spezifischer Nanobody (^{64}Cu-CD4-Nb1) die hochsensitive Erkennung und räumliche Lokalisierung selbst geringer Veränderungen von CD4⁺ Zellinfiltraten in verschiedenen experimentellen Krebsmodellen.

Ein wesentlicher Unterschied zwischen den beiden Tracern liegt in ihrem Molekulargewicht, das ihre pharmakokinetischen Eigenschaften maßgeblich beeinflusst und sie für unterschiedliche Bildgebungszwecke geeignet macht. Die Entwicklung dieser Tracer, die gezielt das humane CD4-Antigen adressieren, sowie der Nachweis, dass keines der beiden Formate die Proliferation oder Funktion von T-Zellen verändert, machen sie zu vielversprechenden Kandidaten für die klinische Anwendung bei einem breiten Spektrum verschiedener Tumoren und Krebsimmuntherapien.

III. List of publications

a. Accepted publications

Pezzana, S., Blaess, S., Kortendieck, J., Hemmer, N., Tako, B., Pietura, C., Ruoff, L., Riel, S., Schaller, M., Gonzalez-Menendez, I., Quintanilla-Martinez, L., Mascioni, A., Aivazian, A., Wilson, I., Maurer, A., Pichler, B.J., Kneilling, M., Sonanini, D. (2024). In-depth cross-validation of human and mouse CD4-specific minibodies for noninvasive PET imaging of CD4+ cells and response prediction to cancer immunotherapy. Theranostics, 14(12), 4582-4597. https://doi.org/10.7150/thno.95173 [1].

Traenkle B, Kaiser PD, **Pezzana S**, Richardson J, Gramlich M, Wagner TR, Seyfried D, Weldle M, Holz S, Parfyonova Y, Nueske S, Scholz AM, Zeck A, Jakobi M, Schneiderhan-Marra N, Schaller M, Maurer A, Gouttefangeas C, Kneilling M, Pichler BJ, Sonanini D, Rothbauer U. Single-Domain Antibodies for Targeting, Detection, and *In Vivo* Imaging of Human CD4$^+$ Cells. Front Immunol. 2021 Dec 9; 12:799910. doi: 10.3389/fimmu.2021.799910 [2].

Wagner TR, Blaess S, Leske IB, Frecot DI, Gramlich M, Traenkle B, Kaiser PD, Seyfried D, Maier S, Rezza A, Sônego F, Thiam K, **Pezzana S**, Zeck A, Gouttefangeas C, Scholz AM, Nueske S, Maurer A, Kneilling M, Pichler BJ, Sonanini D, Rothbauer U. Two birds with one stone: human SIRPα nanobodies for functional modulation and *in vivo* imaging of myeloid cells. Front Immunol. 2023 Dec 18; 14:1264179. doi: 10.3389/fimmu.2023.1264179 [3].

Pezzana S, Blaess S, Traenkle B, Schaefer A, Ruoff L, Tako B, Castaneda Vega S, Kaiser PD, Wagner T, Gonzalez-Menendez I, Quintanilla-Martinez L, Rochwarger A, Schürch CM, Riel S, Schaller M, van Genugten EAJ, van der Hoorn IAE, Gorris MAJ, Steinvoort M, Peeters E, de Vries IJM, van den Heuvel MM, Aarntzen EHJG, Maurer A, Rothbauer U, Pichler BJ, Kneilling M, Sonanini D. PET-based immunomapping of intratumoral CD4$^+$ cells to monitor acquired resistance to checkpoint inhibitors. Sci Adv. 2025 Jun 27;11(26):eadw1924. doi: 10.1126/sciadv.adw1924 [4].

Stammes MA, Koopman G, Wagner TR, Traenkle B, Kaiser PD, Mooij P, van der Werff N, Acar RF, Böszörményi KP, Blaess S, **Pezzana S**, Reischl G, Maurer A, Langermans JAM, Rothbauer U, Kneilling M, Sonanini D. Noninvasive Monitoring of Inflammatory Processes by Myeloid Cell-Directed PET Tracers in an Experimental Severe Acute

Respiratory Syndrome Coronavirus 2 Infection Model. J Nucl Med. 2025 Aug 28:jnumed.125.269721. doi: 10.2967/jnumed.125.269721 [5].

b. Submitted / in revision manuscripts

Tako B, **Pezzana S**, Blaess S, Pietura C, Schaller M, Riel S, Gouttefangeas C, Schuhmacher J, Forchhammer S, Forschner A, Eigentler T, Vega SC, Hihn O, Weigelin B, Traenkle B, Rehbein J, Knopf P, Schoerg B, Wistuba-Hamprecht K, Maurer A, Pichler B, Kneilling M, Sonanini D. CD69 is a reliable imaging biomarker for antitumoral immune responses and therapeutic efficacy.

IV. Author contributions

a. Accepted publication I

Pezzana, S., Blaess, S., Kortendieck, J., Hemmer, N., Tako, B., Pietura, C., Ruoff, L., Riel, S., Schaller, M., Gonzalez-Menendez, I., Quintanilla-Martinez, L., Mascioni, A., Aivazian, A., Wilson, I., Maurer, A., Pichler, B.J., Kneilling, M., Sonanini, D. (2024). In-depth cross-validation of human and mouse CD4-specific minibodies for noninvasive PET imaging of CD4+ cells and response prediction to cancer immunotherapy. Theranostics, 14(12), 4582-4597. https://doi.org/10.7150/thno.95173 [1]

Stefania Pezzana

Research design, animal care, *in vitro* and preclinical experiments, data analysis and interpretation, main writing of the manuscript, figure preparation.

Simone Blaess, Jule Kortendieck, Nicole Hemmer, Bredi Tako, Claudia Pietura, Lara Ruoff

In vitro and preclinical experiments, data analysis and interpretation, manuscript proofreading

Simon Riel, Martin Schaller, Irene Gonzalez-Menendez, Leticia Quintanilla-Martinez

Histology experiments and data interpretation, figure preparation, manuscript proofreading

Alessandro Mascioni, Argin Aivazian, Ian Wilson

Generation and validation of minibody construct, manuscript proofreading

Andreas Maurer

Minibody construct radiolabelling, manuscript proofreading

Bernd Pichler, Manfred Kneilling, Dominik Sonanini

General idea generation, coordination, data interpretation, supervision, proofreading and final approval of the manuscript

b. Accepted publication II

Traenkle B, Kaiser PD, **Pezzana S**, Richardson J, Gramlich M, Wagner TR, Seyfried D, Weldle M, Holz S, Parfyonova Y, Nueske S, Scholz AM, Zeck A, Jakobi M, Schneiderhan-Marra N, Schaller M, Maurer A, Gouttefangeas C, Kneilling M, Pichler BJ, Sonanini D, Rothbauer U. Single-Domain Antibodies for Targeting, Detection, and *In Vivo* Imaging of Human $CD4^+$ Cells. Front Immunol. 2021 Dec 9; 12:799910. doi: 10.3389/fimmu.2021.799910. [2]

Bjoern Traenkle

Nanobody biochemical characterization and functionalization, data interpretation, figure generation, main writing of the manuscript

Philipp D. Kaiser

Nanobody selection, biochemical characterization and functionalization

Stefania Pezzana

In vitro and *in vivo* imaging experiments, data analysis and interpretation, figure generation, manuscript proofreading

Jennifer Richardson

Analysis of nanobody effects on T-cell proliferation and cytokine expression, manuscript proofreading

Marius Gramlich, Anne Zeck

HDX-MS experiments, manuscript proofreading

Teresa R. Wagner

Nanobody biochemical characterization and functionalization, data interpretation, figure generation, manuscript proofreading

Dominik Seyfried

Nanobody radiolabelling, manuscript proofreading

Melissa Weldle

Nanobody biochemical characterization and functionalization, manuscript proofreading

Stefanie Holz, Yana Parfyonova

Nanobody selection, manuscript proofreading

Stefan Nueske, Armin M Scholz

Animal immunization, manuscript proofreading

Meike Jakobi, Nicole Schneiderhan-Marra, Cecile Gouttefangeas

Analysis of nanobody effects on T-cell proliferation and cytokine expression, manuscript proofreading

Martin Schaller

Staining and analysis of xenografts samples, manuscript proofreading

Andreas Maurer

Nanobody radiolabeling, manuscript proofreading

Manfred Kneilling

Project supervision, manuscript proofreading

Dominik Sonanini

Data interpretation, figure generation, manuscript proofreading

Bernd J. Pichler, Ulrich Rothbauer

Project supervision, financial support, manuscript proofreading

c. Accepted publication III

Pezzana S, Blaess S, Traenkle B, Schaefer A, Ruoff L, Tako B, Castaneda Vega S, Kaiser PD, Wagner T, Gonzalez-Menendez I, Quintanilla-Martinez L, Rochwarger A, Schürch CM, Riel S, Schaller M, van Genugten EAJ, van der Hoorn IAE, Gorris MAJ, Steinvoort M, Peeters E, de Vries IJM, van den Heuvel MM, Aarntzen EHJG, Maurer A, Rothbauer U, Pichler BJ, Kneilling M, Sonanini D. PET-based immunomapping of intratumoral $CD4^+$ cells to monitor acquired resistance to checkpoint inhibitors. Sci Adv. 2025 Jun 27;11(26):eadw1924. doi: 10.1126/sciadv.adw1924 [4].

Stefania Pezzana

Research design, animal care, *in vitro* and preclinical experiments, data analysis and interpretation, figure preparation, main writing of the manuscript

Simone Blaess, Anna Schaefer, Lara Ruoff

In vitro and preclinical experiments, data analysis and interpretation, proofreading of the manuscript

Bjoern Traenkle, Philipp D. Kaiser, Teresa R. Wagner

Biochemical characterization and functionalization of Nbs, proofreading of the manuscript

Salvador Vega Castaneda

Data analysis, proofreading of the manuscript

Simon Riel, Martin Schaller, Irene Gonzalez-Menendez, Leticia Quintanilla-Martinez

Histology experiments and data interpretation, figure preparation, proofreading of the manuscript

Andreas Maurer

Nanobody constructs radiolabelling, proofreading of manuscript

Evelien A. J. van Genugten, Iris A. E. van der Hoorn, Mark A. J. Gorris, I. Jolanda M. de Vries, Michel M. van den Heuvel, Erik H. J. G. Aarntzen

Clinical studies and analysis, proofreading of manuscript

Ulrich Rothbauer, Bernd Pichler, Manfred Kneilling

Project supervision, financial support, proofreading of manuscript

Dominik Sonanini

Project supervision, financial support, figure preparation, data interpretation, original draft writing

V. List of abbreviations

%ID/g	percentage of injected dose per gram
%ID/ml	percentage of injected dose per milliliter
^{11}C	Carbon-11
^{131}I	Iodine-131
^{18}F	Fluorine-18
3D	three-dimensional
^{64}Cu	Copper-64
^{64}Cu-CD4-Nb1	Copper-64 labeled human CD4 nanobody
^{68}Ga	Gallium-68
^{68}Ge	Germanium-68
^{89}Zr	Zirconium-89
^{89}Zr-h/mCD4-Mbs	Zirconium-89 labeled human or murine CD4 minibodies
APC	antigen presenting cell
CAF	cancer-associated fibroblasts
CAR-T	chimeric antiegn receptor T
CD	cluster of differentiation
CEA	carcinoembryonic antigen
CH3	constant heavy chain-3
CIT	cancer immunotherapy
CT	computed tomography
CTL	cytotoxic T lymphocytes
CTLA-4	cytotoxic T lymphocyte-associated antigen 4
DC	dendritic cells
DHL	diffuse histiocytic lymphomas
EC	epithelial cells
ECM	extracellular matrix
EMA	European Medicines Agency
Fab	antigen-binding fragment
Fc	fragment crystallizable
FcγR	IgG–Fc-γ-receptors
FDA	Food and Drug Administration
FDG	2-deoxy-2-fluoro-D-glucose

FOXP3	forkhead box P3
HCC	hepatocellular carcinoma
HER2	human epidermal growth factor receptor 2
HNSCC	head and neck squamous carcinoma
HPB-ALL	hematopoietic peripheral blood acute lymphoblastic leukemia tumors
ICI	immune checkpoint inhibitor
ICOS	inducible costimulator
IF	immunofluorescence
IFN	interferon
IgG	immunoglobulin G
IHC	immunohistochemistry
IL	interleukin
irAE	immunotherapy-related adverse events
kDa	kilodalton
keV	kiloelectronvolt
KI	Knock-in
Lag-3	lymphocyte activation gene
M1	type-1 macrophages
M2	type-2 macrophages
mAb	monoclonal antibody
Mb	minibody
MCC	merkel cell carcinoma
MDSC	myeloid-derived suppressor cell
MHC	major histocompatibility complex
MMR	macrophage mannose receptor
MMTV-PyMT	mouse mammary tumor virus-polyoma middle tumor-antigen
MRI	magnetic resonance imaging
Nb	Nanobody
NK	natural killer
NSCLC	non-small cell lung cancer
PD-1	programmed cell death 1
PD-L1	programmed cell death ligand 1
PET	positron emission tomography
PMT	photomultiplier tubes

RCC	renal cell carcinoma
scFv	single-chain fragment variable
TBR	tumor-to-background ratio
TGF-β	transforming growth factor beta
Th	T helper
TME	tumor microenvironment
TNF	tumor necrosis factor
TNFRSF9	tumor necrosis factor receptor superfamily member 9
Treg	regulatory T cell
V_H	heavy chain variable fragments
V_L	light chain variable fragments
WT	wild-type

VI. List of figures and tables

1. Introduction

1.1. Immune system

The immune system comprises a complex network of organs, cells, cytokines and proteins that coordinate a multifaceted defense against pathogens and dysregulated self-antigens. Based on the speed and specificity of the response, the immune system is divided into two categories: innate and adaptive immunity. Innate immunity refers mainly to elements of the immune system that provide immediate host defense, including innate lymphocytes, neutrophils, monocytes, macrophages, dendritic cells (DCs), natural killer (NK) cells, complement, cytokines, and acute phase proteins. However, the lack of specificity of the innate response can damage healthy tissues. The production of cytokines and chemokines by cells part of the innate immunity initiates the adaptive immune response. In contrast to innate immunity, the adaptive response is precise, slower and takes several days or weeks to develop. It is linked to the innate immune response by antigen presenting cells (APCs) in perturbed tissue, which allows the priming, activation, and differentiation of naïve cluster of differentiation (CD)4^+ and $CD8^+$ T cells, as well as monocytes and macrophages. The expanded T-cell population recognizes foreign antigens on the surface of altered or infected cells via major histocompatibility complex (MHC) molecules and efficiently neutralizes the danger at its source. The antigen-specific reactions through T and B lymphocytes allow for the generation of memory immune cells that can act more quickly and precisely upon a second contact with the same antigen [6, 7]. Inflammation resolves when danger is removed, and tissue homeostasis is restored [7].

1.2. Tumor microenvironment

Malignant tumors accounted for nearly 10 million deaths worldwide in 2020 [8]. In 1889, Stephen Paget proposed the “seed and soil” theory, stating that tumor-initiating cells, or “seeds”, need a supportive environment, or “soil”, to grow and metastasize [9, 10]. It is now recognized that cancer is not only mediated by genetic modifications, but also by the interaction of many cellular components [11]. Indeed, tumors represent complex three-dimensional (3D) structures formed by various cell types, including cancer cells and immune cells such as T cells, DCs, NK cells, macrophages and neutrophils. Additionally, these structures include stroma cells, the vasculature, and the extracellular matrix (ECM). Together, these components create a tumor microenvironment (TME) that plays a crucial role in tumor growth, metastasis, and treatment response (**Figure 1**) [7, 11-16].

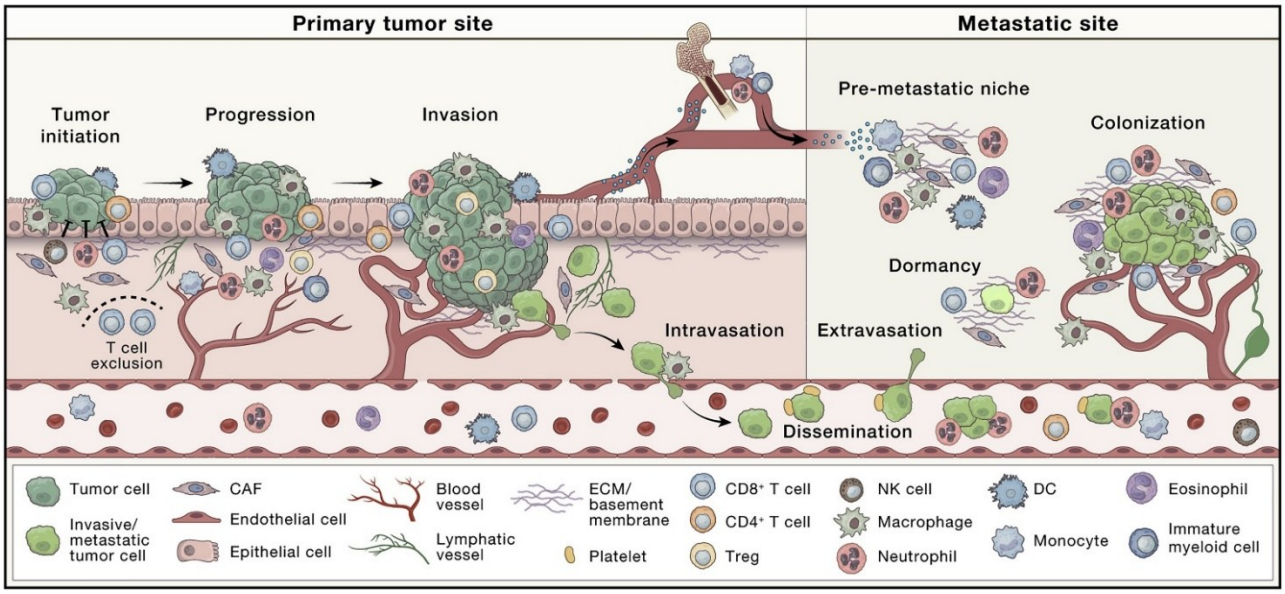

Figure 1. Changes of the tumor microenvironment (TME) during cancer progression and metastasis. The TME includes different immune cell types, as well as cancer associated fibroblasts (CAFs), epithelial cells (ECs) and extracellular matrix (ECM), all co-evolving and varying with the tumor as it progresses. *Depicted from de Visser KE, Joyce JA, 2023* [11].

Immune cells are characterized by different functions, activation states, and phenotypes, representing a heterogeneous component of the TME with a significant impact on tumor progression and response to treatment [17]. In 2013, Chen and Mellman proposed a tumor classification strategy based on patient-specific tumor immune status. They defined three main categories, immune desert (or “cold”), immune excluded, and immune inflamed (or “hot”) tumors, based on the localization and activation profile of the tumor immune infiltrates [18-20].

Immune desert tumors occur because of immunological ignorance, tolerance, or lack of appropriate T-cell priming or activation, generally associated with a poor prognosis. Tumors classified as immune excluded show a specific chemokine state, the existence of vascular barriers, or stroma-based suppression, corresponding to an intermediate prognosis. In contrast, inflamed tumors are infiltrated by proinflammatory cells, such as mature DCs, effector T cells, NK cells, and B cells, as well as anti-inflammatory cells, such as Tregs, myeloid-derived suppressor cells (MDSCs), type I and type II macrophages (M1 and M2, respectively), and cancer-associated fibroblasts (CAFs), associated with a good prognosis [15, 21, 22]. Importantly, the immune phenotype is strongly associated with patient-specific immunotherapy outcomes, with a relatively high response rate in patients with immune-inflamed tumors, highlighting the need for

novel therapeutic approaches for patients with noninflamed phenotypes (**Figure 2**) [22-27].

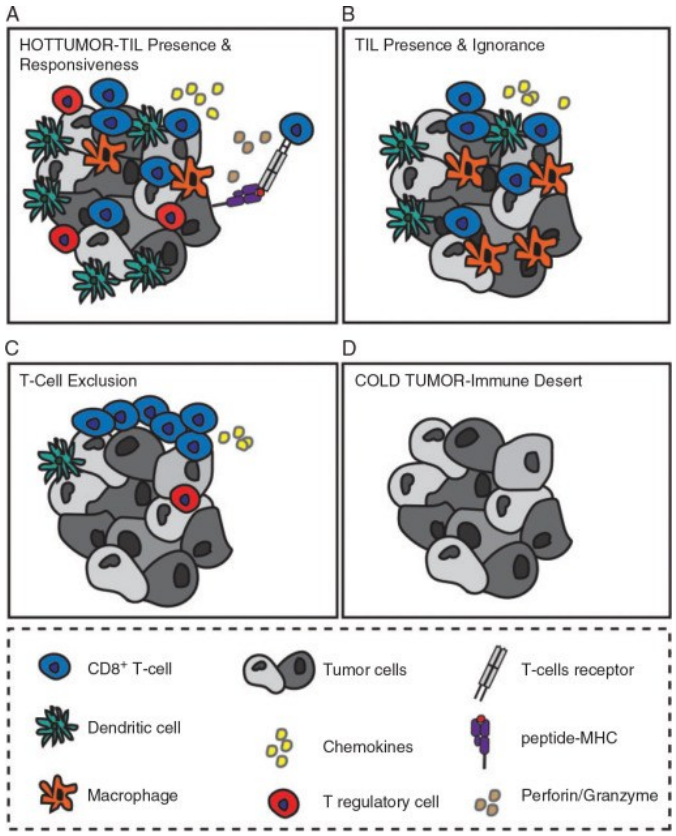

Figure 2. Classification of the Tumor contexture based on the immune infiltrate. Tumors are categorized based on immune cell presence at the tumor site. "Hot" tumors contain immune infiltrates and may either respond to immunotherapy (A) or not (B). Immune cells restricted to the tumor periphery form "excluded" tumors (C), while "cold" tumors are defined by the lack of immune infiltrates (D). *Depicted from Lanitis et al. 2017* [28].

1.3. CD4⁺ immune cells in cancer immunity

For a long time, cytotoxic CD8⁺ T cells were considered the main players in cancer immune response. However, recent research revealed the crucial role of diverse CD4⁺ immune cell subtypes in controlling immune responses, exerting both inflammatory and regulatory effects [29-35]. The evidence of the extensive expression of the CD4 antigen on different immune cell types, such as myeloid and lymphoid cells, underscores the potential of CD4⁺ immune cells as a valuable tool for immune monitoring in cancerous diseases, facilitating more precise prediction of patient-specific therapeutic strategies [32, 35, 36].

The low expression of CD4 antigen on myeloid populations, including monocytes, macrophages, and dendritic cells, contribute to antigen presentation, cell–cell interactions, and immune regulation within the TME [37].

However, the CD4 antigen is mainly expressed by lymphocytes. More in detail, $CD4^+$ T cells represent a heterogeneous group of T lymphocytes with multifaceted roles. Different $CD4^+$ T cells subpopulations have been identified, including T helper (Th) cells (e.g., Th1, Th2, and Th17), T regulatory (Treg) cells, and cytotoxic $CD4^+$ T cells, with functions that range from indirectly assisting cytotoxic T lymphocytes (CTLs) and innate immune cells in fighting tumors to directly killing tumor cells, highlighting their role in orchestrating immune responses [29, 30, 34, 38, 39]. In contrast to CTLs, the differentiation of $CD4^+$ T helper cells into antigen-specific effector cells is induced by phagocytotic cells through MHC-II molecules [38, 40]. This interaction causes the release of cytokines that support $CD8^+$ T-cell proliferation and activation. Furthermore, costimulatory signaling pathways between $CD4^+$ and $CD8^+$ T cells can prime these cell types and facilitate efficient migration to sites of disease [40]. $CD4^+$ Th cells also play a fundamental role in eliciting humoral responses against tumor antigens via CD40L–CD40 signaling on B cells, which drives their differentiation and maturation into affinity-matured plasma cells capable of producing serum antibodies specific to tumor antigens (**Figure 3**) [32] .

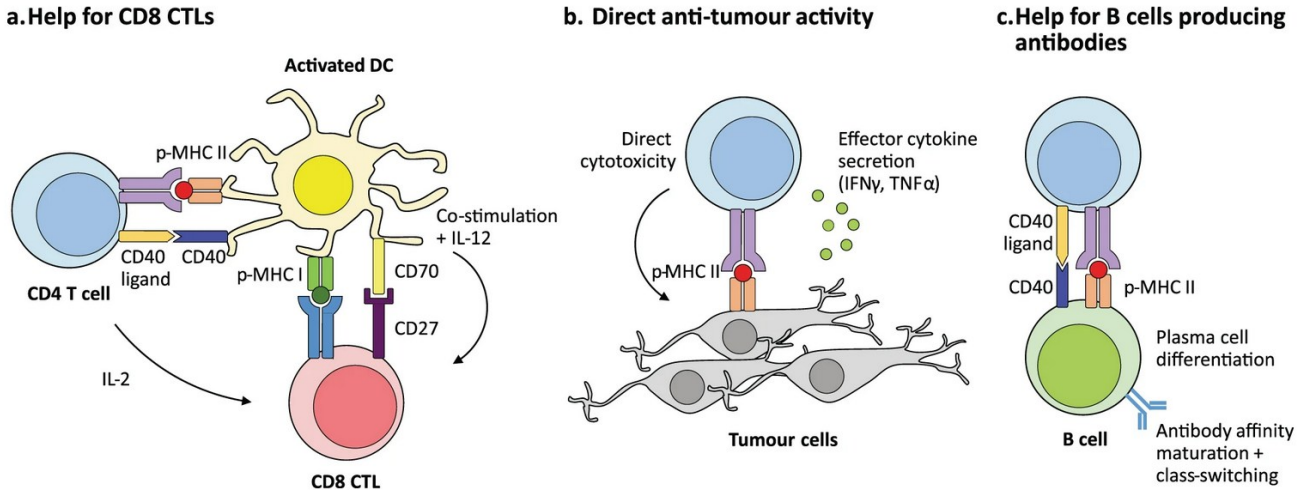

Figure 3. Functions of $CD4^+$ T cells in cancer immunity. (a) $CD4^+$ T-cells support $CD8^+$ CTLs response through the release of IL-12 (direct mechanism) and/or maintaining the activation of DCs, which in turn provide activating signals in support of $CD8^+$ CTLs (indirect mechanism). (b) $CD4^+$ T-cells can have direct anti-tumoral activity by secreting effector cytokines (e.g. IFN-γ and TNF) and (c) induce anti-tumoral humoral responses by activating the CD40L/CD40 signaling pathway on B cells. CD: cluster of differentiation, CTL: cytotoxic T lymphocyte, IL: interleukin, DC: dendritic cells, IFN: interferon, TNF: tumor necrosis factor. *Depicted from Tay et al., 2021* [32].

Th1 cells constitute a proinflammatory subset that promotes cell-mediated toxicity, supporting not only $CD8^+$ cells but also NK cells and macrophages through the secretion of interleukin (IL)-1β, IL-2, IL-12, and tumor necrosis factor (TNF), all of which have

been linked to the eradication of intracellular pathogens and tumors [7, 15, 32, 41, 42]. However, Th1 cells can contribute to tumor escape via the secretion of interferon (IFN)-γ, which increases the expression of the inhibitory checkpoint molecule programmed cell death ligand 1 (PD-L1) by antitumor M1 macrophages and cancer cells [7, 40, 43]. Th2 cells produce cytokines such as IL-4, IL-5, IL-6, IL-10 and IL-13 to activate B cells, M2 macrophages and recruit eosinophils, basophils, and mast cells to the sites of infection, thus promoting tumor progression [44, 45]. On the other hand, Th2 cells promote tissue repair and contribute to inflammatory diseases such as asthma and allergies [46, 47].

Th17 cells not only play a role in the immune response against microorganisms and in autoimmunity through the production of IL-17, IL-21, and IL-23 but also they play a dual role in tumor immunity, being associated with both favorable and unfavorable outcomes [42, 48-50]. Tregs inhibit immune effector cells, prevent tissue damage, and suppress inflammation. In the TME, Tregs are reprogrammed to enhance the suppression of immune responses, ultimately promoting tumor immune escape or tumor progression. Reducing the number of Tregs in the TME by inhibiting their activity or preventing their reprogramming can enhance the body's antitumor immune response [15, 32, 41, 51, 52]. Tregs are characterized by the expression of forkhead box P3 (FOXP3), cytotoxic T lymphocyte-associated antigen 4 (CTLA-4), lymphocyte activation gene (Lag-3), and CD25 [41, 51]. Among their functions, they are known to modulate NK cell homeostasis and function by secreting IL-2 and support the survival of cancer cells by secreting anti-inflammatory cytokines such as IL-10, growth factors such as transforming growth factor-beta (TGF-β), and by interacting with stromal cells (e.g., CAFs and ECs) through CTLA-4 (**Figure 4**) [15, 51].

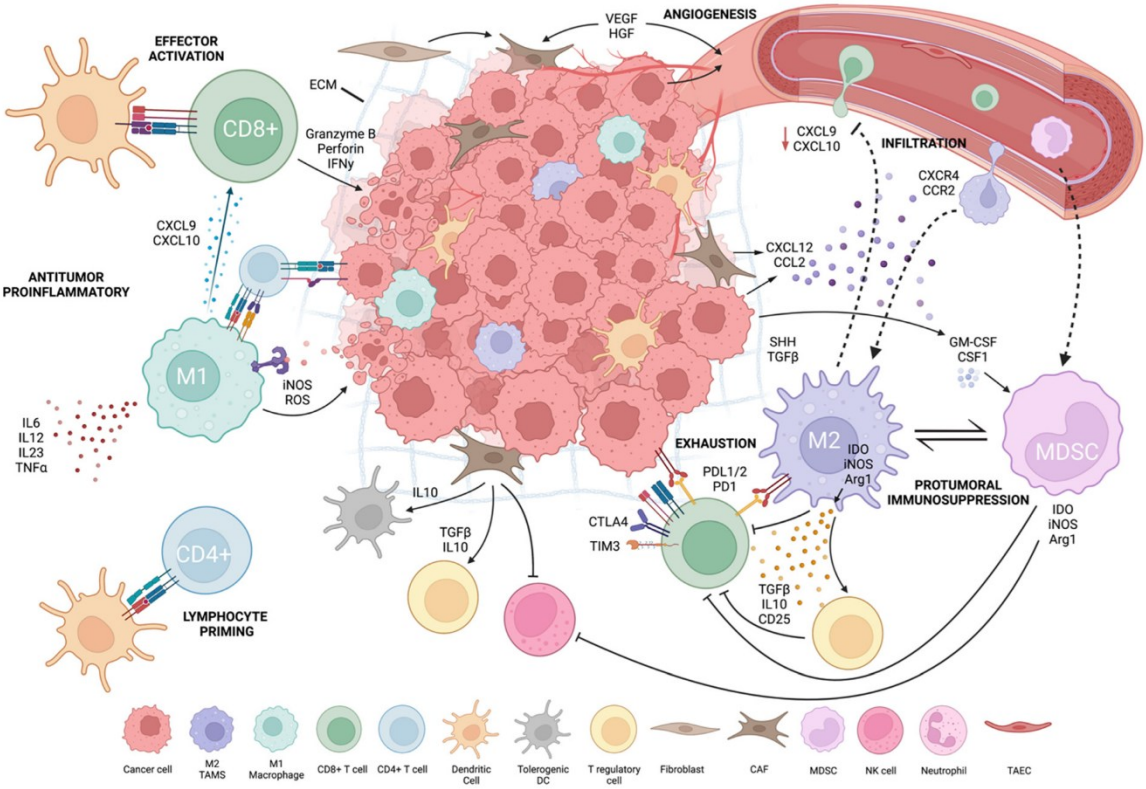

Figure 4. The tumor microenvironment (TME) and immune modulation in cancer progression. This schematic representation illustrates the complex interplay of immune and stromal cells within the TME, highlighting both anti-tumor influences – driven by $CD8^+$ T cells, M1 macrophages, and NK cells – and pro-tumor influences, mediated by M2 macrophages, regulatory T cells, and MDSCs. *Depicted from Peterson et al., 2022* [53].

1.4. Cancer immunotherapy (CIT)

Given that immune cells constitute the cellular basis of immunotherapy, it is crucial to gain insight into patient-specific immune infiltration within the TME to increase response rates and develop new CIT strategies [54].

Unlike traditional treatments such as chemotherapy or radiotherapy that target tumoral cells, CITs focus on the activation and strengthening of the patient's immune system, reshaping it to eradicate tumors or prevent their recurrence [19, 54-56]. The advantages of CITs are the long-term effects, broad applicability across several types of cancer, personalized and tailored application, and in most cases a better tolerance compared to classical approaches [55, 57-59].

In recent decades, clinical trials using antibodies that boost T lymphocyte activation, cancer vaccines, and adoptive T cell treatments have shown remarkable outcomes [55, 60, 61].

Overall, in the last decade, 57 new cancer immunotherapies have been approved by the FDA for the treatment of 17 solid tumor types [59]. In addition to monoclonal

antibodies (mAbs)-based immune checkpoint inhibitor (ICI) therapies, a broad range of cancer immunotherapies are being evaluated in preclinical and clinical settings, with an increasing number also receiving FDA or EMA approval for clinical use. These include oncolytic viruses, which have the ability to infect and destroy cancer cells while inducing an immune response; adoptive T-cell transfer (e.g. chimeric antigen receptor T-cell, CAR-T) therapy, which consists of genetically modified patient T cells that are able to identify and kill cancer cells; cancer vaccines, which prepare the immune system to attack cancer-specific antigens; and cytokine therapy, which boosts immune responses to cancer [56, 58, 61-72].

However, during both cancer development and immunotherapy, the process of cancer immunoediting occurs. This process helps to shape the immunogenic characteristics of tumors, reducing the strength of antitumor immune reactions. Importantly, cancer progression is tightly regulated by immune checkpoints, surface receptors expressed on immune- or cancer cells involved in the control of the activation or suppression of immunological responses [73, 74].

Thus, despite the advantages of CIT, there are still many challenges related to its efficacy and safety [53, 64]. Indeed, despite the long-term clinical benefit of some patients only 15–60% of patients treated with ICIs have a favorable response, highlighting the growing need for biomarkers that can be used to predict individual outcomes [56, 64, 75-77].

Additionally, immunotherapy-related adverse events (irAEs) can affect any organ in the body after ICI administration, representing a major clinical challenge and underscoring the importance of prompt identification and appropriate intervention to prevent complications and ensure positive patient outcomes [78, 79].

1.4.1. Immune checkpoint inhibitor (ICI) therapies

ICI therapies are based on the use of mAbs that target specific immune checkpoints which represent currently the first-line treatment for a wide range of malignancies [73]. However, identifying optimal patient selection strategies and determining the most effective CIT regimens remain crucial areas of investigation [80-82].

The most studied groups of ICIs approved by the FDA for the treatment of different malignant tumors such as melanoma, NSCLCs, , Merkel cell carcinoma (MCC), and head and neck squamous carcinoma (HNSCC) are programmed death (PD)-1 inhibitors (Nivolumab, Pembrolizumab, and Cemiplimab), programmed death-ligand (PD-L)1 inhibitors (Atezolimumab, Durvalumab and Avelumab), CTLA-4 inhibitor (Ipilimumab),

and lymphocyte-activation gene-3 (Lag-3) inhibitors (Relatlimab) (Errore. L'origine riferimento non è stata trovata. **5**) [53, 61, 75, 83-92].

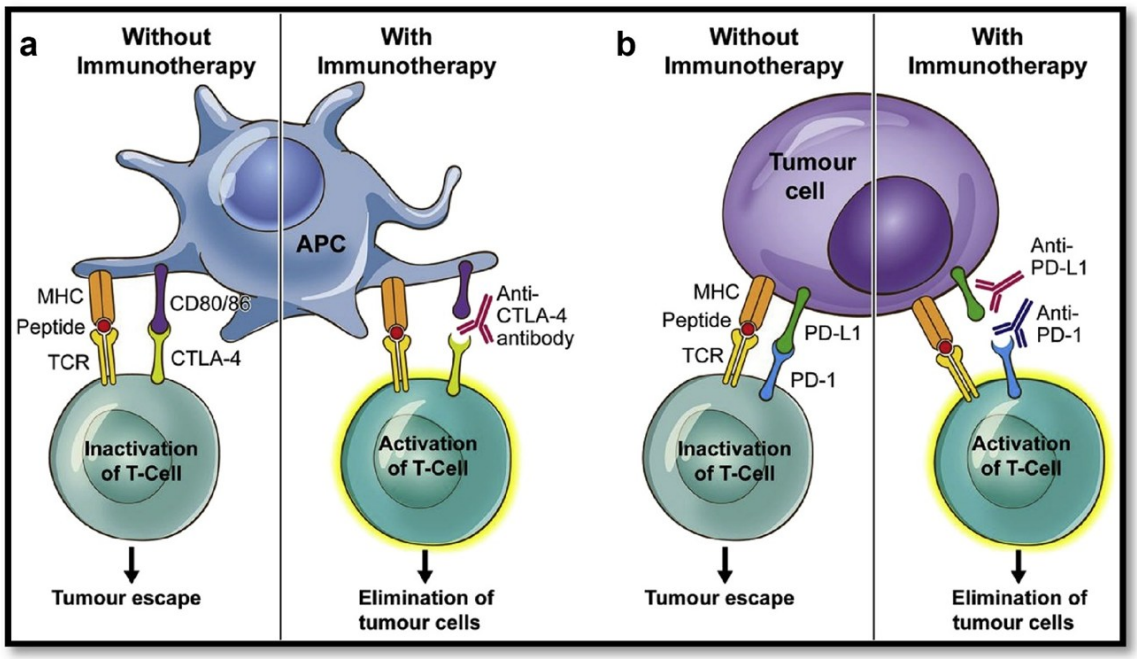

Figure 5. Schematic representation of clinically approved immune checkpoint inhibitors and their basic mechanisms of action. (**a**, left) tumor escape is promoted by the interaction of the CD80 molecule on antigen presenting cells (APCs) and CTLA-4 on T cells. (**a**, right) Anti-CTLA-4 antibody (e.g. Ipilimumab) binds to the CTLA-4 receptor on T cells promoting T-cell activation, thus tumor elimination. (**b**, left) PD-L1/PD-1 interactions inactivate T cells, promoting tumor evasion. (**b**, right) Anti-PD-L1 (e.g. Atezolimumab, Durvalumab, Avelumab) or anti-PD-1 (e.g. Nivolumab, Pembrolizumab, Cemiplimab) antibodies promote the activation of T-cells, initiating tumor elimination. CTLA-4: cytotoxic T lymphocyte-associated antigen 4, PD-1: programmed cell death 1, MHC: major histocompatibility complex, TCR: T-cell receptor. *Depicted from Lewis et al., 2020* [93].

Furthermore, new ICI targets are currently being evaluated in phase I/II clinical trials for patients with advanced solid tumors and B-cell non-Hodgkin's lymphomas. These targets include tumor necrosis factor receptor superfamily member 9 (TNFRSF9, or 4-1BB), which is expressed by activated T cells, NK cells, and antigen-presenting cells (APCs); OX40, which is highly expressed by activated $CD4^+$, $CD8^+$ T cells, and Tregs, as well as to a lesser extent by neutrophils and NK cells; and inducible costimulatory (ICOS), which is expressed mainly by $CD4^+$ T cells [83, 85, 94, 95].

While ICI therapy has revolutionized cancer treatment, many patients experience a limited response or develop resistance [54, 96]. To overcome these limitations, combined treatments have shown greater clinical effectiveness. Keys elements of combination therapies include the application of ICI, adoptive cell therapy, targeted therapy, chemotherapy, where their combination showed improved clinical efficacy and have been approved by the FDA [54, 56, 80, 81, 90, 97]. Several clinical trials are

currently underway to evaluate the safety and efficacy of these combinations in various malignancies. Early clinical data have shown promising results, with manageable toxicity profiles and encouraging signs of antitumoral activity. However, long-term follow-up and robust efficacy data are still needed to establish their clinical benefit [80, 81]. Thus, the identification of reliable biomarkers in guiding clinical treatment approaches are of main importance [56].

Recently, it has become increasingly clear that $CD4^+$ T cells are leading players in initiating and maintaining effective anti-tumor immunity. Furthermore, several studies demonstrate that the intratumoral distribution of these cells allows for the definition of therapy response, and their presence in immunotherapy-naïve patients is associated with favorable clinical outcomes [32, 35, 98-100].

1.5. Noninvasive imaging

Due to its complexity, a comprehensive understanding of the immune system might facilitate the prediction of patient outcomes and the development of effective, personalized treatment strategies for cancer patients. However, current clinical methods, such as tumor biopsies, are invasive for patients and provide only a limited snapshot, representing a significant limitation in the context of ongoing disease and therapy monitoring [101]. Therefore, a more comprehensive approach that encompasses not only cell counts but also spatial distribution, activity levels, and interactions throughout the body is necessary. Thus, *in vivo* molecular imaging offers a promising noninvasive approach for studying the immune system in action [101, 102].

1.5.1. Positron Emission Tomography (PET) imaging

PET imaging utilizes radioactive labelled compounds to evaluate and quantify biochemical alterations and molecules within deep tissues of living organisms. This technique offers picomolar detection sensitivity and is widely used in clinical oncology, neurology, and cardiology [102-105]. Combining PET imaging with anatomical imaging modalities such as X-ray computed tomography (CT) or magnetic resonance imaging (MRI) provides 3D anatomical reference information, enabling accurate quantification and improved image interpretation [104].

PET relies on the unique characteristic of neutron-deficient isotopes, such as fluorine-18 (^{18}F), carbon-11 (^{11}C), copper-64 (^{64}Cu), and zirconium-89 (^{89}Zr) to decay via positron (β^+) emission (**Table 1**) [104-108].

Table 1. Decay half-life of commonly used radioisotopes for PET imaging [104-108]:

Isotope	Half-life
^{18}F	110 min
^{11}C	20.3 min
^{64}Cu	12.8 h
^{89}Zr	78.4 h

Upon decay, the radionuclide emits a positron that travels a short distance (1–2 mm) before being annihilated with an electron. This interaction generates two high-energy (511 keV) photons that move in almost opposite directions (180° +/- 0.5°).

These photons are detected by opposing detectors arranged in a ring around the object, consisting of multiple crystal elements read out, for example, by photomultiplier tubes (PMTs) [104, 106, 109, 110].

The detected coincident photon pairs are sorted into sinograms, and the radioactivity distribution is reconstructed using dedicated image reconstruction algorithms [106]. This allows for the localization of the positron-emitting radiotracer within the tissue-of-interest. However, different types of events can occur during PET measurements: true events, scattered events, or random coincidences.

Among these, only true events provide accurate information. The other two types of events introduce noise and degrade image quality. On one hand, scattered events represent a type of background noise where both annihilated photons are diverted from their original direction. However, these events can be discriminated from true events based on the energy of the scattered photons. On the other hand, random coincidences represent a type of background noise that occurs when two separated annihilation events occur at different locations but very close in time.

In addition, a separate scan either using external sources such as $^{68}Ge/^{68}Ga$ (germanium-68/gallium-68) or Co-57 (cobalt-57), or a Computed Tomography (CT)-scan is required to correct for signal loss due to attenuated photons, enabling a more accurate quantification of activity within the body (**Figure 6**) [106].

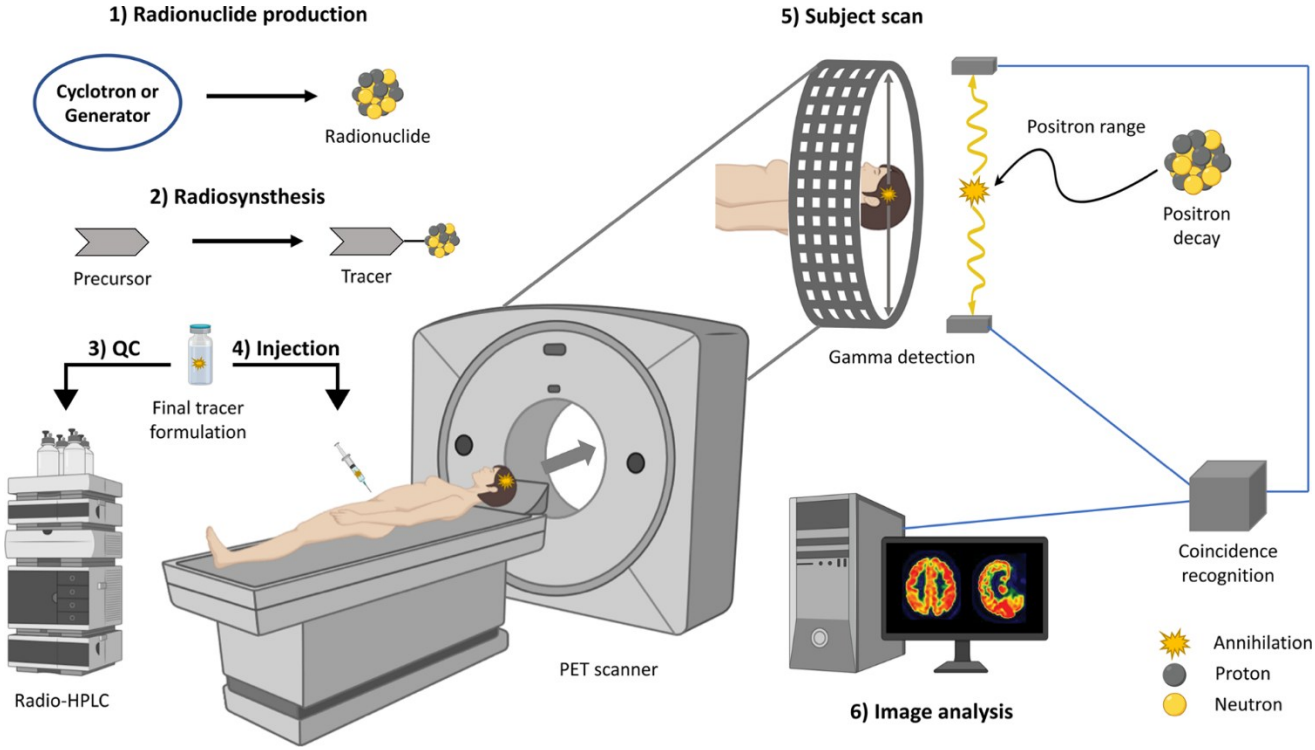

Figure 6. PET imaging workflow. (1) The radionuclide is produced through a cyclotron or generator. This is followed by (2) radiosynthesis where a precursor is labeled with the radionuclide to form a radiotracer. (3) Radio-HPLC is used to perform the quality control (QC) of the final tracer, which is then (4) injected into the patient. During (5) the PET scan, the tracer undergoes positron decay, resulting in γ-photon emission via annihilation, which is detected by the PET scanner. Coincidence detection is used to localize events. Finally, (6) image analysis is performed to generate detailed 3D images of tracer distribution, typically using computational software for visualization and interpretation. *Depicted from Rong et al., 2023* [111].

Since its FDA approval in 2000, 2-deoxy-2-[fluorine-18]fluoro-D-glucose ([^{18}F]FDG) is the most commonly used radiotracer in oncology [104, 106, 112]. As a glucose analog, FDG allows for the visualization of cellular glucose metabolism. Cancer cells, characterized by their elevated glucose uptake and utilization, accumulate and retain [^{18}F]FDG at much higher levels than surrounding healthy tissues. This property underlies the broad applicability of [^{18}F]FDG PET imaging, which is routinely used for cancer staging, treatment monitoring and cancer recurrence detection. However, while applicable to most cancer types, some malignancies, such as prostate cancer, hepatocellular carcinoma (HCC), renal cell carcinoma (RCC), low-grade sarcomas, low-grade lymphomas, and brain tumors, are poorly investigated by [^{18}F]FDG PET likely due to its low target specificity [112].

Furthermore, highly activated immune cells, such as T cells and myeloid cells, exhibit a strongly enhanced glucose metabolism, making [^{18}F]FDG PET a valuable tool for the detection of inflammatory diseases. However, within inflamed tumors, this behavior could lead to a misinterpretation of the [^{18}F]FDG PET results in a phenomenon called

pseudoprogression, a transient increase of tumor burden followed by delayed tumor shrinkage in response to treatment [113-117].

Furthermore, [^{18}F]FDG uptake is not only specific for tumors but can also detect benign pathologies and inflammatory diseases, leading to false-positive. The limited specificity of [^{18}F]FDG PET has driven the development of novel tracers capable of targeting specific antigens expressed by either tumor cells or immune cells, thereby advancing precision oncology through more accurate and biologically informative imaging [112, 118, 119].

1.5.2. ImmunoPET imaging

ImmunoPET imaging integrates the high specificity of target-specific probes with the superior sensitivity of PET, allowing for noninvasive *in vivo* visualization of precise molecular targets, such as cell surface antigens, with potential applications in patient-specific treatment decision-making and monitoring treatment response [120]. The first *in viv*o clinical visualization of solid tumors through immunoPET imaging was achieved in 1978 via iodine-131 (^{131}I)-labeled whole immunoglobulin G (IgG) targeting carcinoembryonic antigen (CEA) [121]. Since then, significant research has been conducted to develop radiotracers for immunoimaging with high specificity for antigens expressed by cancer or immune cells. These tracers include a range of formats, from full-size antibodies to smaller antibody fragments.

Various tumor-targeting probes have been investigated for immunoPET, with full-length mAbs being the most used forms [122]. However, despite their clinical success, several limitations must be considered. These include slow blood clearance, serum toxicity, and a poor target-to-background ratio (TBR). To address these limitations, antibody fragments generated through enzymatic production or protein engineering have been introduced as potential alternatives to mAb immunoPET probes.

Ideally, an immunoPET tracer should exhibit high target specificity, minimal biological interaction, serum stability, rapid biodistribution, and efficient background clearance [112].

1.5.3. Engineered antibody fragments

Engineered antibodies include fragment antigen binding antibodies $(Fab')_2$ (110 kDa) and Fab (50 kDa), which are generated by removing the fragment crystallizable (Fc) region from full-length antibodies, resulting in smaller molecules that retain antigen-binding capabilities while reducing effector functions. Minibodies (Mbs; 80 kDa) are

engineered by fusing a single-chain fragment variables (scFv) molecule with the constant heavy chain-3 (CH3) domain of human IgG1, creating a more stable bivalent antibody fragment with improved pharmacokinetics. Diabodies (55 kDa) are bispecific antibody fragments that are formed by linking heavy chain variable fragments (V_H) and light-chain variable fragments (V_L). ScFv (25 kDa) consisting only of light and heavy variable chains. Nanobodies (Nbs, VHH; 15 kDa), derived from the unique heavy-chain-only antibodies found in camelids, are the smallest antibody fragments currently available, providing exceptional tissue penetration and the ability to bind to cryptic epitopes inaccessible to larger antibodies. Despite their size, nanobodies exhibit high stability and specificity, making them versatile for therapeutic and imaging applications. (**Figure 7**)[122-125].

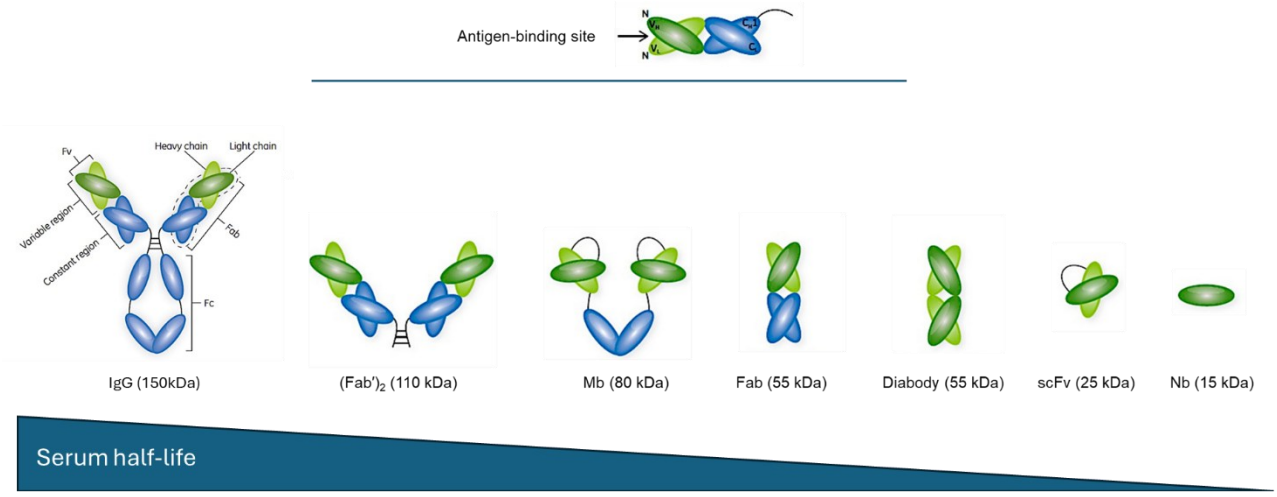

Figure 7. Schematic representation of full-size antibody and engineered antibody fragments. IgG: immunoglobulin G, Fab: fragment antigen binding antibody, Mb: minibody, scFv: single-chain fragment variable, Nb: nanobody. *Adapted from Rodrigo et al., 2015* [126].

Their rapid clearance can address critical limitations of PET imaging, paving the way for same-day imaging and reducing patient radiation exposure [127-134]. This feature is essential when imaging highly complex processes, such as an immune response, where a single imaging tracer may not be sufficient to capture the whole picture [82].

Several immunoPET tracers are currently undergoing clinical trials to detect different types of cancer [117]. For instance, ^{89}Zr-Pertuzumab and ^{89}Zr-Trastuzumab can identify HER2-positive tumors in breast cancer [122, 135-139]. Furthermore, anti-PD1 (^{89}Zr-nivolumab, and ^{89}Zr- pembrolizumab) and anti-PD-L1 (^{89}Zr-atezolizumab) antibodies, are used for the selection of NSCLC patients for immunotherapy [140-145].

Notably, only a few Nbs currently being developed for noninvasive imaging, such as anti-HER2-specific Nb 2Rs15d, have been characterized for their epitopes and evaluated in a phase I clinical study [146, 147].

In addition to immunoPET probes targeting immune checkpoint molecules or tumor-specific antigens, the development of radiotracers for applications in immunology has been significantly enhanced by the availability of a large existing database of “CD” markers expressed on the immune cell surface. These include classic biomarkers, such as CD45, for the primary lineages of hematopoietic cells, including those of the lymphocytic and myeloid varieties, as well as their numerous subsets. The distinction between T- and B-cell lineages and the corresponding malignancies derived from these cell types can be determined by the presence of specific markers such as CD3, CD4, and CD8 (T lineage) or CD19 and CD20 (B lineage). On the other hand, myeloid cells are identified by significant markers such as CD33, CD206, CD163 or SIPRα [148-151].The primary cell types can be further distinguished by functional subsets, such as helper vs regulatory subsets of CD4 T lymphocytes or M1 vs M2 macrophage phenotypes, as well as by their activation state (CD25, CD69, OX40) [82].

The noninvasive evaluation of immune cells may predict the response to immunomodulatory therapies. In this context, engineered Abs have been developed to monitor TIL dynamics after therapy [152-154]. A successful example for clinical use is the anti-CD8 minibody [^{89}Zr]Zr-crefmirlimab berdoxam ([^{89}Zr]Zr-IAB22M2C). [^{89}Zr]Zr-crefmirlimab berdoxam is an engineered scFv-CH3 antibody fragment of approximately 80 kDa obtained from the humanized heavy and light chain sequences of the murine anti-human OKT8 antibody [132]. Owing to the lack of the CH2 domain, it is biologically inert, and no interaction with Fc-gamma receptors or the FcRn recycling receptor has been reported [82].

The evaluation of [^{89}Zr]Zr-crefmirlimab berdoxam in a phase II clinical trial demonstrated not only favorable biodistribution but also its ability to visualize a wide range of tumor lesions within 24–48 hours post-injection [122, 132]. Moreover, PET imaging demonstrated enhanced uptake in patients undergoing immunotherapy, potentially indicating immune system modulation and CD8$^+$ cell infiltration into the tumor [155]. Additionally, [^{89}Zr]Zr-crefmirlimab berdoxam exhibited low nonspecific uptake, suggesting its potential to quantify CD8$^+$ cell infiltrates even in "immune desert" tumors,

which typically have few to no immune infiltrates. These characteristics indicate that minibody-based probes are potentially helpful tools for targeted cancer immunotherapy and other immune-related therapies [82, 127-134, 156].

However, due to their exceptional physical properties, nanobody-based probes are attracting significant interest for potential clinical applications. Key properties include their small size, high stability, rapid tissue penetration, and rapid clearance from nontarget regions [157]. This interest is supported not only by promising results in imaging $CD8^+$ T-cell dynamics during immunotherapy, but also by other nanobody-based imaging tracers targeting different markers tested in preclinical and clinical settings. For example, an early phase I trial with a ^{68}Ga-NOTA-CD8-targeting Nb demonstrated safety, with no adverse events, and showed uptake in lymphoid-rich organs and tumors [158]. Another nanobody-based probe, ^{68}Ga-NOTA-Anti-MMR VHH2, is being developed to visualize $CD206^+$ macrophages and is currently undergoing a phase I/IIa clinical trial with various cancers, including breast cancer, head and neck cancer, melanoma, and other oncological disorders. These developments highlight the growing potential of nanobody-based imaging probes in targeting different aspects of the immune system [159-161]. Nevertheless, despite the relevance of $CD4^+$ cells in cancer progression and immunotherapy response, the focus on CD4-targeting PET tracers remains limited, with only a few candidates currently under preclinical investigation. These include small fragments such as the murine and rhesus CD4-specific F(ab')2 fragment [162-164], the murine CD4-specific cys-diabody [165-167], and the human CD4-targeting scFv-CH3 fragment [168].

However, despite the critical role of $CD4^+$ T cells in tumor progression, there are not clinically available immunoPET tracers in perspective that allow for specific and whole-body visualization of these cells to guide treatment decisions and monitor over-time patient specific outcome [72].

2. Objectives and expected outcomes

The current lack of CD4-targeting immunoPET probes together with the central role of this immune cell population in orchestrating immune responses emphasize the need for noninvasive CD4-specific PET tracers. These tracers would provide valuable tools for monitoring $CD4^+$ cell distribution in patients and enable personalized treatment strategies. Given the favorable clinical outcomes achieved with minibody- and nanobody-based tracers targeting other immune components, this thesis aims to validate minibody (^{89}Zr-h/mCD4-Mbs) and nanobody (^{64}Cu-CD4-Nb1)-based immunoPET tracers for noninvasive whole-body visualization of endogenous $CD4^+$ cells.

Three main objectives were formulated for both CD4-directed tracer formats and pursued within the thesis:

i. to validate their specific binding *in vitro* and *in vivo,* as well as assess *in vivo* organ biodistribution kinetics.

ii. to evaluate their sensitivity for quantifying tumor infiltrating $CD4^+$ cells.

iii. to explore their potential as imaging biomarkers for therapy monitoring and clinical decision-making.

The general hypothesis of this work was that small-sized tracers targeting the CD4 immune cell subset would enable faster and more accurate characterization of the tumor microenvironment, providing insights into $CD4^+$ cell migration dynamics related to immunotherapy, as well as the mechanisms of actions of immune checkpoint inhibitor therapy.

3. Results

This thesis consists of two original publications on the validation of novel immunoPET imaging probes targeting $CD4^+$ cells for the visualization of endogenous immune infiltrates and their dynamics in response to ICI-therapy in preclinical cancer models. The first published manuscript (*Accepted publication I*) focuses on the cross-validation of murine and human CD4-targeting minibodies [1]. The second published manuscript (*Accepted publication II*) focuses on the production and extensive validation of CD4-Nb1 [2], supported by the third manuscript (*Accepted publication III*) about the evaluation of CD4-Nb1 as an imaging probe for precise intratumoral spatial visualization of $CD4^+$ T cells and ICI treatment outcome prediction [4].

3.1. Accepted publication I

Pezzana, S., Blaess, S., Kortendieck, J., Hemmer, N., Tako, B., Pietura, C., Ruoff, L., Riel, S., Schaller, M., Gonzalez-Menendez, I., Quintanilla-Martinez, L., Mascioni, A., Aivazian, A., Wilson, I., Maurer, A., Pichler, B.J., Kneilling, M., Sonanini, D. (2024). In-depth cross-validation of human and mouse CD4-specific minibodies for noninvasive PET imaging of CD4+ cells and response prediction to cancer immunotherapy. Theranostics, 14(12), 4582-4597. https://doi.org/10.7150/thno.95173 [1]

IVYSPRING INTERNATIONAL PUBLISHER

Theranostics

2024; 14(12): 4582-4597. doi: 10.7150/thno.95173

Research Paper

In-depth cross-validation of human and mouse CD4-specific minibodies for noninvasive PET imaging of CD4$^+$ cells and response prediction to cancer immunotherapy

Stefania Pezzana[1], Simone Blaess[1], Jule Kortendieck[1], Nicole Hemmer[1], Bredi Tako[1,2], Claudia Pietura[1], Lara Ruoff[1], Simon Riel[7], Martin Schaller[7], Irene Gonzalez-Menendez[3,4], Leticia Quintanilla-Martinez[3,4], Alessandro Mascioni[5], Argin Aivazian[5], Ian Wilson[5], Andreas Maurer[1,3], Bernd J. Pichler[1,3,6], Manfred Kneilling[1,3,7], Dominik Sonanini[1,3,8,✉]

1. Werner Siemens Imaging Center, Department of Preclinical Imaging and Radiopharmacy, University Hospital Tuebingen, University of Tuebingen, Tuebingen, Germany.
2. Department of Nuclear Medicine, University Hospital Tuebingen, Eberhard Karls University, Tuebingen, Germany.
3. Cluster of Excellence iFIT (EXC2180) "Image-Guided and Functionally Instructed Tumor Therapies", University of Tuebingen, Tuebingen, Germany.
4. Department of Pathology and Neuropathology, University Hospital Tuebingen, University of Tuebingen, Tuebingen, Germany.
5. ImaginAb, Inglewood, United States of America.
6. German Cancer Consortium (DKTK) and German Cancer Research Center (DKFZ) partner site Tuebingen, Tuebingen, Germany.
7. Department of Dermatology, University Hospital Tuebingen, University of Tuebingen, Tuebingen, Germany.
8. Department of Medical Oncology and Pneumology, University Hospital Tuebingen, University of Tuebingen, Tuebingen, Germany.

✉ Corresponding author: Dominik Sonanini, Department of Preclinical Imaging and Radiopharmacy Eberhard Karls University Tübingen Röntgenweg 13, 72076 Tübingen, Germany; Phone: +49-7071-29-87443; Fax: +49-7071-29-4451; E-mail: Dominik.Sonanini@med.uni-tuebingen.de.

Received: 2024.02.08; Accepted: 2024.07.11; Published: 2024.08.01

Abstract

Increasing evidence emphasizes the pivotal role of CD4$^+$ T cells in orchestrating cancer immunity. Noninvasive *in vivo* imaging of the temporal dynamics of CD4$^+$ T cells and their distribution patterns might provide novel insights into their effector and regulator cell functions during cancer immunotherapy (CIT).

Methods: We conducted a comparative analysis of ^{89}Zr-labeled anti-mouse (m) and anti-human (h) CD4-targeting minibodies (Mbs) for *in vivo* positron emission tomography (PET)/magnetic resonance imaging (MRI) of CD4$^+$ T cells in human xenografts, syngeneic tumor-bearing wild-type (WT), and human CD4$^+$ knock-in (hCD4-KI) mouse models.

Results: Both ^{89}Zr-CD4-Mbs yielded high radiolabeling efficiencies of >90%, immunoreactivities of >70%, and specific *in vitro* binding to their target antigens. The specificity of *in vivo* targeting of ^{89}Zr-hCD4-Mb was confirmed by PET/MRI, revealing ~4-fold greater ^{89}Zr-hCD4-Mb uptake in subcutaneous hCD4$^+$ hematopoietic peripheral blood acute lymphoblastic leukemia tumors (HPB-ALL) than in solid hCD4$^-$ diffuse histiocytic lymphomas (DHL) and ^{89}Zr-mCD4-Mb uptake in hCD4$^+$ HPB-ALL tumors. In a comparative cross-validation study in anti-programmed death ligand (αPD-L1)/anti-4-1BB-treated orthotopic PyMT mammary carcinoma-bearing hCD4-KI and WT mice, we detected 2- to 3-fold enhanced species-specific ^{89}Zr-hCD4-Mb or ^{89}Zr-mCD4-Mb uptake within CD4$^+$ cell-enriched secondary lymphatic organs (lymph nodes and spleens). The ^{89}Zr-hCD4-Mb uptake in the PyMT tumors was more pronounced in hCD4-KI mice compared to the WT control littermates. Most importantly, MC38 adenocarcinoma-bearing mice treated with a combination of αPD-L1 and anti-lymphocyte-activation gene 3 (αLag-3) antibodies exhibited ~1.4-fold higher ^{89}Zr-mCD4-Mb uptake than mice that were not responsive to therapy or sham-treated mice.

Conclusion: CD4 PET/MRI enabled monitoring of the CD4$^+$ cell distribution in secondary lymphatic organs and the tumor microenvironment, capable of predicting sensitivity to CIT. Our imaging approach will provide deeper insights into the underlying molecular mechanisms of CD4-directed cancer immunotherapies in preclinical mouse models and is applicable for clinical translation.

Introduction

Many novel cancer immunotherapies have emerged in recent years, reshaping the cancer treatment landscape. These include immune checkpoint inhibitors (ICIs), chimeric antigen receptor T cells, bispecific T-cell engagers, peptide-based vaccines, and oncolytic virotherapies [1-3]. With several FDA/EMA-approved monoclonal antibodies (mAbs) targeting programmed death receptor (PD-1) or its ligand (PD-L1), cytotoxic T lymphocyte antigen 4 (CTLA-4), and lymphocyte-activation gene 3 (LAG-3), ICIs are widely used in clinical practice for several tumor types, including melanoma, lung cancer, lymphoma, and renal cell carcinoma [1, 4-6]. While these immunotherapies have shown remarkable success in achieving long-term remission even in patients with metastatic and chemotherapy-resistant cancers, their current overall response rates remain unsatisfactory, ranging from 12% to 60% depending on the tumor type and therapeutic combination [1, 6-9]. Moreover, currently available genomic or immunohistochemical expression patterns, such as PD-L1 expression, tumor mutational burden, and microsatellite instability, from tumor biopsies exhibit limited predictive value in clinical practice [10-14], underscoring the pressing need for robust biomarker identification that can reliably stratify patients and predict immunotherapy efficacy.

While $CD8^+$ cytotoxic T lymphocytes (CTLs) are well established as the primary cell population conveying cytotoxic antitumoral responses, mounting evidence emphasizes the pivotal role of $CD4^+$ T helper cells in orchestrating cancer immunity [15, 16]. Based on their differentiation, tumor antigen (TA)-specific $CD4^+$ T helper cells can exhibit either protumoral or antitumoral functions [17, 18]. Interferon-gamma (IFNγ)-producing $CD4^+$ T helper (Th1) cells are highly efficient antitumoral players because of their ability to induce polarization into proinflammatory M1 macrophages, cross-prime CTLs, initiate the recruitment of dendritic and natural killer (NK) cells [16, 19-22], or induce tumor senescence [23].

In contrast, TA-specific interleukin (IL)-4-producing $CD4^+$ T helper (Th2) cells evolved as a negative prognostic marker within the tumor microenvironment (TME) as they promote tumor growth by enhancing angiogenesis and inhibiting cell-mediated immunity [24-26]. $CD4^+$ T cells can also acquire a regulatory phenotype (Tregs) essential to downregulate excessive T cell responses and inhibit antitumoral immune responses [27-29].

Besides Th1, Th2 cells, and Tregs, several other $CD4^+$ T cell subsets, including IL-9- (Th9), IL-17- (Th17), and IL-22-producing (Th22) T helper cells, have been identified with distinct functions [16, 30, 31]. Recent studies have described a TA-specific $CD4^+$ T-cell subtype with direct cytotoxic effects [32-34]. The CD4 antigen was found to be expressed on subsets of NK cells, monocytes, and macrophages at lower levels and is involved in differentiation, migration, and cytokine expression [35].

The absence of reliable biomarkers for the prediction of efficient antitumoral immune responses upon cancer immunotherapy and the growing interest in harnessing $CD4^+$ T cells for their antitumoral potential prompted us to embark on in-depth validation of a minibody-based strategy for tracking endogenous $CD4^+$ T-cell dynamics within tumors and lymphatic organs *in vivo* by whole-body immune positron emission tomography (immunoPET). This technique offers a direct and noninvasive imaging approach combining the sensitivity of PET isotopes with the specificity of antibodies applicable for monitoring the expression of cancer and immune cell surface proteins [36, 37].

To date, only few $CD4^+$ cell-targeting PET tracers have been validated for use in animal models. Kim *et al.* evaluated a ^{89}Zr-labeled human CD4-specific therapeutic antibody ibalizumab and a rhesus $F(ab')_2$ fragment to noninvasively quantify $CD4^+$ cells in rhesus macaques [38]. Kristensen *et al.* correlated PET uptake of a murine CD4-specific $F(ab')_2$ tracer with *ex vivo* $CD4^+$ T-cell tumor infiltration in seven preclinical syngeneic tumor models and monitored infiltration upon αPD-1-based checkpoint inhibitor therapy (CIT)[39]. In addition, Clausen *et al.* applied an identical tracer to longitudinally investigate collagen-induced arthritis mouse models [40]. Wu and colleagues developed a biologically inert murine CD4-specific cys-diabody PET tracer (~50 kDa) [41] to monitor the repopulation of $CD4^+$ T cells after hematopoietic stem cell transplantation [42] and $CD4^+$ T-cell migration into sites of inflammation in DSS-induced experimental colitis [43]. Recently, we successfully developed a human CD4-targeting single domain antibody (nanobody)-based immunoPET probe (~15 kDa) to enable $CD4^+$ cell tracking in the clinical setting and validated its biological properties and biodistribution in a human-CD4 knock-in mouse model [44]. Nagle *et al.* implemented a human-specific CD4 scFv-CH3 fragment (minibody, Mb, ~80 kDa) radiolabeled with ^{64}Cu to follow human $CD4^+$ T cell migration into a patient-derived glioblastoma [45].

In this study, we radiolabeled anti-mouse and anti-human CD4-targeting Mbs with ^{89}Zr using the chelator desferrioxamine (dfo) and extensively validated both immunotracers in xenograft, syngeneic, and hCD4 knock-in (KI) tumor mouse models to assess their specificity and cross-species

comparability. Furthermore, we evaluated the potential of these compounds as imaging biomarkers for predicting the efficacy of ICI-based cancer immunotherapies. To our knowledge, this is the first study to analyze human- and mouse-specific immunotracers comparatively. As a cross-species theranostic approach, CD4-PET might be applied to novel immunotherapies in preclinical mouse models and subsequently used in clinical studies for therapy guidance and response evaluation. Thus, noninvasive *in vivo* monitoring of $CD4^+$ cells with CD4-specific immunotracers holds the promise of providing valuable insights into the efficacy of cancer immunotherapy and will facilitate a better understanding of T-cell-based immunotherapies and $CD4^+$ T-cell-mediated immune responses in immune-mediated inflammatory diseases.

Results

^{89}Zr-hCD4-Mbs and ^{89}Zr-mCD4-Mbs specifically bind to their target antigens *in vitro*

For radiolabeling with ^{89}Zr, hCD4- and mCD4-Mbs were conjugated to the radiochelator dfo, which did not impair the affinity in the (sub)nanomolar range as revealed by ELISA (Figure 1A) and flow cytometry (Figure S1A). Subsequent ^{89}Zr-radiolabeling yielded >90% radiolabeling efficiency, as determined by HPLC (Figure 1B). Maximum binding assays with increasing numbers of cells (Figure S1B) showed immunoreactive fractions of 78.4% for ^{89}Zr-hCD4-Mb using CD4-expressing human HPB-ALL cells and 84.3% for ^{89}Zr-mCD4-Mb using murine $CD4^+$ T cells. We further confirmed the hCD4-expression on HPB-ALL cells (Figure S1D) and the specific binding of both tracers to the target antigen by species-specific $CD4^+$ and $CD4^-$ *in vitro* cell assays (Figure 1C, Figure S1E) and through CD4 blocking experiments using a 100-fold excess of unlabeled CD4-Mb. Furthermore, we tested for potential cross-reactivity of both tracers by ELISA with hCD4- or mCD4 using both tracers. Here, neither the hCD4-Mb bound to mouse mCD4, nor the mCD4-Mb to human CD4 (Figure S1C). Most importantly, hCD4-Mb did not induce human PBMC proliferation under coated or soluble conditions (Figure S1E) and remained as stable radioimmunoconjugate over 72 hours in serum (Figure S1F), prerequisite for potential clinical application.

hCD4-specific *in vivo* binding of ^{89}Zr-hCD4-Mb to hCD4$^+$ HPB-ALL xenografts in NSG mice

After we successfully validated radiolabeling and specific *in vitro* binding of ^{89}Zr-hCD4-Mb and ^{89}Zr-mCD4-Mb to $CD4^+$ cells, we examined the *in vivo* PET uptake of ^{89}Zr-hCD4-Mb by HPB-ALL leukemia xenografts (which constitutively express the hCD4 antigen) subcutaneously *(s.c.)* implanted into NSG mice. The tumor volumes at the tracer injection time point ranged between 50 and 700 mm^3 (Figure S2A). We observed a 3.5- to 5-fold increase in the ^{89}Zr-hCD4-Mb uptake within $hCD4^+$ HPB-ALL tumors compared with $hCD4^-$ DHL B-cell lymphomas at 6, 24, and 48 h post tracer injection (Figure 2A, 2C–D; Figure S2C). Interestingly, the ^{89}Zr-mCD4-Mb uptake in $hCD4^+$ HPB-ALL tumors, which served as another control group, was slightly higher than the ^{89}Zr-hCD4-Mb uptake in $CD4^-$ DHL tumors (Figure 2A, 2C - D; Figure S2C), indicating $mCD4^+$ cell infiltration in T-cell-deficient NSG mice. We detected significantly higher ^{89}Zr-mCD4-Mb uptake within the spleen (Figure 2B; Figure S2B, *in vivo*) and in the lymph nodes (Figure 2E, *ex vivo* biodistribution) compared to both groups injected with ^{89}Zr-hCD4-Mb. Immunohistochemistry (IHC) of the tumors and spleens confirmed the presence of a limited number of $mCD4^+$ cells, presumably $CD4^+$ myeloid cells, based on their nuclear morphology and absence of $CD3^+$ cells in the spleen (Figure 2F-G). As expected from the Mb-based tracer, most of both ^{89}Zr-CD4-Mbs cleared from the blood within 48 h with minimal residual uptake in the muscles, lungs, and hearts of all groups (Figure S2C-D). Furthermore, ^{89}Zr-mCD4-Mb exhibited a higher kidney uptake and lower liver uptake than ^{89}Zr-hCD4-Mb at the 48-h *ex vivo* biodistribution time point (Figure S2E), presumably attributed to different excretion kinetics of the radioimmunoconjugates.

In conclusion, this experiment confirmed the specific *in vivo* binding of ^{89}Zr-hCD4-Mb to $hCD4^+$ cells and the presence of limited densities of $mCD4^+$ cells ^{89}Zr-hCD4-Mb in the tumor tissue and lymphatic organs of NSG mice.

Whole-body tracking of endogenous CD4$^+$ immune cells in ICI-treated human CD4 knock-in (KI) and wild-type (WT) syngeneic orthotopic breast cancer mouse models

We orthotopically implanted mammary PyMT tumors into wild-type (WT) and hCD4 antigen knock-in (hCD4-KI) mice to further explore endogenous $CD4^+$ cells in the tumor, spleen, draining and nondraining lymph nodes (dLNs and ndLNs). All experimental mice were subjected to combined αPD-1/α4-1BB immunotherapy two days before injecting ^{89}Zr-hCD4-Mb or ^{89}Zr-mCD4-Mb to increase the $CD4^+$ T cell density of established tumors (Figure 3A, Figure S4A).

We detected 2-3-fold enhanced ^{89}Zr-hCD4-Mb uptake in the spleens and lymph nodes of PyMT

tumor-bearing hCD4-KI mice compared with WT mice (Figure 3B, C; Figure S3A-B, S4B). Likewise, we found a similar 2-3-fold increased PET uptake with ^{89}Zr-mCD4-Mb in the lymphatic organs of PyMT tumor-bearing mCD4$^+$ WT mice compared to non-species-specific hCD4-KI mice (Figure 3B, C; Figure S3A-B, S4B). Interestingly, the absolute ^{89}Zr-mCD4-Mb PET uptake was higher in the lymphatic organs of species-specific and non-species-specific groups than the ^{89}Zr-mCD4-Mb PET uptake (Figure 3B-D). Together with the different excretion kinetics within the NSG mouse models (Figure S2E), these data suggested a slightly different biodistribution between ^{89}Zr-mCD4-Mb and ^{89}Zr-hCD4-Mb in a target-unrelated manner. Also, the *ex vivo* biodistribution analysis of lymphatic organs confirmed our *in vivo* ^{89}Zr-hCD4-Mb-PET/MRI results (Figure 3D). In addition, we detected a similar αCD4 PET uptake in the tumor-draining and non-draining lymph nodes (Figure 3B-D).

Next, we focused on ^{89}Zr-hCD4-Mb and ^{89}Zr-mCD4-Mb uptake within the TME and detected significantly enhanced ^{89}Zr-hCD4-Mb uptake in αPD-1/α4-1BB-treated PyMT tumor-bearing hCD4-KI mice when compared to WT mice (3.22 ± 0.23 vs. 2.51 ± 0.06 %ID/ml, Figure 4A, B). Surprisingly, ^{89}Zr-mCD4-Mb PyMT tumor uptake was even higher in hCD4-KI mice than in target-specific WT mice expressing mCD4$^+$ (Figure 4A, B). To further elaborate on whether target-specific tracer consumption effects in the lymphatic organs occurring only in species-specific mice were responsible for these unexpected observations, we analyzed the *in vivo* blood uptake in all experimental mice. We found a 1.9-fold lower ^{89}Zr-mCD4-Mb PET uptake in the blood of WT mice than hCD4-KI control mice (Figure 4C), resulting in a pronounced species-specific ^{89}Zr-mCD4-Mb PET uptake when corrected for blood background (8.76 ± 0.99 vs. 6.30 ± 0.77, non-significant, Figure 4D). These findings also applied to the ^{89}Zr-hCD4-Mb to a lesser extent (Figure 4C-D) and could be confirmed by *ex vivo* biodistribution analyses of the tumor and blood (Figure 4E-G).

Despite the limitations of knock-in/out mouse models in the absolute quantification of antibody-based immunotracers, we could quantitatively measure increased and comparable PET uptake patterns of the lymphatic organs and the TME in a syngeneic orthotopic tumor mouse model for ^{89}Zr-hCD4-Mb and ^{89}Zr-mCD4-Mb.

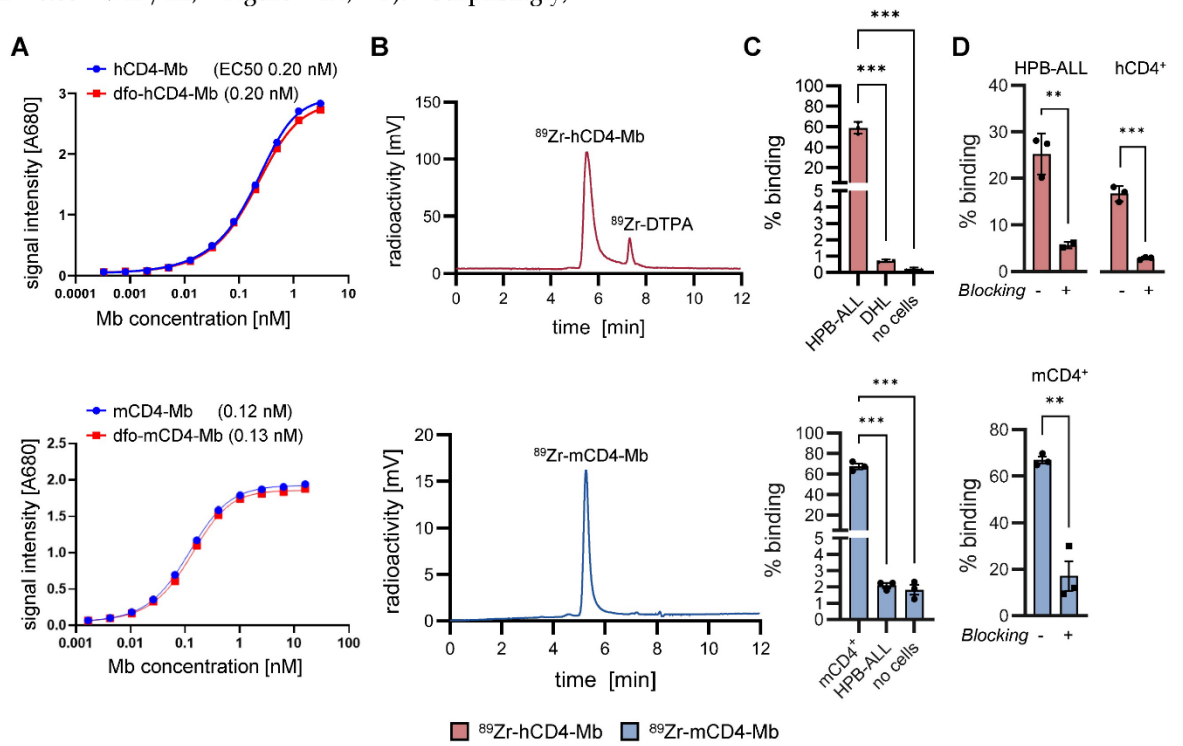

Figure 1. *In vitro* validation of ^{89}Zr-hCD4-Mb and ^{89}Zr-mCD4-Mb. (A) ELISA assay of hCD4-Mb (top) and mCD4-Mb (bottom) with or without dfo conjugation to recombinant human CD4-his or mCD4-his protein. (B) HPLC chromatograms of dfo-h/mCD4-Mb after radiolabeling with ^{89}Zr. (C) Total binding of ^{89}Zr-h/mCD4-Mb under antigen excess conditions using HPB-ALL, DHL, or freshly isolated mCD4$^+$ cells as indicated (40 x 10^6 cells per well, triplicates). (D) Total binding of ^{89}Zr-h/mCD4-Mb to HPB-ALL cells, freshly isolated hCD4$^+$ or mCD4$^+$ cells as indicated (2 x 10^6 cells per well, triplicates) with or without blocking with a 100-fold excess of unlabeled h/mCD4-Mb. *P* values were calculated by ordinary one-way and Tukey post-hoc (C) or unpaired t-test for pairwise comparisons (D). The data are presented as mean ± SD. *$p < 0.05$, **$p < 0.01$, ***$p < 0.001$; ****$p < 0.0001$.

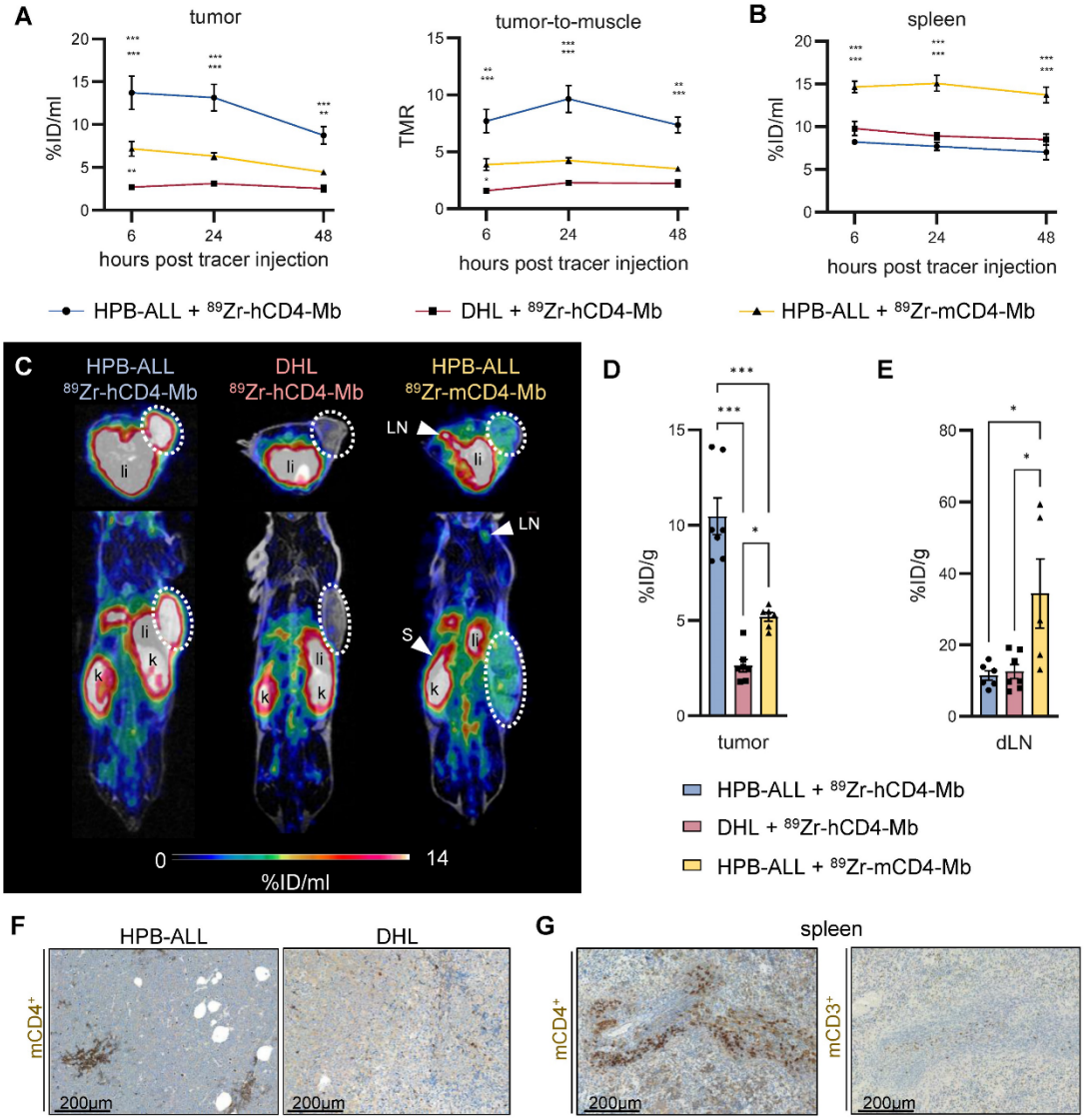

Figure 2. *In vivo* ^{89}Zr-hCD4-Mb and ^{89}Zr-mCD4-Mb binding to CD4$^+$ cells in immunodeficient NSG mice. (A) *In vivo* PET uptake quantification and tumor-to-muscle ratio of hCD4$^+$ HPB-ALL and hCD4$^-$ DHL xenografts 6, 24, and 48 h after ^{89}Zr-hCD4-Mb or ^{89}Zr-mCD4-Mb injection. (B) *In vivo* PET uptake quantification of the spleen. (C) Representative PET/MR images acquired 48 h after ^{89}Zr-hCD4-Mb or ^{89}Zr-mCD4-Mb injection. Tumors are highlighted with a white circle. LN: lymph nodes; s: spleen; k: kidney; li: liver. (D) *Ex vivo* biodistribution of hCD4$^+$ HPB-ALL and hCD4$^-$ DHL tumors and (E) draining lymph nodes (dLNs) measured by γ-counting at 48 h after ^{89}Zr-hCD4-Mb or ^{89}Zr-mCD4-Mb injection. (F) *Ex vivo* immunohistochemistry (IHC) of endogenous mCD4$^+$ cells from HPB-ALL tumors and DHL tumors of NSG mice. (G) *ex vivo* IHC of endogenous mCD4$^+$ cells and mCD3$^+$ cells from the spleens of NSG mice. *P* values were calculated by two-way ANOVA (A, B) or ordinary one-way ANOVA (D, E) using the Tukey post-hoc test. Data derived from two independent experiments (n = 6-7 per group). *p < 0.05, **p < 0.01, ***p < 0.001.

Intratumoral ^{89}Zr-mCD4-Mb uptake as a response indicator for combined immunotherapy

Finally, we aimed to evaluate the sensitivity of ^{89}Zr-mCD4-Mb PET for monitoring moderate alterations in CD4$^+$ T cell density within the TME before and during ICI treatment and its correlation with the treatment sensitivity. We injected ^{89}Zr-mCD4-Mb into CIT-responsive MC38 adenocarcinoma-bearing mice and into CIT-resistant B16F10 melanoma-bearing mice when the tumors reached a diameter of 8-10 mm (mean volume: ~300 mm^3, Figure S54A) before therapy initiation. The noninvasive *in vivo* ^{89}Zr-mCD4-Mb PET/MRI studies and subsequent *ex vivo* analyses revealed no differences in ^{89}Zr-mCD4-Mb tumor uptake within the TME of MC38 and B16F10 tumors at baseline (Figure 5A, B). IHC confirmed the presence of scattered CD4$^+$ T cells in both tumors, mainly located at the tumor periphery (Figure 5C).

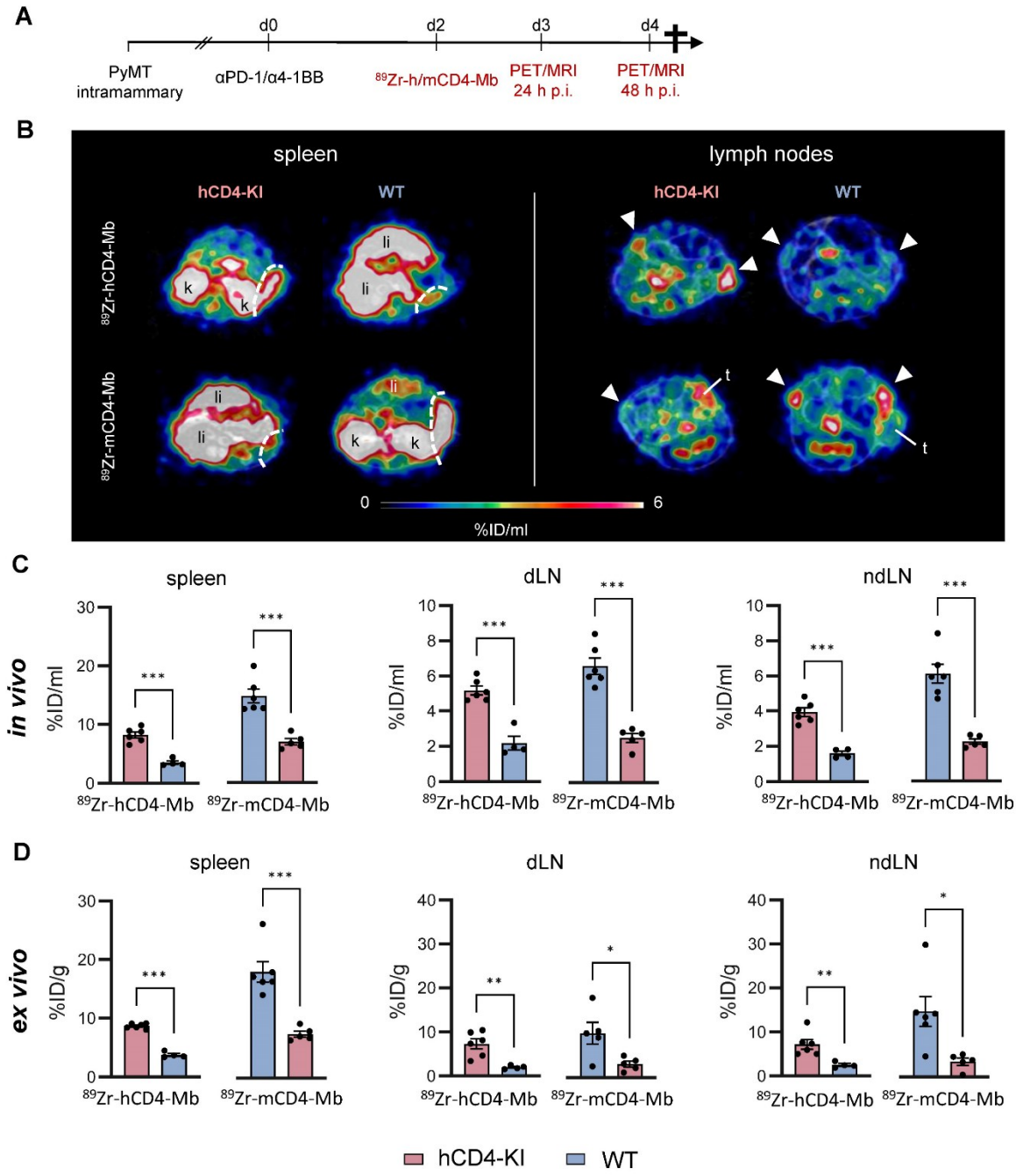

Figure 3. *In vivo* cross-validation of ^{89}Zr-h/mCD4-Mb to visualize endogenous CD4$^+$ cells in lymphatic organs. (A) Treatment and PET imaging schedule. hCD4-KI and WT animals were orthotopically inoculated with 0.5 x10^6 PyMT cells in the 4th mammary fat pad and treated with a combination of the αPD-1/α4-1BB mAbs (200 µg/50 µg per mouse). PET/MRI was performed 3 and 4 days after treatment onset (24 h and 48 h after *i.v.* injection of ^{89}Zr-h/mCD4-Mb). (B) Representative PET/MR images of the spleen (left, separated from the kidney/liver derive uptake by a white broken line) and lymph nodes (right, white triangle) acquired 48 h post-tracer injection. k: kidney; li: liver; t: tumor. (C) *In vivo* quantification of human and murine ^{89}Zr-CD4-Mb uptake in lymphatic organs (spleen, draining lymph node (dLN), and contralateral non-draining lymph node (ndLN)) 48 h post tracer injection. (D) *Ex vivo* quantification of ^{89}Zr-h/mCD4-Mb uptake in lymphatic organs 48 h post tracer injection. *P* values were calculated by an unpaired t-test. Data derived from two independent experiments (n = 4-6 per group). $^*p < 0.05$, $^{**}p < 0.01$, $^{***}p < 0.001$.

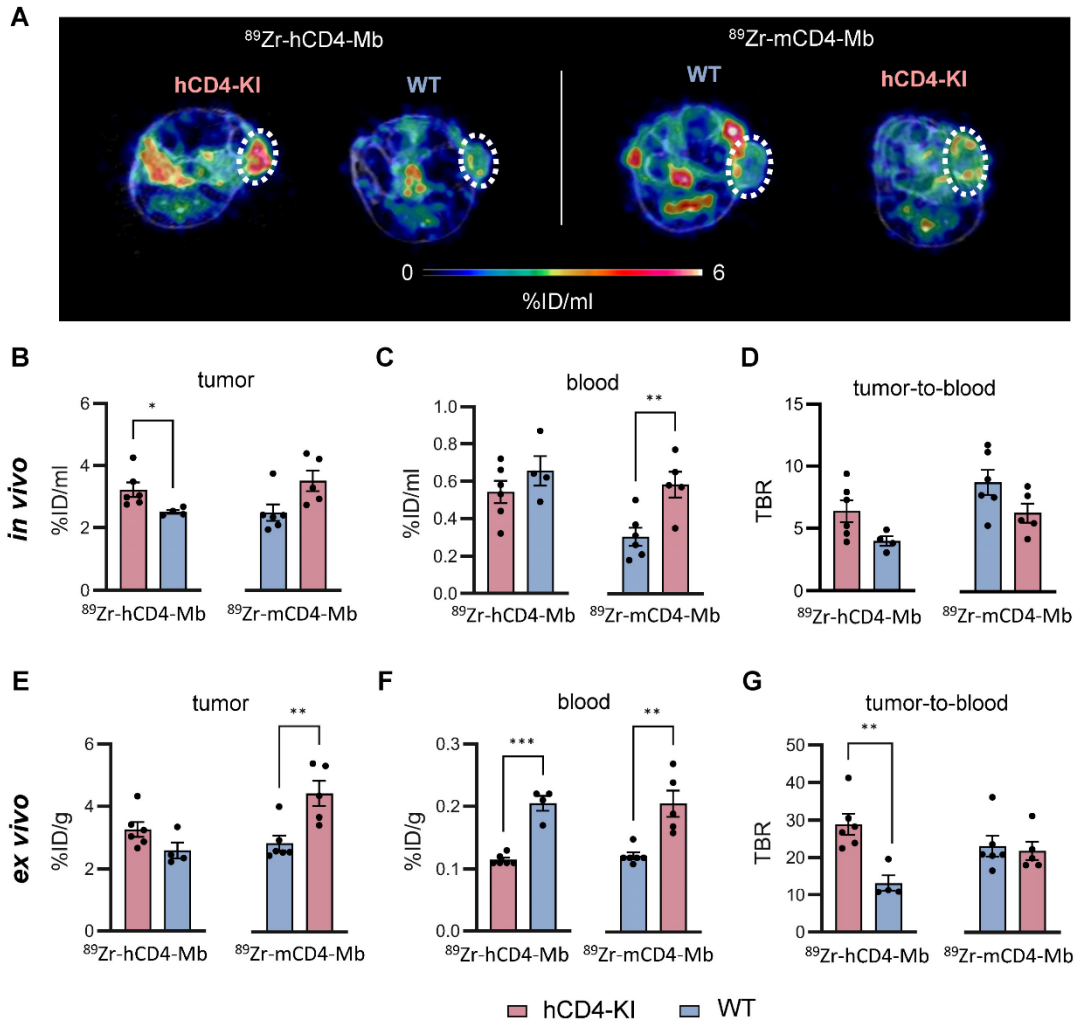

Figure 4. Noninvasive visualization of tumor-infiltrating endogenous CD4⁺ cells in hCD4-KI and WT PyMT mammary tumor-bearing mice. (A) Representative *in vivo* PET/MR images of PyMT mammary tumors acquired 48 h post-^{89}Zr-CD4-Mbs i.v. injection (day 4 post-αPD-1/α4-1BB mAb injection). Tumors are highlighted by white circles. (B) *In vivo* quantification of ^{89}Zr-h/mCD4-Mb uptake in PyMT tumors and (C) blood and (D) the tumor-to-blood ratio in hCD4-KI and WT mice 48 h post tracer injection. (E) *Ex vivo* quantification of ^{89}Zr-h/mCD4-Mb uptake in PyMT tumors and (F) blood as well as (G) the tumor-to-blood ratio for hCD4-KI and WT mice at 48 h post tracer injection measured by γ-counting. *P* values were calculated by unpaired t-test. Data are derived from two independent experiments (n = 4-6 per group). $^{*}p < 0.05$, $^{**}p < 0.01$, $^{***}p < 0.001$.

Next, only MC38 tumor-bearing mice were subjected to combined αPD-L1/αLag-3 ICI therapy. Interestingly, 4 out of 7 ICI-treated mice yielded a 2.5 to 5-times increased CD4⁺ T-cell density within the MC38 TME compared to the sham-treated controls 9 days post αPD-L1/αLag-3 therapy initiation, suggesting therapy-induced and/or response-associated accumulation of CD4⁺ T cells (Figure 5D). Subsequently, we monitored the presence of CD4⁺ cells by ^{89}Zr-mCD4-Mb-PET/MRI on days 7, 8, and 9 after initiating CIT (Figure 5E). αPD-L1/αLag-3-treated MC38 tumor-bearing mice were classified as responders or non-responders based on tumor growth (tumor volume on day 9 / tumor volume on day 0 of therapy) (Figure 5E-F). Strikingly, we observed ~1.4-fold higher ^{89}Zr-mCD4-Mb uptake in responsive MC38 tumors from experimental mice 24 h (5.23 ± 0.42 %ID/ml) and 48 h (3.97 ± 0.27 %ID/ml) after tracer injection than in non-responsive MC38 tumors (24 h %ID/ml: 3.87 ± 0.20; 48 h %ID/ml: 2.72 ± 0.17) and ~1.3-fold higher intratumoral uptake than in sham-treated experimental mice (24 h %ID/ml: 4.12 ± 0.20; 48 h %ID/ml: 3.00 ± 0.14; Figure 5G-H; Figure S5C).

Consistent with our *in vivo* results, *ex vivo* organ biodistribution analysis of the tumors, muscle, and blood revealed increased ^{89}Zr-mCD4-Mb accumulation in the TME and significantly higher tumor-to-blood and tumor-to-muscle ratios in mice responding to ICI non-responsive MC38 tumors or

tumors from sham-treated experimental mice (Figure 5I; Figure S5D). Besides, there were no differences in the *ex vivo* biodistribution of several organs of interest, such as the spleen, draining lymph nodes, liver, kidney, lung, or blood, between all experimental groups (Figure S5D).

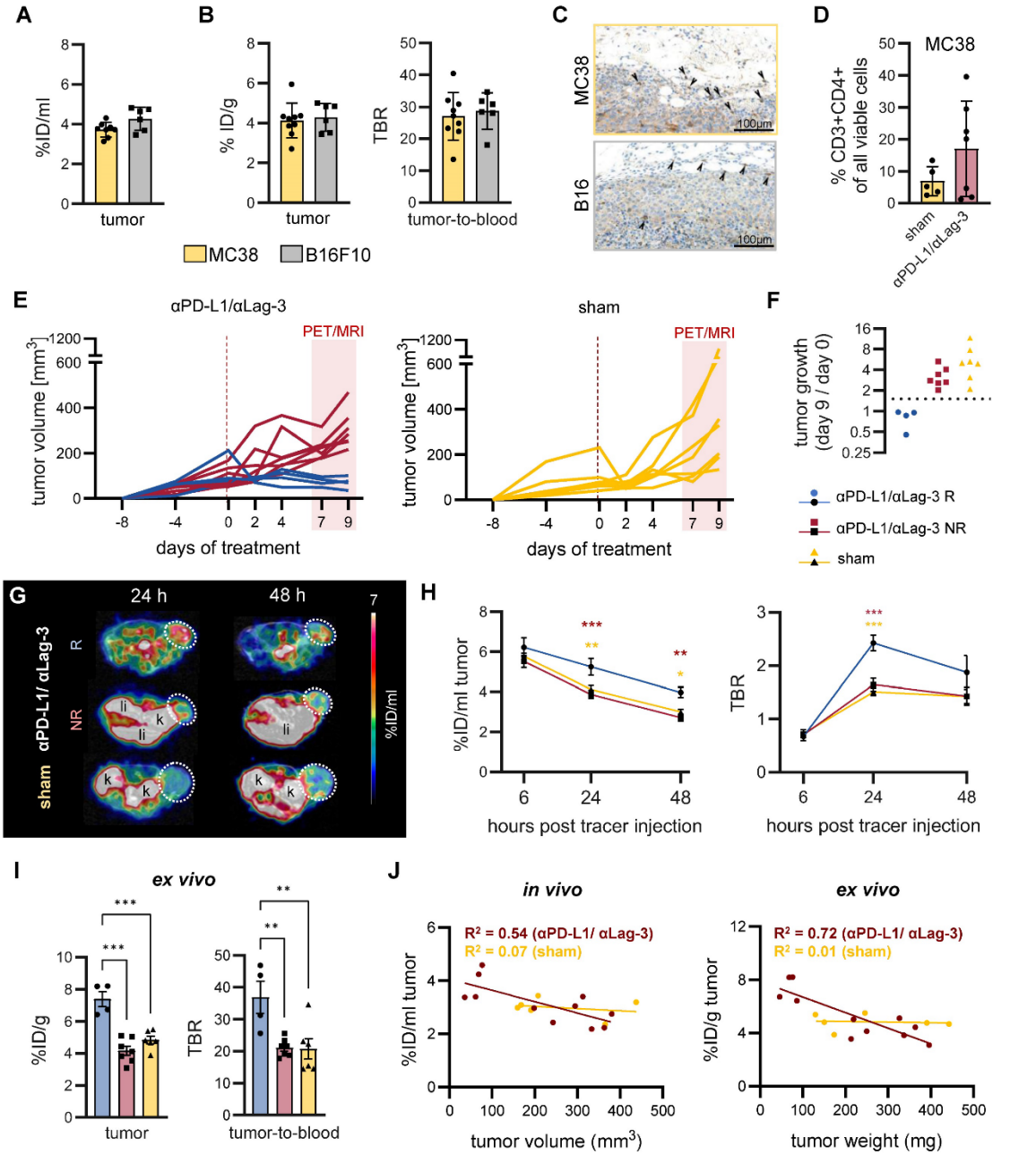

Figure 5. *In vivo* ^{89}Zr-mCD4-Mb PET for monitoring endogenous CD4$^+$ cell dynamics in response to ICI therapy. (A) *In vivo* tumor uptake quantification of endogenous mCD4$^+$ cells in subcutaneous MC38 (n = 9) and B16F10 (n = 6) tumors 48 h after ^{89}Zr-mCD4-Mb tracer injection. (B) *Ex vivo* γ-counting of the tumor and *ex vivo* tumor-to-blood ratio (TBR) 48 h after ^{89}Zr-mCD4-Mb injection. (C) *Ex vivo* mCD4 IHC of MC38 and B16 tumors. Black arrows indicate mCD4$^+$ cells. (D) Fraction of intratumoral CD4$^+$ cells of all cells from αPD-L1/αLag3-treated (n = 7) and sham-treated animals (n = 5) by flow cytometry. (E) MC38 tumor volumes (mm^3) of αPD-L1/αLag-3-treated or sham-treated mice. The red rectangle indicates the PET/MR acquisition period at day 7 (6 h post tracer injection), day 8 (24 h), and day 9 (48 h). (F) Tumor growth ratio on day 9 vs. day 0 (baseline). Based on the tumor growth ratio (tumor volume at day 9 / tumor volume at day 0), mice were considered responsive (<1.5, R, blue) or non-responsive to treatment (>1.5, NR, red). (G) Representative *in vivo* PET/MR images 24 h and 48 h after ^{89}Zr-mCD4-Mb tracer injection. Tumors are highlighted with a white circle. k: kidney; li: liver. (H) *In vivo* ^{89}Zr-mCD4-Mb MC38 tumor uptake and tumor-to-blood ratio (TBR) were quantified at 6 h, 24 h, and 48 h post tracer injection. (I) *Ex vivo* quantification of ^{89}Zr-mCD4-Mb uptake in MC38 tumors and tumor-to-blood ratio measured by γ-counting. (J) Correlation of *in vivo* (left) and *ex vivo* (right) ^{89}Zr-mCD4-Mb uptake with the corresponding tumor volume and tumor weight, respectively, at 48 h after ^{89}Zr-mCD4-Mb tracer injection. Data are derived from two independent experiments (αPD-L1/αLag3: n = 11, sham: n = 6; four mice were excluded from the study because of ulcerated tumors). $^*p < 0.05$, $^{**}p < 0.01$, $^{***}p < 0.001$.

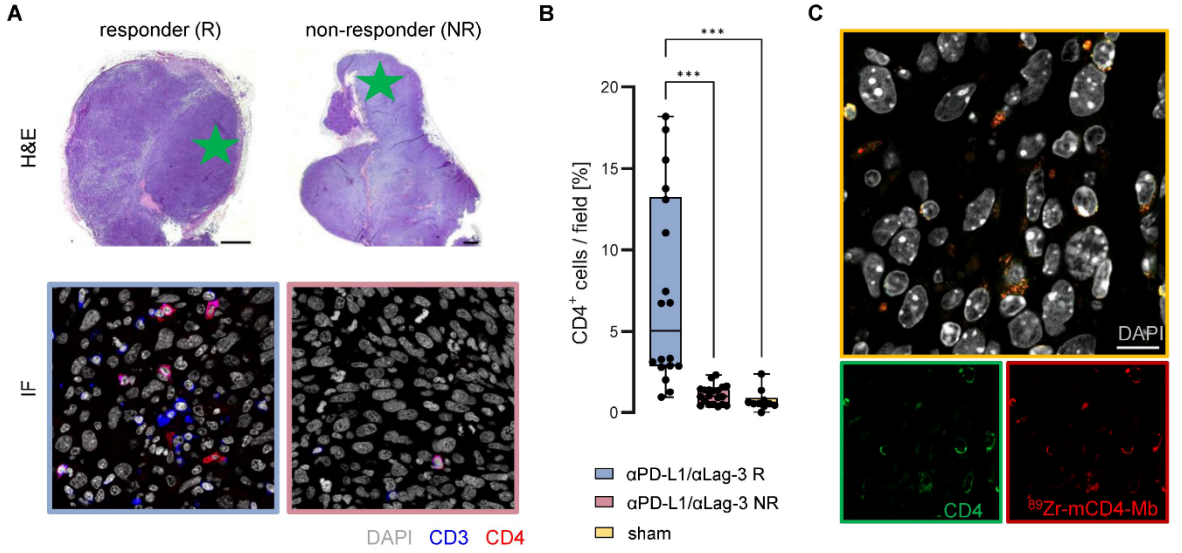

Figure 6. *Ex vivo* validation of ^{89}Zr-mCD4-Mb uptake. (A) *Ex vivo* H&E staining of MC38 tumors from αPD-L1/αLag3-treated mice and representative immunofluorescence (IF) of CD3$^+$ and CD4$^+$ cells (field marked by a green star). Scale bars: 1000 µm H&E, 20 µm IF. (B) Quantification of % intratumoral CD4$^+$ cells of all cells per field (5 fields per tumor) from αPD-L1/αLag3 responders (R, n = 4), non-responders (NR, n = 4) and sham-treated animals (n = 2). (C) Colocalization of intratumoral CD4 protein expression and ^{89}Zr-mCD4-Mb by secondary IF staining. Scale bar: 10 µm. *p < 0.05, **p < 0.01, ***p < 0.001.

To exclude that the differences in tumor volumes between responding and non-responding animals affect the tracer uptake by biological (e.g. tumor penetration and accessibility) or physical (e.g. partial volume effects of the PET detectors) effects, we correlated the *in vivo* tracer uptake with the tumor volumes and the *ex vivo* tracer uptake with the tumor weight (Figure 5J). We observed a homogeneous distribution of the uptake values in the sham-treated group (not influenced by therapy-induced tumor growth inhibition) irrespective of the tumor size. Furthermore, comparable linear regressions and R^2-values between *in vivo* and *ex vivo* analyses indicated that the tracer signals were influenced by partial volume or other physical effects. Noteworthy, flow cytometry of the TME revealed no relevant fraction of CD4$^+$ cells when gated for CD45$^+$CD3$^-$ myeloid cells (Figure S5B).

ICI response-associated infiltration of CD4$^+$ T cells into TME

To better understand the increased ^{89}Zr-mCD4-Mb uptake within the TME and the intra-tumoral CD4$^+$ T cell distribution of therapy responders, we performed immunofluorescence analyses of the MC38 tumors on day 9 of αPD-L1/αLag-3 therapy after the 48 h PET imaging time point. Representative high-resolution images of the tumor margin and the tumor core (Figure 6A) and CD4$^+$ cell quantification (Figure 6B) revealed about 7-fold increased infiltration of CD3$^+$CD4$^+$ T cells into the TME of responsive MC38 tumors, whereas no CD3$^+$CD4$^+$ T cells could be identified in nonresponsive MC38 tumors or tumors from sham-treated mice (Figure 6A, B). Most importantly, we were able to colocalize the ^{89}Zr-mCD4-Mb distribution to endogenous tumor-infiltrating CD4$^+$ cells by secondary staining of the Mb, highlighting the tracer-specific targeting of CD4$^+$ cells within the TME at the cellular level (Figure 6C).

Discussion

Given the inadequate immunotherapy response rates and the urgent need for reliable biomarkers for therapy stratification, immunoPET approaches have been applied clinically to visualize intratumoral CTLs [46, 47] or TME-associated immune checkpoints in cancer patients [48-50]. A pioneering example of the most advanced immunotracer in clinical development was the CD8-targeting PET tracer ^{89}Zr-crefmirlimab berdoxam [51, 52]. This Mb-based radioimmunoconjugate, currently under evaluation in phase II clinical study and in many pharma- and investigator-initiated trials, demonstrated remarkable capability to assess the therapeutic responses to ICIs and other immunotherapies within the first 3-6 weeks of treatment [47, 51, 52]. Due to their lower molecular weight and reduced Fc receptor-mediated interaction compared to full-length antibodies, Mbs have superior molecular imaging characteristics, such as faster tissue penetration, blood clearance, and reduced immunogenicity [47, 51-54]. While PD-(L)1-directed ICI therapies, as a standard-of-care

treatment for several tumor types, critically depend on CTL-mediated immune responses [55-57], emerging ICI combinations, including CTLA-4, Lag-3, or OX40-targeting mAbs, along with innovative tumor vaccination approaches, emphasize the increasing focus on reinvigorating antitumoral $CD4^+$ T-cell activity [31, 56-59].

The lack of clinically translatable human-specific CD4-targeting immunoPET tracers and the promising clinical development of ^{89}Zr-crefmirlimab berdoxam motivated us to develop Mb-based PET tracers to monitor endogenous $CD4^+$ cell dynamics in the TME and lymphatic organs. First, we verified the *in vitro* and *in vivo* target specificity of ^{89}Zr-hCD4-Mb and ^{89}Zr-mCD4-Mb. We demonstrated an ~80-fold higher *in vitro* binding of the ^{89}Zr-hCD4-Mb in the $hCD4^+$ HBP-ALL cells than in the hCD4- DHL B-cell-lymphoma cells while *in vivo* accumulation of s.c. injected cells was only ~4-fold higher. In this context, *in vivo* biodistribution effects, permeability, and unspecific accumulation have to be considered that impair tracer accessibility and specificity, particularly in *s.c.* injected tumors.

We also monitored the presence of endogenous $CD4^+$ cells in immune cell-enriched lymphatic organs, such as the spleen and lymph nodes, and in the TME of tumor-bearing WT and hCD4-KI mice. Interestingly, even low numbers of endogenous $mCD4^+$ cells present in immunodeficient NSG mice [60-62] or in the TME of MC38 tumors could be differentiated by our ^{89}Zr-CD4-Mb immunoPET approach (Figure 2F), highlighting its superior sensitivity. As for visualizing tumor-infiltrating lymphocytes, enhanced tracer accumulation in the lymphatic organs may be considered an antigen sink, resulting in reduced amounts of radiotracer available to bind to target cells at the tumor site [39, 63]. This was expected for larger antibody-based molecules and can explain the limitations of head-to-head comparisons with considerable differences in the ^{89}Zr-CD4-Mb blood biodistribution using knock-out/knock-in mouse models (Figure 4). To avoid this, immune cell-rich organs could be saturated by administering an excess of an unlabeled antibody targeting the same antigen or a higher dose of the immunoPET tracer to increase the availability of the probe at the tumor site [39, 63, 64]. Therefore, optimizing the dose may be essential for obtaining a sufficient imaging signal, while pre-dosing strategies pose a risk of perturbing the binding of tracers to intratumoral immune cells [39].

Besides the target abundance, several factors, including microvascular density, vascular permeability, stromal content, intratumoral pressure, and diffusion, influence tumor accumulation of immunoPET tracers [65]. In our study, correcting for ^{89}Zr-mCD4-Mb and ^{89}Zr-hCD4-Mb uptake in the TME with the blood uptake enabled us to detect a species-specific Mb signal in experimental PyMT tumor-bearing WT and hCD4-KI mice [39]. One of the main concerns in developing new immunotracers is the effects on targeted cells, such as unintentional immune cell activation or the inhibition of immune cell effector functioning. Our study revealed no impact of hCD4-Mb on the proliferation of human PBMCs *in vitro*. Similarly, the injection of ^{64}Cu-labeled hCD4-Mb by Nagle *et al.* did not result in detectable depletion or alterations in the proliferation or polarization of $hCD4^+$ cells in a humanized glioblastoma model [45]. These findings hold particular significance for translational studies on tracking $CD4^+$ cells by hCD4-Mbs in patients. Also, Freise *et al.* could not detect alterations in $CD3^+$ T-cell or $CD45^+CD4^+$ cell compartments in the spleen, lymph nodes, thymus, or blood using a CD4-targeting ^{89}Zr-radiolabeled cys-diabody despite a mild reduction of CD4-expressing immune cells [41]. Interestingly, the investigators reported a dose-dependent downregulation of membranous CD4 expression. Notably, decreased membranous CD4 expression has been reported on activated immune cells [66, 67]. Nevertheless, Freise *et al.* could not identify a CD4-cys-diabody-induced activation of CD4-expressing immune cells.

Our study did not show differences between ICI-responsive MC38 adenocarcinomas ("hot tumors") and ICI-resistant B16F10 melanomas ("cold tumors") at baseline by ^{89}Zr-mCD4-Mb immunoPET. The TME of immunogenic MC38 tumors was characterized by myeloid cells and very few $CD4^+$ cells (Figure 5C) [68, 69]. Also, Kjaer *et al*, who investigated the ^{89}Zr-mCD4-F(ab´)2 fragment in seven preclinical syngeneic tumor models (MC38, CT26, B16F10, 4T1, P815, RenCa, Sa1N), could not show differences in the CD4-derived PET uptake between MC38 and B16F10 tumors. Nevertheless, the group demonstrated a correlation between PET uptake, *ex vivo* $CD4^+$ cells densities, and response to aPD1 ICI therapy in some tumor models, which was not the case using a CD8-directed ^{89}Zr-mCD8-F(ab´)2 [39].

Given the fact that $CD4^+$ cells represent a very heterogenous group with either protumoral or antitumoral function, we investigated whether ^{89}Zr-mCD4-Mb PET could assess early ICI response or resistance. Strikingly, we could discriminate MC38 tumor-bearing mice that were responsive (higher PET uptake) or nonresponsive (lower PET uptake) to αPD-L1/αLag-3 immunotherapy 7 days after therapy initiation. This finding was consistent with our IF analyses, demonstrating significant $CD4^+$ T cell

infiltration into the TME in therapy responders (Figure 6A-C) [70, 71]. In conclusion, our study presented a comprehensive preclinical cross-validation of ^{89}Zr-CD4-Mb as a precision tool for noninvasive monitoring and visualizing endogenous CD4$^+$ cells throughout the body.

Beyond oncological purposes, Mascio *et al.* performed valuable research on the whole-body PET visualization of CD4$^+$ T cells in non-human primates by using dynamic PET data advanced mathematic modeling approaches. They applied the therapeutic anti-human CD4 full-length antibody ibalizumab and rhesus-specific F(ab′)$_2$ antibody fragments to immunocompetent and Simian Immunodeficiency Virus-infected rhesus macaques. The overall capability of both radioimmunoconjugates to differentiate increased CD4$^+$ T-cell densities of the spleen and lymph nodes appeared comparable to our results. However, the limitations of therapeutic antibodies for diagnostic imaging, observed dose- and blood pool-dependent uptake kinetics, and the use of a primarized F(ab′)$_2$ hinder their clinical translatability.

Considering the already demonstrated clinical success of ^{89}Zr-crefmirlimab berdoxam in targeting human CD8$^+$ cells [51, 52], our Mb-based imaging approach offers a remarkable balance between high target specificity and low toxicity due to its rapid biodistribution and clearance from blood. Based on increasing histology-driven evidence from human tumor tissues suggesting CD4$^+$ cells as critical biomarkers to determine therapy efficacy in oncolytic virus [72], CAR T cells [73], and immune checkpoint inhibitor therapy [74-79], ^{89}Zr-CD4-Mb immunoPET holds great promise for clinical translation as a valuable tool for the noninvasive monitoring of CD4$^+$ cells, and the patient-individualized prediction of cancer immunotherapy outcomes.

Methods

Minibody production

Single-chain variable fragment (scFv) sequences were derived from anti-human-specific mAb MAX16H5 and anti-mouse mAb YTA3.1.2. Identical to the clinically established CD8-directed Mb PET tracer 89Zr-crefmirlimab berdoxam, these binding domains were fused with a human Fc-CH3 domain, to generate the hCD4-Mb (IAB41M1-3) or mCD4-Mb (IAB46M2-18), respectively, with a final molecular weight of ~80 kDa. Mbs were produced in transiently transfected Expi293™ cells (ThermoFisher Scientific). The purified proteins were conjugated via coupling to primary amines with parabenzoylisothiocyanate-activated deferoxamine (dfo), yielding chelator-to-minibody ratios of 2.45 (hCD4-Mb) and 1.65 (mCD4-Mb), respectively.

Enzyme-linked Immunosorbent Assay (ELISA)

Recombinant hCD4-His or mCD4-His (both Sino Biologicals) were diluted to 2 µg/mL in the carbonate bicarbonate buffer (Sigma), and 100 µL were added to each well of a flat-bottom plate and incubated at 2-8°C overnight. The following day, the plate was washed 3x with Phosphate-Buffered Saline with Tween (PBST 0.05%) and blocked for 1 h at room temperature with PBS containing 1% bovine serum albumin (BSA) (Sigma). The plate was washed 3x with PBST (0.05%). A serial dilution was prepared by diluting the sample 1:2.5 to achieve a standard curve starting from 16 nM for both hCD4-Mb and mCD4-Mb; 100 µL of the sample was added to each well of the test plate and incubated for 1 h at room temperature. The plate was washed 3x with PBST (0.05%). Mouse anti-human IgG Fc-HRP detection antibody (Southern Biotech) was diluted 1:20,000 in assay buffer, and 100 µL was added to each well of the test plate and incubated for 1 h at room temperature. Subsequently, the plate was washed 3x with PBST (0.05%), 100 µL of TMB substrate (BioFx) was added to each well of the test plate and allowed to develop for 10-20 min at room temperature. The reaction was terminated by adding 100 µL of stop reagent (BioFx). The plate was read at 650 nm using a BioTek Synergy II plate reader.

Human PBMC proliferation assay

The antibodies were coated on plates in triplicate at 40 µg/mL in PBS at +4°C overnight. PBMCs were thawed and incubated in Human Serum AB according to the RESTORE protocol before use and plated at 100,000 cells/well (100 mL total). For the soluble assay format, antibodies were added at a concentration of 65 nM in triplicate to the plate coated with PBMCs. The plates were incubated at 37°C and 5% CO_2 for 5 days, after which the CTG substrate was added, and the plates were placed on a shaker for 5 min. The luminescence of the plates was subsequently read on a plate reader to determine the extent of proliferation.

Radiolabeling

The dfo-conjugated hCD4-Mb and mCD4-Mb were radiolabeled with 200 MBq Zr-89 oxalate (Perkin Elmer) per mg protein. Briefly, the desired activity was neutralized with a 0.45-fold volume of 2 M sodium carbonate and buffered with a 5-fold volume of 0.5 M ammonium acetate to achieve a pH of 6.5-7.0. After adding the protein, labeling was allowed to proceed for 40 minutes at 25°C, after which the reaction was quenched by adding DTPA (0.2% solution, 40 µL per mg protein) and incubated for an

additional 10 min. Incorporation of the radioisotope was confirmed by iTLC analysis (≥95% radiochemical purity (RCP); iTLC-SG (Agilent), mobile phase 10 mM EDTA). The identity of the elution profile with the original protein and radiolabeling of the protein peak was confirmed by high-performance size exclusion chromatography (HPSEC) (BioSep SEC s2000, 300x7.8 mm, Phenomenex). In the case of insufficient RCP (<90%), the protein was purified using a Bio-Spin 6 desalting column (Bio-Rad) according to the manufacturer's instructionsto achieve >95% RCP.

Serum stability

Murine blood was obtained from the retrobulbar vein of C57BL/6 mice and collected in 1.5 mL Eppendorf tubes. The blood was kept at room temperature for 2 h and centrifuged at 12.000 rpm for 15 min. The serum was collected as supernatant and incubated with the radiolabeled ^{89}Zr-hCD4-Mb. HPLC measurements were performed at 0, 24, and 72h after tracer incubation and the % of ^{89}Zr-hCD4-Mb and ^{89}Zr-DTPA was determined.

CD4$^+$ cell isolation and culture

Murine CD4$^+$ cells were isolated from the lymph nodes and spleens of female C57BL/6 mice using CD4$^+$ magnetic microbeads (Miltenyi Biotec). Six-well plates were precoated at +4°C overnight with 0.5 µg/ml αCD3 and 5 µg/ml αCD28 mAbs (Bioxcell) in 5 ml/well PBS. The freshly isolated CD4$^+$ cells were cultured in RPMI medium (Lonza Biosciences) supplemented with 10% FCS, 0.5% penicillin/ streptomycin (P/S), 0.5 µM β-mercaptoethanol and 1% Insulin Transferrin Selenium (ITS). After 24 h, 30 U/ml IL-2 and 0.5 ng/ml IL-7 were added to each well. The medium was renewed every 2 to 3 days, and the cells were cultured for no longer than 14 days.

Human CD4$^+$ cells were isolated from whole-blood samples of healthy donors using StraightFrom Whole Blood CD4 MicroBeads (Miltenyi Biotec) immediately before each *in vitro* experiment.

Tumor cells

The hCD4$^+$ hematopoietic peripheral blood acute lymphoblastic leukemia tumor (HPB-ALL) and hCD4$^-$ diffuse histiocytic lymphoma (DHL) cell lines were purchased from the German Collection of Microorganisms and Cell Cultures (DSMZ) and cultured in RPMI-1640 medium, supplemented with 10% Fetal Calf Serum (FCS) and 1% P/S. The MC38 murine colon adenocarcinoma cell line was purchased from Kerafast and cultured in DMEM (Lonza Biosciences) supplemented with 10% FCS, 1% P/S, and 1% HEPES (Lonza Biosciences). The B16F10 murine melanoma cell line was purchased from ATCC and cultured in DMEM, supplemented with 10% FCS and 1% P/S. The S2WTP3 (PyMT) triple-negative breast cancer cell line was kindly provided by Andreas Moeller (Queensland University, Australia) and cultured in DMEM supplemented with 10% FCS, 1% P/S, and 1% pyruvate (Sigma).

In vitro binding assays

The *in vitro* binding of ^{89}Zr-mCD4-Mb or ^{89}Zr-hCD4-Mb was assessed using freshly isolated or immortalized murine or human CD4$^+$ cells. Different numbers of cells were incubated with 10 ng of ^{89}Zr-mCD4-Mb or ^{89}Zr-hCD4-Mb for 90 min. The cells were washed with PBS/2% FCS and resuspended in 200 µL PBS / 2% FCS. For the antigen-blocking experiments, a 100-fold excess of unlabeled CD4-Mb was added to the wells 30 min before tracer incubation. The residual cell-bound radioactivity was measured in a γ-counter (Wallac 1480 WIZARD 3" Gamma Counter; PerkinElmer). The immunoreactive fraction of each radioimmunoconjugate was determined by calculating the maximum specific binding (Bmax) of a one-site nonlinear regression model within an antigen excess assay with an increasing number of cells (0 – 32 x 10^6).

Animals

All experiments were performed according to the animal use and care protocols of the German Animal Protection Law and were approved by the Regierungspräsidium Tübingen. 6-10-week-old NOD SCID gamma (NSG, NOD.Cg-*Prkdc*^{scid} *Il2rg*^{tm1Wjl}/SzJ, Charles River Laboratories), C57BL/6 (Charles River Laboratories), and human CD4-Knock-in (hCD4-KI, C57BL/6J-Cd4$^{tm1.1(CD4)Geno}$, Genoway, in-house breeding) mice were bred under specific pathogen-free conditions with free access to food and water *ad libitum*.

Tumor models and immunotherapies

10 x10^6 HPB-ALL or DHL cells were injected *s.c.* in the right flank of NSG mice in 200 µl of 50% PBS/50% Matrigel (Corning). 0.125 x10^6 MC38 or B16F10 tumor cells were injected *s.c.* into C57BL/6 mice in 50% PBS/50% Matrigel (Corning). A total of 0.5 x10^6 PyMT mammary tumor cells were orthotopically injected into the 4th mammary fat pad in PBS into C57BL/6 or hCD4-KI mice.

C57BL/6 and hCD4-KI mice with PyMT tumors were injected *intraperitoneally* (*i.p.*) with 200 µg of αPD-1 (clone: RMP1-14l) and 50 µg of α4-1BB (clone: 3H3). C57BL/6 mice with MC38 tumors were injected *i.p.* with 500 µg of αPD-L1 (10F.9G2) and αLag-3 (C9B7W) or isotype control mAbs (LTF-2 and HRPN, respectively). All therapeutic antibodies were purchased from Bioxcell.

Positron Emission Tomography (PET) and Magnetic Resonance Imaging (MRI)

For simultaneous PET/MRI, experimental mice received 2 MBq/10 µg of ^{89}Zr-mCD4-Mb or ^{89}Zr-mCD4-Mb via tail vein injection. Static scans (600 s) were acquired under 1.5% isoflurane anesthesia (100% oxygen) with an in-house manufactured PET insert [80] at 6, 24, and 48 h post tracer injection. Simultaneous T2-weighted MR images [repetition time (TR): 1800 ms, echo time (TE): 4.763 ms, field of view (FoV) 76.8 × 34.8 × 22.8, × mm^3, matrix 256 × 256 × 64, resolution 0.25 × 0.25 × 0.25 µm^3] were acquired in a 7T small animal MR system (ClinScan; Bruker BioSpin).

Image analysis

PET images from list mode were reconstructed using 2-dimensional ordered subset expectation maximization (OSEM-2D), applied to a Gaussian filter of 1.5 mm, and registered to the anatomical T2 MR images using Inveon Research Workplace (Siemens Preclinical Solutions). Volumes of interest (VOIs) of the organs of interest were created based on the anatomical MR images. The uptake values of the respective organs (%ID/mL) were calculated based on the Bq/mL after correction for radioactive decay and normalization to the injected activity. For visual comparison between the PET images, the signal intensity between the groups and the color scale was normalized within one experiment.

Ex vivo biodistribution

The experimental mice were sacrificed by cervical dislocation under deep anesthesia after the final imaging time point. Organs were harvested, and radioactivity was measured by γ-counting using an energy window between 350 and 650 keV. Standardized aliquots of the injected tracer were added to the wells for quantification. The values for each organ are expressed as the percentage of the overall injected dose per g (%ID/g), corrected for radioactive decay, and normalized to the injected activity.

Immunohistochemistry

After γ-counting of the organs, the tumors, spleens, and lymph nodes were fixed in formalin and embedded in paraffin. For histology, 3-5 µm-thick sections were cut and stained with hematoxylin and eosin (H&E). Immunohistochemistry was performed on an automated immunostainer (Ventana Medical Systems, Inc.) according to the manufacturer's protocols for open procedures, with slight modifications. All slides were stained with antibodies against CD4 (SP35; Zytomed, Berlin, Germany) and CD3 (SP7; DCS Innovative Diagnostics-Systeme GmbH & Co., KG). Appropriate positive and negative controls were used to confirm the adequacy of the staining. All samples were scanned with a Ventana DP200 (Roche, Basel, Switzerland) and processed with the Image Viewer MFC Application. Final image preparation was performed with Adobe Photoshop CS6.

Immunofluorescence

Paraffin-embedded MC38 tumor tissues were cut into 3–5 µm-thick sections, deparaffinized, unmasked with EDTA buffer (pH 9.0; Thermo Fisher Scientific), and washed with distilled water, PBS (Sigma´-Aldrich), and PBS containing BSA (Aurion) and Tween 20 (Roth). The tissue sections were blocked with donkey serum, incubated with primary antibodies against CD3 (DCS) and CD4 (R&D Systems), and visualized by incubation with Alexa Fluor 488 donkey anti-rabbit (Dianova), Cy3 donkey anti-goat (Dianova) and Cy3 donkey anti-human (Dianova) antibodies. Nuclei were stained with DAPI (Sigma-Aldrich). Images were analyzed using Zeiss LSM 800 and ZEN 2.3 software (blue edition). CD4 fluorescence staining and nuclei were quantified using ZEN Module Image Analysis and by manually counting.

Flow cytometry

Tumors were excised and digested for 30 min at 37°C on a shaker with 23 mg/ml Collagenase (Sigma-Aldrich) and 2.3 mg/ml DNAse (Sigma-Aldrich) in RPMI 2% FCS. Single-cell suspensions were prepared by passing the tumors through 70 µM and 40 µM cell strainer sieves. The cell pellet was incubated at room temperature in ACK lysis buffer (Gibco Life Technologies). The following fluorescent dyes were used for staining: viability ghost dye UV450 (Cytek), BUV395-CD45 (Clone: 30-F11, BD Horizon), BUV805-CD3 (Clone: 17A2, Thermofisher), PerCP-CD4 (Clone: GK1.5, BioLegend), AF700-CD8a (Clone: 53-6.7, BioLegend), BV650-CD69 (Clone: H1.2F3; BioLegend), PE-mOX40 (Clone: OX-86, BioLegend). HPB-ALL and DHL cells were pelleted and stained with the following fluorescence dyes: FITC-hCD4 (Clone: OKT4; Biolegend) and viability ghost dye UV450 (Cytek). Cell suspensions were measured on a Cytek Aurora cytometer. Data were analyzed with FlowJo Software.

Statistical analyses

All data were analyzed using GraphPad Prism, Version 9 or later (GraphPad Software, Inc., San Diego, California, USA). The values were expressed as the arithmetic mean ± standard error of the mean (SEM), if not otherwise stated in the figure legend. For statistical analyses, unpaired t-tests were applied for

pairwise comparisons. Ordinary one-way ANOVA or two-way ANOVA was used for multiple group comparisons and was corrected for multiple comparisons using the Tukey post-hoc test. Adjusted *P* values less than 0.05 were considered significant, and significance levels are indicated as follows: * for ≤0.05, ** for ≤0.01, and *** for ≤0.001.

Abbreviations

CIT: checkpoint inhibitor therapy; CTL: cytotoxic T lymphocytes; CTLA-4: cytotoxic T lymphocyte antigen 4; dfo: desferrioxamine; DHL: diffuse histiocytic lymphoma; FCS: Fetal Calf Serum; FoV: field of view; H&E: hematoxylin and eosin; hCD4-KI: human CD4$^+$ knock-in; HPB-ALL: hematopoietic peripheral blood acute lymphoblastic leukemia tumors; HPSEC: high-performance size exclusion chromatography; ICI: immune checkpoint inhibitor; ID: injected dose; IF: immunofluorescence; IFNγ: Interferon gamma; IHC: immunohistochemistry; IL: Interleukin; Lag-3: lymphocyte-activation gene 3; mAb: monoclonal antibody; Mb: minibody; MRI: magnetic resonance imaging; NK: natural killer; OSEM-2D: 2-dimensional ordered subset expectation maximization; P/S: penicillin/streptomycin; PBS: phosphate buffer saline; PBST: phosphate-buffered saline with tween; PD-L1: programmed death ligand; PET: positron emission tomography; RCP: radiochemical purity; SD: standard deviation; SEM: standard error of the mean; TA: tumor antigen; TE: echo time; Th: T helper; TME: tumor microenvironment; TR: repetition time; VOI: volumes of interest; WT: wild-type.

Supplementary Material

Supplementary figures.
https://www.thno.org/v14p4582s1.pdf

Acknowledgments

This project was funded by the Innovative Medicines Initiative 2 Joint Undertaking under grant agreement No 831514. This Joint Undertaking received support from the European Union's Horizon 2020 Research and Innovation Program and the EFPIA. The studies were further financed by the Deutsche Forschungsgemeinschaft (DFG, German Research Foundation) under Germany's Excellence Strategy - EXC 2180 - 390900677) and the Swiss Werner Siemens Foundation supported these experiments. We acknowledge support from the Open Access Publication Fund of the University of Tuebingen. We thank Patrick Joyce, Fang Jia, and Tove Olafsen for engineering the IAB41M1-3 and IAB46M2-18 minibodies. We acknowledge Dominik Seyfried, Johannes Kinzler, Linda Schramm, Maren Harant, and Miriam Owczorz for excellent technical assistance.

Author contributions

SP, DS, MK and BP conceived and designed the research. SP, JKo, NH, and SB conducted preclinical experiments and analyzed the data. AMas, AA and IW generated, validated, and provided the minibody constructs. AMau and JKi performed the radiolabeling. SP, JKo, NH, and SB conducted the *in vitro* assays. IGM, LQM, SR, and MS performed histological staining and analyzed the data. MK, BP, and DS supervised the study and interpreted the results. SP, MK, and DS wrote the manuscript. All authors reviewed and edited the manuscript and approved the final version of the manuscript.

Data sharing statement

For original data, please contact Dominik.Sonanini@med.uni-tuebingen.de.

Competing Interests

ImaginAb holds a patent on the CD4 minibodies (W O 2019/236684 Al), in which AMas is listed as inventor.

References

1. Naimi A, Mohammed RN, Raji A, Chupradit S, Yumashev AV, Suksatan W, *et al.* Tumor immunotherapies by immune checkpoint inhibitors (ICIs); the pros and cons. Cell Commun Signal. 2022; 20: 44.
2. Yoo MJ, Long B, Brady WJ, Holian A, Sudhir A, Gottlieb M. Immune checkpoint inhibitors: An emergency medicine focused review. Am J Emerg Med. 2021; 50: 335-44.
3. Riley RS, June CH, Langer R, Mitchell MJ. Delivery technologies for cancer immunotherapy. Nat Rev Drug Discov. 2019; 18: 175-96.
4. Jiang H, Ni H, Zhang P, Guo X, Wu M, Shen H, *et al.* PD-L1/LAG-3 bispecific antibody enhances tumor-specific immunity. Oncoimmunology. 2021; 10: 1943180.
5. Jia Y, Liu L, Shan B. Future of immune checkpoint inhibitors: focus on tumor immune microenvironment. Ann Transl Med. 2020; 8: 1095.
6. Chhabra N, Kennedy J. A Review of Cancer Immunotherapy Toxicity: Immune Checkpoint Inhibitors. J Med Toxicol. 2021; 17: 411-24.
7. Johnson DB, Nebhan CA, Moslehi JJ, Balko JM. Immune-checkpoint inhibitors: long-term implications of toxicity. Nat Rev Clin Oncol. 2022; 19: 254-67.
8. Twomey JD, Zhang B. Cancer Immunotherapy Update: FDA-Approved Checkpoint Inhibitors and Companion Diagnostics. Aaps j. 2021; 23: 39.
9. Wolchok JD, Chiarion-Sileni V, Gonzalez R, Rutkowski P, Grob JJ, Cowey CL, *et al.* Overall Survival with Combined Nivolumab and Ipilimumab in Advanced Melanoma. N Engl J Med. 2017; 377: 1345-56.
10. Hwang S, Kwon AY, Jeong JY, Kim S, Kang H, Park J, *et al.* Immune gene signatures for predicting durable clinical benefit of anti-PD-1 immunotherapy in patients with non-small cell lung cancer. Sci Rep. 2020; 10: 643.
11. Duffy MJ, Crown J. Biomarkers for Predicting Response to Immunotherapy with Immune Checkpoint Inhibitors in Cancer Patients. Clin Chem. 2019; 65: 1228-38.
12. Wang DR, Wu XL, Sun YL. Therapeutic targets and biomarkers of tumor immunotherapy: response versus non-response. Signal Transduct Target Ther. 2022; 7: 331.
13. Herbst RS, Soria JC, Kowanetz M, Fine GD, Hamid O, Gordon MS, *et al.* Predictive correlates of response to the anti-PD-L1 antibody MPDL3280A in cancer patients. Nature. 2014; 515: 563-7.
14. Liu Y, Zugazagoitia J, Ahmed FS, Henick BS, Gettinger SN, Herbst RS, *et al.* Immune Cell PD-L1 Colocalizes with Macrophages and Is Associated with Outcome in PD-1 Pathway Blockade Therapy. Clin Cancer Res. 2020; 26: 970-7.
15. Duhen R, Fesneau O, Samson KA, Frye AK, Beymer M, Rajamanickam V, *et al.* PD-1 and ICOS coexpression identifies tumor-reactive CD4+ T cells in human solid tumors. J Clin Invest. 2022; 132: e156821.
16. Tay RE, Richardson EK, Toh HC. Revisiting the role of CD4(+) T cells in cancer immunotherapy-new insights into old paradigms. Cancer Gene Ther. 2021; 28: 5-17.

17. Luckheeram RV, Zhou R, Verma AD, Xia B. CD4⁺T cells: differentiation and functions. Clin Dev Immunol. 2012; 2012: 925135.
18. Zhu J. T Helper Cell Differentiation, Heterogeneity, and Plasticity. Cold Spring Harb Perspect Biol. 2018; 10.
19. Eisel D, Das K, Dickes E, König R, Osen W, Eichmüller SB. Cognate Interaction With CD4(+) T Cells Instructs Tumor-Associated Macrophages to Acquire M1-Like Phenotype. Front Immunol. 2019; 10: 219.
20. Doorduijn EM, Sluijter M, Salvatori DC, Silvestri S, Maas S, Arens R, *et al.* CD4(+) T Cell and NK Cell Interplay Key to Regression of MHC Class I(low) Tumors upon TLR7/8 Agonist Therapy. Cancer Immunol Res. 2017; 5: 642-53.
21. Bennett SR, Carbone FR, Karamalis F, Miller JF, Heath WR. Induction of a CD8+ cytotoxic T lymphocyte response by cross-priming requires cognate CD4+ T cell help. J Exp Med. 1997; 186: 65-70.
22. Sonanini D, Griessinger CM, Schörg BF, Knopf P, Dittmann K, Röcken M, *et al.* Low-dose total body irradiation facilitates antitumoral Th1 immune responses. Theranostics. 2021; 11: 7700-14.
23. Brenner E, Schörg BF, Ahmetlić F, Wieder T, Hilke FJ, Simon N, *et al.* Cancer immune control needs senescence induction by interferon-dependent cell cycle regulator pathways in tumours. Nat Commun. 2020; 11: 1335.
24. Ellyard JI, Simson L, Parish CR. Th2-mediated anti-tumour immunity: friend or foe? Tissue Antigens. 2007; 70: 1-11.
25. Liblau RS, Singer SM, McDevitt HO. Th1 and Th2 CD4+ T cells in the pathogenesis of organ-specific autoimmune diseases. Immunol Today. 1995; 16: 34-8.
26. Walker JA, McKenzie ANJ. T(H)2 cell development and function. Nat Rev Immunol. 2018; 18: 121-33.
27. Pitt JM, Marabelle A, Eggermont A, Soria JC, Kroemer G, Zitvogel L. Targeting the tumor microenvironment: removing obstruction to anticancer immune responses and immunotherapy. Ann Oncol. 2016; 27: 1482-92.
28. Rajendeeran A, Tenbrock K. Regulatory T cell function in autoimmune disease. J Transl Autoimmun. 2021; 4: 100130.
29. Schlöder J, Shahneh F, Schneider FJ, Wieschendorf B. Boosting regulatory T cell function for the treatment of autoimmune diseases - That's only half the battle! Front Immunol. 2022; 13: 973813.
30. Speiser DE, Chijioke O, Schaeuble K, Münz C. CD4(+) T cells in cancer. Nat Cancer. 2023; 4: 317-29.
31. Richardson JR, Schöllhorn A, Gouttefangeas C, Schuhmacher J. CD4+ T Cells: Multitasking Cells in the Duty of Cancer Immunotherapy. Cancers (Basel). 2021; 13: 596.
32. Takeuchi A, Saito T. CD4 CTL, a Cytotoxic Subset of CD4(+) T Cells, Their Differentiation and Function. Front Immunol. 2017; 8: 194.
33. Cenerenti M, Saillard M, Romero P, Jandus C. The Era of Cytotoxic CD4 T Cells. Front Immunol. 2022; 13: 867189.
34. Perez-Diez A, Joncker NT, Choi K, Chan WF, Anderson CC, Lantz O, Matzinger P. CD4 cells can be more efficient at tumor rejection than CD8 cells. Blood. 2007; 109: 5346-54.
35. Glatzová D, Cebecauer M. Dual Role of CD4 in Peripheral T Lymphocytes. Front Immunol. 2019; 10: 618.
36. Freise AC, Wu AM. *In vivo* imaging with antibodies and engineered fragments. Mol Immunol. 2015; 67: 142-52.
37. Schwenck J, Sonanini D, Cotton JM, Rammensee HG, la Fougère C, Zender L, Pichler BJ. Advances in PET imaging of cancer. Nat Rev Cancer. 2023; 23: 474-90.
38. Kim I, Srinivasula S, DeGrange P, Long B, Jang H, Carrasquillo JA, *et al.* Quantitative PET imaging of the CD4 pool in nonhuman primates. Eur J Nucl Med Mol Imaging. 2022; 50: 14-26.
39. Kristensen LK, Fröhlich C, Christensen C, Melander MC, Poulsen TT, Galler GR, *et al.* CD4(+) and CD8a(+) PET imaging predicts response to novel PD-1 checkpoint inhibitor: studies of Sym021 in syngeneic mouse cancer models. Theranostics. 2019; 9: 8221-38.
40. Clausen AS, Christensen C, Christensen E, Cold S, Kristensen LK, Hansen AE, Kjaer A. Development of a (64)Cu-labeled CD4(+) T cell targeting PET tracer: evaluation of CD4 specificity and its potential use in collagen-induced arthritis. EJNMMI Res. 2022; 12: 62.
41. Freise AC, Zettlitz KA, Salazar FB, Lu X, Tavaré R, Wu AM. ImmunoPET Imaging of Murine CD4(+) T Cells Using Anti-CD4 Cys-Diabody: Effects of Protein Dose on T Cell Function and Imaging. Mol Imaging Biol. 2017; 19: 599-609.
42. Tavaré R, McCracken MN, Zettlitz KA, Salazar FB, Olafsen T, Witte ON, Wu AM. Immuno-PET of Murine T Cell Reconstitution Postadoptive Stem Cell Transplantation Using Anti-CD4 and Anti-CD8 Cys-Diabodies. J Nucl Med. 2015; 56: 1258-64.
43. Freise AC, Zettlitz KA, Salazar FB, Tavaré R, Tsai WK, Chatziioannou AF, *et al.* Immuno-PET in Inflammatory Bowel Disease: Imaging CD4-Positive T Cells in a Murine Model of Colitis. J Nucl Med. 2018; 59: 980-5.
44. Traenkle B, Kaiser PD, Pezzana S, Richardson J, Gramlich M, Wagner TR, *et al.* Single-Domain Antibodies for Targeting, Detection, and *In vivo* Imaging of Human CD4(+) Cells. Front Immunol. 2021; 12: 799910.
45. Nagle VL, Hertz CAJ, Henry KE, Graham MS, Campos C, Pillarsetty N, *et al.* Noninvasive Imaging of CD4+ T Cells in Humanized Mice. Mol Cancer Ther. 2022; 21: 658-66.
46. Kist de Ruijter L, van de Donk PP, Hooiveld-Noeken JS, Giesen D, Elias SG, Lub-de Hooge MN, *et al.* Whole-body CD8(+) T cell visualization before and during cancer immunotherapy: a phase 1/2 trial. Nat Med. 2022; 28: 2601-10.
47. Schwenck J, Sonanini D, Seyfried D, Ehrlichmann W, Kienzle G, Reischl G, *et al. In vivo* imaging of CD8(+) T cells in metastatic cancer patients: first clinical experience with simultaneous [(89)Zr]Zr-Df-IAB22M2C PET/MRI. Theranostics. 2023; 13: 2408-23.
48. Niemeijer AN, Leung D, Huisman MC, Bahce I, Hoekstra OS, van Dongen G, *et al.* Whole body PD-1 and PD-L1 positron emission tomography in patients with non-small-cell lung cancer. Nat Commun. 2018; 9: 4664.
49. Bensch F, van der Veen EL, Lub-de Hooge MN, Jorritsma-Smit A, Boellaard R, Kok IC, *et al.* (89)Zr-atezolizumab imaging as a non-invasive approach to assess clinical response to PD-L1 blockade in cancer. Nat Med. 2018; 24: 1852-8.
50. Miedema IHC, Huisman MC, Zwezerijnen GJC, Grempler R, Pitarch AP, Thiele A, *et al.* (89)Zr-immuno-PET using the anti-LAG-3 tracer [(89)Zr]Zr-BI 754111: demonstrating target specific binding in NSCLC and HNSCC. Eur J Nucl Med Mol Imaging. 2023; 50: 2068-80.
51. Pandit-Taskar N, Postow MA, Hellmann MD, Harding JJ, Barker CA, O'Donoghue JA, *et al.* First-in-Humans Imaging with (89)Zr-Df-IAB22M2C Anti-CD8 Minibody in Patients with Solid Malignancies: Preliminary Pharmacokinetics, Biodistribution, and Lesion Targeting. J Nucl Med. 2020; 61: 512-9.
52. Farwell MD, Gamache RF, Babazada H, Hellmann MD, Harding JJ, Korn R, *et al.* CD8-Targeted PET Imaging of Tumor-Infiltrating T Cells in Patients with Cancer: A Phase I First-in-Humans Study of (89)Zr-Df-IAB22M2C, a Radiolabeled Anti-CD8 Minibody. J Nucl Med. 2022; 63: 720-6.
53. Olafsen T, Torgov M, Zhang GG, Romero J, Zampila C, Marchioni F, *et al.* Pet imaging of cytotoxic human T cells using an 89Zr-labeled anti-CD8 minibody. Journal for ImmunoTherapy of Cancer. 2015; 3: P388.
54. Griessinger CM, Olafsen T, Mascioni A, Jiang ZK, Zamilpa C, Jia F, *et al.* The PET-Tracer (89)Zr-Df-IAB22M2C Enables Monitoring of Intratumoral CD8 T-cell Infiltrates in Tumor-Bearing Humanized Mice after T-cell Bispecific Antibody Treatment. Cancer Res. 2020; 80: 2903-13.
55. Li H, van der Merwe PA, Sivakumar S. Biomarkers of response to PD-1 pathway blockade. Br J Cancer. 2022; 126: 1663-75.
56. Lu Y, Zhang X, Ning J, Zhang M. Immune checkpoint inhibitors as first-line therapy for non-small cell lung cancer: A systematic evaluation and meta-analysis. Hum Vaccin Immunother. 2023; 19: 2169531.
57. Shiravand Y, Khodadadi F, Kashani SMA, Hosseini-Fard SR, Hosseini S, Sadeghirad H, *et al.* Immune Checkpoint Inhibitors in Cancer Therapy. Curr Oncol. 2022; 29: 3044-60.
58. Pauken KE, Dougan M, Rose NR, Lichtman AH, Sharpe AH. Adverse Events Following Cancer Immunotherapy: Obstacles and Opportunities. Trends Immunol. 2019; 40: 511-23.
59. Saillard M, Cenerenti M, Romero P, Jandus C. Impact of Immunotherapy on CD4 T Cell Phenotypes and Function in Cancer. Vaccines (Basel). 2021; 9: 454.
60. Shultz LD, Schweitzer PA, Christianson SW, Gott B, Schweitzer IB, Tennent B, *et al.* Multiple defects in innate and adaptive immunologic function in NOD/LtSz-scid mice. J Immunol. 1995; 154: 180-91.
61. Serreze DV, Gaskins HR, Leiter EH. Defects in the differentiation and function of antigen presenting cells in NOD/Lt mice. J Immunol. 1993; 150: 2534-43.
62. Shultz LD, Lyons BL, Burzenski LM, Gott B, Chen X, Chaleff S, *et al.* Human lymphoid and myeloid cell development in NOD/LtSz-scid IL2R gamma null mice engrafted with mobilized human hemopoietic stem cells. J Immunol. 2005; 174: 6477-89.
63. Smit J, Borm FJ, Niemeijer AN, Huisman MC, Hoekstra OS, Boellaard R, *et al.* PD-L1 PET/CT Imaging with Radiolabeled Durvalumab in Patients with Advanced-Stage Non-Small Cell Lung Cancer. J Nucl Med. 2022; 63: 686-93.
64. Hegi-Johnson F, Rudd S, Hicks RJ, De Ruysscher D, Trapani JA, John T, *et al.* Imaging immunity in patients with cancer using positron emission tomography. NPJ Precis Oncol. 2022; 6: 24.
65. Manafi-Farid R, Ataeinia B, Ranjbar S, Jamshidi Araghi Z, Moradi MM, Pirich C, Beheshti M. ImmunoPET: Antibody-Based PET Imaging in Solid Tumors. Front Med (Lausanne). 2022; 9: 916693.
66. Weyand CM, Goronzy J, Fathman CG. Modulation of CD4 by antigenic activation. J Immunol. 1987; 138: 1351-4.
67. Liu Q, Wang L, Lin H, Wang Z, Wu J, Guo J, *et al.* Tumor-Specific CD4(+) T Cells Restrain Established Metastatic Melanoma by Developing Into Cytotoxic CD4(-) T Cells. Front Immunol. 2022; 13: 875718.
68. Shields NJ, Peyroux EM, Ferguson AL, Steain M, Neumann S, Young SL. Late-stage MC38 tumours recapitulate features of human colorectal cancer - implications for appropriate timepoint selection in preclinical studies. Front Immunol. 2023; 14: 1152035.
69. Lau J, Cheung J, Navarro A, Lianoglou S, Haley B, Totpal K, *et al.* Tumour and host cell PD-L1 is required to mediate suppression of anti-tumour immunity in mice. Nat Commun. 2017; 8: 14572.
70. Knopf P, Stowbur D, Hoffmann SHL, Hermann N, Maurer A, Bucher V, *et al.* Acidosis-mediated increase in IFN-γ-induced PD-L1 expression on cancer cells as an immune escape mechanism in solid tumors. Mol Cancer. 2023; 22: 207.
71. Woo SR, Turnis ME, Goldberg MV, Bankoti J, Selby M, Nirschl CJ, *et al.* Immune inhibitory molecules LAG-3 and PD-1 synergistically regulate T-cell function to promote tumoral immune escape. Cancer Res. 2012; 72: 917-27.
72. Ribas A, Dummer R, Puzanov I, VanderWalde A, Andtbacka RHI, Michielin O, *et al.* Oncolytic Virotherapy Promotes Intratumoral T Cell Infiltration and Improves Anti-PD-1 Immunotherapy. Cell. 2017; 170: 1109-19.e10.

73. Reiss DJ, Do T, Kuo D, Gray VE, Olson NE, Lee C-W, *et al.* Multiplexed Immunofluorescence (IF) Analysis and Gene Expression Profiling of Biopsies from Patients with Relapsed/Refractory (R/R) Diffuse Large B Cell Lymphoma (DLBCL) Treated with Lisocabtagene Maraleucel (liso-cel) in Transcend NHL 001 Reveal Patterns of Immune Infiltration Associated with Durable Response. Blood. 2019; 134: 202-.
74. Liakou CI, Kamat A, Tang DN, Chen H, Sun J, Troncoso P, *et al.* CTLA-4 blockade increases IFNgamma-producing CD4+ICOShi cells to shift the ratio of effector to regulatory T cells in cancer patients. Proc Natl Acad Sci U S A. 2008; 105: 14987-92.
75. Wei SC, Levine JH, Cogdill AP, Zhao Y, Anang NAS, Andrews MC, *et al.* Distinct Cellular Mechanisms Underlie Anti-CTLA-4 and Anti-PD-1 Checkpoint Blockade. Cell. 2017; 170: 1120-33.e17.
76. Jiao S, Subudhi SK, Aparicio A, Ge Z, Guan B, Miura Y, Sharma P. Differences in Tumor Microenvironment Dictate T Helper Lineage Polarization and Response to Immune Checkpoint Therapy. Cell. 2019; 179: 1177-90.e13.
77. Monkman J, Moradi A, Yunis J, Ivison G, Mayer A, Ladwa R, *et al.* Spatial insights into immunotherapy response in non-small cell lung cancer (NSCLC) by multiplexed tissue imaging. J Transl Med. 2024; 22: 239.
78. Aggarwal V, Workman CJ, Vignali DAA. LAG-3 as the third checkpoint inhibitor. Nat Immunol. 2023; 24: 1415-22.
79. Phillips D, Matusiak M, Gutierrez BR, Bhate SS, Barlow GL, Jiang S, *et al.* Immune cell topography predicts response to PD-1 blockade in cutaneous T cell lymphoma. Nat Commun. 2021; 12: 6726.
80. Pichler BJ, Wehrl HF, Kolb A, Judenhofer MS. Positron emission tomography/magnetic resonance imaging: the next generation of multimodality imaging? Semin Nucl Med. 2008; 38: 199-208.

3.2. Accepted publication II

Traenkle B, Kaiser PD, **Pezzana S**, Richardson J, Gramlich M, Wagner TR, Seyfried D, Weldle M, Holz S, Parfyonova Y, Nueske S, Scholz AM, Zeck A, Jakobi M, Schneiderhan-Marra N, Schaller M, Maurer A, Gouttefangeas C, Kneilling M, Pichler BJ, Sonanini D, Rothbauer U. Single-Domain Antibodies for Targeting, Detection, and *In Vivo* Imaging of Human $CD4^+$ Cells. Front Immunol. 2021 Dec 9;12:799910. doi: 10.3389/fimmu.2021.799910. [2]

frontiers in Immunology

ORIGINAL RESEARCH
published: 09 December 2021
doi: 10.3389/fimmu.2021.799910

Single-Domain Antibodies for Targeting, Detection, and *In Vivo* Imaging of Human CD4$^+$ Cells

*Bjoern Traenkle[1], Philipp D. Kaiser[1], Stefania Pezzana[2], Jennifer Richardson[3], Marius Gramlich[1], Teresa R. Wagner[1,4], Dominik Seyfried[2,5], Melissa Weldle[4], Stefanie Holz[4], Yana Parfyonova[4], Stefan Nueske[6], Armin M. Scholz[6], Anne Zeck[1], Meike Jakobi[1], Nicole Schneiderhan-Marra[1], Martin Schaller[7], Andreas Maurer[2,8], Cécile Gouttefangeas[3,5,8], Manfred Kneilling[2,7,8], Bernd J. Pichler[2,5,8], Dominik Sonanini[2,9] and Ulrich Rothbauer[1,4,8]**

[1] NMI Natural and Medical Sciences Institute at the University of Tübingen, Reutlingen, Germany, [2] Werner Siemens Imaging Center, Department of Preclinical Imaging and Radiopharmacy, University of Tübingen, Tübingen, Germany, [3] Department of Immunology, Institute of Cell Biology, University of Tübingen, Tübingen, Germany, [4] Pharmaceutical Biotechnology, University of Tübingen, Tübingen, Germany, [5] German Cancer Consortium (DKTK) and German Cancer Research Center (DKFZ) partner site Tübingen, Tübingen, Germany, [6] Livestock Center of the Faculty of Veterinary Medicine, Ludwig Maximilians University Munich, Oberschleissheim, Germany, [7] Department of Dermatology, University of Tübingen, Tübingen, Germany, [8] Cluster of Excellence iFIT (EXC2180) "Image-Guided and Functionally Instructed Tumor Therapies," University of Tübingen, Tübingen, Germany, [9] Department of Medical Oncology and Pneumology, University of Tübingen, Tübingen, Germany

The advancement of new immunotherapies necessitates appropriate probes to monitor the presence and distribution of distinct immune cell populations. Considering the key role of CD4$^+$ cells in regulating immunological processes, we generated novel single-domain antibodies [nanobodies (Nbs)] that specifically recognize human CD4. After in-depth analysis of their binding properties, recognized epitopes, and effects on T-cell proliferation, activation, and cytokine release, we selected CD4-specific Nbs that did not interfere with crucial T-cell processes *in vitro* and converted them into immune tracers for noninvasive molecular imaging. By optical imaging, we demonstrated the ability of a high-affinity CD4-Nb to specifically visualize CD4$^+$ cells *in vivo* using a xenograft model. Furthermore, quantitative high-resolution immune positron emission tomography (immunoPET)/MR of a human CD4 knock-in mouse model showed rapid accumulation of ^{64}Cu-radiolabeled CD4-Nb1 in CD4$^+$ T cell-rich tissues. We propose that the CD4-Nbs presented here could serve as versatile probes for stratifying patients and monitoring individual immune responses during personalized immunotherapy in both cancer and inflammatory diseases.

Keywords: CD4, nanobody, immune tracer, PET imaging, magnetic resonance imaging, immunotherapies

OPEN ACCESS

Edited by:
Marco Erreni, Humanitas Research Hospital, Italy

Reviewed by:
Serge Muyldermans, Vrije University Brussel, Belgium
Alexis Broisat, Institut National de la Santé et de la Recherche Médicale (INSERM), France

***Correspondence:**
Ulrich Rothbauer
ulrich.rothbauer@uni-tuebingen.de
orcid.org/0000-0001-5923-8986

Specialty section:
This article was submitted to Cancer Immunity and Immunotherapy, a section of the journal Frontiers in Immunology

Received: *22 October 2021*
Accepted: *17 November 2021*
Published: *09 December 2021*

Citation:
Traenkle B, Kaiser PD, Pezzana S, Richardson J, Gramlich M, Wagner TR, Seyfried D, Weldle M, Holz S, Parfyonova Y, Nueske S, Scholz AM, Zeck A, Jakobi M, Schneiderhan-Marra N, Schaller M, Maurer A, Gouttefangeas C, Kneilling M, Pichler BJ, Sonanini D and Rothbauer U (2021) Single-Domain Antibodies for Targeting, Detection, and In Vivo Imaging of Human CD4$^+$ Cells. Front. Immunol. 12:799910. doi: 10.3389/fimmu.2021.799910

INTRODUCTION

In precision medicine, diagnostic classification of the disease-associated immune status should guide the selection of appropriate therapies. A comprehensive analysis of a patient's specific immune cell composition, activation state, and infiltration of affected tissue has been shown to be highly informative for patient stratification (1–3). In this context, CD4 is an important marker, as it is found on the surface of immune cells such as monocytes, macrophages, and dendritic cells and most

abundant on $CD4^+$ T cells (4, 5). $CD4^+$ T cells are a key determinant of the immune status due to their essential role in orchestrating immune responses in autoimmune diseases, immune-mediated inflammatory diseases (IMIDs), cancer, and chronic viral infections (6–13). Current diagnostic standards such as intra-cytoplasmic flow cytometry analysis (IC-FACS), immunohistochemistry, and *ex vivo* cytokine assays or RT-PCR analysis are exclusively invasive and therefore limited with respect to repetitive analyses over time (14–17). Considering the emerging role of infiltrating lymphocytes and the impact of $CD4^+$ T cells on the outcome of immunotherapies, novel approaches are needed to assess $CD4^+$ T cells more holistically (18). In this context, noninvasive imaging approaches offer a significant benefit compared to the current diagnostic standard. To date, radiolabeled antibodies have been applied to image $CD4^+$ cells in preclinical models (10, 19–21). Due to the recycling effect mediated by the neonatal Fc receptor, full-length antibodies have a long serum half-life, which requires long clearance times of several days before high-contrast images can be acquired (22). Additionally, effector function *via* the Fc region was shown to induce depletion or functional changes in $CD4^+$ cells including the induction of proliferation or cytokine release (23–25). Notably, also higher dosages of recombinant antibody fragments like Fab fragments or Cys-diabodies derived from the monoclonal anti-CD4 antibody GK1.5 were recently shown to decrease CD4 expression *in vivo* and inhibit proliferation and interferon (IFN)-γ production *in vitro* (24–26). These studies highlight the importance of carefully investigating $CD4^+$ cell-specific immunoprobes for their epitopes, binding properties, and functional effects.

During the last decade, antibody fragments derived from heavy-chain-only antibodies of camelids, referred to as VHHs or nanobodies (Nbs) (27), have emerged as versatile probes for molecular imaging [reviewed in (28)]. In combination with highly sensitive and/or quantitative whole-body molecular imaging techniques such as optical or radionuclide-based modalities, particularly positron emission tomography (PET), Nbs have been shown to bind their targets within several minutes of systemic application (29). Due to their great potential as highly specific imaging probes, numerous Nbs targeting immune- or tumor-specific cellular antigens are currently in preclinical development and even in clinical trials (28, 30, 31).

Here, we generated a set of human CD4 (hCD4)-specific Nbs. Following in-depth characterization of their binding properties, we selected candidates that did not affect T-cell proliferation, activation, or cytokine release and converted them into immune tracers for noninvasive optical and PET imaging. Using a mouse xenograft model and an hCD4 knock-in mouse model, we successfully demonstrated the capacity of these CD4-Nbs to visualize $CD4^+$ cells *in vivo*.

RESULTS

Generation of High-Affinity CD4 Nanobodies

To generate Nbs directed against hCD4, we immunized an alpaca (*Vicugna pacos*) with the recombinant extracellular portion of hCD4 following an 87-day immunization protocol. Subsequently, we generated a Nb phagemid library comprising ~4×10^7 clones that represent the full repertoire of variable heavy chains of heavy-chain antibodies (VHHs or Nbs) of the animal. We performed phage display using either passively adsorbed purified hCD4 or CHO and HEK293 cells stably expressing full-length hCD4 (CHO-hCD4 and HEK293-hCD4 cell lines, respectively). Following two cycles of phage display for each condition, we analyzed a total of 612 individual clones by whole-cell phage ELISA and identified 78 positive binders. Sequence analysis revealed 13 unique Nbs representing five different B-cell lineages according to their complementarity determining region (CDR) 3 (**Figure 1A**). One representative Nb of each lineage, termed CD4-Nb1–CD4-Nb5, was expressed in bacteria (*Escherichia coli*) and isolated with high purity using immobilized metal ion affinity chromatography (IMAC) followed by size exclusion chromatography (SEC) (**Figure 1B**). To test whether selected Nbs are capable of binding to full-length hCD4 localized at the plasma membrane of mammalian cells, we performed live-cell staining of CHO-hCD4 cells (**Figure 1C**, **Supplementary Figure 1**). Executed at 4°C, images showed a prominent staining of the plasma membrane, whereas at 37°C, the fluorescent signal was mainly localized throughout the cell body, presumably a consequence of endocytotic uptake of receptor-bound Nbs. CHO wild-type (wt) cells were not stained by any of the five CD4-Nbs at both temperatures (data not shown). CD4-Nb1 and CD4-Nb3, both identified by whole-cell panning, displayed strong staining of CHO-hCD4 cells. Of the Nbs derived from panning with recombinant hCD4, CD4-Nb2 also showed strong cellular staining, whereas staining with CD4-Nb4 revealed weak signals. CD4-Nb5 showed no staining under these conditions and was consequently excluded from further analyses (**Figure 1C**). To quantitatively assess binding affinities, we performed biolayer interferometry (BLI), measuring serial dilutions of Nbs on the biotinylated extracellular domain of hCD4 immobilized at the sensor tip. For CD4-Nb1 and CD4-Nb2, K_D values were determined to be ~5 and ~7 nM, respectively, while CD4-Nb3 and CD4-Nb4 displayed lower affinities of 75 and 135 nM, respectively (**Figure 1D**, **Table 1**, **Supplementary Figure 2A**). In addition, we determined corresponding EC_{50} values with full-length plasma membrane-located hCD4 on HEK293-hCD4 cells by flow cytometry. In accordance with cellular staining and biochemically determined affinities, these values revealed a strong functional binding for CD4-Nb1 and CD4-Nb2 with EC_{50} values in the subnanomolar range (~0.7 nM), whereas CD4-Nb3 and CD4-Nb4 displayed substantially lower cellular affinities (**Figure 1E**, **Table 1**, **Supplementary Figure 2B**). In summary, we generated four CD4-Nbs that bind isolated and cell-resident hCD4. While CD4-Nb3 and CD4-Nb4 appeared less affine, CD4-Nb1 and CD4-Nb2 displayed high affinities in the low nanomolar range.

Domain Mapping

Next, we applied chemo-enzymatic coupling using sortase A for site-directed functionalization of CD4-Nbs (32, 33). We thereby linked peptides conjugated to a single fluorophore to the C-terminus of CD4-Nbs, yielding a defined labeling ratio of 1:1 (34). Live-cell immunofluorescence imaging showed that all sortase-coupled CD4-Nbs retained their capability of binding

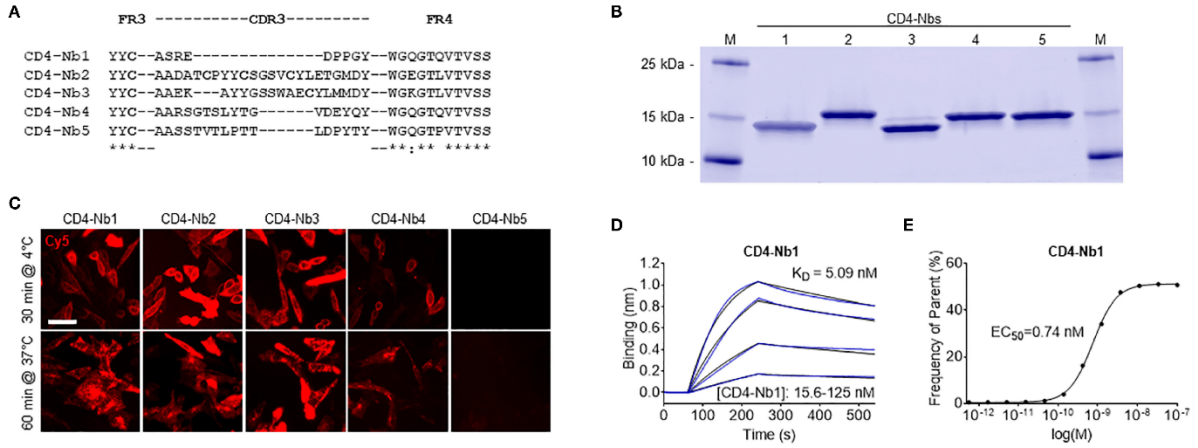

FIGURE 1 | Identification and characterization of nanobodies (Nbs) against human CD4 (hCD4). **(A)** Amino acid sequences of the complementarity determining region (CDR) 3 from unique CD4-Nbs selected after two rounds of biopanning are listed. **(B)** Recombinant expression and purification of CD4-Nbs using immobilized metal ion affinity chromatography (IMAC) and size exclusion chromatography (SEC). Coomassie-stained SDS-PAGE of 2 µg of purified Nbs is shown. **(C)** Representative images of live CHO-hCD4 cells stained with CD4-Nbs for 30 min at 4°C (top row) or 60 min at 37°C (bottom row); scale bar: 50 µm. **(D)** For biolayer interferometry (BLI)-based affinity measurements, biotinylated hCD4 was immobilized on streptavidin biosensors. Kinetic measurements were performed using four concentrations of purified Nbs ranging from 15.6 to 1,000 nM. As an example, the sensogram of CD4-Nb1 at indicated concentrations is shown. **(E)** EC_{50} determination by flow cytometry. Exemplarily shown for CD4-Nb1, the percentage of positively stained HEK293-hCD4 (frequency of parent) was plotted against indicated concentrations of CD4-Nbs.

TABLE 1 | Summary of affinities (k_D) and association (k_{on}) and dissociation constants (k_{off} and coefficient of determination R_2) determined by BLI (left side) and EC_{50} values of flow cytometry (right side).

	Dissociation constant K_D	k_{on} (10^5 M^{-1} s^{-1})	k_{off} (10^{-4} s^{-1})	R^2	EC_{50}
CD4-Nb1	5.1 nM	1.21 ± 0.022	6.13 ± 0.27	0.996	0.74 nM
CD4-Nb2	6.5 nM	1.22 ± 0.015	7.95 ± 0.18	0.998	0.73 nM
CD4-Nb3	75.3 nM	0.82 ± 0.026	61.8 ± 2.00	0.983	533 nM
CD4-Nb4	135 nM	1.18 ± 0.014	160 ± 0.97	0.998	7.36 µM

to cell-resident hCD4 of CHO-hCD4 cells (**Supplementary Figure 3A**). To localize the binding sites of the selected CD4-Nbs, we generated domain-deletion mutants of hCD4. Expression and correct surface localization of these mutants in CHO cells were confirmed by staining with antibody RPA-T4 binding to domain 1 of CD4. For mutants lacking domain 1, we introduced an N-terminal BC2 tag (35) to allow for live-cell surface detection with a fluorescently labeled bivBC2-Nb (34) (**Supplementary Figure 3B**). Transiently expressed domain-deletion mutants were then tested for binding of CF568-labeled CD4-Nbs by live-cell immunofluorescence imaging, including a non-specific fluorescently labeled green fluorescent protein (GFP)-binding Nb (GFP-Nb) as negative control. Based on these results, we allocated binding of CD4-Nb1 and CD4-Nb3 to domain 1, whereas CD4-Nb2 and CD4-Nb4 bind to domain 3 and/or 4 of hCD4 (**Figure 2A**, **Supplementary Figure 3C**).

To further examine combinatorial binding of the different CD4-Nbs, we performed an epitope binning analysis by BLI. Recombinant full-length hCD4 was immobilized at the sensor tip, and combinations of CD4-Nbs were allowed to bind consecutively (**Supplementary Figure 4**). Unsurprisingly, CD4-Nbs binding to different domains displayed combinatorial binding. Interestingly, a simultaneous binding was also detected for the combination of CD4-Nb1 and CD4-Nb3, suggesting that both CD4-Nbs bind to different epitopes within domain 1. In contrast, we did not observe simultaneous binding for CD4-Nb2 and CD4-Nb4, which might be due to close-by or overlapping epitopes at domain 3/4 for the latter Nb pair.

For a more precise epitope analysis, we conducted a hydrogen–deuterium exchange mass spectrometry (HDX-MS) analysis of hCD4 bound to CD4-Nb1, CD4-Nb2, or CD4-Nb3 (**Figures 2B–E**, **Supplementary Figure 5**). Due to its low affinity, CD4-Nb4 was not considered for HDX-MS analysis (data not shown). In accordance with our previous findings, binding of CD4-Nb1 and CD4-Nb3 protected sequences of domain 1 from HDX, whereas CD4-Nb2 protected sequences of domains 3 and 4 of hCD4 (**Figure 2B**). The results obtained for binding of CD4-Nb1 (**Figure 2C**) are similar to those obtained for CD4-Nb3 (**Figure 2D**) in that binding of either Nb reduced hydrogen exchange at amino acid (aa) residues from aa T17 to N73, albeit with a different extent of protection at individual sequence segments. For CD4-Nb1, the greatest protection from HDX

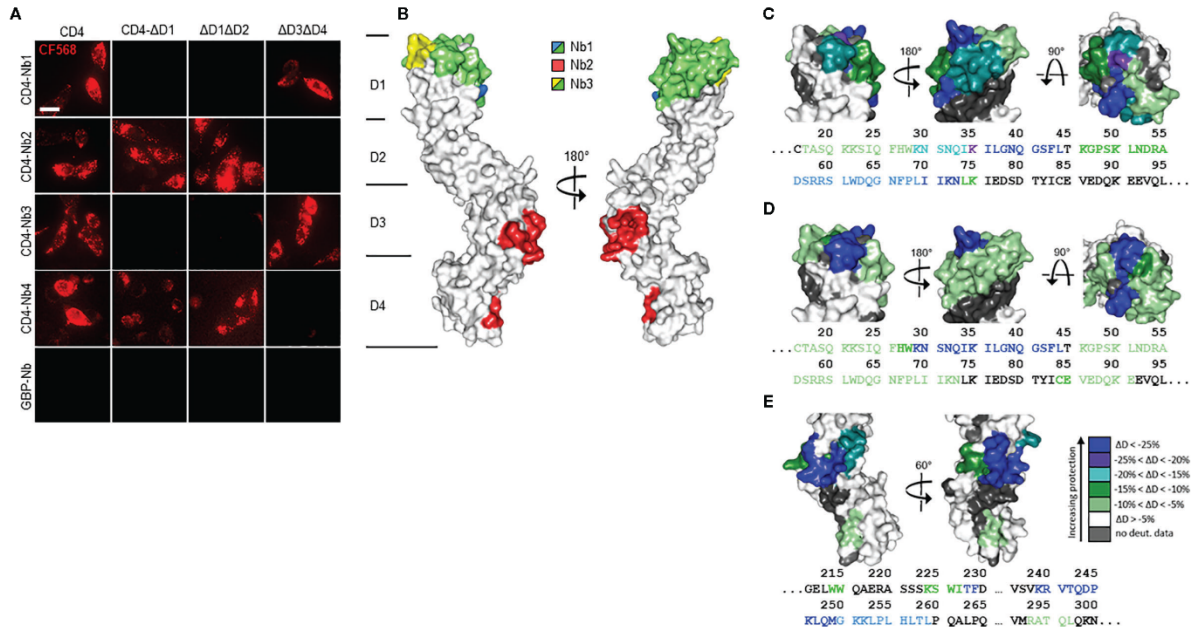

FIGURE 2 | Localization of CD4-nanobody (Nb) binding epitopes. **(A)** Representative images of live CHO cells expressing full-length or domain-deletion mutants of human CD4 (hCD4) stained with fluorescently labeled CD4-Nbs (CF568) are shown; scale bar 10 µm. **(B)** Surface structure model of hCD4 (PDBe 1wiq) (36) and the hydrogen-deuterium exchange mass spectrometry (HDX-MS) epitope mapping results of CD4-Nb1–3 are depicted. Different colors highlight the amino acid residues protected by CD4-Nb1 (blue), CD4-Nb2 (red), or CD4-Nb3 (yellow). Overlapping residues protected by both Nb1 and Nb3 are colored green. A more detailed surface map (%ΔD) of these specific regions is highlighted in **(C)** (CD4-Nb1), **(D)** (CD4-Nb3), and **(E)** (CD4-Nb2) with the corresponding CD4 amino acid sequence.

was observed for the sequence ranging from aa K35 to L44 corresponding to β strand C′ and C′′ of the immunoglobulin fold of domain 1 and residues aa K46–K75, comprising β strands D and E. In contrast, binding of CD4-Nb3 confers only a minor reduction in HDX within the latter sequence but additionally protects sequence aa C84–E91, which correspond to β strands G and F and their intermediate loop. For CD4-Nb2, we found protection of sequences aa W214–F229 (β strands C and C′) and aa K239–L259 (β strands C′′–E) and to a minor extent sequence aa R293–L296 as part of β strand A of domain 4 (**Figure 2E**). In summary, our HDX-MS analysis revealed that all three tested Nbs bind three dimensional epitopes within different parts of hCD4. It further provides an explanation how CD4-Nb1 and CD4-Nb3 can bind simultaneously to domain 1 of hCD4 and confirms that the epitope of CD4-Nb2 is mainly located at domain 3.

Binding of CD4-Nbs to Human Peripheral Blood Mononuclear Cells

Having demonstrated that all selected Nbs bind to recombinant and exogenously overexpressed cellular hCD4, we next examined their capability and specificity of binding to physiologically relevant levels of $CD4^+$ T cells within peripheral blood mononuclear cell (PBMC) samples. We costained human PBMCs from three donors with CD4-Nb1–CD4-Nb4 coupled to CF568 (100 nM for high-affine CD4-Nb1 and CD4-Nb2; 1,000 nM for low-affine CD4-Nb3 and CD4-Nb4) in combination with an anti-CD3 antibody and analyzed the percentage of double-positive cells ($CD3^+CD4^+$) by flow cytometry (**Figure 3**, **Supplementary Figure 6**). Compared to staining with an anti-CD4 antibody used as a positive control, all CD4-Nbs stained a similar percentage of $CD4^+$ T cells for all tested donors, while the non-specific GFP-Nb yielded a negligible percentage of double-positive cells even at the highest concentration (1,000 nM) (**Table 2**). Our analysis further revealed that, as observed with a conventional anti-CD4 antibody, the CD4-Nbs stain a substantial proportion of $CD3^-$ cells, indicating that all selected candidates are also able to recognize cells such as monocytes, macrophages, or dendritic cells that express lower levels of CD4 (**Figure 3**).

Impact of CD4-Nbs on Activation, Proliferation, and Cytokine Release of $CD4^+$ T and Immune Cells

In view of the envisioned application as clinical imaging tracer, we next evaluated the potential of the Nbs to be further developed into clinically approved binding molecules. Since CD4-Nb2 and CD4-Nb3 contain a number of cysteine residues in their CDR3, we excluded them at this stage because such non-canonical unpaired cysteines are often associated with expression

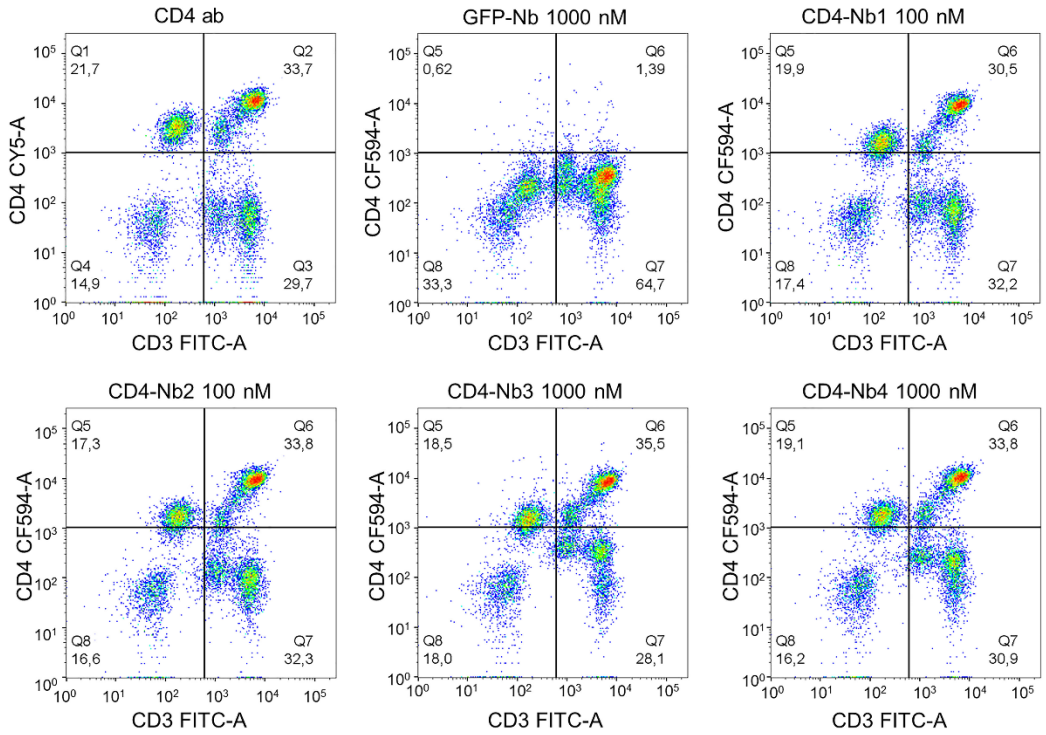

FIGURE 3 | Flow cytometry analysis of human peripheral blood mononuclear cells (PBMCs) stained with fluorescently labeled CD4-nanobodies (Nbs). Schematic representation of the final gating step for $CD3^+CD4^+$ double-positive cells derived from donor 1.

problems and a higher tendency to form aggregates in downstream production (37, 38). With CD4-Nb1 and CD4-Nb4, we pursued two candidates that do not contain non-canonical cysteines and also cover a broad affinity spectrum. For these two Nbs and a non-specific GFP-Nb as a control, we then examined their influence on $CD4^+$ T-cell activation, proliferation, and cytokine release. To rule out adverse effects of bacterial endotoxins in the Nb preparations, we first removed endotoxins by depletion chromatography, resulting in Food and Drug Administration (FDA)-acceptable endotoxin levels of <0.25 EU per mg. Typically, Nb-based radiotracers are applied at serum concentrations between 0.01 and 0.2 μM in (pre)clinical imaging (39, 40). To investigate the effects of Nbs at the expected, but also at a 10-fold increased concentration and consequently elongated serum retention times that might occur during *in vivo* (pre)clinical imaging, we treated carboxyfluorescein succinimidyl ester (CFSE)-labeled human PBMCs from three preselected healthy donors with three Nbs at concentrations ranging from 0.05 from 5 μM for 1 h at 37°C. Subsequently, cells were washed to remove Nbs and stimulated with an antigenic [cognate major histocompatibility complex (MHC)II peptides] or a non-antigenic stimulus (phytohemagglutinin, PHA-L) and analyzed after 4, 6, and 8 days by flow cytometry with the gating strategy shown in **Supplementary Figure 7A**. According to the highly similar CFSE intensity profiles observed, the total number of cell divisions was not affected by the different Nb treatments (exemplarily shown for one of three donors on day 6; **Supplementary Figure 7A**). For samples of the same donor and time point, no substantial differences in the percentage of proliferated cells were observed between mock incubation and individual Nb treatments.

For both stimuli, the average percentage of proliferated cells increased over time in all donors tested, with no clear differences between conditions (**Figure 4A**). As a quantitative measure of T-cell activation, we also determined the cell surface induction of a very early activation marker (CD69) and of the interleukin (IL)-2 receptor α chain (CD25) on $CD4^+$ T cells (**Figure 4B**). Among samples of the same donor and stimulation, we found highly similar activation profiles for all Nb treatments. While the percentage of $CD4^+CD25^+$ cells steadily increased over time for MHCII peptide stimulation, for the PHA-stimulated condition, the percentage of positive cells was similarly high at all times of analysis. Importantly, regardless of the differences between donors, the individual Nb treatments from the same donor did not result in significant differences in the percentage of $CD4^+CD25^+$ or $CD4^+CD69^+$ cells for either stimulation at any point in the analysis.

Next, we analyzed cytokine expression of $CD4^+$ T cells by intracellular cytokine staining after restimulation with cognate MHCII peptides. The corresponding gating strategy is shown in

TABLE 2 | Percentage of double-positive cells of three donors, stained with CD4-Nb1 or CD4-Nb2 (100 nM), or CD4-Nb3 or CD4-Nb4 (1,000 nM), compared to anti-CD4 antibody and negative control Nb (GFP-Nb, 1,000 nM).

		Frequency $CD3^+$ $CD4^+$ (%)		
	c (nM)	Donor 1	Donor 2	Donor 3
Anti-CD4 antibody	~1	33.7	27.0	*24.3*
CD4-Nb1	100	30.5	29.2	22.7
CD4-Nb2	100	33.8	25.6	18.4
CD4-Nb3	1,000	35.5	26.5	20.4
CD4-Nb4	1,000	33.8	26.9	23.9
GFP-Nb	1,000	1.4	0.3	1.0

Supplementary Figure 7B. Samples of the same donor treated with different Nbs had highly similar percentages of cytokine [tumor necrosis factor (TNF), IFN-γ, or IL-2] or activation marker (CD154)-positive cells without stimulation and upon stimulation with MHCII peptides (**Figure 4C**). Overall, exposure to CD4-Nbs did not affect the proliferation, activation, or cytokine production of $CD4^+$ T cells. In addition, we analyzed potential effects of CD4-Nbs on the release of cytokines from full-blood samples of three further donors. Upon stimulation with lipopolysaccharide (LPS) or PHA–L, we determined the serum concentrations with a panel of pro- and anti-inflammatory cytokines (**Supplementary Table 2**). Although there was significant inter-donor variation for some cytokines, Nb treatment did not result in significant differences in either stimulated or unstimulated samples (**Supplementary Figure 8**).

CD4-Nbs for *In Vivo* Imaging

For optical *in vivo* imaging, we labeled CD4-Nbs with the fluorophore Cy5.5 (CD4-Nb-Cy5.5) by sortase-mediated attachment of an azide group followed by click-chemistry addition of dibenzocyclooctyne (DBCO)-Cy5.5. First, we tested potential cross-reactivity of the four Cy5.5-labeled CD4-Nbs to murine $CD4^+$ lymphocytes. Notably, flow cytometric analysis showed that none of the selected CD4-Nbs bound murine $CD4^+$

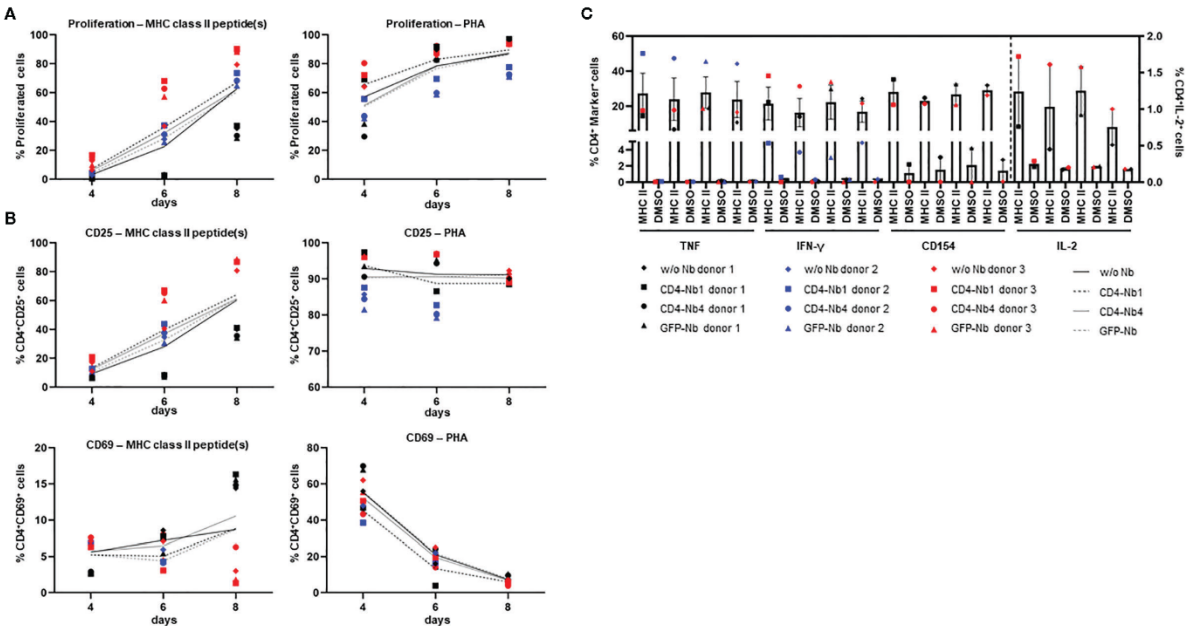

FIGURE 4 | Impact of CD4-nanobodies (Nbs) on activation, proliferation, and cytokine release of T cells. Cells were stained with carboxyfluorescein succinimidyl ester (CFSE), treated with 5 μM Nbs or without for 1 h (one replicate each), washed, stimulated with 5 μg/ml MHCII peptides, 10 μg/ml PHA or not stimulated, and cultured for 12 days. **(A)** Cells were analyzed by flow cytometry for proliferation (CFSE-low/negative fraction) and activation (CD25 and CD69) on days 4, 6, and 8. Proliferation of $CD4^+$ cells after stimulation with MHCII peptide(s) (left) or PHA (right). **(B)** Activation markers on $CD4^+$ cells. Top: CD25 expression after stimulation with MHCII peptide(s) (left) or PHA (right); Bottom: CD69 expression after stimulation with MHCII peptide(s) (left) or PHA (right). Mean percentages of all three donors are shown as plain or dotted lines. **(C)** Cytokine and activation marker expression of $CD4^+$ cells—TNF, IFN-γ, CD154 (left y-axis), or IL-2 (right y-axis). Cells were restimulated on day 12 with MHCII peptide(s) or dimethyl sulfoxide (DMSO) (background) for 14 h in the presence of Golgi Stop and brefeldin A and analyzed by flow cytometry. Error bars display SEM. Gating strategy is shown in **Supplementary Figure 6**; all percentages are given within $CD4^+$ T cells.

cells, suggesting exclusive binding to hCD4. Moreover, low-affine binding CD4-Nb4 bound neither mouse nor human $CD4^+$ cells at the concentration used here (0.75 µg/ml, ~49 nM) (**Supplementary Figure 9**). Consequently, we focused on CD4-Nb1 as the most promising candidate and CD4-Nb4 as a candidate with a high off-target rate, both of which we further analyzed for their *in vivo* target specificity and dynamic distribution using a murine xenograft model.

To establish hCD4-expressing tumors, NOD SCID gamma (NSG) mice were inoculated subcutaneously with $CD4^+$ T-cell leukemia HPB-ALL cells (41). After 2–3 weeks, mice bearing HPB-ALL xenografts were intravenously (i.v.) injected with 5 µg of CD4-Nb1-Cy5.5, CD4-Nb4-Cy5.5, or a control Nb (GFP-Nb-Cy5.5) and non-invasively *in vivo* investigated by optical imaging (OI) in intervals over the course of 24 h (**Figure 5A**, **Supplementary Figure 10A**). The Cy5.5 signal intensity (SI) of the control Nb peaked within 10–20 minutes and rapidly declined thereafter to approximately the half and a quarter of maximum level at 2 and 24 h, respectively (**Figure 5B**, **Supplementary Figure 10B**). While the SI of the low-affinity CD4-Nb4-Cy5.5 did not exceed the SI of the control Nb at any time (**Supplementary Figure 10B**), CD4-Nb1-Cy5.5 reached its maximum SI within the HPB-ALL xenograft of ~1.8-fold above the control Nb at 30 min and slowly declined to ~90% and ~80% of maximum after 2 and 4 h, respectively (**Figure 5B**). Based on the differences in the SI between CD4-Nb1-Cy5.5 and GFP-Nb-Cy5.5, we observed constant high target accumulation and specificity between 30 and 480 min post injection (**Figure 5B**). After 24 h, mice were euthanized, and the presence of fluorophore-labeled CD4-Nbs within the explanted tumors was analyzed by OI (**Figure 5C**, **Supplementary Figure 10C**). Compared to control, tumors from mice injected with CD4–Nb1–Cy5.5 had ~4-fold higher Cy5.5 SI, indicating a good signal-to-background ratio for this Nb-derived fluorescently labeled immunoprobe even at later time points. To confirm CD4-specific targeting of CD4-Nb1 within the xenograft, we additionally performed *ex vivo* immunofluorescence of HPB-ALL tumors at 2 and 24 h post injection (**Supplementary Figure S11**). At the early time point, when the *in vivo* OI signal peaked, CD4-Nb1 was widely distributed throughout the whole tumor, whereas no Cy5.5 signal was detected in the GFP-Nb-injected mice (**Supplementary Figures 11A, B**). Semiquantitative analysis at the single-cell level revealed intense CD4-Nb1 binding at the surface of HBP-ALL cells that correlated with the CD4 antibody signal and internalization of CD4-Nb1 in some cells (**Supplementary Figure 11C**). In contrast, no binding was observed upon administration of unrelated GFP-Nb (**Supplementary Figure 11D**). At 24 h post injection, we observed regions of strongly internalized CD4-Nb1 (**Supplementary Figures 11E, G**), but also regions showing a low residual CD4-Nb1 uptake (**Supplementary Figures 11E, H**).

The OI data from the xenograft model clearly indicates that the high-affinity CD4-Nb1 but not CD4-Nb4 is suitable to specifically visualize $CD4^+$ cells *in vivo* within a short period

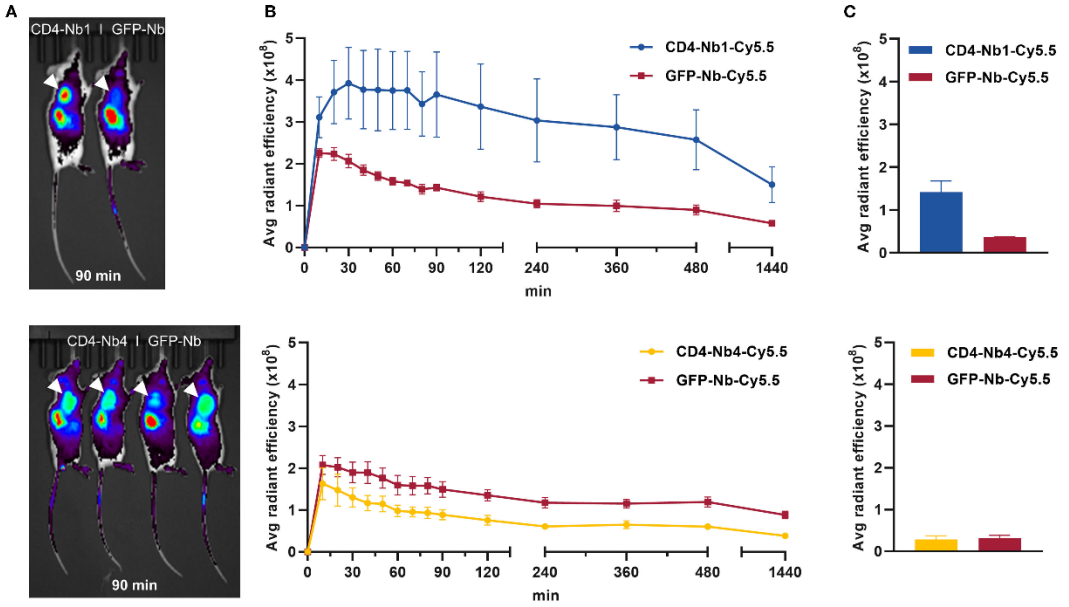

FIGURE 5 | *In vivo* optical imaging (OI) with CD4-Nbs-Cy5.5. Here, 5 µg of CD4-Nbs-Cy5.5 (top) or CD4-Nb4-Cy5.5 (bottom) or GFP-Nb-Cy5.5 (top and bottom) were administered intravenously (i.v.) to subcutaneously human $CD4^+$ HPB-ALL-bearing NSG mice, and tumor biodistribution was monitored by repetitive OI measurements over the course of 24h **(A)** Acquired images of each measurement time point of one representative mouse injected with CD4-Nbs-Cy5.5 (left) or GFP-Nb-Cy5.5 (right, ctrl). Red circles and white arrows indicate the tumor localization at the right upper flank. **(B)** Quantification of the fluorescence signal from the tumors (n = 4 per group, arithmetic mean of the average radiant efficiency ± SEM) determined at indicated time points. **(C)** After the last imaging time point, tumors were explanted for *ex vivo* OI, confirming increased accumulation of CD4-Nb1-Cy5.5 compared to the GFP-Nb-Cy5.5 (n = 2 per group, arithmetic mean ± SEM).

(30–120 min) after administration. Considering that this model does not reflect the natural distribution of $CD4^+$ T cells in an organism, we continued with a model that allowed us to visualize the physiological composition of $CD4^+$ immune cells. Thus, we employed a humanized CD4 murine knock-in model (hCD4KI) in which the extracellular fraction of the mouse CD4 antigen was replaced by the hCD4 while normal immunological function and T-cell distribution is restored (42).

^{64}Cu-CD4-Nb1 Specifically Accumulates in $CD4^+$ T Cell-Rich Organs

To generate immunoPET compatible tracers, CD4-Nb1 and GFP-Nb were labeled with the PET isotope ^{64}Cu using a copper-chelating BCN-NODAGA group added to our azide-coupled Nbs. Radiolabeling yielded high radiochemical purity (≥95%) and specific binding of ^{64}Cu-hCD4-Nb1 to CD4-expressing HBP-ALL cells (46.5% ± 5.6%) *in vitro* that was ~30 times higher than the non-specific binding to CD4-negative DHL cells or of the radiolabeled ^{64}Cu-GFP-Nb control (**Supplementary Figure 12A**).

Subsequently, we injected ^{64}Cu-CD4-Nb1 i.v. in hCD4KI and wt C57BL/6 mice and performed PET/MRI repetitively over 24 h. In two of the hCD4KI animals, we additionally followed tracer biodistribution over the first 90 min by dynamic PET (**Supplementary Figure 12B**). As expected for small-sized immunotracers, after an initial uptake peak within the first 10 min, ^{64}Cu-CD4-Nb1 is rapidly cleared from the blood, lung, and liver *via* renal elimination. In comparison to wild type, mice carrying the hCD4 antigen on T cells showed an increased tracer accumulation in lymph nodes, thymus, liver, and spleen (**Figure 6A**). In these organs, which are known to harbor high numbers of $CD4^+$ T cells (43), discrimination of $CD4^+$-specific signal from organ background was optimal 3 h post injection (**Figure 6B**). Here, lymph nodes yielded a ~3-fold, spleen a ~2.5-fold, and liver a ~1.4-fold higher ^{64}Cu-CD4-Nb1 accumulation in hCD4KI mice compared to wt littermates (**Figure 6B**). In contrast, we observed similar uptake levels for blood, muscle, lung, and kidney in both groups (**Supplementary Figure 12C**). Analyzing *ex vivo* biodistribution 24 h post tracer injection confirmed persistent accumulation of ^{64}Cu-CD4-Nb1 in lymph nodes and spleen of hCD4-expressing mice, although the limited number of animals per group did not allow statistical analysis (**Supplementary Figure 12D**). In summary, these results demonstrate that CD4-Nb1 is capable of visualizing and monitoring $CD4^+$ T cells in both optical and PET-based imaging.

DISCUSSION

Given the important role of CD4 as a marker for a variety of immune cells including monocytes, macrophages, dendritic cells, and $CD4^+$ T cells, detailed monitoring of this marker is proving to be extremely important for the diagnosis and concomitant therapeutic monitoring of a variety of diseases. Several mouse studies and early clinical trials have already indicated the value of noninvasive imaging of $CD4^+$ cells in rheumatoid arthritis (20), colitis (21), allogeneic stem cell transplantation (44), organ transplant rejection (45), acquired immunodeficiency disease (10), and in the context of cancer immunotherapies (46), using radiolabeled full-length antibodies or fragments thereof. However, biological activity, particularly $CD4^+$ T-cell depletion, and long-term systemic retention of full-length antibodies limit their development into clinically applied immunoprobes (20, 24, 47, 48).

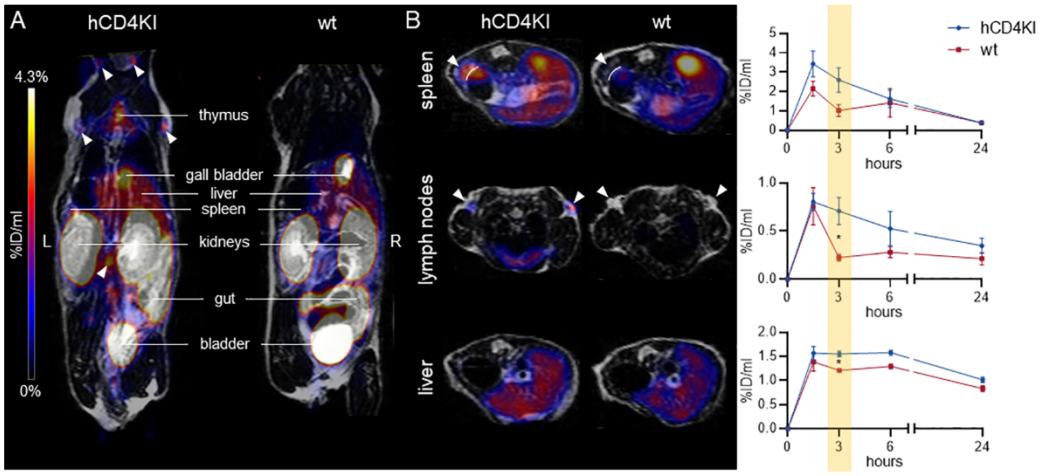

FIGURE 6 | ^{64}Cu-CD4-Nb1 specifically accumulates in $CD4^+$ T cell-rich organs. **(A)** Representative maximum intensity projection PET/MR images of human CD4 knock-in (hCD4KI) and wild-type (wt) C57BL/6 mice 3 h post intravenous (i.v.) injection of ^{64}Cu-CD4-Nb1. White arrows indicate localization of lymph nodes. **(B)** Exemplary transversal PET/MR images of spleen, lymph nodes, and liver (3 h post injection) and dynamic organ uptake quantification of ^{64}Cu-CD4-Nb1 over 24 h [n = 3 per group, arithmetic mean of the % injected dose per ml (%ID/ml) ± SEM, unpaired t-test of the 3-h time point, * $p < 0.05$]. White arrows indicate the target organ.

The aim of this study was to develop hCD4-specific Nbs as novel *in vivo* imaging probes to overcome the limitations of previous noninvasive imaging approaches. To identify binders that recognize the cellular exposed CD4, we employed two screening strategies where we selected Nbs either against adsorbed recombinant CD4 or against hCD4-expressing cells. Interestingly, both panning strategies proved successful, as demonstrated by the selection of two Nbs each that efficiently bind cell-resident CD4. Combining different biochemical analyses including epitope binning, cellular imaging, and HDX-MS, we were able to elucidate in detail the detected domains, as well as the three-dimensional epitopes addressed by the individual Nbs, and thus identified two candidates, CD4-Nb1 and CD4-Nb3, that can simultaneously bind to different segments within domain 1, while CD4-Nb2 has been shown to bind to domain 3 of CD4.

Notably, for most Nbs currently being developed for *in vivo* imaging purposes, detailed information about their epitopes is not available (49–55). There are only few examples such as the anti-HER2-specific Nb 2Rs15d, where the precise epitope was elucidated by complex crystallization (56) and that was successfully applied in a phase I study for clinical imaging (39). However, for CD4-specific Nbs, this knowledge is all the more important because epitope-specific targeting of $CD4^+$ T-cell functions has far-reaching implications. This is true especially for cancer treatment, as $CD4^+$ T cells have opposing effects on tumor growth and response to immunotherapies, crucially depending on the CD4 effector cell differentiation and tumor entity (57, 58). In this context, it was shown that domain 1 of CD4 mediates transient interaction of the CD4 receptor and the MHCII complex (59–61), while T-cell activation is abrogated when T-cell receptor (TCR) and CD4 colocalization is blocked *via* domain 3 (62). To further elucidate a possible impact on immunomodulation, we analyzed the effect of CD4-Nb1 and CD4-Nb4 targeting two different domains on $CD4^+$ Tcell proliferation and cytokine expression. Notably, neither CD4-Nb1 nor CD4-Nb4 affected the behavior of endogenous $CD4^+$ T-cells *in vitro* or induced increased cytokine levels in whole blood samples when employed at concentrations that are intended for molecular imaging purposes in patients. From these data, it can be concluded that these Nbs are mostly biologically inert and thus might be beneficial compared to full-length antibodies (24) or other antibody fragments such as the anti-CD4 Cys-diabody, which was recently reported to inhibit the proliferation of $CD4^+$ cells and IFN-γ production *in vitro* (26).

Following our initial intention to generate immune tracer for *in vivo* imaging, we performed a site-directed labeling approach employing C-terminal sortagging to conjugate an azide group, which can be universally used to attach a multitude of detectable moieties by straightforward DBCO-mediated click chemistry (49). For the fluorescent and radiolabeled CD4-Nb1, we observed rapid recruitment and sustained targeting of $CD4^+$ cells in a xenograft and hCD4 knock-in mouse model. Using a quantitative high-resolution PET/MR imaging approach, our radiolabeled ^{64}Cu-CD4-Nb1 allowed visualizing T cell-rich organs with high sensitivity. Beyond immune organs including lymph nodes, thymus, and spleen, we could detect enhanced CD4-Nb1 uptake in liver. At this point, we cannot distinguish whether this is due to the presence of $CD4^+$ cells or non-specific elimination occurring through this organ. Consequently, further experiments are needed to analyze whether CD4-Nbs lacking the Fc region are advantageous compared to larger antibody formats, which have a higher tendency to accumulate non-specifically in the spleen and liver due to Fcγ receptor-mediated uptake. However, to further modify serum retention times in order to improve specific tissue targeting, CD4-Nbs could easily be modified, as shown by the addition of an albumin-binding fragment (63) or PEGylation (49).

Considering the translation of the CD4-Nb1 for clinical imaging, additional aspects such as potential immunogenicity have to be assessed. Due to their high homology to the human type 3 VH domain, Nbs were described as weakly immunogenic in humans (64), and several strategies are available to humanize Nbs by exchanging a small number of aa residues in the framework regions (65). Moreover, a recent study of two Nbs in phase II clinical trials for PET imaging reported that very few patients developed low levels of anti-drug antibodies after prolonged administration of Nbs (66), indicating that monomeric Nbs present a low immunogenicity risk profile. In addition, long-term kidney retention of radiolabeled Nbs, mediated primarily by the endocytic receptor megalin (67), can cause undesirable nephrotoxicity and interfere with imaging of molecular targets near the kidneys. However, this can be overcome by targeted engineering of Nbs, e.g., removal of charged aa tags or simultaneous administration of positively charged components that interact with megalin receptors (68, 69). Of note, compared to other radiolabeled Nbs used for preclinical imaging of similar targets (49), CD4-Nb1 showed relatively low renal accumulation. However, as the molecular reasons for this are unclear at this stage, further studies are needed to gain deeper insight into this phenomenon.

In summary, this study demonstrates for the first time the generation and detailed characterization of Nbs specific for hCD4 and their comprehensive experimental evaluation *in vitro* and *in vivo*. In particular, CD4-Nb1 turned out as a promising candidate for a noninvasive whole-body study of $CD4^+$ cells in mice. Considering the increasing importance of advanced molecular imaging in clinical practice, we anticipate that this Nb-based immunotracer could become a highly versatile tool as a novel theranostic to accompany the clinical translation of emerging immunotherapies.

MATERIALS AND METHODS

Nanobody Library Generation

Alpaca immunization and Nb library construction were carried out as described previously (70, 71). Animal immunization has been approved by the government of Upper Bavaria (Permit number: 55.2-1-54-2532.0-80-14). In brief, an alpaca (*Vicugna pacos*) was immunized with the purified extracellular domains of

hCD4 (aa26-390) recombinantly produced in HEK293 cells (antibodies-online GmbH, Germany). After initial priming with 1 mg, the animal received six boost injections with 0.5 mg hCD4 each, every second week. Then, 87 days after initial immunization, ~100 ml of blood were collected and lymphocytes were isolated by Ficoll gradient centrifugation using Lymphocyte Separation Medium (PAA Laboratories GmbH). Total RNA was extracted using TRIzol (Life Technologies), and mRNA was transcribed into cDNA using the First-Strand cDNA Synthesis Kit (GE Healthcare). The Nb repertoire was isolated in three subsequent PCR reactions using the following primer combinations: 1) CALL001 and CALL002; 2) forward primer set FR1-1, FR1-2, FR1-3, FR1-4, and reverse primer CALL002; and 3) forward primer FR1-ext1 and FR1-ext2 and reverse primer set FR4-1, FR4-2, FR4-3, FR4-4, FR4-5, and FR4-6 introducing SfiI and NotI restriction sites. The Nb library was subcloned into the SfiI/NotI sites of the pHEN4 phagemid vector (72).

Nanobody Screening

For the selection of CD4-specific Nbs, two consecutive phage enrichment rounds were performed, both with immobilized recombinant antigen and CHO-hCD4 cells. *E. coli* TG1 cells comprising the hCD4-Nb library in pHEN4 were infected with the M13K07 helper phage to generate Nb-presenting phages. For each round, 1×10^{11} phages of the hCD4-Nb library were applied on immunotubes coated with hCD4 (10 µg/ml). In each selection round, extensive blocking of antigen and phages was performed with 5% milk or bovine serum albumin (BSA) in phosphate-buffered saline containing 0.05% (v/v) Tween 20 PBS-T, and with increasing panning rounds, PBS-T washing stringency was increased. Bound phages were eluted in 100 mM triethylamine (TEA; pH 10.0), followed by immediate neutralization with 1 M Tris/HCl pH 7.4. For cell-based panning, 2×10^6 CHO-hCD4 or HEK293-hCD4 cells were non-enzymatically detached using dissociation buffer (Gibco) and suspended in 5% fetal bovine serum (FBS) in PBS. Antigen-expressing cells were incubated with 1×10^{11} phages under constant mixing at 4°C for 3 h. Cells were washed 3× with 5% FBS in PBS. Cell lines were alternated between panning rounds. Phages were eluted with 75 mM citric acid buffer at pH 2.3 for 5 min. To deplete non-CD4-specific phages, eluted phages were incubated 3× with 1×10^7 wt cells. Exponentially growing *E. coli* TG1 cells were infected with eluted phages from both panning strategies and spread on selection plates for the following panning rounds. Antigen-specific enrichment for each round was monitored by counting colony-forming units (CFUs).

Whole-Cell Phage ELISA

Polystyrene Costar 96-well cell culture plates (Corning) were coated with poly-L-lysine (Sigma Aldrich) and washed once with H_2O. CHO-wt and CHO-hCD4 were plated at 2×10^4 cells per well in 100 µl and grown to confluency overnight. Next day, 70 µl of phage supernatant was added to the culture medium of each cell type and incubated at 4°C for 3 h. Cells were washed 5× with 5% FBS in PBS. M13-horseradish peroxidase (HRP)-labeled antibody (Progen) was added at a concentration of 0.5 ng/ml for 1 h, washed 3× with 5% FBS in PBS. One-Step Ultra TMB 32048 ELISA Substrate [Thermo Fisher Scientific (TFS)] was added and incubated until color change was visible, and the reaction was stopped by addition of 100 µl of 1 M H_2SO_4. Detection occurred at 450 nm at a Pherastar plate reader, and phage ELISA-positive clones were defined by a 2-fold signal above wt control cells.

Expression Constructs

The cDNA of hCD4 (UniProtKB-P01730) was amplified from hCD4-mOrange plasmid DNA (hCD4-mOrange was a gift from Sergi Padilla Parra; addgene plasmid #110192; http://n2t.net/addgene:110192; RRID : Addgene_110192) by PCR using forward primer hCD4 fwd and reverse primer hCD4 rev and introduced into BamHI and XhoI sites of a pcDNA3.1 vector variant [pcDNA3.1(+)IRES GFP, a gift from Kathleen_L Collins; addgene plasmid #51406; http://n2t.net/addgene:51406; RRID : Addgene_51406]. We replaced the neomycin resistance gene (NeoR) with the cDNA for Blasticidin S deaminase (bsd), amplified with forward primer bsd fwd and reverse primer bsd rev, by integration into the XmaI and BssHII sites of the vector. CD4 domain deletion mutants were generated using the Q5 Site-Directed Mutagenesis Kit (NEB) according to the manufacturer's protocol. For mutants lacking domain 1 of hCD4, we introduced an N-terminal BC2-tag (35). For the generation of plasmid pcDNA3.1_CD4_ΔD1_IRES-eGFP, we used forward primer ΔD1 fwd and reverse primer ΔD1 rev; for pcDNA3.1_CD4_ΔD1ΔD2_IRES-eGFP, forward primer ΔD1ΔD2 fwd and reverse primer ΔD1ΔD2 rev; for pcDNA3.1_CD4_ΔD3ΔD4_IRES-EGFP, forward primer ΔD3ΔD4 fwd and reverse primer ΔD3ΔD4 rev. For bacterial expression of Nbs, sequences were cloned into the pHEN6 vector (73), thereby adding a C-terminal sortase tag LPETG followed by 6× His-tag for IMAC purification as described previously (34). For protein production of the extracellular domains 1-4 of hCD4 in Expi293 cells, corresponding cDNA was amplified from plasmid DNA containing full-length hCD4 cDNA (addgene plasmid #110192) using forward primer CD4-D1-4 f and reverse primer CD4-D1-4 r. A 6× His tag was introduced by the reverse primer. Esp3I and EcoRI restriction sites were used to introduce the cDNA into a pcDNA3.4 expression vector with the signal peptide MGWTLVFLFLLSVTAGVHS from the antibody JF5 (74).

Cell Culture, Transfection, Stable Cell Line Generation

HEK293T and CHO-K1 cells were obtained from ATCC (CCL-61, LGC Standards GmbH, Germany). As this study does not include cell line-specific analysis, cells were used without additional authentication. Cells were cultivated according to standard protocols. Briefly, growth media containing Dulbecco's modified Eagle's medium (DMEM) (HEK293) or DMEM/F12 (CHO) [both high glucose, pyruvate (TFS)] supplemented with 10% (v/v) FBS, L-glutamine, and penicillin/streptomycin (P/S; all from TFS) were used for cultivation. Cells were passaged using 0.05% trypsin-EDTA (TFS) and were cultivated at 37°C and 5% CO_2 atmosphere in a humidified chamber. Plasmid DNA was transfected using Lipofectamine

2000 (TFS) according to the manufacturer's protocol. For the generation of the stable HEK293-hCD4 and CHO-hCD4 cell line, 24 h post transfection, cells were subjected to a 2-week selection period using 5 µg/ml Blasticidin S (Sigma Aldrich) followed by single cell separation. Individual clones were analyzed by live-cell fluorescence microscopy regarding their level and uniformity of GFP and CD4 expression.

Protein Expression and Purification

CD4-specific Nbs were expressed and purified as previously published (71, 75). Extracellular fragment of hCD4 comprising domains 1–4 of hCD4 and a C-terminal His6-tag was expressed in Expi293 cells according to the manufacturer's protocol (TFS). Cell supernatant was harvested by centrifugation 4 days after transfection, sterile filtered and purified according to previously described protocols (76). For quality control, all purified proteins were analyzed *via* sodium dodecyl sulfate-polyacrylamide gel electrophoresis (SDS-PAGE) according to standard procedures. Therefore, protein samples were denaturized (5 min, 95°C) in 2× SDS sample buffer containing 60 mM Tris/HCl, pH 6.8; 2% (w/v) SDS; 5% (v/v) 2-mercaptoethanol, 10% (v/v) glycerol, 0.02% bromphenole blue. All proteins were visualized by InstantBlue Coomassie (Expedeon) staining. For immunoblotting, proteins were transferred to a nitrocellulose membrane (Bio-Rad Laboratories) and detection was performed using anti-His primary antibody (Penta-His Antibody, #34660, Qiagen) followed by donkey anti-mouse secondary antibody labeled with Alexa Fluor 647 (Invitrogen) using a Typhoon Trio scanner (GE Healthcare, excitation 633 nm, emission filter settings 670 nm BP 30).

Live-Cell Immunofluorescence

CHO-hCD4 and CHO wt cells transiently expressing CD4 domain-deletion mutants were plated at ~10,000 cells per well of a µClear 96-well plate (Greiner Bio One, cat. #655090) and cultivated at standard conditions. Next day, medium was replaced by live-cell visualization medium DMEMgfp-2 (Evrogen, cat. #MC102) supplemented with 10% FBS, 2 mM L-glutamine, 2 µg/ml Hoechst 33258 (Sigma Aldrich) for nuclear staining and fluorescently labeled or unlabeled CD4-Nbs at concentrations between 1 and 100 nM. Unlabeled CD4-Nbs were visualized by addition of 2.5 µg/ml anti-VHH secondary Cy5 AffiniPure Goat Anti-Alpaca IgG (Jackson ImmunoResearch). Images were acquired with a MetaXpress Micro XL system (Molecular Devices) at ×20 or ×40 magnification.

Biolayer Interferometry

To determine the binding affinity of purified Nbs to recombinant hCD4, biolayer interferometry (BLItz, ForteBio) was performed. First, CD4 was biotinylated by 3-fold molar excess of biotin-N-hydroxysuccinimide ester. CD4 was then immobilized at single-use streptavidin biosensors (SA) according to manufacturer's protocols. For each Nb, we executed four association/dissociation runs with concentrations appropriate for the affinities of the respective Nbs (overall between 15.6 nM and 1 µM). As a reference run, PBS was used instead of Nb in the association step. As a negative control, the GFP-Nb (500 nM) was applied in the binding studies. Recorded sensograms were analyzed using the BLItzPro software, and dissociation constants (K_D) were calculated based on global fits. For the epitope competition analysis, two consecutive application steps were performed, with a short dissociation period of 30 s after the first association.

Peripheral Blood Mononuclear Cell Isolation, Freezing, and Thawing

Fresh blood, buffy coats, or mononuclear blood cell concentrates were obtained from healthy volunteers at the Department of Immunology or from the ZKT Tübingen gGmbH. Participants gave informed consent, and the studies were approved by the ethical review committee of the University of Tübingen, projects 156/2012B01 and 713/2018BO2. Blood products were diluted with PBS 1× (homemade from 10× stock solution, Lonza, Switzerland), and PBMCs were isolated by density gradient centrifugation with Biocoll separation solution (Biochrom, Germany). PBMCs were washed twice with PBS 1×, counted with an NC-250 cell counter (Chemometec, Denmark), and resuspended in heat-inactivated (h.i.) FBS (Capricorn Scientific, Germany) containing 10% dimethyl sulfoxide (DMSO; Merck). Cells were immediately transferred into a -80°C freezer in a freezing container (Mr. Frosty; TFS). After at least 24 h, frozen cells were transferred into a liquid nitrogen tank and were kept frozen until use. For the experiments, cells were thawed in Iscove´s Modified Dulbecco´s Medium (IMDM) (+L-Glutamin + 25 mM HEPES; Life Technologies) supplemented with 2.5% h.i. human serum (HS; PanBiotech, Germany), 1× P/S (Sigma-Aldrich), and 50 µm β-mercaptoethanol (β-ME; Merck), washed once, counted, and used for downstream assays.

Affinity Determination by Flow Cytometry

For cell-based affinity determination, HEK293-hCD4 cells were detached using enzyme-free cell dissociation buffer (Gibco) and resuspended in FACS buffer (PBS containing 5% FBS). For each staining condition, 200,000 cells were incubated with suitable dilution series of CD4-Nbs at 4°C for 30 min. Cells were washed two times, and for detection of Cy5 AffiniPure Goat Anti-Alpaca IgG, VHH domain (Jackson ImmunoResearch) was applied for 15 min. PBMCs (Department of Immunology/ZKT Tübingen gGmbH, Germany) were freshly thawed and resuspended in FACS buffer. For each sample, 200,000 cells were incubated with suitable concentrations of CD4-Nbs coupled to CF568 in combination with 1:500 dilution of anti-CD3-FITC (BD Biosciences) at 4°C for 30 min. For control staining, PE/Cy5-labeled anti-hCD4 antibody (RPA-T4, BioLegend) was used. After two washing steps, samples were resuspended in 200 µl FACS buffer and analyzed with a BD FACSMelody Cell Sorter. Final data analysis was performed *via* FlowJo10® software (BD Biosciences).

Sortase Labeling of Nanobodies

Sortase A pentamutant (eSrtA) in pET29 was a gift from David Liu (Addgene plasmid # 75144) and was expressed and purified as described (77). CF568-coupled peptide H-Gly-Gly-Gly-Doa-

Lys-NH_2 (sortase substrate) was custom-synthesized by Intavis AG. For the click chemistry, a peptide H-Gly-Gly-Gly-propyl-azide was synthesized. In brief, for sortase coupling 50 µM Nb, 250 µM sortase peptide dissolved in sortase buffer (50 mM Tris, pH 7.5, and 150 mM NaCl) and 10 µM sortase were mixed in coupling buffer (sortase buffer with 10 mM $CaCl_2$) and incubated for 4 h at 4°C. Uncoupled Nb and sortase were depleted by IMAC. Unbound excess of unreacted sortase peptide was removed using Zeba Spin Desalting Columns (TFS, cat. #89890). Azide-coupled Nbs were labeled by strain-promoted azide-alkyne cycloaddition (SPAAC) click chemistry reaction with 2-fold molar excess of DBCO-Cy5.5 (Jena Bioscience) for 2 h at 25°C. Excess DBCO-Cy5.5 was subsequently removed by dialysis (GeBAflex-tube, 6-8 kDa, Scienova). Finally, to remove untagged Nb (side product of the sortase reaction), we used hydrophobic interaction chromatography (HIC; HiTrap Butyl-S FF, Cytiva). Binding of DBCO-Cy5.5-coupled Nb occurred in 50 mM H_2NaPO_4, 1.5 M $(NH4)_2SO_4$, pH7.2. Elution took place with 50 mM H_2NaPO_4, pH 7.2. Dye-labeled protein fractions were analyzed by SDS-PAGE followed by fluorescent scanning on a Typhoon Trio (GE-Healthcare; CF568: excitation 532 nm, emission filter settings 580 nm BP 30; Cy5.5: excitation 633 nm, emission filter settings 670 nm BP 30; 546) and subsequent Coomassie staining. Identity and purity of final products were determined by liquid chromatography-mass spectrometry (LC-MS) (CD4-Nbs-CF568, >60%; CD4-Nb1-Cy5.5, ~94%; CD4-Nb4-Cy5.5, ~99%; GBP-Cy5.5, ~94%; CD4-Nb1-3, ~99%; bivGFP-Nb, ~99%).

Hydrogen–Deuterium Exchange

CD4 Deuteration Kinetics and Epitope Elucidation

On the basis of the affinity constants of 5.1 nM (CD4-Nb1), 6.5 nM (CD4-Nb2), and 75.3 nM (CD4-Nb3) (predetermined by BLI analysis), the molar ratio of antigen to Nb was calculated, ensuring 90% complex formation according to Kochert et al. (78). CD4 (5 µl, 65.5 µM) was preincubated with CD4-specific Nbs (5 µl; 60.3, 67.4, and 143.1 µM for Nb1, Nb2, and Nb3, respectively) for 10 min at 25°C. Deuteration samples containing CD4 only were preincubated with PBS instead of the Nbs. HDX of the preincubated samples was initiated by 1:10 dilution with PBS (pH 7.4) prepared with D_2O, leading to a final concentration of 90% D_2O. After 5- and 50-min incubation at 25°C, aliquots of 20 µl were taken and quenched by adding 20 µl ice-cold quenching solution (0.2 M TCEP with 1.5% formic acid and 4 M guanidine HCl in 100 mM ammonium formate solution pH 2.2), resulting in a final pH of 2.5. Quenched samples were immediately snap-frozen.

Immobilized pepsin (TFS) was prepared using 60 µl of 50% slurry (in ammonium formate solution pH 2.5) that was then centrifuged (1,000 × g for 3 min at 0°C). The supernatant was discarded. Prior to each analysis, samples were thawed and added to the pepsin beads. After digestion for 2 min in a water ice bath, samples were separated from the beads by centrifugation at 1,000 × g for 30 s at 0°C using a 0.22-µm filter (Merck, Millipore) and immediately analyzed by LC-MS. Undeuterated control samples for each complex and CD4 alone were prepared under the same conditions using H_2O instead of D_2O. Additionally, each Nb was digested without addition of CD4 to generate a list of peptic peptides deriving from the Nb. The HDX experiments of the CD4-Nb complexes were performed in triplicate. The back-exchange of the method as determined using a standard peptide mixture of 14 synthetic peptides was 24%.

Chromatography and Mass Spectrometry

HDX samples were analyzed as described previously (75).

HDX Data Analysis

A peptic peptide list was generated in a preliminary LC-MS/MS experiment as described previously (75). For data-based search, no enzyme selectivity was applied; furthermore, identified peptides were manually evaluated to exclude peptides originated through cleavage after arginine, histidine, lysine, proline, and the residue after proline (79). Additionally, a separate list of peptides for each Nb was generated, and peptides overlapping in mass, retention time, and charge with the antigen digest were manually removed. Analysis of the deuterated samples was performed in MS mode only, and HDExaminer v2.5.0 (Sierra Analytics, USA) was used to calculate the deuterium uptake (centroid mass shift). HDX could be determined for peptides covering 87%–88% of the CD4 sequence (**Supplementary Figure 11**). The calculated percentages of deuterium uptake of each peptide between CD4-Nb and CD4-only were compared. Any peptide with uptake reduction of 5% or greater upon Nb binding was considered protected. All relevant HDX parameters are shown in **Supplementary Table S3** as recommended (80).

Endotoxin Determination and Removal

The concentration of bacterial endotoxins was determined with Pierce LAL Chromogenic Endotoxin Quantitation Kit (TFS), and removal occurred using EndoTrap HD 1 ml (Lionex) according to the manufacturer's protocols.

Synthetic Peptides

The following human leukocyte antigen (HLA)-class II peptides were used for the stimulations: MHCII pool (HCMVA pp65 aa 109-123 MSIYVYALPLKMLNI, HCMV pp65 aa 366-382 HPTFTSQYRIQGKLEYR, EBVB9 EBNA2 aa 276-290 PRSPTVFYNIPPMPL, EBVB9 EBNA1 aa 514-527 KTSLYNLRRGTALA, EBV BXLF2 aa 126-140 LEKQLFYYIGTMLPNTRPHS, EBV BRLF1 aa 119-133 DRFFIQAPSNRVMIP, EBVB9 EBNA3 aa 381-395 PIFIRRLHRLLLMRA, EBVB9 GP350 aa 167-181 STNITAVVRAQGLDV, IABAN HEMA aa 306-318 PKYVKQNTLKLAT) or CMVpp65 aa 510-524 YQEFFWDANDIYRIF. All peptides were synthesized and dissolved in water 10% DMSO as previously described (purity ≥80%) and were kindly provided by S. Stevanović (81).

Stimulation and Cultivation of Peripheral Blood Mononuclear Cells

PBMCs from donors previously screened for *ex vivo* $CD4^+$ T-cell reactivities against MHCII peptides were thawed and rested in T-cell medium (TCM; IMDM + 1× P/S + 50 µM β-ME + 10% h.i.

HS) containing 1 µg/ml DNase I (Sigma-Aldrich) at a concentration of 2–3 × 10^6 cells/ml for 3 h at 37°C and 7.5% CO_2. After resting, cells were washed once and counted, and up to 1 × 10^8 cells were labeled with 1.5–2 µM carboxyfluorescein succinimidyl ester (CFSE; BioLegend, USA) in 1 ml PBS 1× for 20 min according to the manufacturer's protocol. The cells were washed twice in medium containing 10% FBS after CFSE labeling and incubated with 5, 0.5, or 0.05 µM of CD4-Nb1, CD4-Nb4, or a control Nb for 1 h at 37°C in serum-free IMDM medium. Concentrations and duration were chosen to mimic the expected approximate concentration and serum retention time during clinical application. After incubation, cells were washed twice and counted, and each condition was separated into three parts and seeded in a 48-well cell culture plate (1.6–2.5 × 10^6 cells/well in triplicate). Cells were stimulated with either 10 µg/ml PHA-L (Sigma-Aldrich) or 5 µg/ml MHCII peptide(s) or left unstimulated and cultured at 37°C and 7.5% CO_2. Then, 2 ng/ml recombinant human IL-2 (R&D, USA) were added on days 3, 5, and 7. One-third of the culture on day 4, one half of the culture on days 6 and 8, and the remaining cells on day 12 were harvested, counted, and stained for flow cytometry analyses. For donor 1, the proliferation/activation status and cytokine production were analyzed in two different experiments, whereas for donors 2 and 3, cells from a single experiment were used for the three assays.

Assessment of T-Cell Proliferation and Activation

Cells from days 4, 6, and 8 were transferred into a 96-well round-bottom plate and washed twice with FACS buffer [PBS + 0.02% sodium azide (Roth, Germany) + 2 mM EDTA (Sigma-Aldrich) + 2% h.i. FBS]. Extracellular staining was performed with CD4 APC-Cy7 (RPA-T4; BD Biosciences), CD8 BV605 (RPA-T8; BioLegend), the dead cell marker Zombie Aqua (BioLegend), CD25 PE-Cy7 (BC96; BioLegend), CD69 PE (FN50; BD Biosciences) and incubated for 20 min at 4°C. All antibodies were used at pretested optimal concentrations. Cells were washed twice with FACS buffer. Approximately 500,000 cells were acquired on the same day using an LSRFortessaTM SORP (BD Biosciences, USA) equipped with the DIVA Software (Version 6, BD Biosciences, USA). The percentage of proliferating $CD4^+$ cells was determined by assessment of CFSE-negative cells and activation by the percentage of $CD69^+$ or $CD25^+$.

Assessment of T-Cell Function by Intracellular Cytokine Staining

On day 12, the MHCII peptide(s)-stimulated and cultured cells were transferred into a 96-well round-bottom plate (0.5–1 × 10^6 cells/well) and restimulated using 10 µg/ml of the same peptide (s), 10 µg/ml staphylococcal enterotoxin B (SEB; Sigma-Aldrich; positive control), or 10% DMSO (negative control). Protein transport inhibitors brefeldin A (10 µg/ml; Sigma-Aldrich) and Golgi Stop (BD Biosciences) were added at the same time as the stimuli. After 14-h stimulation at 37°C and 7.5% CO_2, cells were stained extracellularly with the fluorescently labeled antibodies CD4 APC-Cy7, CD8 BV605, and Zombie Aqua and incubated for 20 min at 4°C. Afterward, cells were washed once, fixed, and permeabilized using the BD Cytofix/Cytoperm solution (BD Biosciences) according to the manufacturer's instructions; stained intracellularly with TNF Pacific Blue (Mab11), IL-2 PE-Cy7 (MQ1-17H12), IFN-γ Alexa Fluor 700 (4S.B7), and CD154 APC (2431) antibodies (all BioLegend) (82); and washed twice. Approximately 500,000 cells were acquired on the same day using an LSRFortessaTM SORP (BD Biosciences, USA) equipped with the DIVA Software (Version 6; BD Biosciences). All flow cytometry analyses were performed with FlowJo version 10.6.2; gating strategies are shown in **Supplementary Figure 6**. Statistical analyses were performed with GraphPad Prism version 9.0.0.

Full Blood Stimulation and Cytokine Release Assay

Here, 100 µl of lithium-heparin blood was incubated for 1 h at 37°C and 7.5% CO_2. The blood was stimulated with 5 µM Nb (CD4-Nb1, CD4-Nb4, or control Nb), 100 ng/ml LPS (Invivogen, USA), or 2 µg/ml PHA-L in a final volume of 250 µl (serum-free IMDM medium) or left unstimulated for 24 h at 37°C and 7.5% CO_2. After two centrifugations, supernatant was collected without transferring erythrocytes. The supernatants were frozen at -80°C until cytokine measurements. Levels of IL-1β, IL-1Ra, IL-4, IL-6, IL-8, IL-10, IL-12p70, IL-13, granulocyte-macrophage colony-stimulating factor (GM-CSF), IFN-γ, macrophage chemotactic protein (MCP)-1, macrophage inflammatory protein (MIP)-1β, TNFα, and vascular endothelial growth factor (VEGF) were determined using a set of in-house-developed Luminex-based sandwich immunoassays each consisting of commercially available capture and detection antibodies and calibrator proteins. All assays were thoroughly validated ahead of the study with respect to accuracy, precision, parallelism, robustness, specificity, and sensitivity (83, 84). Samples were diluted at least 1:4 or higher. After incubation of the prediluted samples or calibrator protein with the capture coated microspheres, beads were washed and incubated with biotinylated detection antibodies. Streptavidin-phycoerythrin was added after an additional washing step for visualization. For control purposes, calibrators and quality control samples were included on each microtiter plate. All measurements were performed on a Luminex FlexMap® 3D analyzer system using Luminex xPONENT® 4.2 software (Luminex, USA). For data analysis, MasterPlex QT, version 5.0, was employed. Standard curve and quality control samples were evaluated according to internal criteria adapted to the Westgard Rules (85) to ensure proper assay performance.

Analysis of Cross-Species Reactivity Binding to Mouse $CD4^+$ Cells by Flow Cytometry

Murine $CD4^+$ cells were isolated from spleen and lymph nodes of C57BL/6N mice by positive selection over CD4 magnetic microbeads (Miltenyi Biotech, Germany). Human $CD4^+$ cells were extracted from blood using StraightFrom® Whole Blood CD4 MicroBeads (Miltenyi Biotech). Single-cell suspensions were incubated with 0.75 µg/ml of CD4-Nbs-Cy5.5 (~47–60

nM) or GFP-Nb-Cy5.5 (~51 nM) in 1% FPS/PBS at 4°C for 20 min and subsequently analyzed on an LSR-II cytometer (BD Biosciences).

Optical Imaging of CD4-Expressing HPB-ALL Tumors

Human T-cell leukemia HPB-ALL cells (German Collection of Microorganisms and Cell Cultures GmbH, DSMZ, Braunschweig, Germany) were cultured in RPMI-1640 supplemented with 10% FBS and 1% P/S. Here, 10^7 HPB-ALL cells were injected subcutaneously in the right upper flank of 7-week-old NSG (NOD.Cg-*Prkdc*^{scid} *Il2rg*^{tm1Wjl}/SzJ; Charles River Laboratories, Sulzfeld, Germany) mice, and tumor growth was monitored for 2–3 weeks. When tumors reached a diameter of ~7 mm, 5 µg of CD4-Nbs-Cy5.5 or control Nb (GFP-Nb-Cy5.5) were administered into the tail vein of two mice each. Optical imaging (OI) was performed repetitively in short-term isoflurane anesthesia over a period of 24 h using the IVIS Spectrum *In Vivo* Imaging System (PerkinElmer, Waltham, MA, USA). Four days after the first Nb administration, the CD4-Nbs-Cy5.5 groups received the GFP-Nb-Cy5.5 (and *vice versa*), and tumor biodistribution was analyzed identically by OI over 24 h. After the last imaging time point, animals were sacrificed and tumors were explanted for *ex vivo* OI analysis. Data were analyzed with Living Image 4.4 software (PerkinElmer). The fluorescence intensities were quantified by drawing regions of interest around the tumor borders and were expressed as average radiant efficiency (photons/s)/(µW/cm^2) subtracted by the background fluorescence signal before Nb injection to eliminate potential residual signal from the previous Nb application. All mouse experiments were performed according to the German Animal Protection Law and were approved by the local authorities (Regierungspräsidium Tübingen).

Immunofluorescence Staining of Explanted Xenograft Tumors

Freshly frozen 5-µm sections of hCD4-Nb1-Cy5.5-containing mouse tumors were analyzed using an LSM 800 laser scanning microscope (Zeiss). Afterward, the sections were fixed with perjodate-lysine-paraformaldehyde, blocked using donkey serum, and stained with primary rabbit-anti-CD4 antibody (Cell Marque, USA). Bound antibody was visualized using donkey-anti-rabbit-Cy3 secondary antibody (Dianova, Germany). YO-PRO-1 (Invitrogen, USA) was used for nuclear staining. Acquired images of the same areas were manually overlaid.

Radiolabeling With NODAGA and ^{64}Cu

All procedures for conjugation and radiolabeling with ^{64}Cu were performed using metal-free equipment and Chelex 100 (Sigma-Aldrich) pretreated buffers. Azide-modified Nbs (100 µg) were treated with 4 µl of 5 mM EDTA in 250 mM sodium acetate buffer (pH 6) for 30 min at room temperature (RT). The protein was reacted with 15 molar equivalents of BCN-NODAGA (CheMatech, Dijon, France) in 250 mM sodium acetate pH 6 for 30 min at RT followed by incubation at 4°C for 18 h. Excess of chelator was removed by ultrafiltration (Amicon Ultra 0.5 ml, 3 kDa MWCO, Merck Millipore) using the same buffer. [^{64}Cu]$CuCl_2$ (150 MBq in 0.1 M HCl) was neutralized by addition of 1.5 volumes of 0.5 M ammonium acetate solution (pH 6), resulting in a pH of 5.5. To this solution, 50 µg of conjugate was added and incubated at 42°C for 60 min. Then, 1 µl of 20% diethylenetriaminepentaacetic acid (DTPA) solution was added to quench the labeling reaction. Complete incorporation of the radioisotope was confirmed after each radiosynthesis by thin-layer chromatography (iTLC-SA; Agilent Technologies; mobile phase 0.1 M citric acid pH 5) and high-performance size exclusion chromatography (HPSEC; BioSep SEC-s2000, 300 × 7.8 mm, Phenomenex; mobile phase DPBS with 0.5 mM EDTA). All radiolabeled preparations used for *in vivo* PET imaging had radiochemical purities of ≥97% (iTLC) and ≥94% (HPSEC).

In Vitro Radioimmunoassay

Here, 10^7 HPB-ALL or DHL cells were incubated in triplicate with 1 ng (3 MBq/µg) of radiolabeled ^{64}Cu-CD4-Nb1 or ^{64}Cu-GFP-Nb for 1 h at 37°C and washed twice with PBS/2% FCS. The remaining cell-bound radioactivity was measured using a Wizard^2 2480 gamma counter (PerkinElmer Inc., Waltham, MA, USA) and quantified as percentage of total added activity.

PET/MRI

Human CD4 knock-in (hCD4KI, genOway, Lyon, France) and wt C57BL/6J mice (Charles River) were injected intravenously with 5 µg (~15 MBq) of ^{64}Cu-CD4-Nb1. During the scans, mice were anesthetized with 1.5% isoflurane in 100% oxygen and warmed by water-filled heating mats. Ten-minute static PET scans were performed after 1.5, 3, 6, and 24 h in a dedicated small-animal Inveon microPET scanner (Siemens Healthineers, Knoxville, TN, USA; acquisition time: 600 s). For anatomical information, sequential T2 TurboRARE MR images were acquired immediately after the PET scans on a small animal 7 T ClinScan magnetic resonance scanner (Bruker BioSpin GmbH, Rheinstetten, Germany). Dynamic PET data of the first 90 min post injection were gained in two mice and divided into 10-min frames. After attenuation correction by a cobalt-57 point source, PET images were reconstructed using an ordered subset expectation maximization (OSEM3D) algorithm and analyzed with Inveon Research Workplace (Siemens Preclinical Solutions). The volumes of interest of each organ were drawn based on the anatomical MRI to acquire corresponding PET tracer uptake. The resulting values were decay-corrected and presented as percentage of injected dose per volume (%ID/ml). *Ex vivo* γ-counting was conducted after the last imaging time point by measuring the weight and radioactivity of each organ. For quantification, standardized aliquots of the injected radiotracer were added to the measurement.

Analyses and Statistics

Data analysis of the flow cytometry data was performed with the FlowJo Software Version 10.6.2 (FlowJo LLT, USA), and graph preparation and statistical analysis were performed using the GraphPad Prism Software (Version 8.3.0 or higher).

DATA AVAILABILITY STATEMENT

The original contributions presented in the study are included in the article/**Supplementary Material**. Further inquiries can be directed to the corresponding author.

ETHICS STATEMENT

The animal study was reviewed and approved by Regierungspräsidium Tübingen Konrad-Adenauer-Straße 20 72072 Tübingen.

AUTHOR CONTRIBUTIONS

BT, MK, DSo, BP, and UR designed the study. SN and AS immunized the animal. PK, SH, and YP performed Nb selection. PK, BT, MW, TW, and AM performed biochemical characterization and functionalization of Nbs. MG and AZ performed HDX-MS analysis. AZ and MG performed HDX-MS experiments. JR, CG, MJ, and NS-M analyzed the Nb effects on T-cell proliferation and cytokine expression. DSe, AM, and SP radiolabeled the Nbs. SP and DSo performed *in vivo* imaging. MS performed staining of xenograft cryosections. BT, JR, CG, MK, BP, DSo, and UR drafted the article. MK, BP, and UR supervised the study. All authors contributed to the article and approved the submitted version.

FUNDING

This work received financial support from the State Ministry of Baden-Wuerttemberg for Economic Affairs, Labour and Tourism (Grant: Predictive diagnostics of immune-associated diseases for personalized medicine. FKZ: 35-4223.10/8). We acknowlegde support by Open Access Publishing Fund of University of Tuebingen.

ACKNOWLEDGMENTS

The authors thank Sandra Maier and Ulrich Kratzer (both Natural and Medical Sciences Institute) for technical support with MS analyses and Birgit Fehrenbacher (Department of Dermatology, University of Tuebingen) for technical support with imaging of xenograft cryosections.

SUPPLEMENTARY MATERIAL

The Supplementary Material for this article can be found online at: https://www.frontiersin.org/articles/10.3389/fimmu.2021.799910/full#supplementary-material

REFERENCES

1. Delhalle S, Bode SFN, Balling R, Ollert M, He FQ. A Roadmap Towards Personalized Immunology. *NPJ Syst Biol Appl* (2018) 4:9. doi: 10.1038/s41540-017-0045-9
2. Rossi JF, Ceballos P, Lu ZY. Immune Precision Medicine for Cancer: A Novel Insight Based on the Efficiency of Immune Effector Cells. *Cancer Commun (Lond)* (2019) 39(1):34. doi: 10.1186/s40880-019-0379-3
3. Scheuenpflug J. Precision Medicine in Oncology and Immuno-Oncology: Where We Stand and Where We're Headed. *BioMed Hub* (2017) 2(Suppl 1):79–86. doi: 10.1159/000481878
4. Collman R, Godfrey B, Cutilli J, Rhodes A, Hassan NF, Sweet R, et al. Macrophage-Tropic Strains of Human Immunodeficiency Virus Type 1 Utilize the CD4 Receptor. *J Virol* (1990) 64(9):4468–76. doi: 10.1128/JVI.64.9.4468-4476.1990
5. Claeys E, Vermeire K. The CD4 Receptor: An Indispensable Protein in T Cell Activation and A Promising Target for Immunosuppression. *Arch Microbiol Immunol* (2019) 3(3):133–50. doi: 10.26502/ami.93650036
6. Chitnis T. The Role of CD4 T Cells in the Pathogenesis of Multiple Sclerosis. *Int Rev Neurobiol* (2007) 79:43–72. doi: 10.1016/S0074-7742(07)79003-7
7. Goverman J. Autoimmune T Cell Responses in the Central Nervous System. *Nat Rev Immunol* (2009) 9(6):393–407. doi: 10.1038/nri2550
8. Becker W, Emmrich F, Horneff G, Burmester G, Seiler F, Schwarz A, et al. Imaging Rheumatoid Arthritis Specifically With Technetium 99m CD4-Specific (T-Helper Lymphocytes) Antibodies. *Eur J Nucl Med* (1990) 17(3-4):156–9. doi: 10.1007/BF00811445
9. Borst J, Ahrends T, Babala N, Melief CJM, Kastenmuller W. CD4(+) T Cell Help in Cancer Immunology and Immunotherapy. *Nat Rev Immunol* (2018) 18(10):635–47. doi: 10.1038/s41577-018-0044-0
10. Di Mascio M, Paik CH, Carrasquillo JA, Maeng JS, Jang BS, Shin IS, et al. Noninvasive *In Vivo* Imaging of CD4 Cells in Simian-Human Immunodeficiency Virus (SHIV)-Infected Nonhuman Primates. *Blood* (2009) 114(2):328–37. doi: 10.1182/blood-2008-12-192203
11. Byrareddy SN, Arthos J, Cicala C, Villinger F, Ortiz KT, Little D, et al. Sustained Virologic Control in SIV+ Macaques After Antiretroviral and Alpha4beta7 Antibody Therapy. *Science* (2016) 354(6309):197–202. doi: 10.1126/science.aag1276
12. Aubert RD, Kamphorst AO, Sarkar S, Vezys V, Ha SJ, Barber DL, et al. Antigen-Specific CD4 T-Cell Help Rescues Exhausted CD8 T Cells During Chronic Viral Infection. *Proc Natl Acad Sci USA* (2011) 108(52):21182–7. doi: 10.1073/pnas.1118450109
13. Penaloza-MacMaster P, Barber DL, Wherry EJ, Provine NM, Teigler JE, Parenteau L, et al. Vaccine-Elicited CD4 T Cells Induce Immunopathology After Chronic LCMV Infection. *Science* (2015) 347(6219):278–82. doi: 10.1126/science.aaa2148
14. Mousset CM, Hobo W, Woestenenk R, Preijers F, Dolstra H, van der Waart AB. Comprehensive Phenotyping of T Cells Using Flow Cytometry. *Cytometry A* (2019) 95(6):647–54. doi: 10.1002/cyto.a.23724
15. Doan M, Vorobjev I, Rees P, Filby A, Wolkenhauer O, Goldfeld AE, et al. Diagnostic Potential of Imaging Flow Cytometry. *Trends Biotechnol* (2018) 36(7):649–52. doi: 10.1016/j.tibtech.2017.12.008
16. Hartmann FJ, Babdor J, Gherardini PF, Amir ED, Jones K, Sahaf B, et al. Comprehensive Immune Monitoring of Clinical Trials to Advance Human Immunotherapy. *Cell Rep* (2019) 28(3):819–831 e4. doi: 10.1016/j.celrep.2019.06.049
17. Matos LL, Trufelli DC, de Matos MG, da Silva Pinhal MA. Immunohistochemistry as an Important Tool in Biomarkers Detection and Clinical Practice. *Biomark Insights* (2010) 5:9–20. doi: 10.4137/bmi.s2185
18. Tay RE, Richardson EK, Toh HC. Revisiting the Role of CD4(+) T Cells in Cancer Immunotherapy-New Insights Into Old Paradigms. *Cancer Gene Ther* (2021) 28(1-2):5–17. doi: 10.1038/s41417-020-0183-x
19. Rubin RH, Baltimore D, Chen BK, Wilkinson RA, Fischman AJ. *In Vivo* Tissue Distribution of CD4 Lymphocytes in Mice Determined by Radioimmunoscintigraphy With an 111In-Labeled Anti-CD4 Monoclonal Antibody. *Proc Natl Acad Sci USA* (1996) 93(15):7460–3. doi: 10.1073/pnas.93.15.7460
20. Steinhoff K, Pierer M, Siegert J, Pigla U, Laub R, Hesse S, et al. Visualizing Inflammation Activity in Rheumatoid Arthritis With Tc-99 M Anti-CD4-mAb Fragment Scintigraphy. *Nucl Med Biol* (2014) 41(4):350–4. doi: 10.1016/j.nucmedbio.2013.12.018

21. Kanwar B, Gao DW, Hwang AB, Grenert JP, Williams SP, Franc B, et al. *In Vivo* Imaging of Mucosal CD4+ T Cells Using Single Photon Emission Computed Tomography in a Murine Model of Colitis. *J Immunol Methods* (2008) 329(1-2):21–30. doi: 10.1016/j.jim.2007.09.008
22. Dammes N, Peer D. Monoclonal Antibody-Based Molecular Imaging Strategies and Theranostic Opportunities. *Theranostics* (2020) 10(2):938–55. doi: 10.7150/thno.37443
23. Dialynas DP, Wilde DB, Marrack P, Pierres A, Wall KA, Havran W, et al. Characterization of the Murine Antigenic Determinant, Designated L3T4a, Recognized by Monoclonal Antibody GK1.5: Expression of L3T4a by Functional T Cell Clones Appears to Correlate Primarily With Class II MHC Antigen-Reactivity. *Immunol Rev* (1983) 74:29–56. doi: 10.1111/j.1600-065x.1983.tb01083.x
24. Wilde DB, Marrack P, Kappler J, Dialynas DP, Fitch FW. Evidence Implicating L3T4 in Class II MHC Antigen Reactivity; Monoclonal Antibody GK1.5 (Anti-L3T4a) Blocks Class II MHC Antigen-Specific Proliferation, Release of Lymphokines, and Binding by Cloned Murine Helper T Lymphocyte Lines. *J Immunol* (1983) 131(5):2178–83.
25. Haque S, Saizawa K, Rojo J, Janeway CAJr. The Influence of Valence on the Functional Activities of Monoclonal Anti-L3T4 Antibodies. Discrimination of Signaling From Other Effects. *J Immunol* (1987) 139(10):3207–12.
26. Freise AC, Zettlitz KA, Salazar FB, Lu X, Tavare R, Wu AM. ImmunoPET Imaging of Murine CD4(+) T Cells Using Anti-CD4 Cys-Diabody: Effects of Protein Dose on T Cell Function and Imaging. *Mol Imaging Biol* (2017) 19 (4):599–609. doi: 10.1007/s11307-016-1032-z
27. Hamers-Casterman C, Atarhouch T, Muyldermans S, Robinson G, Hamers C, Songa EB, et al. Naturally Occurring Antibodies Devoid of Light Chains. *Nature* (1993) 363(6428):446–8. doi: 10.1038/363446a0
28. Lecocq Q, De Vlaeminck Y, Hanssens H, D'Huyvetter M, Raes G, Goyvaerts C, et al. Theranostics in Immuno-Oncology Using Nanobody Derivatives. *Theranostics* (2019) 9(25):7772–91. doi: 10.7150/thno.34941
29. Chakravarty R, Goel S, Cai W. Nanobody: The "Magic Bullet" for Molecular Imaging? *Theranostics* (2014) 4(4):386–98. doi: 10.7150/thno.8006
30. Yang EY, Shah K. Nanobodies: Next Generation of Cancer Diagnostics and Therapeutics. *Front Oncol* (2020) 10:1182. doi: 10.3389/fonc.2020.01182
31. Chanier T, Chames P. Nanobody Engineering: Toward Next Generation Immunotherapies and Immunoimaging of Cancer. *Antibodies (Basel)* (2019) 8(1):13. doi: 10.3390/antib8010013
32. Popp MWL, Ploegh HL. Making and Breaking Peptide Bonds: Protein Engineering Using Sortase. *Angew Chem Int Edition* (2011) 50(22):5024–32. doi: 10.1002/anie.201008267
33. Massa S, Vikani N, Betti C, Ballet S, Vanderhaegen S, Steyaert J, et al. Sortase A-Mediated Site-Specific Labeling of Camelid Single-Domain Antibody-Fragments: A Versatile Strategy for Multiple Molecular Imaging Modalities. *Contrast Media Mol Imaging* (2016) 11(5):328–39. doi: 10.1002/cmmi.1696
34. Virant D, Traenkle B, Maier J, Kaiser PD, Bodenhofer M, Schmees C, et al. A Peptide Tag-Specific Nanobody Enables High-Quality Labeling for dSTORM Imaging. *Nat Commun* (2018) 9(1):930. doi: 10.1038/s41467-018-03191-2
35. Braun MB, Traenkle B, Koch PA, Emele F, Weiss F, Poetz O, et al. Peptides in Headlock–a Novel High-Affinity and Versatile Peptide-Binding Nanobody for Proteomics and Microscopy. *Sci Rep* (2016) 6:19211. doi: 10.1038/srep19211
36. Wu H, Kwong PD, Hendrickson WA. Dimeric Association and Segmental Variability in the Structure of Human CD4. *Nature* (1997) 387(6632):527–30. doi: 10.1038/387527a0
37. Raybould MIJ, Marks C, Krawczyk K, Taddese B, Nowak J, Lewis AP, et al. Five Computational Developability Guidelines for Therapeutic Antibody Profiling. *Proc Natl Acad Sci USA* (2019) 116(10):4025–30. doi: 10.1073/pnas.1810576116
38. Xu Y, Wang D, Mason B, Rossomando T, Li N, Liu D, et al. Structure, Heterogeneity and Developability Assessment of Therapeutic Antibodies. *MAbs* (2019) 11(2):239–64. doi: 10.1080/19420862.2018.1553476
39. Keyaerts M, Xavier C, Heemskerk J, Devoogdt N, Everaert H, Ackaert C, et al. Phase I Study of 68Ga-HER2-Nanobody for PET/CT Assessment of HER2 Expression in Breast Carcinoma. *J Nucl Med* (2016) 57(1):27–33. doi: 10.2967/jnumed.115.162024
40. Xavier C, Vaneycken I, D'Huyvetter M, Heemskerk J, Keyaerts M, Vincke C, et al. Synthesis, Preclinical Validation, Dosimetry, and Toxicity of 68Ga-NOTA-Anti-HER2 Nanobodies for iPET Imaging of HER2 Receptor Expression in Cancer. *J Nucl Med* (2013) 54(5):776–84. doi: 10.2967/jnumed.112.111021
41. Masuda S, Kumano K, Suzuki T, Tomita T, Iwatsubo T, Natsugari H, et al. Dual Antitumor Mechanisms of Notch Signaling Inhibitor in a T-Cell Acute Lymphoblastic Leukemia Xenograft Model. *Cancer Sci* (2009) 100(12):2444–50. doi: 10.1111/j.1349-7006.2009.01328.x
42. Killeen N, Sawada S, Littman DR. Regulated Expression of Human CD4 Rescues Helper T Cell Development in Mice Lacking Expression of Endogenous CD4. *EMBO J* (1993) 12(4):1547–53. doi: 10.1002/j.1460-2075.1993.tb05798.x
43. Sckisel GD, Mirsoian A, Minnar CM, Crittenden M, Curti B, Chen JQ, et al. Differential Phenotypes of Memory CD4 and CD8 T Cells in the Spleen and Peripheral Tissues Following Immunostimulatory Therapy. *J Immunother Cancer* (2017) 5:33. doi: 10.1186/s40425-017-0235-4
44. Tavare R, McCracken MN, Zettlitz KA, Salazar FB, Olafsen T, Witte ON, et al. Immuno-PET of Murine T Cell Reconstitution Postadoptive Stem Cell Transplantation Using Anti-CD4 and Anti-CD8 Cys-Diabodies. *J Nucl Med* (2015) 56(8):1258–64. doi: 10.2967/jnumed.114.153338
45. Li H, Chen Y, Jin Q, Wu Y, Deng C, Gai Y, et al. Noninvasive Radionuclide Molecular Imaging of the CD4-Positive T Lymphocytes in Acute Cardiac Rejection. *Mol Pharm* (2021) 18(3):1317–26. doi: 10.1021/acs.molpharmaceut.0c01155
46. Kristensen LK, Prohlich C, Christensen C, Melander MC, Poulsen TT, Galler GR, et al. CD4(+) and CD8a(+) PET Imaging Predicts Response to Novel PD-1 Checkpoint Inhibitor: Studies of Sym021 in Syngeneic Mouse Cancer Models. *Theranostics* (2019) 9(26):8221–38. doi: 10.7150/thno.37513
47. Choy EH, Panayi GS, Emery P, Madden S, Breedveld FC, Kraan MC, et al. Repeat-Cycle Study of High-Dose Intravenous 4162W94 Anti-CD4 Humanized Monoclonal Antibody in Rheumatoid Arthritis. A Randomized Placebo-Controlled Trial. *Rheumatol (Oxford)* (2002) 41(10):1142–8. doi: 10.1093/rheumatology/41.10.1142
48. Moreland LW, Pratt PW, Mayes MD, Postlethwaite A, Weisman MH, Schnitzer T, et al. Double-Blind, Placebo-Controlled Multicenter Trial Using Chimeric Monoclonal Anti-CD4 Antibody, cM-T412, in Rheumatoid Arthritis Patients Receiving Concomitant Methotrexate. *Arthritis Rheum* (1995) 38(11):1581–8. doi: 10.1002/art.1780381109
49. Rashidian M, Ingram JR, Dougan M, Dongre A, Whang KA, LeGall C, et al. Predicting the Response to CTLA-4 Blockade by Longitudinal Noninvasive Monitoring of CD8 T Cells. *J Exp Med* (2017) 214(8):2243–55. doi: 10.1084/jem.20161950
50. Huang L, Gainkam LO, Caveliers V, Vanhove C, Keyaerts M, De Baetselier P, et al. SPECT Imaging With 99mtc-Labeled EGFR-Specific Nanobody for *In Vivo* Monitoring of EGFR Expression. *Mol Imaging Biol* (2008) 10(3):167–75. doi: 10.1007/s11307-008-0133-8
51. Roovers RC, Laeremans T, Huang L, De Taeye S, Verkleij AJ, Revets H, et al. Efficient Inhibition of EGFR Signaling and of Tumour Growth by Antagonistic Anti-EFGR Nanobodies. *Cancer Immunol Immunother* (2007) 56(3):303–17. doi: 10.1007/s00262-006-0180-4
52. Evazalipour M, D'Huyvetter M, Tehrani BS, Abolhassani M, Omidfar K, Abdoli S, et al. Generation and Characterization of Nanobodies Targeting PSMA for Molecular Imaging of Prostate Cancer. *Contrast Media Mol Imaging* (2014) 9(3):211–20. doi: 10.1002/cmmi.1558
53. Blykers A, Schoonooghe S, Xavier C, D'Hoe K, Laoui D, D'Huyvetter M, et al. PET Imaging of Macrophage Mannose Receptor-Expressing Macrophages in Tumor Stroma Using 18f-Radiolabeled Camelid Single-Domain Antibody Fragments. *J Nucl Med* (2015) 56(8):1265–71. doi: 10.2967/jnumed.115.156828
54. Bala G, Baudhuin H, Remory I, Gillis K, Debie P, Krasniqi A, et al. Evaluation of [(99m)Tc]Radiolabeled Macrophage Mannose Receptor-Specific Nanobodies for Targeting of Atherosclerotic Lesions in Mice. *Mol Imaging Biol* (2018) 20(2):260–7. doi: 10.1007/s11307-017-1117-3
55. Jailkhani N, Ingram JR, Rashidian M, Rickelt S, Tian C, Mak H, et al. Noninvasive Imaging of Tumor Progression, Metastasis, and Fibrosis Using a Nanobody Targeting the Extracellular Matrix. *Proc Natl Acad Sci USA* (2019) 116(28):14181–90. doi: 10.1073/pnas.1817442116
56. D'Huyvetter M, De Vos J, Xavier C, Pruszynski M, Sterckx YGJ, Massa S, et al. (131)I-Labeled Anti-HER2 Camelid sdAb as a Theranostic Tool in Cancer

Treatment. *Clin Cancer Res* (2017) 23(21):6616–28. doi: 10.1158/1078-0432.CCR-17-0310
57. Bruni D, Angell HK, Galon J. The Immune Contexture and Immunoscore in Cancer Prognosis and Therapeutic Efficacy. *Nat Rev Cancer* (2020) 20 (11):662–80. doi: 10.1038/s41568-020-0285-7
58. Accogli T, Bruchard M, Vegran F. Modulation of CD4 T Cell Response According to Tumor Cytokine Microenvironment. *Cancers (Basel)* (2021) 13 (3):373. doi: 10.3390/cancers13030373
59. Sakihama T, Smolyar A, Reinherz EL. Oligomerization of CD4 Is Required for Stable Binding to Class II Major Histocompatibility Complex Proteins But Not for Interaction With Human Immunodeficiency Virus Gp120. *Proc Natl Acad Sci USA* (1995) 92(14):6444–8. doi: 10.1073/pnas.92.14.6444
60. Jonsson P, Southcombe JH, Santos AM, Huo J, Fernandes RA, McColl J, et al. Remarkably Low Affinity of CD4/peptide-Major Histocompatibility Complex Class II Protein Interactions. *Proc Natl Acad Sci USA* (2016) 113(20):5682–7. doi: 10.1073/pnas.1513918113
61. Cruikshank WW, Greenstein JL, Theodore AC, Center DM. Lymphocyte Chemoattractant Factor Induces CD4-Dependent Intracytoplasmic Signaling in Lymphocytes. *J Immunol* (1991) 146(9):2928–34.
62. Vignali DA, Vignali KM. Profound Enhancement of T Cell Activation Mediated by the Interaction Between the TCR and the D3 Domain of CD4. *J Immunol* (1999) 162(3):1431–9.
63. Tijink BM, Laeremans T, Budde M, Stigter-van Walsum M, Dreier T, de Haard HJ, et al. Improved Tumor Targeting of Anti-Epidermal Growth Factor Receptor Nanobodies Through Albumin Binding: Taking Advantage of Modular Nanobody Technology. *Mol Cancer Ther* (2008) 7(8):2288–97. doi: 10.1158/1535-7163.MCT-07-2384
64. Muyldermans S, Baral TN, Retamozzo VC, De Baetselier P, De Genst E, Kinne J, et al. Camelid Immunoglobulins and Nanobody Technology. *Vet Immunol Immunopathol* (2009) 128(1-3):178–83. doi: 10.1016/j.vetimm.2008.10.299
65. Vincke C, Loris R, Saerens D, Martinez-Rodriguez S, Muyldermans S, Conrath K. General Strategy to Humanize a Camelid Single-Domain Antibody and Identification of a Universal Humanized Nanobody Scaffold. *J Biol Chem* (2009) 284(5):3273–84. doi: 10.1074/jbc.M806889200
66. Ackaert C, Smiejkowska N, Xavier C, Sterckx YGJ, Denies S, Stijlemans B, et al. Immunogenicity Risk Profile of Nanobodies. *Front Immunol* (2021) 12:632687. doi: 10.3389/fimmu.2021.632687
67. Gainkam LO, Caveliers V, Devoogdt N, Vanhove C, Xavier C, Boerman O, et al. Localization, Mechanism and Reduction of Renal Retention of Technetium-99m Labeled Epidermal Growth Factor Receptor-Specific Nanobody in Mice. *Contrast Media Mol Imaging* (2011) 6(2):85–92. doi: 10.1002/cmmi.408
68. D'Huyvetter M, Vincke C, Xavier C, Aerts A, Impens N, Baatout S, et al. Targeted Radionuclide Therapy With A 177Lu-Labeled Anti-HER2 Nanobody. *Theranostics* (2014) 4(7):708–20. doi: 10.7150/thno.8156
69. de Jong M, Barone R, Krenning E, Bernard B, Melis M, Visser T, et al. Megalin Is Essential for Renal Proximal Tubule Reabsorption of (111)In-DTPA-Octreotide. *J Nucl Med* (2005) 46(10):1696–700.
70. Traenkle B, Emele F, Anton R, Poetz O, Haeussler RS, Maier J, et al. Monitoring Interactions and Dynamics of Endogenous Beta-Catenin With Intracellular Nanobodies in Living Cells. *Mol Cell Proteomics* (2015) 14 (3):707–23. doi: 10.1074/mcp.M114.044016
71. Maier J, Traenkle B, Rothbauer U. Real-Time Analysis of Epithelial-Mesenchymal Transition Using Fluorescent Single-Domain Antibodies. *Sci Rep* (2015) 5:13402. doi: 10.1038/srep13402
72. Arbabi Ghahroudi M, Desmyter A, Wyns L, Hamers R, Muyldermans S. Selection and Identification of Single Domain Antibody Fragments From Camel Heavy-Chain Antibodies. *FEBS Lett* (1997) 414(3):521–6. doi: 10.1016/S0014-5793(97)01062-4
73. Rothbauer U, Zolghadr K, Muyldermans S, Schepers A, Cardoso MC, Leonhardt H. A Versatile Nanotrap for Biochemical and Functional Studies With Fluorescent Fusion Proteins. *Mol Cell Proteomics* (2008) 7(2):282–9. doi: 10.1074/mcp.M700342-MCP200
74. Davies G, Rolle AM, Maurer A, Spycher PR, Schillinger C, Solouk-Saran D, et al. Towards Translational ImmunoPET/MR Imaging of Invasive Pulmonary Aspergillosis: The Humanised Monoclonal Antibody JF5 Detects Aspergillus Lung Infections *In Vivo*. *Theranostics* (2017) 7 (14):3398–414. doi: 10.7150/thno.20919
75. Wagner TR, Ostertag E, Kaiser PD, Gramlich M, Ruetalo N, Junker D, et al. NeutrobodyPlex-Monitoring SARS-CoV-2 Neutralizing Immune Responses Using Nanobodies. *EMBO Rep* (2021) 22(5):e52325. doi: 10.15252/embr.202052325
76. Becker M, Strengert M, Junker D, Kaiser PD, Kerrinnes T, Traenkle B, et al. Exploring Beyond Clinical Routine SARS-CoV-2 Serology Using MultiCoV-Ab to Evaluate Endemic Coronavirus Cross-Reactivity. *Nat Commun* (2021) 12(1):1152. doi: 10.1038/s41467-021-20973-3
77. Chen I, Dorr BM, Liu DR. A General Strategy for the Evolution of Bond-Forming Enzymes Using Yeast Display. *Proc Natl Acad Sci USA* (2011) 108 (28):11399–404. doi: 10.1073/pnas.1101046108
78. Kochert BA, Iacob RE, Wales TE, Makriyannis A, Engen JR. Hydrogen-Deuterium Exchange Mass Spectrometry to Study Protein Complexes. *Methods Mol Biol* (2018) 1764:153–71. doi: 10.1007/978-1-4939-7759-8_10
79. Hamuro Y, Coales SJ. Optimization of Feasibility Stage for Hydrogen/Deuterium Exchange Mass Spectrometry. *J Am Soc Mass Spectrom* (2018) 29(3):623–9. doi: 10.1007/s13361-017-1860-3
80. Masson GR, Burke JE, Ahn NG, Anand GS, Borchers C, Brier S, et al. Recommendations for Performing, Interpreting and Reporting Hydrogen Deuterium Exchange Mass Spectrometry (HDX-MS) Experiments. *Nat Methods* (2019) 16(7):595–602. doi: 10.1038/s41592-019-0459-y
81. Loffler MW, Nussbaum B, Jager G, Jurmeister PS, Budczies J, Pereira PL, et al. A Non-Interventional Clinical Trial Assessing Immune Responses After Radiofrequency Ablation of Liver Metastases From Colorectal Cancer. *Front Immunol* (2019) 10:2526. doi: 10.3389/fimmu.2019.02526
82. Widenmeyer M, Griesemann H, Stevanovic S, Feyerabend S, Klein R, Attig S, et al. Promiscuous Survivin Peptide Induces Robust CD4+ T-Cell Responses in the Majority of Vaccinated Cancer Patients. *Int J Cancer* (2012) 131(1):140–9. doi: 10.1002/ijc.26365
83. EMEA. *Guideline on Bioanalytical Method Validation*. European Medicines Agency; Comittee for Medicinal Products for Human Use. London (CHMP (2013).
84. FDA. *Bioanalytical Method Validation: Guidance for Industry*. Silver Spring, Rockville: U.S. Department of Health and Human Services, Food and Drug Administration, Center for Drug Evaluation and Research, Center for Veterinary Medicine.
85. Westgard JO, Barry PL, Hunt MR, Groth T. A Multi-Rule Shewhart Chart for Quality Control in Clinical Chemistry. *Clin Chem* (1981) 27(3):493–501. doi: 10.1093/clinchem/27.3.493

Conflict of Interest: DSo, MK, BP, BT, PK, and UR are named as inventors on a patent application claiming the use of the described nanobodies for diagnosis and therapeutics filed by the Natural and Medical Sciences Institute and the Werner Siemens Imaging Center.

The remaining authors declare that the research was conducted in the absence of any commercial or financial relationships that could be construed as a potential conflict of interest.

3.3. Accepted publication III

Pezzana S, Blaess S, Traenkle B, Schaefer A, Ruoff L, Tako B, Castaneda Vega S, Kaiser PD, Wagner T, Gonzalez-Menendez I, Quintanilla-Martinez L, Rochwarger A, Schürch CM, Riel S, Schaller M, van Genugten EAJ, van der Hoorn IAE, Gorris MAJ, Steinvoort M, Peeters E, de Vries IJM, van den Heuvel MM, Aarntzen EHJG, Maurer A, Rothbauer U, Pichler BJ, Kneilling M, Sonanini D. PET-based immunomapping of intratumoral $CD4^+$ cells to monitor acquired resistance to checkpoint inhibitors. Sci Adv. 2025 Jun 27;11(26):eadw1924. doi: 10.1126/sciadv.adw1924 [4].

IMMUNOLOGY

PET-based immunomapping of intratumoral CD4$^+$ cells to monitor acquired resistance to checkpoint inhibitors

**Stefania Pezzana[1], Simone Blaess[1], Bjoern Traenkle[2], Anna Schaefer[1], Lara Ruoff[1], Bredi Tako[1], Salvador Castaneda Vega[1,3], Philipp D. Kaiser[2], Teresa Wagner[2,4], Irene Gonzalez-Menendez[5,6], Leticia Quintanilla-Martinez[5,6], Alexander Rochwarger[6], Christian M. Schürch[5,6], Simon Riel[7], Martin Schaller[7], Evelien A. J. van Genugten[8], Iris A. E. van der Hoorn[9,10], Mark A. J. Gorris[9], Megan Steinvoort[8,9], Eva Peeters[8], I. Jolanda M. de Vries[9], Michel M. van den Heuvel[10,11], Erik H. J. G. Aarntzen[3,8,12], Andreas Maurer[1,5], Ulrich Rothbauer[4,5], Bernd J. Pichler[1,5,13], Manfred Kneilling[1,5,7], Dominik Sonanini[1,2,5,13,14]*

CD4$^+$ T cells are crucial in shaping response and resistance to immunotherapy. To enhance our understanding of their multifaceted functions, we developed copper-64–radiolabeled nanobodies targeting the human CD4 receptor (^{64}Cu-CD4-Nb1) for positron emission tomography (PET). In human CD4-receptor knock-in mice, ^{64}Cu-CD4-Nb1 specifically accumulated in different orthotopic tumors, correlating with histological CD4$^+$ cell densities. Based on intratumoral CD4$^+$ cell distribution patterns within the core and periphery, we distinguished responders to combined αPD-1/4-1BB antibodies early on-treatment. CD4-PET identified resistance to αPD-1 monotherapy, which was mitigated by adding regulatory T cell–depleting α4-1BB antibodies. Patients with early-stage non–small cell lung cancer who relapsed after neoadjuvant αPD-L1 therapy revealed low CD4$^+$ T cell densities in the tumor core. In human and mouse tumor tissues, regulatory T cells correlated with CD4$^+$ cell densities. Thus, visualizing the spatial distribution patterns of CD4$^+$ cells by PET offers mechanistic insights into CD4-mediated therapy efficacy, with great potential for guiding combinatorial immunotherapies in patients with cancer.

INTRODUCTION

T cells are crucially involved in the development and treatment of cancer. Whereas CD8$^+$ cytotoxic T lymphocytes (CTLs) primarily mediate antitumoral immunity, CD4$^+$ T cells are a heterogeneous group of cells with complex and multifaceted roles in either orchestrating or suppressing therapeutic immune responses (*1*, *2*). On the basis of their differentiation, CD4$^+$ T helper cells can induce the cytotoxic activity of CTLs and activate B cells, dendritic cells, natural killer cells, and macrophages (*3*). In addition, specific subsets of CD4$^+$ T cells exert direct antitumoral cytotoxicity and induce tumor senescence (*4*–*6*). In contrast, regulatory T (T_{reg}) cells inhibit antitumoral immune responses within the tumor microenvironment (TME) (*7*).

[1]Werner Siemens Imaging Center, Department of Preclinical Imaging and Radiopharmacy, University Hospital Tuebingen, University of Tuebingen, Tuebingen, Germany. [2]NMI Natural and Medical Sciences Institute at the University of Tuebingen, Reutlingen, Germany. [3]Department of Nuclear Medicine, University Hospital Tuebingen, University of Tuebingen, Tuebingen, Germany. [4]Pharmaceutical Biotechnology, University of Tuebingen, Tuebingen, Germany. [5]Cluster of Excellence iFIT (EXC2180) "Image-Guided and Functionally Instructed Tumor Therapies", University of Tuebingen, Tuebingen, Germany. [6]Department of Pathology and Neuropathology, University Hospital and Comprehensive Cancer Center Tuebingen, University of Tuebingen, Tuebingen, Germany. [7]Department of Dermatology, University Hospital Tuebingen, University of Tuebingen, Tuebingen, Germany. [8]Department of Medical Imaging, Radboud University Medical Center, Nijmegen, Netherlands. [9]Department of Medical Biosciences, Radboud University Medical Center, Nijmegen, Netherlands. [10]Department of Pulmonology, Radboud University Medical Center, Nijmegen, Netherlands. [11]Department of Pulmonology, University Medical Center Utrecht, Utrecht, Netherlands. [12]Department of Nuclear Medicine and Molecular Imaging, University Medical Center Groningen, Groningen, Netherlands. [13]German Cancer Consortium (DKTK) and German Cancer Research Center (DKFZ), Partner site Tuebingen, Tuebingen, Germany. [14]Department of Medical Oncology and Pneumology, University Hospital Tuebingen, University of Tuebingen, Tuebingen, Germany.
*Corresponding author. Email: dominik.sonanini@med.uni-tuebingen.de

T_{reg} cells have been identified as key drivers of resistance to immune checkpoint inhibitors (ICIs) targeting the programmed death protein 1 (PD-1) or its ligand (PD-L1) (*8*). PD-(L)1–directed ICIs have become the standard of care for many types of metastatic cancer (*9*, *10*), but overall response rates remain unsatisfactory, ranging from 12 to 40% depending on the tumor type (*11*–*15*). To improve therapeutic outcomes, αPD-(L)1 ICIs have been combined with other immunotherapies targeting additional immune checkpoints—such as cytotoxic T lymphocyte antigen 4 (CTLA-4), lymphocyte activation antigen 3 (LAG-3), chemokine receptor 7 (CCR-7), and 4-1BB—or with tumor vaccination. All of these approaches have been shown to specifically modulate CD4$^+$ T cell function (*16*–*21*).

Positron emission tomography (PET), a noninvasive molecular imaging method, enables visualization of immune cells by using radiolabeled antibodies or antibody fragments targeting cell-specific surface markers (*22*). To better understand the mechanisms underlying CD4-mediated immunity and to individually stratify patients for combinatorial immunotherapies, various radiotracers, including full-length antibodies, radiolabeled F(ab′)$_2$ fragments, engineered scFv dimers (cys-diabodies), or scFv-CH3 (minibodies), have been developed for the specific targeting of mouse, nonhuman primate, or human CD4$^+$ cells (*23*–*29*). Recently, we compared zirconium-89 (^{89}Zr)–labeled human and mouse CD4-specific minibodies in different syngeneic tumor models and successfully identified responders to combined αPD-L1/αLAG-3 ICI therapy in an MC38 tumor mouse model based on the whole-tumor PET uptake (*30*).

Increasing histology-driven evidence from mouse and human tumor tissues highlights the spatial location of specific CD4$^+$ subsets within the TME and their proximity to other immune cells as critical biomarkers for determining ICI efficacy (*31*–*37*). To

meet the requirement for highly specific and sensitive radiotracers capable of capturing the dynamic distribution patterns of immune cell with sufficient spatial resolution, we recently generated alpaca-derived single-domain antibodies [nanobodies (Nbs)] that target the human CD4 receptor for clinical PET imaging of $CD4^+$ T cells in vivo (*38*). Because of their low molecular and picomolar binding affinities, Nbs offer advanced imaging properties including rapid tissue penetration and clearance from blood (*39*). From a set of 78 positive binders, we selected CD4-Nb1 as the lead candidate based on its binding characteristics, recognized epitopes, and lack of effects on T cell proliferation, activation, or cytokine release in vitro. CD4-Nb1 was subsequently radiolabeled with copper-64 (^{64}Cu) for in vivo imaging (*38*).

In this study, we applied ^{64}Cu-CD4-Nb1 to track intratumoral $CD4^+$ T cells in human CD4 receptor knock-in (hCD4-KI) and wild-type (WT) C57BL/6J mouse models to explore whether clinically relevant changes $CD4^+$ cells within the TME and lymphatic organs can be visualized by in vivo PET imaging. Spatially resolved PET uptake patterns observed during αPD-L1 monotherapy and combined ICI therapy were correlated with histological distribution of $CD4^+$ cells and therapy response. Notably, we demonstrate that differential core and marginal $CD4^+$ cell quantifications of whole tumor tissues derived from patients with non–small cell lung cancer (NSCLC) after neoadjuvant αPD-L1 therapy were predictive of therapy resistance. These findings underscore the potential of ^{64}Cu-CD4-Nb1 PET imaging to provide mechanistic insights into CD4-mediated immune responses and resistance, paving the way for its use in guiding combinatorial immunotherapy strategies in patients with cancer.

RESULTS

^{64}Cu-CD4-Nb1 specifically binds to human CD4 in vitro and in vivo

For in vivo PET imaging of $CD4^+$ cells, our CD4-Nb1 was conjugated site-specifically to p-NCS-benzyl-NODA-GA (NODAGA) and radiolabeled with ^{64}Cu, with labeling efficiencies of over 90% (Fig. 1A). We revealed a maximum binding of 92.6% for ^{64}Cu-CD4-Nb1 using hCD4-coated beads (Fig. 1B) and confirmed specific binding to freshly isolated $hCD4^+$ T cells (Fig. 1C).

To determine the CD4-specific biodistribution kinetics in vivo, we analyzed ^{64}Cu-CD4-Nb1 uptake in orthotopic S2WTP3 polyoma virus middle T antigen (PyMT) breast cancer–bearing hCD4 knock-in (hCD4-KI) and WT C57BL/6J mice (fig. S1A). Whereas ^{64}Cu-CD4-Nb1 was rapidly cleared from the blood within the first 90 min after injection in both groups, we observed increased PET uptake in the lymphatic organs and PyMT tumors of hCD4-KI mice over time in vivo (1.5 to 6 hours) (Fig. 1D and fig. S1B) and ex vivo (6 hours) (fig. S1D). At the 3-hour imaging time point, CD4-derived PET signals could be clearly distinguished visually (Fig. 1E) and quantification revealed ~3.6-fold higher uptake in the spleen, ~3.5-fold higher uptake in tumor-draining lymph nodes, and ~1.8-fold higher uptake in PyMT tumors in hCD4-KI mice than in WT mice (Fig. 1, F and G, and fig. S1C). In contrast, organs with low $CD4^+$ T cell infiltration, such as the lung, kidney, and muscle, as well as blood, showed a similar ^{64}Cu-CD4-Nb1 uptake (fig. S1, B and C). This observation indicates that the presence or absence of the target antigen does not influence the biodistribution of the tracer in vivo.

^{64}Cu-CD4-Nb1 PET imaging can detect clinically relevant changes in intratumoral $CD4^+$ cell density

Next, we analyzed the sensitivity of ^{64}Cu-CD4-Nb1 to detect variations in intratumoral $CD4^+$ T cell densities. For this purpose, we orthotopically inoculated cells of the low-immunogenic B16F10 melanoma tumor cell line (*40*) and the immunogenic PyMT breast cancer cell line (*41*) into hCD4-KI or WT mice. The tumor-bearing mice were either left untreated or received combined αPD-1/α4-1BB ICI therapy for 7 days before ^{64}Cu-CD4-Nb1 PET imaging (fig. S2A).

In untreated hCD4-KI mice, ^{64}Cu-CD4-Nb1 uptake was slightly higher in PyMT tumors (0.30 ± 0.05 %ID/ml) than in B16F10 tumors (0.23 ± 0.02 %ID/ml) (Fig. 2, A and B). In the ICI-treated PyMT tumor-bearing hCD4-KI mice, the ^{64}Cu-CD4-Nb1 uptake was significantly higher (0.44 ± 0.04 %ID/ml) than in the ICI-treated PyMT tumor-bearing WT mice. The latter showed a ^{64}Cu-CD4-Nb1 uptake of 0.23 ± 0.02 %ID/ml, similar to that of the poorly immunogenic B16F10 melanomas (Fig. 2, A and B, and fig. S3A). Quantitative ex vivo biodistribution analysis of the tumors demonstrated values similar to the in vivo uptake values for each group (Fig. 2C and fig. S3C). The immunohistochemical analysis revealed that the $CD4^+$ T cell densities correlated with ^{64}Cu-CD4-Nb1 in vivo and ex vivo uptake when corrected for nonspecific background ^{64}Cu-CD4-Nb1 uptake in tumors of WT animals (Fig. 2D). To note, we observed an accumulation of ^{64}Cu-CD4-Nb1 preferentially at the tumor margins of nontreated PyMT tumors (Fig. 2A). In sharp contrast, in ICI-treated mice ^{64}Cu-CD4-Nb1 mainly accumulated within the tumor cores (Fig. 2A). This ICI-related $CD4^+$ T cell infiltration into the TME was also confirmed by immunohistochemical staining (Fig. 2, D and E).

Furthermore, we detected higher ^{64}Cu-CD4-Nb1 uptake in the spleen and tumor-draining and contralateral lymph nodes of PyMT-bearing ICI-treated hCD4-KI mice when compared to untreated PyMT- and B16F10-bearing hCD4-KI mice (Fig. 3, A to C, and fig. S2, B and C). This observation was validated by ex vivo CD4 immunofluorescence microscopy of the spleen (Fig. 3D), suggesting a systemic αPD-1/α4-1BB treatment-related increase in $CD4^+$ cells in the secondary lymphoid organs.

$CD4^+$ immune cell infiltration in the tumor core is correlated with sensitivity to αPD-1/α4-1BB therapy

To further investigate whether dynamic changes in $CD4^+$ T cell density within the TME provide early insights into immunotherapy efficacy, we subjected additional PyMT tumor-bearing ICI-treated hCD4-KI mice to in vivo ^{64}Cu-CD4-Nb1-PET imaging. Following ICI treatment, 7 of the 13 animals were classified as responders based on inhibited tumor growth (Fig. 4A). Notably, in responsive tumors of hCD4-KI mice, ^{64}Cu-CD4-Nb1 uptake was significantly higher (0.47 ± 0.03 %ID/ml) than in nonresponsive tumors (0.36 ± 0.02 %ID/ml) (Fig. 4B). In addition, we identified different uptake patterns within the TME. In responders, ^{64}Cu-CD4-Nb1 predominantly accumulated in the tumor core (classified as T cell–enriched). In contrast, nonresponsive tumors showed a ubiquitously reduced ^{64}Cu-CD4-Nb1 uptake (T cell–deserted) or signal accumulation predominantly at the tumor margin (T cell–excluded; Fig. 4C). To quantitatively assess these distinct spatial uptake patterns, we analyzed the tumor core and periphery separately. This was done by defining a tumor region of interest (ROI) reduced by 50% for the core, with the corresponding peripheral region encompassing the

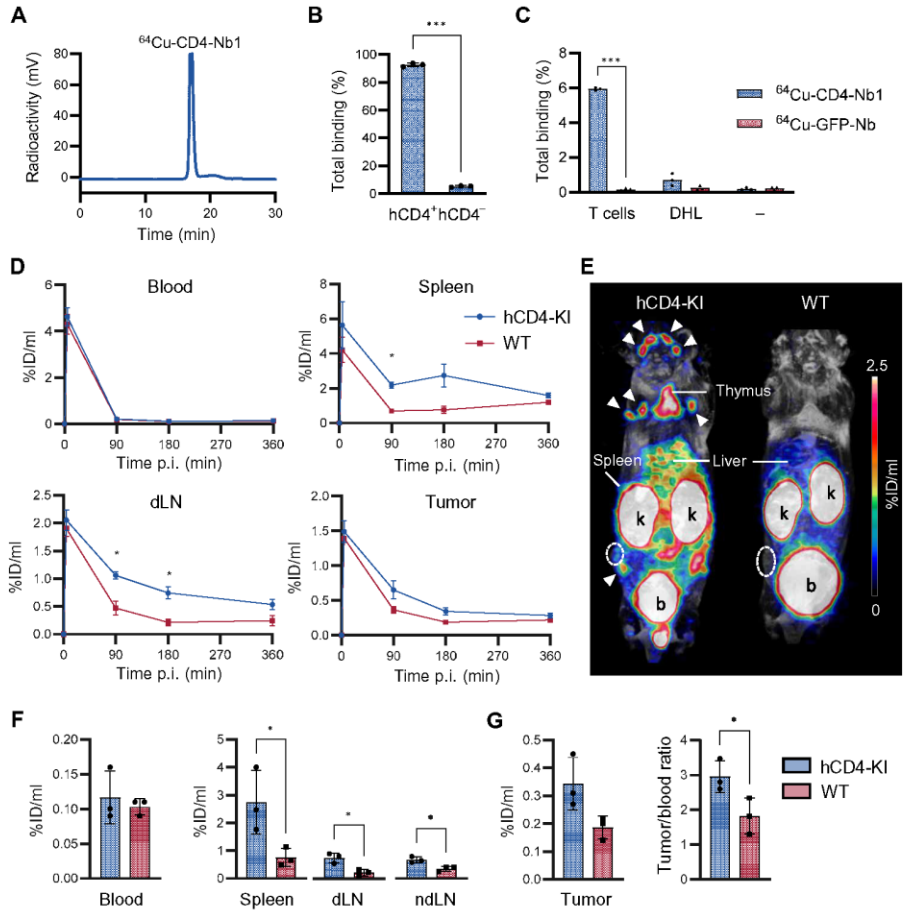

Fig. 1. Specific binding and biodistribution dynamics of ^{64}Cu-CD4-Nb1. (**A**) High-performance liquid chromatography chromatogram of ^{64}Cu-CD4-Nb1. Representative data from >3 independent experiments. (**B**) Immunoreactive fraction of ^{64}Cu-CD4-Nb1 using magnetic beads coated with human CD4 (hCD4$^+$) or left uncoated (hCD4$^-$). $n = 3$ per group, means ± SD, representative data from >3 independent experiments. (**C**) In vitro binding of ^{64}Cu-CD4-Nb1 and a control Nb (^{64}Cu-GFP-Nb) to freshly isolated hCD4$^+$ T cells, hCD4$^-$ DHL cells, or no cells (–). $n = 3$ per group. (**D**) ^{64}Cu-CD4-Nb1 PET uptake dynamics 5 to 360 min post-tracer injection (p.i.) in the blood, spleen, draining lymph nodes (dLNs), and tumors ($n = 3$ per group, means ± SD). The data are presented as the mean percent of the injected dose per ml (%ID/ml). (**E**) Representative maximum intensity projection PET images overlaid with anatomical MR images acquired 180 min after ^{64}Cu-CD4-Nb1 injection in human CD4 knock-in (hCD4-KI) or WT mice with orthotopic PyMT triple-negative breast cancer tumors. The tumors are outlined with white circles, and the lymph nodes are highlighted by white arrows; k: kidney; b: bladder. (**F**) ^{64}Cu-CD4-Nb1 PET uptake quantification 180 min after tracer injection in the blood, spleen, dLNs, and nondraining lymph nodes (ndLNs). (**G**) ^{64}Cu-CD4-Nb1 PET uptake quantification 180 min after tracer injection in PyMT tumors and the tumor-to-blood ratio. Pairwise comparisons were performed with Student's *t* test and corrected for multiple comparisons using the Holm-Sidak method (*$P < 0.05$; ***$P < 0.001$).

remaining area (Fig. 4C). The calculation of the core-to-periphery tracer uptake ratio determined for each tumor enabled us to differentiate between responders and nonresponders on an individual basis (Fig. 4D). These findings are in line with the results of quantitative ex vivo immunohistochemical analysis, which revealed higher CD4$^+$ cell densities in the tumor core of therapy-responsive mice and higher CD4$^+$ cell densities in the tumor periphery of two nonresponsive hCD4-KI mice classified with immune excluded PET uptake patterns (Fig. 4, E and F). Noteworthy, there was no correlation between therapy outcome and ^{64}Cu-CD4-Nb1 uptake in the secondary lymphatic organs (fig. S3, D and E).

Unexpectedly, we detected greater fractions of FoxP3$^+$ T$_{reg}$ cells in both the tumor core of responding animals and the tumor periphery of nonresponsive animals (Fig. 4, G and H). Thus, at least in this animal model, we found that the intratumoral distribution of T$_{reg}$ cells was associated with the CD4$^+$ cell densities and no individual indicator of therapy resistance, highlighting the ability of our PET approach to capture CD4$^+$ cell–mediated immune responses based on the spatial localization during treatment.

CD4-directed PET imaging to guide treatment regimens in MC38 tumor-bearing mice

On the basis of ex vivo studies in αPD-1–treated WT animals showing a huge variety of 7.5 to 20.3% CD4$^+$ T cells within the MC38 tumor infiltrate (fig. S4A), we aimed to investigate whether on-treatment CD4-PET imaging can be used to identify early therapy resistance, thus enabling timely therapy adaptation. To achieve heterogeneous therapeutic responses in a preclinical model similar to

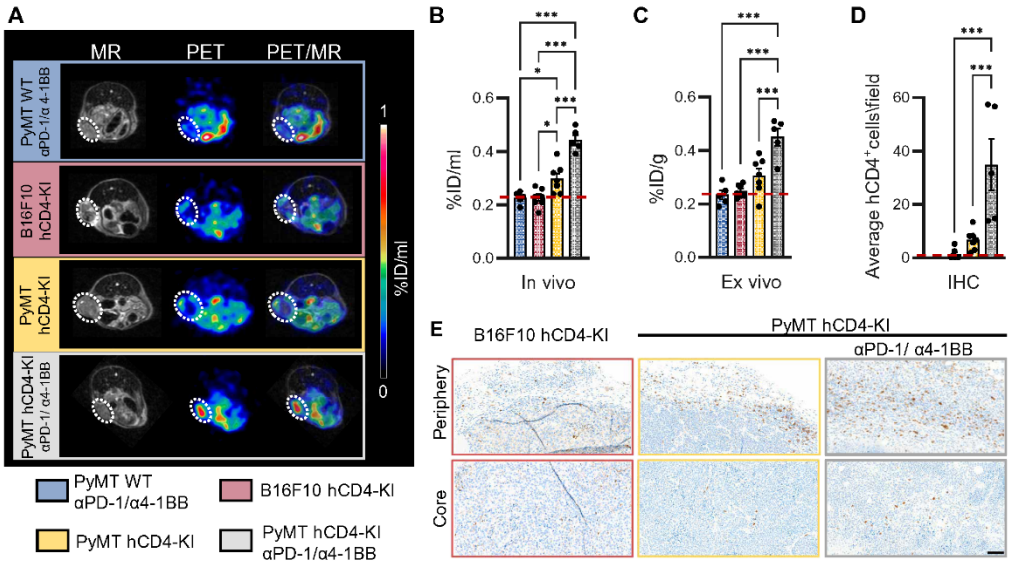

Fig. 2. ^{64}Cu-hCD4-Nb1 PET to quantify varying intratumoral CD4$^+$ cell densities. (**A**) Representative MR, PET, and coregistered PET/MR images 180 min after ^{64}Cu-hCD4-Nb1 injection of PyMT and B16F10 tumors, which were implanted in WT (no hCD4 antigen) or hCD4-KI mice. Two groups were treated with αPD-1/α4-1BB antibodies for 1 week to increase CD4$^+$ T cell infiltration. (**B**) Quantification of in vivo and (**C**) ex vivo ^{64}Cu-CD4-Nb1 uptake at 180 min post-tracer injection and (**D**) mean hCD4$^+$ cell/HPF ratio in the tumor center analyzed by IHC. Red horizontal lines represent background levels compared with those in the WT group. Pooled data from two independent experiments. n = 5 to 7 (two to four per experiment) per group, means ± SEM. (**E**) Representative hCD4 immunohistochemical images of the tumor core and periphery of PyMT and B16F10 tumors from hCD4-KI mice. Scale bar, 50 μm. Pairwise comparisons were performed with one-way ANOVA and corrected for multiple comparisons using the Holm-Sidak method (*P < 0.05; ***P < 0.001).

those observed in patients with cancer, we administered an ineffective dose αPD-1 treatment to MC38 colon adenocarcinoma-bearing hCD4-KI mice (*42*). Here, single αPD-1 ICI therapy resulted in a response rate of 42% (5 of 12 animals) (Fig. 5A). In a second group of animals, we applied ^{64}Cu-CD4-Nb1-PET imaging 5 days after onset of αPD-1 treatment for early assessment of potential therapy resistance (Fig. 5B). Here, 33% of mice (7 of 21 animals) showed an increased ^{64}Cu-CD4-Nb1 uptake in the tumor core (Fig. 5C). These mice were considered as potential responders and continued to receive αPD-1 monotherapy. Notably, all seven mice with continued αPD-1 monotherapy presented delayed tumor growth (Fig. 5D). Of these, five mice demonstrated a clear therapy response (Fig. 5D). In contrast, the animals that exhibited either enhanced tracer uptake patterns in the tumor periphery or no increased tracer uptake within the whole tumor at day 5 received α4-1BB monoclonal antibodies (mAbs) in addition to the αPD-1 antibodies from day 6 onward. This treatment was administered to overcome suspected CD4$^+$ cell–mediated treatment failure. Here, another 10 of the 14 mice receiving subsequent combined αPD-1/α4-1BB therapy exhibited regressing MC38 tumors (Fig. 5E). In conclusion, we were able to increase the response rates of MC38 tumor-bearing mice from 36% in the αPD-1 monotherapy group to 71% when early CD4-PET–guided therapy adaptation was applied.

Furthermore, in the second cohort of 13 animals, we conducted additional follow-up CD4-PET imaging 12 days after therapy initiation (6 days after α4-1BB treatment). Here, we observed a significant decrease in the tumor core/margin ratio between day 5 and day 12 within the αPD-1 monotherapy group and in one animal that did not respond to combined αPD-1/α4-1BB ICI (Fig. 5F). Most animals of the combined αPD-1/α4-1BB ICI group demonstrated a stable or increased tumor core/margin ratio at the later imaging time point, suggesting that α4-1BB therapy increased the influx of CD4$^+$ T cells into the TME (Fig. 5F).

Low intratumoral CD4$^+$ T cell densities are associated with early relapse after neoadjuvant αPD-L1 therapy in patients with NSCLC

Last, we aimed to determine the extent to which the differential distribution patterns of tumor-infiltrating CD4$^+$ cells could serve as predictors of therapy efficacy in a clinical setting. For this purpose, we analyzed the immune cell infiltration in 35 tumor biopsies (pretreatment) and subsequent whole tumor samples (on-treatment) from patients with NSCLC enrolled in two prospective clinical trials (NCT03853187 and NCT03514719) and treated with two cycles of αPD-L1 mAbs (durvalumab or avelumab) in a neoadjuvant setting (Fig. 6A). Because the multiplex immunofluorescence panel lacked CD4, CD3$^+$CD8$^-$ cells were classified as CD4$^+$ T cells after confirming that the densities of CD4$^-$CD8$^-$ cells were <10% of all T cells within the TME (fig. S4, B and C). As expected from the relatively low response rates in patients with NSCLC, CD4$^+$ T cells were significantly enriched in the tumor margin, whereas only a few patients presented increased CD4$^+$ T cell accumulation within the tumor core between baseline and after αPD-L1 treatment (Fig. 6B). On the basis of the on-treatment CD4$^+$ T cell densities at the tumor core and margin, we differentiated T cell–enriched (n = 9), T cell–excluded (n = 11), and T cell–deserted tumors (n = 15) (Fig. 6, C and D). Notably, five of the six patients who relapsed within 1 year after surgery were classified as having T cell–deserted tumors on-treatment, and all patients with NSCLC exhibited low CD4$^+$ T cell densities within the tumor core

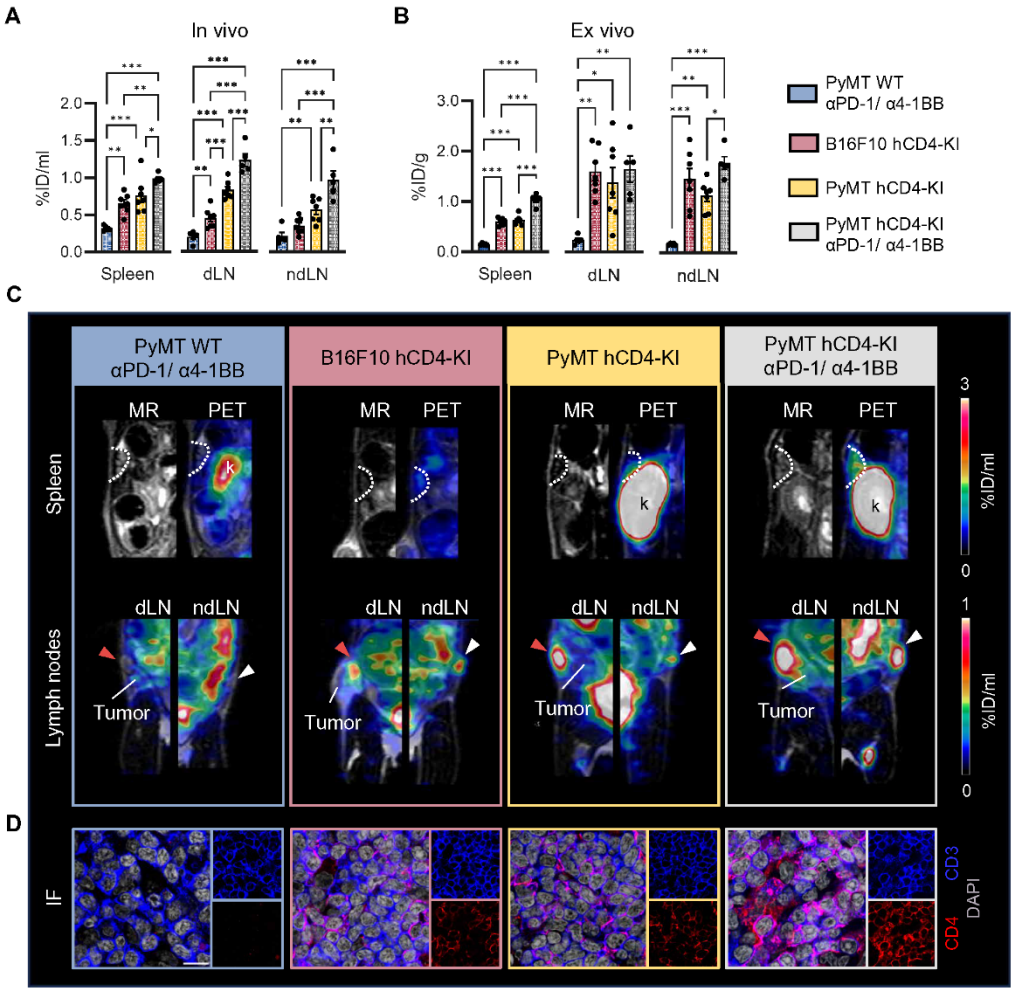

Fig. 3. Noninvasive visualization of lymphatic organs in mice treated with or without αPD-1/α4-1BB immunotherapy. (**A**) In vivo and (**B**) ex vivo quantification of the spleen, dLNs, and contralateral ndLNs of PyMT and B16F10 tumor-bearing hCD4-KI and WT mice acquired, with or without αPD-1/α4-1BB treatment, 180 min after ^{64}Cu-CD4-Nb1 injection. Pooled data from two independent experiments. $n = 5$ to 7 (two to four per experiment) per group, means ± SEM. Pairwise comparisons were performed with ordinary one-way ANOVA and corrected for multiple comparisons using the Holm-Sidak method (*$P < 0.05$; **$P < 0.01$; ***$P < 0.001$). (**C**) Representative MR and coregistered PET/MR images acquired 180 min post-tracer injection, with a focus on the lymphatic organs. Spleens are highlighted by white lines, dLNs are highlighted by red arrows, and ndLNs are highlighted by white arrows. (**D**) Immunofluorescence (IF) microscopy of the spleens of each group. Scale bar, 10 μm.

(Fig. 6E). Patients with NSCLC who experienced a later relapse (after >2 years) revealed an increased CD4$^+$ T cell density in both the tumor core (nonsignificant) and the tumor margin compared to patients with early relapse (<1 year) (Fig. 6F). In line with our preclinical data, we did not detect relevant changes in the fraction of FoxP3$^+$ T_{reg} cells between the relapse groups and the intratumoral location (Fig. 6F). These observations suggest that spatial CD4$^+$ T cell distribution is a clinically relevant biomarker for primary (low core CD4) and secondary (high margin CD4) resistance to αPD-(L)1 therapy. In contrast, the pathological response, which is based on the fraction of residual vital tumor cells upon treatment and considered as the gold standard for the evaluation of therapy responsiveness in neoadjuvant regimens, was not correlated with patient relapse (Fig. 6G).

DISCUSSION

Starting with the approval of the CTLA-4–targeting ICI ipilimumab for metastatic melanoma in 2011, the subsequent decade of immunotherapy has introduced several antibody-based, cell-based, and vaccine-based treatment options for patients with cancer, with many more options expected in the next 5 to 10 years (*43*). However, all these approaches suffer from limited response rates and a lack of reliable biomarkers to predict therapeutic efficacy (*44*). Tumor-derived parameters such as immunohistochemical assessed PD-(L)1 expression or tumor mutational burden (*45*–*48*) and blood-based biomarkers (*49*–*51*) have been identified as promising indicators for predicting therapeutic efficacy. However, even artificial intelligence–based multimodal integration of these different parameters has demonstrated very limited predictive value in larger patient cohorts (*52*, *53*).

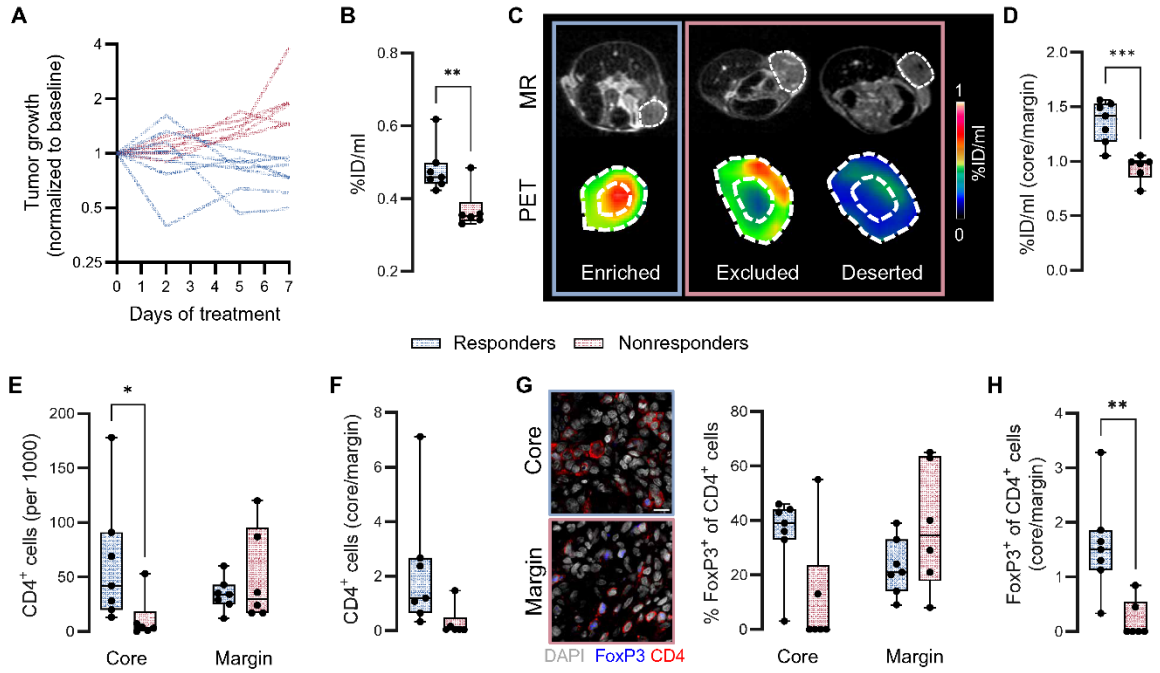

Fig. 4. Spatial distribution of intratumoral CD4$^+$ T cells determines the response to immunotherapy. (**A**) Tumor growth of PyMT hCD4-KI mice treated with αPD-1/α4-1BB antibodies (day 0 and day 3). Combined data from αPD-1/α4-1BB–treated animals of Fig. 2 ($n = 5$) and a second treatment cohort ($n = 8$). Seven mice were classified as responders (tumor volume d7/d0 < 1, blue), and six mice were classified as nonresponders (tumor volume d7/d0 > 1, red). (**B**) ^{64}Cu-CD4-Nb1 PET uptake 7 days after αPD-1/α4-1BB therapy initiation in responders and nonresponders. (**C**) Representative MR (axial slice) and PET images (axial slice, tumor only) acquired 180 min after ^{64}Cu-CD4-Nb1 injection. Tumors were classified as T cell–"enriched," T cell–"excluded," or T cell–"deserted" on the basis of the spatial distribution of ^{64}Cu-CD4-Nb1 PET uptake. The tumor core and tumor margin uptake values were differentiated by a centered 50% reduced ROI (white circles). (**D**) The intratumoral CD4$^+$ T cell distribution was quantified by the ratio of the tumor core and tumor margin ^{64}Cu-CD4-Nb1 PET uptake. (**E**) Ex vivo quantification of CD4$^+$ cells in the tumor core and the tumor margin by immunofluorescence. (**F**) Tumor core-to-margin ratios of CD4$^+$ T cells. (**G**) Representative immunofluorescence images and fractions of CD4$^+$FoxP3$^+$ T_{reg} cells within the tumor core and tumor margin (gray: DAPI; blue: FoxP3; red: CD4). Scale bar, 10 μm. (**H**) Tumor core-to-margin ratios of CD4$^+$FoxP3$^+$ T_{reg} cells. Pairwise comparisons were performed with Student's *t* test and corrected for multiple comparisons using the Holm-Sidak method (*$P < 0.05$; **$P < 0.01$; ***$P < 0.001$).

On the basis of the hypothesis that immune responses and resistance mechanisms become visible only after treatment has been initiated, we introduced a noninvasive imaging approach for the early monitoring of immunotherapy. In contrast to cancer cell–specific targets (such as PSMA, HER-2, and SSTR), immune cell imaging faces the challenge of limited target-expressing cell densities, necessitating tracers with exceptional sensitivity and spatial resolution to achieve accurate detection. Recently, Nbs have been introduced in the diagnostic field for their unique structural and functional properties, including high stability and binding affinity, and low molecular weight. In a previous study (*38*), we developed and extensively validated different CD4-targeting Nbs and selected our lead candidate, which exhibited the ability to quantitatively assess CD4$^+$ cells within the TME and lymphatic tissues. The advantageous biological properties of Nbs, as well as the high spatial resolution of ^{64}Cu (*54*, *55*), allowed us to differentiate clinically relevant variations in CD4$^+$ cell densities and even intratumoral distribution patterns of mouse tumors with diameters below 5 mm. Our hCD4-KI versus WT mouse comparisons demonstrated that specific uptake is not affected by varying levels of CD4 antigen in the system, which occurs in the context of chemotherapeutics or CD4$^+$-depleting therapies. This characteristic is unique compared with other published CD4-targeting PET tracers with human or murine specificity (*23*–*28*, *56*, *57*). Notably, fluorescence-based imaging approaches have been developed to track CD4$^+$ T helper and other immune cells with high sensitivity (*58*, *59*). However, the limited tissue penetration depth and the semiquantitative nature of the signals largely restrict the clinical use of optical imaging to certain endoscopic or cutaneous applications.

CD4$^+$ cells comprise a diverse group of T helper cells, T_{reg} cells, and T effector cells, and as such, their role as predictive biomarkers remains a topic of ongoing and controversial debate (*1*, *2*, *32*–*36*, *60*–*64*). Moreover, the CD4 antigen is also expressed to a lesser extent on other immune cells, including subsets of natural killer cells, monocytes, and macrophages (*65*). In contrast to inducible immune cell targets (*66*, *67*), CD4 expression exhibits only minor variations following antigenic activation (*68*), virus infection (*69*) or epigenetic regulation during thymic differentiation (*70*), thereby enabling accurate quantification of CD4$^+$ cells by PET.

Through ^{64}Cu-CD4-Nb1 PET imaging, we could spatially localize CD4$^+$ cells within the TME of both immunologically "cold" B16F10 melanomas and "hot" PyMT breast tumors, discerning minimal variations in CD4$^+$ cell densities in the TME (*23*, *71*). Notably, we observed different CD4$^+$ cell infiltration patterns in PyMT tumors with ineffectively αPD1/α4-1BB–treated animals showing infiltration predominantly at the tumor periphery, whereas effectively treated animals exhibited increased infiltration within the tumor core.

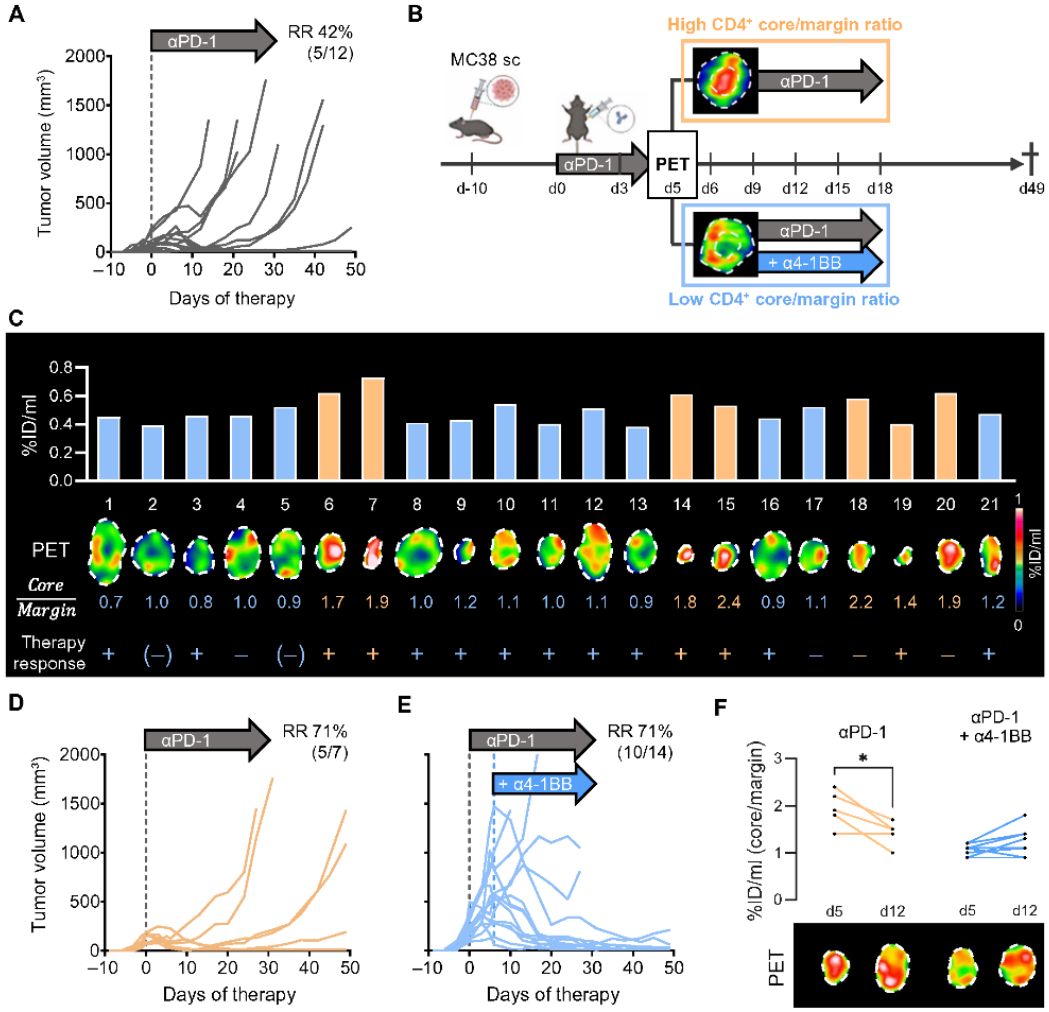

Fig. 5. PET-guided therapy adaptation in MC38 tumor-bearing animals. (**A**) Tumor growth of αPD-1–treated mice and the related response rate (RR). MC38 tumor cells were subcutaneously (sc) implanted into C57BL/6 hCD4-KI mice 10 days before the initiation of αPD-1 mAb therapy. Antibodies were applied every 3 days for a total of seven injections. n = 11, data from one experiment. (**B**) Schematic illustration of the treatment adaptation based on the ^{64}Cu-CD4-Nb1 PET uptake 5 days post–αPD-1 therapy initiation. Additional α4-1BB mAbs were applied starting on day 6. (**C**) ^{64}Cu-CD4-Nb1 PET uptake, PET image of the tumor, calculated tumor core-to-margin ratio, and therapy response per individual mouse. Animals with an increased tumor core-to-margin ratio (>1.3) continued αPD-1 therapy (orange). αPD-1 therapy was combined with α4-1BB mAbs when the core-to-margin ratio was less than <1.3 (blue). n = 21, combined data from two independent experiments (n = 8 to 13 per experiment). (**D**) Tumor growth and related response rates of αPD-1–treated mice. (**E**) Tumor growth and related response rates of αPD-1 and subsequently added α4-1BB treatment group. (**F**) ^{64}Cu-CD4-Nb1 PET core-to-margin ratio and representative PET images 5 and 12 days post-therapy initiation of mice administered either with αPD-1 monotherapy or the sequential combination of αPD-1/α4-1BB therapy. n = 13, data from one experiment. Pairwise comparisons were performed with Student's t test and corrected for multiple comparisons using the Holm-Sidak method (*P < 0.05).

Consistent with our findings of increased CD4-derived PET uptake in lymph nodes and spleens, Kim *et al.* similarly observed the accumulation of CD4$^+$ and CD8$^+$ cells in αPD-1/α4-1BB–treated C57BL/6 mice. The authors further reported pronounced lymph node swelling and interferon-γ–driven macrophage recruitment following repeated α4-1BB administration, which they associated with impaired CD8$^+$ T cell function and the development of adverse events (*72*).

T_{reg} cells have been reported to form physical, metabolic, and trafficking barriers that limit the entry of effector T cells into the tumor core (*73*). Thus, we hypothesized that the CD4-derived tracer signal from tumor margins in nonresponding animals were due to increased accumulation of T_{reg} cells, which suppress the therapeutic response and immune cell infiltration into the tumor. Ex vivo immunofluorescence of mouse and NSCLC patient samples confirmed the correlating accumulation of both CD4$^+$ helper cells and T_{reg} cells in the tumor periphery and in the tumor core, suggesting that immune effector function induces regulatory immune responses irrespective of therapy response or resistance.

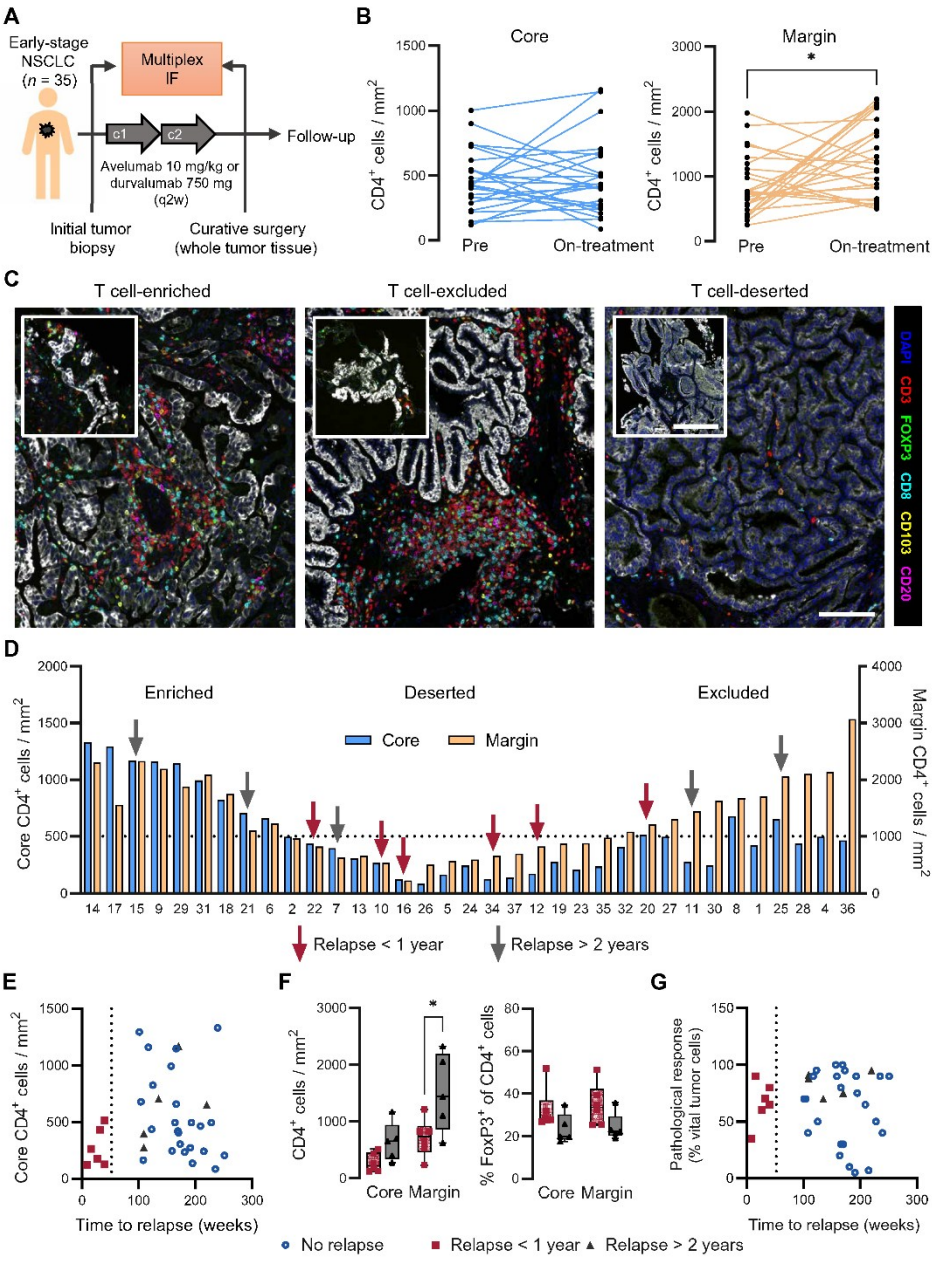

Fig. 6. Ex vivo multiplex immunofluorescence of whole tumor samples from patients with NSCLC treated with neoadjuvant PD-L1 ICI. (**A**) Schematic illustration of the clinical study. (**B**) Quantification of $CD3^+CD8^-$ T cell densities (considered as $CD4^+$ T cells) within the tumor core (left) and tumor margin (right) from pretreatment and on-treatment tissue. $n = 35$, combined data from two independent clinical studies. (**C**) Multiplex immunofluorescence microscopy images of the indicated seven-marker antibody panel. Tumor biopsy samples before treatment (upper left image) and corresponding posttreatment whole tumor samples from three representative cases are displayed. Scale bars, 100 μm. (**D**) Classification of T cell–enriched, T cell–deserted, and T cell–excluded tumors on-treatment on the basis of the CD4 core and margin quantification. Red arrows indicate that patients relapsed within 1 year after surgery ($n = 6$). Gray arrows indicate that patients relapsed after more than 2 years after surgery ($n = 5$). (**E**) Correlation between the time to relapse after surgery and the number of $CD4^+$ cells within the core of the resected tumors. (**F**) Tumor core and margin densities of $CD4^+$ cells (left) and $FoxP3^+$ T_{reg} fraction of $CD4^+$ cells (right) of patients relapsed within 1 year and >2 years after surgery. (**G**) Correlation of time to relapse after surgery and pathological response based on the fraction of vital cells. Pairwise comparisons were performed with Student's *t* test and corrected for multiple comparisons using the Holm-Sidak method (*$P < 0.05$).

To substantiate the value of CD4-directed PET imaging as a decision-making approach, we applied additional α4-1BB mAbs, which have been shown to deplete T_{reg} cells (*74*), to standard-of-care αPD-1–treated MC38 tumor-bearing animals, which presented increased ^{64}Cu-CD4-Nb1 PET tracer uptake in the tumor periphery. Most animals were correctly selected for therapy response, and combined treatment was successful even in mice with larger tumors. In tumor samples from patients with NSCLC treated with ICIs, high $CD4^+$ cell densities in the tumor cores correlated with favorable clinical outcomes, highlighting the clinical utility of our noninvasive PET imaging approach.

With respect to clinical application, ^{64}Cu is a valuable radionuclide, combining preferable decay characteristics (radiation exposure) compared to frequently used long-living isotopes such as ^{89}Zr, with the advantages of centralized tracer production and continent-wide overnight shipping capabilities (*54*, *55*). Nevertheless, combining Nb technology with fluorine-18 (^{18}F) labeling, which has recently been established for Nbs (*75*, *76*), could pave the way for multiparametric imaging approaches allowing noninvasive 1-day visualization and localization of multiple immune cell populations, thereby providing a comprehensive assessment of a patient's immune status without relying on invasive techniques such as biopsy (*23*, *28*, *77*).

Various metabolic factors such as hypoxia (*78*), immunological components including suppressive immune cells, cytokines, and MHC-II expression (*79*), as well as tumor-intrinsic drivers such as oncogenic mutations (e.g., *KRAS*, *TP53*, and *BRAF*) and aberrant signaling pathways (*80*), collectively influence the infiltration of $CD4^+$ T cells. To better understand the underlying mechanisms of our findings, it will be crucial to colocalize the PET-based macroscopic distribution patterns of $CD4^+$ T cells with spatial transcriptomics and immunogenomics.

In conclusion, analysis of CD4-directed PET tracer uptake patterns allowed us to identify distinct immune features within the TME that are associated with sensitivity to ICIs and have the potential to guide the development and optimization of combinatorial immunotherapy strategies. Moreover, the spatially resolved ^{64}Cu-CD4-Nb1-PET data of the TME enables us to forecast treatment resistance, which was further validated through immunofluorescence analysis in both mouse and human NSCLC tumor tissues. Thus, Nb-based PET imaging of $CD4^+$ cells provides mechanistic insights into the therapeutic actions of immunotherapies and underlying resistance mechanisms, extending beyond the mere monitoring of therapeutic responses. This approach holds great potential for guiding combinatorial immunotherapy strategies in patients with cancer.

MATERIALS AND METHODS

Nb production

CD4-Nb1 and GFP-Nb were either produced and labeled as previously described (*38*), or adapted versions that allow for site-directed chemical conjugation (*81*) were produced using the ExpiCHO Expression System according to the manufacturer's protocols (Thermo Fisher Scientific, Germany). The latter Nbs were isolated from the cell-free culture supernatant by a combination of protein affinity chromatography, anion exchange chromatography, and cation exchange chromatography. Nbs were reacted with *p*-NCS-benzyl-NODA-GA (Chematech, France) to produce Nb-NODAGA conjugates. The integrity and high purity of the Nbs and Nb-NODAGA conjugates were confirmed via liquid chromatography–mass spectrometry (LC-MS) and SDS–polyacrylamide gel electrophoresis. The comparability of the Nb-NODAGA conjugates from the two production systems was confirmed by highly similar target-binding affinities using biolayer interferometry (Octet RED96e system, Sartorius).

Radiolabeling

[^{64}Cu] $CuCl_2$ [150 megabecquerel (MBq) in 0.1 M HCl] was neutralized by addition of 1.5 volumes of 0.5 M ammonium acetate solution (pH 6), resulting in a pH of 5.5. To this solution, 50 μg of the conjugate was added and incubated at 42°C for 60 min. Then, 1 μl of 20% diethylenetriamine pentaacetic acid solution was added to quench the labeling reaction. Complete incorporation of the radioisotope was confirmed after each radiosynthesis by thin layer chromatography [iTLC-SA; Agilent Technologies; mobile phase: 0.1 M citric acid (pH 5)] and high-performance size exclusion chromatography [HPSEC; BioSep SEC-s2000, 300 mm by 7.8 mm, Phenomenex; mobile phase: Dulbecco's Balanced Salt Solution (DPBS) with 0.5 mM EDTA]. All radiolabeled preparations used for in vivo PET imaging had radiochemical purities of ≥90% (iTLC and HPSEC).

Bead assay

A total of 20 μl of Ni-NTA beads (nickel–nitrilotriacetic acid; HisPur Ni-NTA magnetic beads; Thermo Fisher Scientific) was washed with 380 μl of phosphate-buffered saline (PBS) containing 0.05% Tween 20 (PBS-T), vortexed for 5 s, and placed on a magnetic rack (12321D; DynaMag-2; Thermo Fisher Scientific) for 30 to 45 s to isolate the magnetic beads. The His-tagged hCD4 antigen (Thermo Fisher Scientific) was resuspended as per the manufacturer's instructions to achieve a concentration of 0.1 mg/ml. The washed beads were resuspended in 190 μl of PBS-T, incubated with 1 μg of His-tagged hCD4 antigen for 15 min on a rotating mixer at room temperature (RT), and then washed with PBS-T. A large excess (1 μg) of the unlabeled ligand was added to the antigen-coated beads in the blocking arm and incubated for 15 min on a rotating mixer at RT. Afterward, 1 ng of ^{64}Cu-CD4-Nb1 was incubated with antigen-coated beads for 30 min on a rotating mixer at RT. The beads were isolated using a magnet, and half of the supernatant (SN) was transferred to a γ-counter tube. The solutions of beads + SN (BS) and SN only (S) were measured by γ-counting (Wallac 1480 WIZARD 3" Gamma Counter; PerkinElmer, Waltham, MA, USA), and the immunoreactive fraction was calculated as (BS − S)/(BS + S).

Tumor cells

$hCD4^-$ diffuse histiocytic lymphoma (DHL) cell lines were purchased from the German Collection of Microorganisms and Cell Cultures (DSMZ, Braunschweig, Germany) and cultured in RPMI 1640 medium supplemented with 10% fetal calf serum (FCS) and 1% penicillin/streptomycin (P/S). The B16F10 murine melanoma cell line was purchased from the American Type Culture Collection (ATCC) and cultured in Dulbecco's modified Eagle's medium (DMEM) supplemented with 10% FCS and 1% P/S. The S2WTP3 (PyMT) triple-negative breast cancer cell line was kindly provided by A. Moeller (Queensland University, Australia) and cultured in DMEM supplemented with 10% FCS, 1% P/S, and 1% pyruvate (Sigma-Aldrich). The MC38 murine colon adenocarcinoma cell line was purchased from Kerafast and cultured in DMEM supplemented with 10% FCS, 1% P/S, and 1% Hepes.

In vitro binding assays

The binding of ^{64}Cu-CD4-Nb1 or ^{64}Cu-GBP-Nb to freshly isolated hCD4$^+$ T cells and hCD4$^-$ SU-DHL-4 cells was assessed in vitro. A total of 1×10^6 cells was incubated with 2 ng of ^{64}Cu-CD4-Nb1 or ^{64}Cu-GBP-Nb for 90 min at 37°C on a shaker. The cells were washed twice with PBS/1% FCS and resuspended in 200 µl. The radioactivity was measured by γ-counting.

Animals

All experiments were performed according to the animal use and care protocols (R 04/22 G, R 08/21 G) of the German Animal Protection Law and were approved by the local authorities (Regierungspräsidium Tübingen). Eight- to 16-week-old WT C57BL/6J (Charles River Laboratories) and hCD4-KI (C57BL/6J-*Cd4*$^{tm1.1(CD4)Geno}$, Genoway, in-house breeding) mice were bred under specific pathogen–free conditions with free access to food and water ad libitum.

Tumor models

A total of 0.12×10^6 B16F10 tumor cells was implanted by intradermal injection into hCD4-KI mice in PBS. A total of 0.5×10^6 to 0.6×10^6 PyMT mammary tumor cells were orthotopically injected into the fourth mammary fat pad in PBS into C57BL/6J or hCD4-KI mice. WT or hCD4-KI mice with PyMT tumors were injected intraperitoneally with 200 µg of αPD-1 (clone: RMP1-14; Bioxcell) and 50 µg of α4-1BB (clone: 3H3; Bioxcell) mAbs 7 days prior to in vivo imaging. hCD4-KI mice with MC38 tumors were injected intraperitoneally with 100 µg of αPD-1 mAbs every 3 days for a total of seven injections. Animals with low tumor core PET tracer uptake on day 5 received five additional α4-1BB antibodies (50 µg) beginning on day 6 in combination with the αPD-1 mAbs.

PET/MR imaging

For noninvasive in vivo imaging, 5 µg (~2 MBq/µg) ^{64}Cu-CD4-Nb1 or ^{64}Cu-GFP-Nb was administered intravenously via the tail vein of experimental mice. PET and magnetic resonance (MR) scans were acquired at 5 and 90 min and 3 and 6 hours post-tracer injection (longitudinal scans) or only at the 3-hour post-tracer injection time point. Anatomic images were acquired by MR on a dedicated 7T small animal MR tomograph (ClinScan; Bruker BioSpin, Ettlingen, Germany). A T2-weighted image three-dimensional space sequence [repetition time (TR): 1800 ms, echo time (TE): 4.7 ms, field of view (FoV): 76.8 mm by 34.8 mm by 22.8 × mm, matrix: 256 × 116 × 76] was acquired in ~9 min. The animals were kept under 1.5% isoflurane (100% oxygen) anesthesia, and the breathing frequency was monitored with a control unit (SA Instruments, Stony Brook, NY, USA). Static PET images (600 s) were acquired with dedicated Inveon small animal PET scanners (Siemens Preclinical Solutions, Knoxville, TN, USA).

Image analysis

PET images from list mode were reconstructed using three-dimensional ordered subset expectation maximization (OSEM-3D) and coregistered to the anatomical T2 MR images using Inveon Research Workplace (Siemens Preclinical Solutions). The volumes of interest (VOIs) of the organs of interest were created based on the anatomical MR images. The uptake values of the respective organs were calculated from the mean Bq/ml, corrected for radioactive decay and normalized to the injected activity, and presented as percentage injected dose per milliliter (%ID/ml).

Spatial distribution analyses were performed by defining tumor margin and tumor core ROIs as 50% of the tumor diameter in a centered cross section of the PET-acquired image using open-source ImageJ software. PET signal intensity was quantified as the mean intensity of the tumor margin and core.

Ex vivo biodistribution

The experimental mice were euthanized by cervical dislocation under deep anesthesia after the final imaging time point. Organs were harvested, and radioactivity was measured by γ-counting. For quantification, standardized aliquots of the injected tracer were added to the measurement. The values for each organ are expressed as the percentage of the overall injected dose per gram (%ID/g), corrected for radioactive decay and normalized to the injected activity.

Immunohistochemistry of PyMT tumors

After the organs were γ-counted, the tumors, spleens, and draining and contralateral nondraining lymph nodes were fixed in formalin and embedded in paraffin. For histology, 3- to 5-µm-thick sections from paraffin-embedded tissues were cut and stained with hematoxylin and eosin (H&E). Immunohistochemistry (IHC) was performed on an automated immunostainer (Ventana Medical Systems Inc.) according to the manufacturer's protocols for open procedures, with slight modifications. All the slides were stained with antibodies against anti-human CD4 (SP35, Zytomed). Appropriate positive and negative controls were used to confirm the adequacy of the staining. All the samples were scanned with a Ventana DP200 (Roche, Basel, Switzerland) and processed with the Image Viewer MFC application. The final image preparation was performed with Adobe Photoshop CS6. The number of CD4$^+$ T cells was counted in at least 10 high-power fields (HPFs). The data are presented as the number of CD4$^+$ T cells per field.

Immunofluorescence microscopy of PyMT tumors and spleens

Fresh-frozen 5-µm cryosections fixed with iodate-lysine-paraformaldehyde or sections from paraffin-embedded tissues were blocked with donkey serum and incubated with rabbit anti-FoxP3 (polyclonal, Novus Biologicals, USA) or rabbit anti-CD3 (DCM-39, DCS, Germany) and goat anti-CD4 (polyclonal, R&D Systems, USA). Bound mAbs were visualized with Alexa Fluor 647–Donkey anti-rabbit-F(ab′)2 (H+L, Dianova, USA) and Cy3-Donkey anti-goat-F(ab′)2 (H+L, Dianova). For nuclear staining, we used 4′,6-diamidino-2-phenylindole (DAPI) (Sigma-Aldrich). Immunofluorescence images were acquired with an LSM 800 confocal laser scanning microscope (Carl Zeiss) and processed with ZEN Blue software, version 2.6. The analysis of cell nuclei was performed using Zeiss Zen software, whereas the number of CD4$^+$, FoxP3$^+$, and CD4$^+$FoxP3$^+$ cells was counted manually. For each section, the sum of a minimum of six different areas—three intratumoral and three marginal—was normalized to the automated counted cell number based on the DAPI-derived nuclei.

Multiplex immunofluorescence of human lung cancer samples

Baseline biopsy and on-treatment resected tumor samples from patients with early-stage NSCLC enrolled in either of two prospective clinical trials, NCT03514719 or NCT03853187, were subjected to multiplex immunofluorescence. In these trials, patients received two

courses of neoadjuvant αPD-L1 antibodies (10 mg/kg avelumab) or 750 mg durvalumab at a 2-week interval, followed by surgical resection. A formalin-fixed, paraffin-embedded material was cut into 4-μm-thick sections and mounted on Superfrost PLUS slides (AR9222, Leica Biosystems). Automated mIHC staining using the Opal 7-Color Automation IHC Kit, Opal480, and Opal780 (NEL821001KT, FP1500001KT, and FP1501001KT, Akoya Biosciences) was performed on the Leica Bond system (BOND-Rx Fully Automated IHC and ISH, Leica Biosystems), as described previously (*82*–*84*). This staining identified $CD8^+$ T cells ($CD3^+CD8^+$), $CD4^+$ T cells ($CD3^+CD8^-$), T_{reg} cells ($CD3^+FoxP3^+$), tissue-resident T cells ($CD3^+CD103^+CD8^{+/-}$), and B cells ($CD20^+$) (*83*). To quantify lymphocytes in different tumor regions, pretreatment biopsy and posttreatment resection materials were segmented into tumor cores and invasive margins via Qupath software (*84*, *85*). These regions were confirmed by a certified pathologist. The invasive margin was defined as the portion of the TME where tumor cells interface with the surrounding tissue, and the maximum distance of the invasive margin was set at 100 μm surrounding the tumor core (*84*).

Statistical analysis

All the data were analyzed using GraphPad Prism, version 9 or later (GraphPad Software Inc., San Diego, CA, USA). The values are expressed as the arithmetic means ± SD for single experiments or as the arithmetic means ± SEM for combined experiments. For statistical analyses, unpaired/paired *t* tests were applied for pairwise comparisons. Ordinary one-way analysis of variance (ANOVA) or two-way ANOVA was used for multiple group comparisons and was corrected for multiple comparisons using the Sidak post hoc test. Adjusted *P* values less than 0.05 were considered significant, and significance levels are indicated as follows: $*P \leq 0.05$, $**P \leq 0.01$, and $***P \leq 0.001$.

Supplementary Materials

This PDF file includes:

Figs. S1 to S4

REFERENCES AND NOTES

1. R. Duhen, O. Fesneau, K. A. Samson, A. K. Frye, M. Beymer, V. Rajamanickam, D. Ross, E. Tran, B. Bernard, A. D. Weinberg, T. Duhen, PD-1 and ICOS coexpression identifies tumor-reactive $CD4^+$ T cells in human solid tumors. *J. Clin. Invest.* **132**, e156821 (2022).
2. R. E. Tay, E. K. Richardson, H. C. Toh, Revisiting the role of $CD4^+$ T cells in cancer immunotherapy-new insights into old paradigms. *Cancer Gene Ther.* **28**, 5–17 (2021).
3. D. E. Speiser, O. Chijioke, K. Schaeuble, C. Münz, $CD4^+$ T cells in cancer. *Nat. Cancer* **4**, 317–329 (2023).
4. D. Y. Oh, L. Fong, Cytotoxic $CD4^+$ T cells in cancer: Expanding the immune effector toolbox. *Immunity* **54**, 2701–2711 (2021).
5. X. Yang, J. Wu, L. Fan, B. Chen, S. Zhang, W. Zheng, Single-cell analysis identifies distinct populations of cytotoxic $CD4^+$ T cells linked to the therapeutic efficacy of immune checkpoint inhibitors in metastatic renal cell carcinoma. *J. Inflamm. Res* **17**, 4505–4523 (2024).
6. M. Cenerenti, M. Saillard, P. Romero, C. Jandus, The era of cytotoxic CD4 T cells. *Front. Immunol.* **13**, 867189 (2022).
7. J. M. Pitt, A. Marabelle, A. Eggermont, J. C. Soria, G. Kroemer, L. Zitvogel, Targeting the tumor microenvironment: Removing obstruction to anticancer immune responses and immunotherapy. *Ann. Oncol.* **27**, 1482–1492 (2016).
8. M. van Gulijk, A. van Krimpen, S. Schetters, M. Eterman, M. van Elsas, J. Mankor, L. Klaase, M. de Bruijn, M. van Nimwegen, T. van Tienhoven, W. van Ijcken, L. Boon, J. van der Schoot, M. Verdoes, F. Scheeren, S. H. van der Burg, B. N. Lambrecht, R. Stadhouders, F. Dammeijer, J. Aerts, T. van Hall, PD-L1 checkpoint blockade promotes regulatory T cell activity that underlies therapy resistance. *Sci. Immunol.* **8**, eabn6173 (2023).
9. A. Abaza, F. Sid Idris, H. A. Shaikh, I. Vahora, K. P. Moparthi, M. T. Al Rushaidi, M. R. Muddam, O. A. Obajeun, A. P. Jaramillo, S. Khan, Programmed cell death protein 1 (PD-1) and programmed cell death ligand 1 (PD-L1) immunotherapy: A promising breakthrough in cancer therapeutics. *Cureus* **15**, e44582 (2023).
10. A. Parvez, F. Choudhary, P. Mudgal, R. Khan, K. A. Qureshi, H. Farooqi, A. Aspatwar, PD-1 and PD-L1: Architects of immune symphony and immunotherapy breakthroughs in cancer treatment. *Front. Immunol.* **14**, 1296341 (2023).
11. J. R. Brahmer, S. S. Tykodi, L. Q. Chow, W. J. Hwu, S. L. Topalian, P. Hwu, C. G. Drake, L. H. Camacho, J. Kauh, K. Odunsi, H. C. Pitot, O. Hamid, S. Bhatia, R. Martins, K. Eaton, S. Chen, T. M. Salay, S. Alaparthy, J. F. Grosso, A. J. Korman, S. M. Parker, S. Agrawal, S. M. Goldberg, D. M. Pardoll, A. Gupta, J. M. Wigginton, Safety and activity of anti-PD-L1 antibody in patients with advanced cancer. *N. Engl. J. Med.* **366**, 2455–2465 (2012).
12. A. Naimi, R. N. Mohammed, A. Raji, S. Chupradit, A. V. Yumashev, W. Suksatan, M. N. Shalaby, L. Thangavelu, S. Kamrava, N. Shomali, A. D. Sohrabi, A. Adili, A. Noroozi-Aghideh, E. Razeghian, Tumor immunotherapies by immune checkpoint inhibitors (ICIs); the pros and cons. *Cell Commun. Signal* **20**, 44 (2022).
13. N. Chhabra, J. Kennedy, A review of cancer immunotherapy toxicity: Immune checkpoint inhibitors. *J. Med. Toxicol.* **17**, 411–424 (2021).
14. D. B. Johnson, C. A. Nebhan, J. J. Moslehi, J. M. Balko, Immune-checkpoint inhibitors: Long-term implications of toxicity. *Nat. Rev. Clin. Oncol.* **19**, 254–267 (2022).
15. J. D. Wolchok, V. Chiarion-Sileni, R. Gonzalez, P. Rutkowski, J. J. Grob, C. L. Cowey, C. D. Lao, J. Wagstaff, D. Schadendorf, P. F. Ferrucci, M. Smylie, R. Dummer, A. Hill, D. Hogg, J. Haanen, M. S. Carlino, O. Bechter, M. Maio, I. Marquez-Rodas, M. Guidoboni, G. McArthur, C. Lebbé, P. A. Ascierto, G. V. Long, J. Cebon, J. Sosman, M. A. Postow, M. K. Callahan, D. Walker, L. Rollin, R. Bhore, F. S. Hodi, J. Larkin, Overall survival with combined nivolumab and ipilimumab in advanced melanoma. *N. Engl. J. Med.* **377**, 1345–1356 (2017).
16. Y. Lu, X. Zhang, J. Ning, M. Zhang, Immune checkpoint inhibitors as first-line therapy for non-small cell lung cancer: A systematic evaluation and meta-analysis. *Hum. Vaccin. Immunother.* **19**, 2169531 (2023).
17. Y. Shiravand, F. Khodadadi, S. M. A. Kashani, S. R. Hosseini-Fard, S. Hosseini, H. Sadeghirad, R. Ladwa, K. O'Byrne, A. Kulasinghe, Immune checkpoint inhibitors in cancer therapy. *Curr. Oncol.* **29**, 3044–3060 (2022).
18. K. E. Pauken, M. Dougan, N. R. Rose, A. H. Lichtman, A. H. Sharpe, Adverse events following cancer immunotherapy: Obstacles and opportunities. *Trends Immunol.* **40**, 511–523 (2019).
19. J. R. Richardson, A. Schöllhorn, C. Gouttefangeas, J. Schuhmacher, $CD4^+$ T cells: Multitasking cells in the duty of cancer immunotherapy. *Cancers (Basel)* **13**, 596 (2021).
20. M. Saillard, M. Cenerenti, P. Romero, C. Jandus, Impact of immunotherapy on CD4 T cell phenotypes and function in cancer. *Vaccines (Basel)* **9**, 454 (2021).
21. L. C. Villaruz, G. R. Blumenschein Jr., G. A. Otterson, T. A. Leal, Emerging therapeutic strategies for enhancing sensitivity and countering resistance to programmed cell death protein 1 or programmed death-ligand 1 inhibitors in non–small cell lung cancer. *Cancer* **129**, 1319–1350 (2023).
22. J. Schwenck, D. Sonanini, J. M. Cotton, H. G. Rammensee, C. la Fougère, L. Zender, B. J. Pichler, Advances in PET imaging of cancer. *Nat. Rev. Cancer* **23**, 474–490 (2023).
23. L. K. Kristensen, C. Fröhlich, C. Christensen, M. C. Melander, T. T. Poulsen, G. R. Galler, J. Lantto, I. D. Horak, M. Kragh, C. H. Nielsen, A. Kjaer, $CD4^+$ and $CD8a^+$ PET imaging predicts response to novel PD-1 checkpoint inhibitor: Studies of Sym021 in syngeneic mouse cancer models. *Theranostics* **9**, 8221–8238 (2019).
24. A. S. Clausen, C. Christensen, E. Christensen, S. Cold, L. K. Kristensen, A. E. Hansen, A. Kjaer, Development of a 64Cu-labeled $CD4^+$ T cell targeting PET tracer: Evaluation of CD4 specificity and its potential use in collagen-induced arthritis. *EJNMMI Res.* **12**, 62 (2022).
25. A. C. Freise, K. A. Zettlitz, F. B. Salazar, X. Lu, R. Tavaré, A. M. Wu, ImmunoPET imaging of murine $CD4^+$ T cells using anti-CD4 cys-diabody: Effects of protein dose on T cell function and imaging. *Mol. Imaging Biol.* **19**, 599–609 (2017).
26. A. C. Freise, K. A. Zettlitz, F. B. Salazar, R. Tavaré, W.-T. K. Tsai, A. F. Chatziioannou, N. Rozengurt, J. Braun, A. M. Wu, Immuno-PET in inflammatory bowel disease: Imaging CD4-positive T cells in a murine model of colitis. *J. Nucl. Med.* **59**, 980–985 (2018).
27. R. Tavaré, M. N. McCracken, K. A. Zettlitz, F. B. Salazar, T. Olafsen, O. N. Witte, A. M. Wu, Immuno-PET of murine T cell reconstitution postadoptive stem cell transplantation using anti-CD4 and anti-CD8 cys-diabodies. *J. Nucl. Med.* **56**, 1258–1264 (2015).
28. V. L. Nagle, C. A. J. Hertz, K. E. Henry, M. S. Graham, C. Campos, N. Pillarsetty, A. Schietinger, I. K. Mellinghoff, J. S. Lewis, Noninvasive imaging of $CD4^+$ T cells in humanized mice. *Mol. Cancer Ther.* **21**, 658–666 (2022).
29. M. Di Mascio, C. H. Paik, J. A. Carrasquillo, J. S. Maeng, B. S. Jang, I. S. Shin, S. Srinivasula, R. Byrum, A. Neria, W. Kopp, M. Catalfamo, Y. Nishimura, K. Reimann, M. Martin, H. C. Lane, Noninvasive in vivo imaging of CD4 cells in simian-human immunodeficiency virus (SHIV)-infected nonhuman primates. *Blood* **114**, 328–337 (2009).
30. S. Pezzana, S. Blaess, J. Kortendieck, N. Hemmer, B. Tako, C. Pietura, L. Ruoff, S. Riel, M. Schaller, I. Gonzalez-Menendez, L. Quintanilla-Martinez, A. Mascioni, A. Aivazian, I. Wilson, A. Maurer, B. J. Pichler, M. Kneilling, D. Sonanini, In-depth cross-validation of human and mouse CD4-specific minibodies for noninvasive PET imaging of $CD4^+$ cells and response prediction to cancer immunotherapy. *Theranostics* **14**, 4582–4597 (2024).

31. C. I. Liakou, A. Kamat, D. N. Tang, H. Chen, J. Sun, P. Troncoso, C. Logothetis, P. Sharma, CTLA-4 blockade increases IFNγ-producing $CD4^+ICOS^{hi}$ cells to shift the ratio of effector to regulatory T cells in cancer patients. *Proc. Natl. Acad. Sci. U.S.A.* **105**, 14987–14992 (2008).
32. S. C. Wei, J. H. Levine, A. P. Cogdill, Y. Zhao, N.-A. A. Anang, M. C. Andrews, P. Sharma, J. Wang, J. A. Wargo, D. Pe'er, Distinct cellular mechanisms underlie anti-CTLA-4 and anti-PD-1 checkpoint blockade. *Cell* **170**, 1120–1133.e17 (2017).
33. S. Jiao, S. K. Subudhi, A. Aparicio, Z. Ge, B. Guan, Y. Miura, P. Sharma, Differences in tumor microenvironment dictate T helper lineage polarization and response to immune checkpoint therapy. *Cell* **179**, 1177–1190.e13 (2019).
34. J. Monkman, A. Moradi, J. Yunis, G. Ivison, A. Mayer, R. Ladwa, K. O'Byrne, A. Kulasinghe, Spatial insights into immunotherapy response in non-small cell lung cancer (NSCLC) by multiplexed tissue imaging. *J. Transl. Med.* **22**, 239 (2024).
35. V. Aggarwal, C. J. Workman, D. A. A. Vignali, LAG-3 as the third checkpoint inhibitor. *Nat. Immunol.* **24**, 1415–1422 (2023).
36. D. Phillips, M. Matusiak, B. R. Gutierrez, S. S. Bhate, G. L. Barlow, S. Jiang, J. Demeter, K. S. Smythe, R. H. Pierce, S. P. Fling, N. Ramchurren, M. A. Cheever, Y. Goltsev, R. B. West, M. S. Khodadoust, Y. H. Kim, C. M. Schürch, G. P. Nolan, Immune cell topography predicts response to PD-1 blockade in cutaneous T cell lymphoma. *Nat. Commun.* **12**, 6726 (2021).
37. G. Espinosa-Carrasco, E. Chiu, A. Scrivo, P. Zumbo, A. Dave, D. Betel, S. W. Kang, H. J. Jang, M. D. Hellmann, B. M. Burt, H. S. Lee, A. Schietinger, Intratumoral immune triads are required for immunotherapy-mediated elimination of solid tumors. *Cancer Cell* **42**, 1202–1216.e8 (2024).
38. B. Traenkle, P. D. Kaiser, S. Pezzana, J. Richardson, M. Gramlich, T. R. Wagner, D. Seyfried, M. Weldle, S. Holz, Y. Parfyonova, S. Nueske, A. M. Scholz, A. Zeck, M. Jakobi, N. Schneiderhan-Marra, M. Schaller, A. Maurer, C. Gouttefangeas, M. Kneilling, B. J. Pichler, D. Sonanini, U. Rothbauer, Single-domain antibodies for targeting, detection, and in vivo imaging of human $CD4^+$ cells. *Front. Immunol.* **12**, 799910 (2021).
39. E. Alexander, K. W. Leong, Discovery of nanobodies: A comprehensive review of their applications and potential over the past five years. *J. Nanobiotechnol.* **22**, 661 (2024).
40. G. Dolton, C. Rius, A. Wall, B. Szomolay, V. Bianchi, S. A. E. Galloway, M. S. Hasan, T. Morin, M. E. Caillaud, H. L. Thomas, S. Theaker, L. R. Tan, A. Fuller, K. Topley, M. Legut, M. Attaf, J. R. Hopkins, E. Behiry, J. Zabkiewicz, C. Alvares, A. Lloyd, A. Rogers, P. Henley, C. Fegan, O. Ottmann, S. Man, M. D. Crowther, M. Donia, I. M. Svane, D. K. Cole, P. E. Brown, P. Rizkallah, A. K. Sewell, Targeting of multiple tumor-associated antigens by individual T cell receptors during successful cancer immunotherapy. *Cell* **186**, 3333–3349.e27 (2023).
41. J. Lau, J. Cheung, A. Navarro, S. Lianoglou, B. Haley, K. Totpal, L. Sanders, H. Koeppen, P. Caplazi, J. McBride, H. Chiu, R. Hong, J. Grogan, V. Javinal, R. Yauch, B. Irving, M. Belvin, I. Mellman, J. M. Kim, M. Schmidt, Tumour and host cell PD-L1 is required to mediate suppression of anti-tumour immunity in mice. *Nat. Commun.* **8**, 14572 (2017).
42. M. Rashidian, M. W. LaFleur, V. L. Verschoor, A. Dongre, Y. Zhang, T. H. Nguyen, S. Kolifrath, A. R. Aref, C. J. Lau, C. P. Paweletz, X. Bu, G. J. Freeman, M. I. Barrasa, R. A. Weinberg, A. H. Sharpe, H. L. Ploegh, Immuno-PET identifies the myeloid compartment as a key contributor to the outcome of the antitumor response under PD-1 blockade. *Proc. Natl. Acad. Sci. U.S.A.* **116**, 16971–16980 (2019).
43. S. Goswami, K. E. Pauken, L. Wang, P. Sharma, Next-generation combination approaches for immune checkpoint therapy. *Nat. Immunol.* **25**, 2186–2199 (2024).
44. C. Pilard, M. Ancion, P. Delvenne, G. Jerusalem, P. Hubert, M. Herfs, Cancer immunotherapy: It's time to better predict patients' response. *Br. J. Cancer* **125**, 927–938 (2021).
45. D. R. Wang, X. L. Wu, Y. L. Sun, Therapeutic targets and biomarkers of tumor immunotherapy: Response versus non-response. *Signal Transduct. Target. Ther.* **7**, 331 (2022).
46. M. Yarchoan, A. Hopkins, E. M. Jaffee, Tumor mutational burden and response rate to PD-1 inhibition. *N. Engl. J. Med.* **377**, 2500–2501 (2017).
47. T. André, K. K. Shiu, T. W. Kim, B. V. Jensen, L. H. Jensen, C. Punt, D. Smith, R. Garcia-Carbonero, M. Benavides, P. Gibbs, C. de la Fouchardiere, F. Rivera, E. Elez, J. Bendell, D. T. Le, T. Yoshino, E. Van Cutsem, P. Yang, M. Z. H. Farooqui, P. Marinello, L. A. Diaz Jr., Pembrolizumab in microsatellite-instability-high advanced colorectal cancer. *N. Engl. J. Med.* **383**, 2207–2218 (2020).
48. R. Banchereau, N. Leng, O. Zill, E. Sokol, G. Liu, D. Pavlick, S. Maund, L. F. Liu, E. Kadel III, N. Baldwin, S. Jhunjhunwala, D. Nickles, Z. J. Assaf, D. Bower, N. Patil, M. McCleland, D. Shames, L. Molinero, M. Huseni, S. Sanjabi, C. Cummings, I. Mellman, S. Mariathasan, P. Hegde, T. Powles, Molecular determinants of response to PD-L1 blockade across tumor types. *Nat. Commun.* **12**, 3969 (2021).
49. M. F. Sanmamed, J. L. Perez-Gracia, K. A. Schalper, J. P. Fusco, A. Gonzalez, M. E. Rodriguez-Ruiz, C. Oñate, G. Perez, C. Alfaro, S. Martín-Algarra, M. P. Andueza, A. Gurpide, M. Morgado, J. Wang, A. Bacchiocchi, R. Halaban, H. Kluger, L. Chen, M. Sznol, I. Melero, Changes in serum interleukin-8 (IL-8) levels reflect and predict response to anti-PD-1 treatment in melanoma and non-small-cell lung cancer patients. *Ann. Oncol.* **28**, 1988–1995 (2017).
50. C. Hinterleitner, J. Strähle, E. Malenke, M. Hinterleitner, M. Henning, M. Seehawer, T. Bilich, J. Heitmann, M. Lutz, S. Mattern, S. Scheuermann, M. Horger, S. Maurer, J. Walz, F. Fend, R. Handgretinger, C. Seitz, B. Weigelin, S. Singer, H. Salih, O. Borst, H. G. Kopp, L. Zender, Platelet PD-L1 reflects collective intratumoral PD-L1 expression and predicts immunotherapy response in non-small cell lung cancer. *Nat. Commun.* **12**, 7005 (2021).
51. P. B. Subrahmanyam, Z. Dong, D. Gusenleitner, A. Giobbie-Hurder, M. Severgnini, J. Zhou, M. Manos, L. M. Eastman, H. T. Maecker, F. S. Hodi, Distinct predictive biomarker candidates for response to anti-CTLA-4 and anti-PD-1 immunotherapy in melanoma patients. *J. Immunother. Cancer* **6**, 18 (2018).
52. R. S. Vanguri, J. Luo, A. T. Aukerman, J. V. Egger, C. J. Fong, N. Horvat, A. Pagano, J. A. B. Araujo-Filho, L. Geneslaw, H. Rizvi, R. Sosa, K. M. Boehm, S. R. Yang, F. M. Bodd, K. Ventura, T. J. Hollmann, M. S. Ginsberg, J. Gao, M. D. Hellmann, J. L. Sauter, S. P. Shah, Multimodal integration of radiology, pathology and genomics for prediction of response to PD-(L)1 blockade in patients with non-small cell lung cancer. *Nat. Cancer* **3**, 1151–1164 (2022).
53. K. Litchfield, J. L. Reading, C. Puttick, K. Thakkar, C. Abbosh, R. Bentham, T. B. K. Watkins, R. Rosenthal, D. Biswas, A. Rowan, E. Lim, M. Al Bakir, V. Turati, J. A. Guerra-Assunção, L. Conde, A. J. S. Furness, S. K. Saini, S. R. Hadrup, J. Herrero, S. H. Lee, P. Van Loo, T. Enver, J. Larkin, M. D. Hellmann, S. Turajlic, S. A. Quezada, N. McGranahan, C. Swanton, Meta-analysis of tumor- and T cell-intrinsic mechanisms of sensitization to checkpoint inhibition. *Cell* **184**, 596–614.e14 (2021).
54. A. Braune, L. Oehme, R. Freudenberg, F. Hofheinz, J. van den Hoff, J. Kotzerke, S. Hoberück, Comparison of image quality and spatial resolution between ^{18}F, ^{68}Ga, and ^{64}Cu phantom measurements using a digital Biograph Vision PET/CT. *EJNMMI Phys.* **9**, 58 (2022).
55. J. Rong, A. Haider, T. E. Jeppesen, L. Josephson, S. H. Liang, Radiochemistry for positron emission tomography. *Nat. Commun.* **14**, 3257 (2023).
56. C. Li, C. Han, S. Duan, P. Li, I. S. Alam, Z. Xiao, Visualizing T-cell responses: The T-cell PET imaging toolbox. *J. Nucl. Med.* **63**, 183–188 (2022).
57. A. Bouleau, V. Lebon, C. Truillet, PET imaging of immune checkpoint proteins in oncology. *Pharmacol. Ther.* **222**, 107786 (2021).
58. L. M. Braun, S. Giesler, G. Andrieux, R. Riemer, N. Talvard-Balland, S. Duquesne, T. Rückert, S. Unger, S. Kreutmair, M. Zwick, M. Follo, A. Hartmann, N. Osswald, W. Melchinger, S. Chapman, J. A. Hutchinson, S. Haferkamp, L. Torster, J. Kött, C. Gebhardt, D. Hellwig, N. Karantzelis, T. Wallrabenstein, T. Lowinus, M. Yücel, N. Brehm, J. Rawluk, D. Pfeifer, P. Bronsert, M. Rogg, S. Mattern, M. Heikenwälder, S. Fusco, N. P. Malek, S. Singer, A. Schmitt-Graeff, F. Ceteci, F. R. Greten, B. R. Blazar, M. Boerries, N. Köhler, J. Duyster, G. Ihorst, S. Lassmann, P. Keye, S. Minguet, D. Schadendorf, S. Ugurel, D. Rafei-Shamsabadi, R. Thimme, P. Hasselblatt, B. Bengsch, C. Schell, E. L. Pearce, F. Meiss, B. Becher, C. Funke-Lorenz, J. M. Placke, P. Apostolova, R. Zeiser, Adiponectin reduces immune checkpoint inhibitor-induced inflammation without blocking anti-tumor immunity. *Cancer Cell* **43**, 269–291.e19 (2025).
59. C. M. Griessinger, A. M. Schmid, D. Sonanini, B. F. Schörg, M. A. Jarboui, D. Bukala, N. Mucha, B. Fehrenbacher, J. Steinhilber, M. Martella, U. Kohlhofer, M. Schaller, L. Zender, H. G. Rammensee, L. Quintanilla-Martinez, M. Röcken, M. Kneilling, B. J. Pichler, The administration route of tumor-antigen-specific T-helper cells differentially modulates the tumor microenvironment and senescence. *Carcinogenesis* **40**, 289–302 (2019).
60. A. Narsale, B. Lam, R. Moya, T. Lu, A. Mandelli, I. Gotuzzo, B. Pessina, G. Giamporcaro, R. Geoffrey, K. Buchanan, M. Harris, A. S. Bergot, R. Thomas, M. J. Hessner, M. Battaglia, E. Serti, J. D. Davies, $CD4^+CD25^+CD127^{hi}$ cell frequency predicts disease progression in type 1 diabetes. *JCI Insight* **6**, e136114 (2021).
61. H. J. Boyle, O. Tredan, S. Chabaud, A. Bajard, D. Perol, T. D. Bachelot, CD4 levels as a prognostic marker for metastatic breast cancer. *J. Clin. Oncol.* **28**, 1140–1140 (2010).
62. G. Eberst, D. Vernerey, C. Laheurte, A. Meurisse, V. Kaulek, L. Cuche, P. Jacoulet, H. Almotlak, J. Lahourcade, M. Gainet-Brun, E. Fabre, F. Le Pimpec-Barthes, O. Adotevi, V. Westeel, Prognostic value of $CD4^+$ T lymphopenia in non-small cell lung cancer. *BMC Cancer* **22**, 529 (2022).
63. Z. Hui, Y. Ren, D. Zhang, Y. Chen, W. Yu, J. Cao, L. Liu, T. Wang, S. Xiao, L. Zheng, Y. Pu, F. Wei, J. You, X. Ren, PD-1 blockade potentiates neoadjuvant chemotherapy in NSCLC via increasing $CD127^+$ and $KLRG1^+$ CD8 T cells. *NPJ Precis. Oncol.* **7**, 48 (2023).
64. D. E. Ramirez, C. P. C. Dragnev, T. G. Searles, N. Spicer, T. Chen, J. L. Lines, A. R. Hawkes, W. L. Davis, A. Mohamed, K. Shirai, J. D. Phillips, P. C. Rosato, Y. H. Huang, M. J. Turk, Depletion of conventional $CD4^+$ T cells is required for robust priming and dissemination of tumor antigen-specific $CD8^+$ T cells in the setting of anti-CD4 therapy. *J. Immunother. Cancer* **12**, e010170 (2024).
65. D. Glatzová, M. Cebecauer, Dual role of CD4 in peripheral T lymphocytes. *Front. Immunol.* **10**, 618 (2019).
66. J. M. Vinnakota, F. Biavasco, M. Schwabenland, C. Chhatbar, R. C. Adams, D. Erny, S. Duquesne, N. El Khawanky, D. Schmidt, V. Fetsch, A. Zähringer, H. Salié, D. Athanassopoulos, L. M. Braun, N. R. Javorniczky, J. Ho, K. Kierdorf, R. Marks, R. Wäsch, F. Simonetta, G. Andrieux, D. Pfeifer, G. Monaco, C. Capitini, T. J. Fry, T. Blank, B. R. Blazar, E. Wagner, M. Theobald, C. Sommer, M. Stelljes, C. Reicherts, A. Jeibmann, J. Schittenhelm, C. M. Monoranu, A. Rosenwald, M. Kortüm, L. Rasche, H. Einsele, P. T. Meyer, J. Brumberg, S. Völkl, A. Mackensen, R. Coras, M. von Bergwelt-Baildon, N. L. Albert, L. M. Bartos,

M. Brendel, A. Holzgreve, M. Mack, M. Boerries, C. L. Mackall, J. Duyster, P. Henneke, J. Priller, N. Köhler, F. Strübing, B. Bengsch, M. Ruella, M. Subklewe, L. von Baumgarten, S. Gill, M. Prinz, R. Zeiser, Targeting TGFβ-activated kinase-1 activation in microglia reduces CAR T immune effector cell-associated neurotoxicity syndrome. *Nat. Cancer* **5**, 1227–1249 (2024).
67. I. S. Alam, F. Simonetta, L. Scheller, A. T. Mayer, S. Murty, O. Vermesh, T. W. Nobashi, J. K. Lohmeyer, T. Hirai, J. Baker, K. H. Lau, R. Negrin, S. S. Gambhir, Visualization of activated T cells by OX40-immunoPET as a strategy for diagnosis of acute graft-versus-host disease. *Cancer Res.* **80**, 4780–4790 (2020).
68. C. M. Weyand, J. Goronzy, C. G. Fathman, Modulation of CD4 by antigenic activation. *J. Immunol.* **138**, 1351–1354 (1987).
69. R. Geleziunas, S. Bour, M. A. Wainberg, Cell surface down-modulation of CD4 after infection by HIV-1. *FASEB J.* **8**, 593–600 (1994).
70. M. M. Chong, N. Simpson, M. Ciofani, G. Chen, A. Collins, D. R. Littman, Epigenetic propagation of CD4 expression is established by the Cd4 proximal enhancer in helper T cells. *Genes Dev.* **24**, 659–669 (2010).
71. S. Demehri, T. J. Cunningham, S. Manivasagam, K. H. Ngo, S. Moradi Tuchayi, R. Reddy, M. A. Meyers, D. G. DeNardo, W. M. Yokoyama, Thymic stromal lymphopoietin blocks early stages of breast carcinogenesis. *J. Clin. Invest.* **126**, 1458–1470 (2016).
72. S. H. Kim, R. Singh, C. Han, E. Cho, Y. I. Kim, D. G. Lee, Y. H. Kim, S. S. Kim, D. H. Shin, H. J. You, H. W. Lee, B. S. Kwon, B. K. Choi, Chronic activation of 4-1BB signaling induces granuloma development in tumor-draining lymph nodes that is detrimental to subsequent $CD8^+$ T cell responses. *Cell. Mol. Immunol.* **18**, 1956–1968 (2021).
73. E. N. Scott, A. M. Gocher, C. J. Workman, D. A. A. Vignali, Regulatory T cells: Barriers of immune infiltration into the tumor microenvironment. *Front. Immunol.* **12**, 702726 (2021).
74. S. E. Smith, D. B. Hoelzinger, A. L. Dominguez, J. Van Snick, J. Lustgarten, Signals through 4-1BB inhibit T regulatory cells by blocking IL-9 production enhancing antitumor responses. *Cancer Immunol. Immunother.* **60**, 1775–1787 (2011).
75. C. Xavier, A. Blykers, I. Vaneycken, M. D'Huyvetter, J. Heemskerk, T. Lahoutte, N. Devoogdt, V. Caveliers, ^{18}F-nanobody for PET imaging of HER2 overexpressing tumors. *Nucl. Med. Biol.* **43**, 247–252 (2016).
76. F. Cleeren, J. Lecina, J. Bridoux, N. Devoogdt, T. Tshibangu, C. Xavier, G. Bormans, Direct fluorine-18 labeling of heat-sensitive biomolecules for positron emission tomography imaging using the $Al^{18}F$-RESCA method. *Nat. Protoc.* **13**, 2330–2347 (2018).
77. C. M. Schürch, S. S. Bhate, G. L. Barlow, D. J. Phillips, L. Noti, I. Zlobec, P. Chu, S. Black, J. Demeter, D. R. McIlwain, S. Kinoshita, N. Samusik, Y. Goltsev, G. P. Nolan, Coordinated cellular neighborhoods orchestrate antitumoral immunity at the colorectal cancer invasive front. *Cell* **182**, 1341–1359.e19 (2020).
78. A. M. Westendorf, K. Skibbe, A. Adamczyk, J. Buer, R. Geffers, W. Hansen, E. Pastille, V. Jendrossek, Hypoxia enhances immunosuppression by inhibiting $CD4^+$ effector T cell function and promoting Treg activity. *Cell. Physiol. Biochem.* **41**, 1271–1284 (2017).
79. E. Montauti, D. Y. Oh, L. Fong, $CD4^+$ T cells in antitumor immunity. *Trends Cancer* **10**, 969–985 (2024).
80. S. Kumagai, Y. Momoi, H. Nishikawa, Immunogenomic cancer evolution: A framework to understand cancer immunosuppression. *Sci. Immunol.* **10**, eabo5570 (2025).
81. T. R. Wagner, S. Blaess, I. B. Leske, D. I. Frecot, M. Gramlich, B. Traenkle, P. D. Kaiser, D. Seyfried, S. Maier, A. Rezza, F. Sônego, K. Thiam, S. Pezzana, A. Zeck, C. Gouttefangeas, A. M. Scholz, S. Nueske, A. Maurer, M. Kneilling, B. J. Pichler, D. Sonanini, U. Rothbauer, Two birds with one stone: Human SIRPα nanobodies for functional modulation and in vivo imaging of myeloid cells. *Front. Immunol.* **14**, 1264179 (2023).
82. M. A. J. Gorris, L. L. van der Woude, L. I. Kroeze, K. Bol, K. Verrijp, A. L. Amir, J. Meek, J. Textor, C. G. Figdor, I. J. M. de Vries, Paired primary and metastatic lesions of patients with ipilimumab-treated melanoma: High variation in lymphocyte infiltration and HLA-ABC expression whereas tumor mutational load is similar and correlates with clinical outcome. *J. Immunother. Cancer* **10**, e004329 (2022).
83. S. Sultan, M. A. J. Gorris, E. Martynova, L. L. van der Woude, F. Buytenhuijs, S. van Wilpe, K. Verrijp, C. G. Figdor, I. J. M. de Vries, J. Textor, ImmuNet: A segmentation-free machine learning pipeline for immune landscape phenotyping in tumors by multiplex imaging. *Biol. Methods Protoc.* **10**, bpae094 (2025).
84. M. A. J. Gorris, E. Martynova, M. W. D. Sweep, I. A. E. van der Hoorn, S. Sultan, M. Claassens, L. L. van der Woude, K. Verrijp, C. G. Figdor, J. Textor, I. J. M. de Vries, Multiplex immunohistochemical analysis of the spatial immune cell landscape of the tumor microenvironment. *J. Vis. Exp.* **198**, e65717 (2023).
85. P. Bankhead, M. B. Loughrey, J. A. Fernández, Y. Dombrowski, D. G. McArt, P. D. Dunne, S. McQuaid, R. T. Gray, L. J. Murray, H. G. Coleman, J. A. James, M. Salto-Tellez, P. W. Hamilton, QuPath: Open source software for digital pathology image analysis. *Sci. Rep.* **7**, 16878 (2017).

Acknowledgments: We thank J. Kinzler, L. Schramm, M. Harant, M. Owczorz, D. Haupt, and B. Fehrenbacher for excellent technical assistance. **Funding:** This work was supported by the Federal Ministry for Economic Affairs and Climate Action and the European Social Fund as part of the EXIST program 03EFVBW253–REVELICE (S.B., B.Tr., P.D.K., T.W., and D.S.), German Research Foundation (Deutsche Forschungsgemeinschaft, DFG) under Germany's Excellence Strategy–EXC 2180–390900677 (I.G., L.Q., C.M.S., A.M., U.R., B.J.P., M.K., and D.S.), State of Baden-Württemberg and EU EFRE funds within the flagship project "Biologicals Development Center" (BioDevCenter-FZK: RegioInn_2449401) of the regional development concept FORTUNA^2 of the RegioWINRegion Neckar-Alb (P.D.K., A.M., B.J.P., and D.S.), and Swiss Werner Siemens Foundation (B.J.P.). **Author contributions:** Writing—original draft: L.R., S.P., S.B., M.Sch., and D.S. Conceptualization: L.R., B.J.P., S.P., M.K., M.M.v.d.H., M.Sch., and D.S. Investigation: L.R., S.P., S.R., B.Ta., E.A., A.S., S.B., A.M., I.A.E.v.d.H., I.G.-M., T.W., A.R., M.Sch., L.Q.-M., P.D.K., and D.S. Writing—review and editing: L.R., B.J.P., S.P., M.K., B.Ta., E.A., S.C.V., A.S., S.B., M.M.v.d.H., A.M., I.A.E.v.d.H., I.J.M.d.V., T.W., M.Sch., B.Tr., M.A.J.G., U.R., L.Q.-M., P.D.K., D.S., and C.M.S. Methodology: L.R., B.J.P., S.P., S.C.V., A.S., M.M.v.d.H., A.M., I.A.E.v.d.H., I.G.-M., M.Sch., U.R., L.Q.-M., P.D.K., D.S., and C.M.S. Resources: L.R., E.A.J.v.G., B.J.P., E.A., M.M.v.d.H., A.M., I.A.E.v.d.H., I.G.-M., M.Sch., B.Tr., L.Q.-M., P.D.K., D.S., and C.M.S. Funding acquisition: L.R., B.J.P., M.K., M.M.v.d.H., B.Tr., U.R., and D.S. Data curation: L.R., E.A.J.v.G., S.P., M.M.v.d.H., I.A.E.v.d.H., M.St., M.A.J.G., and D.S. Validation: L.R., S.P., M.K., B.Ta., S.B., A.M., I.A.E.v.d.H., M.Sch., D.S., and C.M.S. Supervision: L.R., B.J.P., M.K., S.B., M.M.v.d.H., I.J.M.d.V., M.A.J.G., U.R., and D.S. Formal analysis: L.R., S.P., S.R., E.P., B.Ta., E.A., S.C.V., A.S., S.B., I.A.E.v.d.H., M.Sch., and D.S. Software: L.R., S.C.V., M.Sch., and D.S. Project administration: L.R., B.J.P., SB, M.M.v.d.H., and D.S. Visualization: L.R., S.P., B.Ta., S.B., I.G.-M., M.A.J.G., L.Q.-M., D.S., and C.M.S. **Competing interests:** B.T., P.D.K., U.R., B.J.P., M.K., and D.S. are inventors on a pending patent related to this work filed by the NMI Natural and Medical Science Institute, the University Hospital Tuebingen, and the University of Tuebingen (no. EP 4 112 640 A1, filed 29 June 2021, published 4 January 2023). The authors declare that they have no other competing interests. **Data and materials availability:** All data needed to evaluate the conclusions in the paper are present in the paper and/or the Supplementary Materials.

Submitted 22 January 2025
Accepted 20 May 2025
Published 25 June 2025
10.1126/sciadv.adw1924

4. Discussion

CIT has emerged as a pivotal component in treating various malignancies and significantly improved outcomes, particularly in situations where traditional treatments such as chemotherapy and radiation therapy are less effective [61]. Heterogeneity within the TME represents a crucial hallmark of cancer, and spatial and temporal variations in immune cell profiles have been linked to immunotherapy efficacy in both preclinical and clinical studies across multiple cancer types [72, 169-173]. In fact, there is an unmet need to increase the efficacy of immunotherapies for a broader range of patients and cancers beyond the currently approved indications [82, 174]. However, optimal patient selection strategies and determining the most effective CIT regimens remain crucial areas of investigation [80-82].

The widespread expression of the CD4 antigen on various immune cells highlights the potential of $CD4^+$ cells as key biomarkers for immune monitoring in cancer, enabling more precise patient-specific therapeutic strategies [32, 35, 36].

Thus, understanding $CD4^+$ cell dynamics within the TME is essential, particularly in the context of cancer immunotherapy. Early quantification of the presence of $CD4^+$ cells could provide valuable information on potential resistance to therapies such as PD-1 checkpoint blockade, allowing for personalized treatment approaches that combine immunotherapy with other modalities such as chemo- and radiotherapy and targeted therapy [2, 81, 167, 175]. However, current methods for tracking and detecting $CD4^+$ cells, such as blood sampling or local biopsies, are invasive, provide limited information on whole-body distribution, preclude whole tumor characterization, and do not allow for longitudinal observations [72].

To address these challenges, the following sections delve into the discussion of the results we obtained from the evaluation of both Zirconium-89 (^{89}Zr)-labeled murine and human CD4-targeting minibodies (m/hCD4-Mbs) and the Copper-64 (^{64}Cu)-labeled human CD4-targeting nanobody (hCD4-Nb1) for immunoPET imaging in experimental cancer immunotherapy models.

4.1. Impact on T-cell function

The lack of the Fc region is an important characteristic of antibody fragments, as it is known to interact with IgG–Fc-γ-receptors (FcγR) on immune cells possibly triggering immune reactions [82, 107, 176, 177]. Both tracer formats validated in this thesis - CD4-Mbs and CD4-Nb1 – lack this region. Remarkably, neither tracer format influenced peripheral blood mononuclear cell (PBMC) activation, proliferation, or cytokine secretion *in vitro,* an essential prerequisite for clinical translation.

Although most Nbs developed for *in vivo* imaging lack detailed epitope characterization, the diverse roles of $CD4^+$ T cells in tumor progression and sensitivity to immunotherapy motivated us to conduct an in-depth structural analysis of our hCD4-targeting nanobody candidates [2, 159, 169, 178-184]. Furthermore, for *in vivo* imaging applications, we functionalized their C-terminal region with an azide group. This approach enables versatile conjugation of detectable moieties by DBCO-mediated click chemistry [185, 186].

Initial *in vitro* experiments demonstrated high target specificity of both the ^{89}Zr-m/hCD4-Mbs and the ^{64}Cu-CD4-Nb1. In contrast, other studies examining Fab fragments or Cys-diabodies derived from the monoclonal anti-CD4 antibody GK1.5 found that higher doses of these fragments led to increased interferon (IFN)-γ production *in vitro* and reduced CD4 expression *in vivo* [1, 167, 187]. It is known in literature that the GK1.5 antibody binds to the first extracellular immunoglobulin-like domain (D1) of murine CD4 antigen, which is critical for interaction with MHC-II molecules, thus triggering a domain-specific cellular activation [188]. Notably, during our *in vivo* studies no single mouse suffered from tracer injection-associated adverse events. Our observations were supported by findings of a study by Nagle et al, where the *in vivo* injection of ^{64}Cu-labeled hCD4-Mb in a humanized glioblastoma model did not result in detectable depletion or alterations in the proliferation or polarization of $hCD4^+$ cells [168].

4.2. Biodistribution, Sensitivity and Specificity testing

^{89}Zr-m/hCD4-targeting Mbs were cross-validated *in vivo* using preclinical cancer models to determine their binding specificity to $m/hCD4^+$ cells. While *in vitro* ^{89}Zr-hCD4-Mb uptake by $hCD4^+$ hematopoietic peripheral blood acute lymphoblastic leukemia tumors (HPB-ALL) cells was approximately 80-fold greater than by $hCD4^-$ diffuse histiocytic lymphomas (DHL) B-cell lymphoma cells, the *in vivo* accumulation in $hCD4^+$HPB-ALL

xenografts was only about 4-fold greater than in hCD4$^-$ DHL xenografts. This discrepancy underscores the impact of *in vivo* factors such as biodistribution, tissue permeability, and nonspecific accumulation, which can limit tracer accessibility [1, 122]. In contrast to ^{89}Zr-m/hCD4-Mbs which exhibited specific uptake by hCD4$^+$ HPB-ALL tumors from 6 to 48 hours post injection, two selected CD4-targeting Nbs candidates (CD4-Nb1 – high binding affinity, and CD4-Nb4 – low binding affinity) firstly labeled with a fluorescent dye (Cy5.5) showed a rapid recruitment (10-30 min post-injection) at the tumor site of hCD4$^+$ HPB-ALL xenografts. Importantly, the high affinity CD4-Nb1-Cy5.5 exhibited constant high accumulation at the target site and specificity when compared to the low affinity CD4-Nb4-Cy5.5, confirming their different binding potential observed *in vitro.* Furthermore, *ex vivo* immunofluorescence (IF) staining of excised hCD4$^+$ HPB-ALL tumors enabled co-registration of the signal obtained from the previously injected CD4-Nb1-Cy5.5 tracer, with the signal obtained from *ex vivo* staining of the hCD4 antigen. Interestingly, some hCD4$^+$ HPB-ALL cells exhibited internalization of the Nb-based tracer, characteristic which was also identified by other authors [2, 124, 189]. These results confirm the specificity and suitability of CD4-Nb1 for the fast *in vivo* visualization of CD4$^+$ cells [190-192], opposite to bigger engineered antibodies, such as our ^{89}Zr-m/hCD4-Mbs, which allowed for the detection of differences in uptake only at later time-points. However, xenograft models do not reflect the natural distribution of CD4$^+$ cells *in vivo*. Thus, to better validate our hCD4-targeting Mb and Nb in a model resembling natural conditions, we employed the hCD4-KI mouse model. Furthermore, to enhance clinical translational potential and spatial resolution of our newly developed CD4-Nb1, we radiolabeled the Nb with ^{64}Cu. The radiolabeling did not affect the biological properties of our Nb and neither its rapid clearance profile.

Both, the ^{89}Zr-m/hCD4-Mbs and the ^{64}Cu-CD4-Nb1 tracers successfully enabled visualization of endogenous CD4$^+$ cells in immune cell-enriched lymphatic organs, such as the spleen and lymph nodes. However, the optimal imaging windows differed significantly between the two tracers. While Mbs required imaging at later time-points post-injection (24 – 48 hours) to achieve optimal signal-to-background ratios, the Nb probe reached optimal contrast much earlier, between 90- and 180-minutes post-injection [1, 2]. This characteristic is likely attributed to the rapid blood clearance which is typical of small fragments [122]. The assessed tracer kinetics are consistent with previously reported biodistribution profiles of Mb- and Nb-based imaging agents and

reflect the inherent differences in size, clearance, and tissue penetration [131, 162, 163, 165-168, 177, 193, 194].

While enhanced tracer accumulation in lymphatic organs act as an antigen sink reducing its availability at tumor sites [162, 195], immunoPET imaging with ^{89}Zr-mCD4-Mb allowed detection of low densities of endogenous mCD4$^+$ cells in the spleens of immunodeficient NSG mice [196-198] and in the TME of orthotopic mouse mammary tumor virus-polyoma middle tumor-antigen (MMTV-PyMT, PyMT) tumors, underscoring its high sensitivity as CD4-specific immunoPET probe [1]. However, the antigen sink effect likely contributed to the challenges observed when comparing blood biodistribution of ^{89}Zr-CD4-Mb in knock-out/knock-in mouse models. By normalizing tracer uptake in the TME to corresponding blood values, we were able to identify a species-specific Mb signal in experimental PyMT tumor-bearing WT and hCD4-KI mice [1, 162]. This was true also for other tracers, such as the CD4- and CD8-targeting F(ab)'2 fragments evaluated by Kristensen et al. in several preclinical cancer models [162]. On the other hand, the smaller fragment ^{64}Cu-CD4-Nb1 allowed for the visualization of endogenous hCD4$^+$ cells in the TME of orthotopic PyMT tumor-bearing mice at early time points with no need to normalize the tumor uptake for blood uptake values, highlighting its fast clearance from blood and rapid binding to the target [4].

To mitigate the antigen sink effects, several strategies can be employed. These include pre-dosing with an excess of unlabeled antibody targeting the same antigen as the immunoPET tracer, to saturate immune cell-rich organs and reduce non-specific tracer uptake, or increasing the dose of the immunoPET tracer to enhance its availability at tumor sites [162, 195, 199]. However, these strategies have inherent limitations, such as potentially saturating the target and reducing tracer sensitivity.

Interestingly, ^{64}Cu-CD4-Nb1 showed peak uptake in all organs of interest, the spleen, lymph nodes, blood, lung, and muscle (2 - 8 %ID/ml) at 10 min post-injection, with particularly high uptake in the kidneys (approximatively 60 %ID/ml), consistent with renal excretion [1]. Indeed, conversely to bigger fragments (> 70 kDa) which are excreted via the liver, small fragments, including Nbs are primarily cleared through kidney filtration [122, 158, 162, 200]. Moreover, Nbs are characterized by prolonged kidney retention, which is mainly mediated by the endocytic receptor megalin [200]. When nanobodies are conjugated with a radioisotope, long-term renal retention can

cause nephrotoxicity and interfere with the imaging of nearby molecular targets [201]. Nevertheless, this limitation can be mitigated through the targeted engineering of Nbs, such as glycosylation, PEGylation, or albumin-binding unit fusion, which can reduce renal retention and prolong serum persistence, although they may delay optimal target-to-background signal detection [178, 202, 203]. Another approach to overcome kidney retention is the co-injection of the tracer with compounds such as gelofusine, lysins, or monosodium glutamate, which can impede nanobody binding to crucial transporters expressed in the kidneys [200, 204, 205].

Moreover, compared to full-size mAbs, engineered fragments lacking the Fc region do not bind to the neonatal Fc receptor, preventing antibody recycling. This results in faster clearance, and reduced non-specific accumulation, favoring their use as immunoPET tracers [107]. The rapid target-to-background uptake and reduced immunogenicity was detected not only for our candidate, but also for other Nb-based probes. A recent study successfully evaluated a gallium-68 (^{68}Ga)-labeled anti-hCD8β Nb for PET imaging which enabled the specific targeting of CD8$^+$ T cells in both murine and primate experimental models, and the monitoring of T cell dynamics during tumor growth [2, 194]. Given the challenges of targeting immune cell populations due to their dynamic and lower antigen expression across the body compared to tumor-specific molecules like HER2, these preclinical studies show promising results for further clinical translation [206]. Notably, a HER2-targeting Nb is already under clinical evaluation, further supporting the feasibility of this approach [147, 207].

4.3. Predictive value for ICI efficacy

Due to their fast clearance from blood, imaging probes based on antibody fragments are regarded as favorable for the visualization of minimal variations in the tumor immune infiltrate [162, 208]. Thus, we evaluated the sensitivity of the different tracer formats to visualize dynamic variations of CD4$^+$ cell infiltrates over the tumor growth and treatment response. While ^{89}Zr-mCD4-Mb immunoPET did not allow for the differentiation between ICI-responsive syngenic MC38 adenocarcinomas ("hot tumors") and ICI-resistant B16F10 melanomas ("cold tumors") at baseline, ^{64}Cu-CD4-Nb1 immunoPET delineated CD4$^+$ cell densities from immunologically "cold" B16F10 melanomas and "hot" orthotopic PyMT breast tumors and control tumors without hCD4 expression [1, 4, 162, 208]. In fact, the TME of immunogenic MC38 tumors is mainly characterized by myeloid cells and only a few CD4$^+$ cells [209, 210]. Another research group examined

the ^{89}Zr-mCD4-F(ab')$_2$ in multiple syngeneic tumor models (MC38, CT26, B16F10, 4T1, P815, RenCa, Sa1N) and could not detect differences in the ^{89}Zr-mCD4-F(ab')$_2$ uptake between MC38 and B16F10 tumors. However, they reported a correlation between the tumoral ^{89}Zr-mCD4-F(ab')$_2$ uptake, *ex vivo* CD4$^+$ cell density, and the response to αPD-1 ICI therapy in CT26, Sa1N and P815 tumor models [162].

Given that CD4$^+$ cells represent highly heterogeneous immune cell populations with both pro-tumoral and anti-tumoral functions, we explored whether ^{89}Zr-mCD4-Mb PET could be used for the assessment of ICI therapy sensitivity. Notably, ^{89}Zr-mCD4-Mb PET enabled us to differentiate responsive from nonresponsive MC38 tumors of experimental mice with αPD-L1/αLag-3 immunotherapy. Responsive MC38 tumors exhibited an enhanced ^{89}Zr-mCD4-Mb uptake compared to nonresponsive MC38 tumors 7 to 9 days after therapy initiation. This observation was consistent with our *ex vivo* immunofluorescence analyses, which revealed a significant enhanced CD4$^+$ T-cell infiltration in the TME of responsive MC38 tumors [1].

With respect to our ^{64}Cu-CD4-Nb1, we were able to distinguish minor variations in hCD4$^+$ cell infiltrates between immune-hot and immune-cold tumors at baseline. In addition, we could spatially localize the hCD4$^+$ infiltrates within the tumors, making it possible to distinguish between immunological "hot" and "cold" tumors, as well as giving hints about ICI treatment effectiveness [4].Indeed, we observed an increased ^{64}Cu-hCD4-Nb uptake mainly at the tumor margins of hCD4-KI mice bearing immunologically "hot" PyMT tumors when compared to immunologically "cold" B16F10 melanomas. Furthermore, we could detect higher ^{64}Cu-hCD4-Nb uptake at the tumor core following the administration of the combined αPD-1 and α4-1BB ICI therapy, indicating an increased infiltration of hCD4$^+$ cells into the tumor [4].

The uptake differences observed by noninvasive ^{64}Cu-CD4-Nb1 PET imaging were consistent with *ex vivo* histological findings. Both analyses confirmed the spatial localization of hCD4$^+$ cell infiltrates and demonstrated enhanced hCD4$^+$ cell accumulation in the TME of responsive tumors, suggesting that ^{64}Cu-CD4-Nb1 could serve as a promising tracer for distinguishing between immunologically "hot" and "cold" tumors, as well as a potential predictor of immunotherapy response or valuable decision-making tool [4].

The ability of ^{64}Cu-CD4-Nb1 to visualize hCD4$^+$ cells at the tumor periphery of mice non-responsive to αPD-1/α4-1BB mAbs treatment and the known ability of regulatory T cells (Tregs) to form physical and metabolic barriers that limit the infiltration in the tumor core

of effector T cells, let us hypothesize that the tracer signal detected in the tumor margins of non-responsive animals was linked to the accumulation of Tregs, which suppress immune cell infiltration in the tumor, and thus therapeutic response [211].

This hypothesis was confirmed using another experimental model where MC38 tumor-bearing animals were treated with the standard-of-care αPD-1 therapy and the additional α4-1BB mAbs were administered only to mice showing increased ^{64}Cu-CD4-Nb1 uptake at the tumor periphery, aiming to deplete Tregs thus improving treatment success [212, 213]. With this approach we could specifically select and thus increase the response rate to therapy, even in mice bearing larger tumors [4]. Moreover, ^{64}Cu-CD4-Nb1 PET imaging enabled insights into systemic immune responses following immunotherapy. Indeed, mice treated with αPD1/α4-1BB immunotherapy presented greater ^{64}Cu-CD4-Nb1 uptake in lymphoid tissues, reflecting the increased activation and proliferation of immune cells in response to treatment. Additionally, tumor-draining lymph nodes showed higher tracer uptake when compared to contralateral, non-draining counterparts, suggesting localized immune engagement in response to tumor antigen presentation [4]. This differential uptake was not only indicative of treatment-induced immune activation but also appeared to correlate with individual responsiveness to therapy. The different uptake patterns of secondary lymphatic organs, specifically the higher uptake in the tumor-draining lymph node compared to the contralateral part, aligns with observations from other studies using immune cell-specific tracers, such as a recent investigation employing CD8-specific T cell-targeting Nb for monitoring CD8 T cell dynamics in preclinical models of cancer immunotherapy [4, 194]. Collectively, these findings underscore the potential of CD4-targeted nanobody PET imaging as a noninvasive, whole-body approach for early therapy monitoring and patient stratification, highlighting its high sensitivity in detecting subtle variations in CD4$^+$ cell infiltration [4].

The situation differed for larger fragments, such as the ^{89}Zr-m/hCD4-Mbs evaluated in this thesis as well as for other antibody-based constructs, like cys-diabodies examined by other research groups [1, 162]. Owing to their larger size and slower clearance compared to Nb-based probes, it was necessary to consider the TBR to accurately assess differences in CD4$^+$ cell infiltration within the TME. However, even after normalizing the tumor uptake, the imaging data only allowed for the differentiation between tumors with relatively higher or lower levels of CD4$^+$ cell infiltration, corresponding to their responsiveness to CIT [1].

4.4. Prerequisites for Clinical Translation

Before imaging probes targeting immune cells can be translated into clinical use, their potential immunogenicity must be assessed to determine whether they might interact with the human immune system. Recent clinical studies involving other Mbs, such as ^{89}Zr-crefmirlimab berdoxam, and Nbs, such as ^{68}Ga-NOTA-Anti-MMR revealed that only a few patients developed low levels of antibodies against the administered PET tracers, suggesting that these engineered fragments have a low risk of immunogenicity [131, 157, 190]. Interestingly, Nbs are known to share high sequence homology with the human VH3 domain, which contributes to their low immunogenicity in humans. To further minimize the risk of unwanted immune reactions, a small number of amino acid residues were substituted in our CD4-Nb1 construct. This humanization step is known to improve tolerance of the probe by the host immune system, thereby reducing the probability of adverse immune responses upon administration [4, 192, 214, 215].

Another important consideration is the choice of radioisotope used to label the tracer. Although ^{89}Zr is widely used in clinical applications and can be shipped world-wide, several limitations remain. Its production requires a high-energy cyclotron, which is available only at a limited number of institutions world-wide. Furthermore, ^{89}Zr exposes patients to relatively high radiation doses compared to short-lived radionuclides, and the instability of the ^{89}Zr-DFO chelation complex can result in the release of free ^{89}Zr, which tends to accumulate in bone marrow. However, these drawbacks are acceptable for imaging probes with slow pharmacokinetics, which matches the long half-life of ^{89}Zr [216].

In contrast, ^{64}Cu offers more favorable decay characteristics, lower radiation exposure, and easier production, while still enabling continent-wide shipping [111, 217].

For smaller tracers such as Nbs, short-lived radioisotopes like ^{18}F are particularly advantageous. Their short half-life aligns with the fast pharmacokinetics of Nbs, allowing rapid and specific visualization of the target. In addition, the quick clearance of the tracer from the body and the low energy of ^{18}F reduces patient radiation exposure and enables the administration of other imaging probes within the same day. This same-day, multi-target imaging approach paves the way for a more comprehensive assessment of the patient's immune status, supporting a more precise and personalized therapeutic strategy [218, 219].

5. Conclusion

Overall, both the ^{89}Zr-m/hCD4-Mbs and ^{64}Cu-CD4-Nb1 evaluated in this thesis demonstrated high target sensitivity and specificity for CD4$^+$ cells, enabling the detection of clinically relevant differences in immune-cell densities within the TME [1, 2, 4].

While both tracer formats allowed early visualization of responses to CIT, only ^{64}Cu-CD4-Nb1 provided sufficient spatial resolution to localize CD4$^+$ cells within the tumor, distinguishing their accumulation at the invasive margins from that in the tumor core. This feature makes ^{64}Cu-CD4-Nb1 a powerful tool for uncovering patient-specific immune patterns associated with sensitivity to CIT, highlighting its potential to guide and optimize combinatorial treatment approaches [4].

Taken together, these findings indicate that both tracer formats hold strong promise for the noninvasive whole-body visualization of endogenous CD4$^+$ cells, paving the way for future clinical approaches.

Additionally, their distinct pharmacokinetic profiles suggest their possible use for different clinical applications. On the one hand, the slower clearance of the ^{89}Zr-m/hCD4-Mbs makes it suitable for longitudinal studies to monitor CD4$^+$ cell dynamics and treatment outcomes. On the other hand, the faster clearance of ^{64}Cu-CD4-Nb1 tracer enables same-day and multiple-tracer imaging with additional tracers targeting other immune cell subsets. This feature could provide a more integrated view of immune-cell interactions within the TME during immune responses [220].

In conclusion, the successful preclinical validation of these CD4-targeting immunoPET probes makes them optimal candidates for clinical translation, offering new opportunities to visualize, understand, and personalize immune-based cancer treatments.

6. Bibliography

1. Pezzana S, Blaess S, Kortendieck J, Hemmer N, Tako B, Pietura C, et al. In-depth cross-validation of human and mouse CD4-specific minibodies for noninvasive PET imaging of CD4(+) cells and response prediction to cancer immunotherapy. Theranostics. 2024; 14: 4582-97.

2. Traenkle B, Kaiser PD, Pezzana S, Richardson J, Gramlich M, Wagner TR, et al. Single-Domain Antibodies for Targeting, Detection, and In Vivo Imaging of Human CD4(+) Cells. Front Immunol. 2021; 12: 799910.

3. Wagner TR, Blaess S, Leske IB, Frecot DI, Gramlich M, Traenkle B, et al. Two birds with one stone: human SIRPα nanobodies for functional modulation and in vivo imaging of myeloid cells. Front Immunol. 2023; 14: 1264179.

4. Pezzana S, Blaess S, Traenkle B, Schaefer A, Ruoff L, Tako B, et al. PET-based immunomapping of intratumoral CD4(+) cells to monitor acquired resistance to checkpoint inhibitors. Sci Adv. 2025; 11: eadw1924.

5. Stammes MA, Koopman G, Wagner TR, Traenkle B, Kaiser PD, Mooij P, et al. Noninvasive Monitoring of Inflammatory Processes by Myeloid Cell-Directed PET Tracers in an Experimental Severe Acute Respiratory Syndrome Coronavirus 2 Infection Model. J Nucl Med. 2025.

6. Parkin J, Cohen B. An overview of the immune system. Lancet. 2001; 357: 1777-89.

7. Pitt JM, Marabelle A, Eggermont A, Soria J-C, Kroemer G, Zitvogel L. Targeting the tumor microenvironment: removing obstruction to anticancer immune responses and immunotherapy. Annals of Oncology. 2016; 27: 1482-92.

8. Sung H, Ferlay J, Siegel RL, Laversanne M, Soerjomataram I, Jemal A, Bray F. Global Cancer Statistics 2020: GLOBOCAN Estimates of Incidence and Mortality Worldwide for 36 Cancers in 185 Countries. CA: A Cancer Journal for Clinicians. 2021; 71: 209-49.

9. Langley RR, Fidler IJ. The seed and soil hypothesis revisited-The role of tumor-stroma interactions in metastasis to different organs. International Journal of Cancer. 2011; 128: 2527-35.

10. Paget S. The distribution of secondary growths in cancer of the breast. Cancer Metastasis; 1889.

11. de Visser KE, Joyce JA. The evolving tumor microenvironment: From cancer initiation to metastatic outgrowth. Cancer Cell. 2023; 41: 374-403.

12. Hanahan D, Weinberg A, Robert. Hallmarks of Cancer: The Next Generation. Cell. 2011; 144: 646-74.

13. Hinshaw D, Shevde LA. The Tumor Microenvironment Innately Modulates Cancer Progression. Cancer research; 2019.

14. E. Weber C, Kuo PC. The Tumor Microenvironment. surgical oncology; 2012.

15. Anderson NM, Simon MC. The tumor microenvironment. Current Biology. 2020; 30: R921-R5.

16. Fu L-Q, Dub W-L, Caia M-H, Yao J-Y, Zhao Y-Y, Mou X-Z. The roles of tumor-associated macrophages in tumor angiogenesis and metastasis. Cellular Immunology; 2020.

17. Wang J, Li D, Cang H, Guo B. Crosstalk between cancer and immune cells: Role of tumor-associated macrophages in the tumor microenvironment. Cancer Medicine. 2019; 8: 4709-21.

18. Chen DS, Mellman I. Elements of cancer immunity and the cancer–immune set point. Nature. 2017; 541: 321-30.

19. Chen S, Daniel, Mellman I. Oncology Meets Immunology: The Cancer-Immunity Cycle. Immunity. 2013; 39: 1-10.

20. Wu B, Zhang B, Li B, Wu H, Jiang M. Cold and hot tumors: from molecular mechanisms to targeted therapy. Signal Transduction and Targeted Therapy. 2024; 9: 274.

21. Slebe M, Pouw JEE, Hashemi SMS, Menke-Van Der Houven Van Oordt CW, Yaqub MM, Bahce I. Current state and upcoming opportunities for immunoPET biomarkers in lung cancer. Lung Cancer. 2022; 169: 84-93.

22. Tiwari A, Oravecz T, Dillon LA, Italiano A, Audoly L, Fridman WH, Clifton GT. Towards a consensus definition of immune exclusion in cancer. Front Immunol. 2023; 14: 1084887.

23. Herbst RS, Soria JC, Kowanetz M, Fine GD, Hamid O, Gordon MS, et al. Predictive correlates of response to the anti-PD-L1 antibody MPDL3280A in cancer patients. Nature. 2014; 515: 563-7.

24. Gide TN, Wilmott JS, Scolyer RA, Long GV. Primary and Acquired Resistance to Immune Checkpoint Inhibitors in Metastatic Melanoma. Clin Cancer Res. 2018; 24: 1260-70.

25. Hegde PS, Karanikas V, Evers S. The Where, the When, and the How of Immune Monitoring for Cancer Immunotherapies in the Era of Checkpoint Inhibition. Clin Cancer Res. 2016; 22: 1865-74.

26. Hammerl D, Martens JWM, Timmermans M, Smid M, Trapman-Jansen AM, Foekens R, et al. Spatial immunophenotypes predict response to anti-PD1 treatment and capture distinct paths of T cell evasion in triple negative breast cancer. Nat Commun. 2021; 12: 5668.

27. Demaria S, Romano E, Brackstone M, Formenti SC. Immune induction strategies to enhance responses to PD-1 blockade: lessons from the TONIC trial. J Immunother Cancer. 2019; 7: 318.

28. Lanitis E, Dangaj D, Irving M, Coukos G. Mechanisms regulating T-cell infiltration and activity in solid tumors. Oxford University Press; 2017. p. xii18-xii32.

29. Fang D, Zhu J. Dynamic balance between master transcription factors determines the fates and functions of CD4 T cell and innate lymphoid cell subsets. J Exp Med. 2017; 214: 1861-76.

30. Zhu X, Zhu J. CD4 T Helper Cell Subsets and Related Human Immunological Disorders. Int J Mol Sci. 2020; 21.

31. Duhen R, Fesneau O, Samson KA, Frye AK, Beymer M, Rajamanickam V, et al. PD-1 and ICOS coexpression identifies tumor-reactive CD4+ T cells in human solid tumors. Journal of Clinical Investigation. 2022; 132.

32. Tay RE, Richardson EK, Toh HC. Revisiting the role of CD4+ T cells in cancer immunotherapy—new insights into old paradigms. Cancer Gene Therapy. 2021; 28: 5-17.

33. Oliveira G, Wu CJ. Dynamics and specificities of T cells in cancer immunotherapy. Nat Rev Cancer. 2023; 23: 295-316.

34. Luckheeram RV, Zhou R, Verma AD, Xia B. CD4+T Cells: Differentiation and Functions. Clinical and Developmental Immunology. 2012; 2012: 1-12.

35. Speiser DE, Chijioke O, Schaeuble K, Münz C. CD4+ T cells in cancer. Nature Cancer. 2023; 4: 317-29.

36. Yang W, Yu T, Cong Y. CD4+ T cell metabolism, gut microbiota, and autoimmune diseases: implication in precision medicine of autoimmune diseases. Precision Clinical Medicine. 2022; 5.

37. Jardine L, Barge D, Ames-Draycott A, Pagan S, Cookson S, Spickett G, et al. Rapid detection of dendritic cell and monocyte disorders using CD4 as a lineage marker of the human peripheral blood antigen-presenting cell compartment. Front Immunol. 2013; 4: 495.

38. Kravtsov DS, Erbe AK, Sondel PM, Rakhmilevich AL. Roles of CD4+ T cells as mediators of antitumor immunity. Frontiers in Immunology; 2022.

39. Zhu J. T Helper Cell Differentiation, Heterogeneity, and Plasticity. Cold Spring Harbor Perspectives in Biology. 2018; 10: a030338.

40. Farhood B, Najafi M, Mortezaee K. $CD8^+$ cytotoxic T lymphocytes in cancer immunotherapy: A review. Journal of Cellular Physiology. 2019; 234: 8509-21.

41. Corthay A. How do Regulatory T Cells Work? Scandinavian Journal of Immunology. 2009; 70: 326-36.

42. Lee HL, Jang JW, Lee SW, Yoo SH, Kwon JH, Nam SW, et al. Inflammatory cytokines and change of Th1/Th2 balance as prognostic indicators for hepatocellular carcinoma in patients treated with transarterial chemoembolization. Scientific Reports. 2019; 9.

43. Zhu J, Yamane H, Paul WE. Differentiation of effector CD4 T cell populations (*). Annu Rev Immunol. 2010; 28: 445-89.

44. Gurram RK, Zhu J. Orchestration between ILC2s and Th2 cells in shaping type 2 immune responses. Cell Mol Immunol. 2019; 16: 225-35.

45. Le L, Tokumaru Y, Oshi M, Asaoka M, Yan L, Endo I, et al. Th2 cell infiltrations predict neoadjuvant chemotherapy response of estrogen receptor-positive breast cancer. Gland Surg. 2021; 10: 154-65.

46. Walker JA, McKenzie ANJ. T(H)2 cell development and function. Nat Rev Immunol. 2018; 18: 121-33.

47. Schnell A, Littman DR, Kuchroo VK. TH17 cell heterogeneity and its role in tissue inflammation. Nature Immunology. 2023; 24: 19-29.

48. Ruterbusch M, Pruner KB, Shehata L, Pepper M. In Vivo CD4+ T Cell Differentiation and Function: Revisiting the Th1/Th2 Paradigm. Annual Review of Immunology. 2020; 38: 705-25.

49. Marques HS, de Brito BB, da Silva FAF, Santos MLC, de Souza JCB, Correia TML, et al. Relationship between Th17 immune response and cancer. World J Clin Oncol. 2021; 12: 845-67.

50. Bailey SR, Nelson MH, Himes RA, Li Z, Mehrotra S, Paulos CM. Th17 Cells in Cancer: The Ultimate Identity Crisis. Frontiers in Immunology. 2014; 5.

51. Balkwill FR, Capasso M, Hagemann T. The tumor microenvironment at a glance. Journal of Cell Science. 2012; 125: 5591-6.

52. Wu X, Zhou Z, Cao Q, Chen Y, Gong J, Zhang Q, et al. Reprogramming of Treg cells in the inflammatory microenvironment during immunotherapy: a literature review. Front Immunol. 2023; 14: 1268188.

53. Peterson C, Denlinger N, Yang Y. Recent Advances and Challenges in Cancer Immunotherapy. Cancers. 2022; 14: 3972.

54. Rui R, Zhou L, He S. Cancer immunotherapies: advances and bottlenecks. Front Immunol. 2023; 14: 1212476.

55. Coulie PG, Van Den Eynde BJ, Van Der Bruggen P, Boon T. Tumour antigens recognized by T lymphocytes: at the core of cancer immunotherapy. Nature Reviews Cancer. 2014; 14: 135-46.

56. Liu C, Yang M, Zhang D, Chen M, Zhu D. Clinical cancer immunotherapy: Current progress and prospects. Front Immunol. 2022; 13: 961805.

57. Tan S, Li D, Zhu X. Cancer immunotherapy: Pros, cons and beyond. Biomed Pharmacother. 2020; 124: 109821.

58. Jogalekar MP, Lakshmi Rajendran R, Khan F, Dmello C, Gangadaran P, Ahn B-C. CAR T-Cell-Based gene therapy for cancers: new perspectives, challenges,and clinical developments. Frontiers in Immunology; 2022.

59. De Miguel M, Calvo E. Clinical Challenges of Immune Checkpoint Inhibitors. Cancer Cell. 2020; 38: 326-33.

60. Lee DH. Update of early phase clinical trials in cancer immunotherapy. BMB Reports. 2021; 54: 70-88.

61. Waldman AD, Fritz JM, Lenardo MJ. A guide to cancer immunotherapy: from T cell basic science to clinical practice. Nature Reviews Immunology. 2020; 20: 651-68.

62. Andtbacka RHI, Kaufman HL, Collichio F, Amatruda T, Senzer N, Chesney J, et al. Talimogene Laherparepvec Improves Durable Response Rate in Patients With Advanced Melanoma. Journal of Clinical Oncology. 2015; 33: 2780-8.

63. Soiffer RJ, Kooshesh KA, Ho V. Whole tumor cell vaccines engineered to secrete GM-CSF (GVAX). ImmunoMedicine. 2021; 1.

64. Riley RS, June CH, Langer R, Mitchell MJ. Delivery technologies for cancer immunotherapy. Nature Reviews Drug Discovery. 2019; 18: 175-96.

65. Berraondo P, Sanmamed MF, Ochoa MC, Etxeberria I, Aznar MA, Pérez-Gracia JL, et al. Cytokines in clinical cancer immunotherapy. British Journal of Cancer. 2019; 120: 6-15.

66. Bach PB, Giralt SA, Saltz LB. FDA Approval of Tisagenlecleucel: Promise and Complexities of a $475 000 Cancer Drug. JAMA. 2017; 318: 1861-2.

67. Rosewell Shaw A, Suzuki M. Oncolytic Viruses Partner With T-Cell Therapy for Solid Tumor Treatment. Frontiers in Immunology. 2018; 9.

68. Ott PA, Hu Z, Keskin DB, Shukla SA, Sun J, Bozym DJ, et al. An immunogenic personal neoantigen vaccine for patients with melanoma. Nature. 2017; 547: 217-21.

69. Ribas A, Dummer R, Puzanov I, VanderWalde A, Andtbacka RHI, Michielin O, et al. Oncolytic Virotherapy Promotes Intratumoral T Cell Infiltration and Improves Anti-PD-1 Immunotherapy. Cell. 2017; 170: 1109-19.e10.

70. Reiss DJ, Do T, Kuo D, Gray VE, Olson NE, Lee C-W, et al. Multiplexed Immunofluorescence (IF) Analysis and Gene Expression Profiling of Biopsies from Patients with Relapsed/Refractory (R/R) Diffuse Large B Cell Lymphoma (DLBCL) Treated with Lisocabtagene Maraleucel (liso-cel) in Transcend NHL 001 Reveal Patterns of Immune Infiltration Associated with Durable Response. Blood. 2019; 134: 202-.

71. Balança CC, Salvioni A, Scarlata CM, Michelas M, Martinez-Gomez C, Gomez-Roca C, et al. PD-1 blockade restores helper activity of tumor-infiltrating, exhausted PD-1hiCD39+ CD4 T cells. JCI Insight. 2021; 6.

72. Lu Y, Houson HA, Gallegos CA, Mascioni A, Jia F, Aivazian A, et al. Evaluating the immunologically "cold" tumor microenvironment after treatment with immune checkpoint inhibitors utilizing PET imaging of CD4 + and CD8 + T cells in breast cancer mouse models. Breast Cancer Res. 2024; 26: 104.

73. Esfahani K, Roudaia L, Buhlaiga N, Del Rincon SV, Papneja N, Miller WH. A review of cancer immunotherapy: from the past, to the present, to the future. Current Oncology; 2020.

74. Gubin MM, Vesely MD. Cancer Immunoediting in the Era of Immuno-oncology. Clinical Cancer Research. 2022; 28: 3917-28.

75. Shiravand Y, Khodadadi F, Kashani SMA, Hosseini-Fard SR, Hosseini S, Sadeghirad H, et al. Immune Checkpoint Inhibitors in Cancer Therapy. Current Oncology. 2022; 29: 3044-60.

76. Das S, Johnson DB. Immune-related adverse events and anti-tumor efficacy of immune checkpoint inhibitors. J Immunother Cancer. 2019; 7: 306.

77. Vranic S, Gatalica Z. PD-L1 testing by immunohistochemistry in immuno-oncology. Biomol Biomed. 2023; 23: 15-25.

78. Casagrande S, Sopetto GB, Bertalot G, Bortolotti R, Racanelli V, Caffo O, et al. Immune-Related Adverse Events Due to Cancer Immunotherapy: Immune Mechanisms and Clinical Manifestations. Cancers (Basel). 2024; 16.

79. Conroy M, Naidoo J. Immune-related adverse events and the balancing act of immunotherapy. Nat Commun. 2022; 13: 392.

80. Kraehenbuehl L, Weng CH, Eghbali S, Wolchok JD, Merghoub T. Enhancing immunotherapy in cancer by targeting emerging immunomodulatory pathways. Nat Rev Clin Oncol. 2022; 19: 37-50.

81. Butterfield LH, Najjar YG. Immunotherapy combination approaches: mechanisms, biomarkers and clinical observations. Nat Rev Immunol. 2024; 24: 399-416.

82. Wu AM, Pandit-Taskar N. ImmunoPET: harnessing antibodies for imaging immune cells. Mol Imaging Biol. 2022; 24: 181-97.

83. Granier C, De Guillebon E, Blanc C, Roussel HB, Cecile, Colin E, Saldmann A, et al. Mechanisms of action and rationale for the use of checkpoint inhibitors in cancer. 2017.

84. Hodi FS, O'Day SJ, Mcdermott DF, Weber RW, Sosman JA, Haanen JB, et al. Improved Survival with Ipilimumab in Patients with Metastatic Melanoma. New England Journal of Medicine. 2010; 363: 711-23.

85. Marin-Acevedo JA, Dholaria B, Soyano AE, Knutson KL, Chumsri S, Lou Y. Next generation of immune checkpoint therapy in cancer: new developments and challenges. Journal of hematology & oncology. 2018; 11: 39-.

86. Darvin P, Toor SM, Sasidharan Nair V, Elkord E. Immune checkpoint inhibitors: recent progress and potential biomarkers. Exp Mol Med. 2018; 50: 1-11.

87. Kaptein P, Jacoberger-Foissac C, Dimitriadis P, Voabil P, de Bruijn M, Brokamp S, et al. Addition of interleukin-2 overcomes resistance to neoadjuvant CTLA4 and PD1 blockade in ex vivo patient tumors. Sci Transl Med. 2022; 14: eabj9779.

88. Hodi FS, Chiarion-Sileni V, Gonzalez R, Grob JJ, Rutkowski P, Cowey CL, et al. Nivolumab plus ipilimumab or nivolumab alone versus ipilimumab alone in advanced melanoma (CheckMate 067): 4-year outcomes of a multicentre, randomised, phase 3 trial. Lancet Oncol. 2018; 19: 1480-92.

89. Wang Z, Zou X, Wang H, Hao Z, Li G, Wang S. Companion diagnostics and predictive biomarkers for PD-1/PD-L1 immune checkpoint inhibitors therapy in malignant melanoma. Front Immunol. 2024; 15: 1454720.

90. Tawbi HA, Schadendorf D, Lipson EJ, Ascierto PA, Matamala L, Gutiérrez EC, et al. Relatlimab and Nivolumab versus Nivolumab in Untreated Advanced Melanoma. New England Journal of Medicine. 2022; 386: 24-34.

91. Chocarro L, Bocanegra A, Blanco E, Fernández-Rubio L, Arasanz H, Echaide M, et al. Cutting-Edge: Preclinical and Clinical Development of the First Approved Lag-3 Inhibitor. Cells. 2022; 11.

92. Johnson DB, Nebhan CA, Moslehi JJ, Balko JM. Immune-checkpoint inhibitors: long-term implications of toxicity. Nat Rev Clin Oncol. 2022; 19: 254-67.

93. Lewis AL, Chaft J, Girotra M, Fischer GW. Immune checkpoint inhibitors: a narrative review of considerations for the anaesthesiologist. British Journal of Anaesthesia. 2020; 124: 251-60.

94. Singh R, Kim YH, Lee SJ, Eom HS, Choi BK. 4-1BB immunotherapy: advances and hurdles. Exp Mol Med. 2024; 56: 32-9.

95. Chester C, Sanmamed MF, Wang J, Melero I. Immunotherapy targeting 4-1BB: mechanistic rationale, clinical results, and future strategies. Blood. 2018; 131: 49-57.

96. Zhang Y, Cao M, Wu Y, Malih S, Xu D, Yang E, et al. Preclinical development of novel PD-L1 tracers and first-in-human study of [(68)Ga]Ga-NOTA-RW102 in patients with lung cancers. J Immunother Cancer. 2024; 12.

97. Woo SR, Turnis ME, Goldberg MV, Bankoti J, Selby M, Nirschl CJ, et al. Immune inhibitory molecules LAG-3 and PD-1 synergistically regulate T-cell function to promote tumoral immune escape. Cancer Res. 2012; 72: 917-27.

98. Ling A, Lundberg IV, Eklöf V, Wikberg ML, Öberg Å, Edin S, Palmqvist R. The infiltration, and prognostic importance, of Th1 lymphocytes vary in molecular subgroups of colorectal cancer. J Pathol Clin Res. 2016; 2: 21-31.

99. Laheurte C, Dosset M, Vernerey D, Boullerot L, Gaugler B, Gravelin E, et al. Distinct prognostic value of circulating anti-telomerase CD4(+) Th1 immunity and exhausted PD-1(+)/TIM-3(+) T cells in lung cancer. Br J Cancer. 2019; 121: 405-16.

100. Bawden EG, Wagner T, Schröder J, Effern M, Hinze D, Newland L, et al. CD4(+) T cell immunity against cutaneous melanoma encompasses multifaceted MHC II-dependent responses. Sci Immunol. 2024; 9: eadi9517.

101. Zeelen C, Paus C, Draper D, Heskamp S, Signore A, Galli F, et al. In-vivo imaging of tumor-infiltrating immune cells: implications for cancer immunotherapy. The Quarterly Journal of Nuclear Medicine and Molecular Imaging. 2018; 62.

102. James ML, Gambhir SS. A MOLECULAR IMAGING PRIMER: MODALITIES, IMAGING AGENTS, AND APPLICATIONS. Physiological Reviews. 2012; 92: 897-965.

103. Pichler BJ, Wehrl HF, Kolb A, Judenhofer MS. Positron Emission Tomography/Magnetic Resonance Imaging: The Next Generation of Multimodality Imaging? Seminars in Nuclear Medicine. 2008; 38: 199-208.

104. Vaquero JJ, Kinahan P. Positron Emission Tomography: Current Challenges and Opportunities for Technological Advances in Clinical and Preclinical Imaging Systems. Annual Review of Biomedical Engineering. 2015; 17: 385-414.

105. Cherry SR. Fundamentals of Positron Emission Tomography and Applications in Preclinical Drug Development. The Journal of Clinical Pharmacology. 2001; 41: 482-91.

106. Valk PE, Delbeke D, Bailey DL, Townswnd DW, Maisey MN. Positron Emission Tomography. Basic Science and Clinical Practice.: Springer; 2003.

107. Dewulf J, Adhikari K, Vangestel C, Wyngaert TVD, Elvas F. Development of Antibody Immuno-PET/SPECT Radiopharmaceuticals for Imaging of Oncological Disorders-An Update. Cancers (Basel). 2020; 12.

108. Velikyan I. Prospective of ^{68}Ga-radiopharmaceutical development. Theranostics. 2013; 4: 47-80.

109. Kiessling FP, BJ; Hauff, P. Small Animal Imaging: Basics and Practical Guide. 2011: 1-597.

110. Ziegler SI. Positron Emission Tomography: Principles, Technology, and Recent Developments. Nuclear Physics A; 2005.

111. Rong J, Haider A, Jeppesen TE, Josephson L, Liang SH. Radiochemistry for positron emission tomography. Nat Commun. 2023; 14: 3257.

112. Lopci E, Fanti S. Non-FDG PET/CT. Molecular Imaging in Oncology: Springer International Publishing; 2020. p. 669-718.

113. Rahman WT, Wale DJ, Viglianti BL, Townsend DM, Manganaro MS, Gross MD, et al. The impact of infection and inflammation in oncologic (18)F-FDG PET/CT imaging. Biomed Pharmacother. 2019; 117: 109168.

114. Safaie E, Matthews R, Bergamaschi R. PET scan findings can be false positive. Tech Coloproctol. 2015; 19: 329-30.

115. Ma Y, Wang Q, Dong Q, Zhan L, Zhang J. How to differentiate pseudoprogression from true progression in cancer patients treated with immunotherapy. Am J Cancer Res. 2019; 9: 1546-53.

116. Miele E, Spinelli GP, Tomao F, Zullo A, De Marinis F, Pasciuti G, et al. Positron Emission Tomography (PET) radiotracers in oncology – utility of 18F-Fluoro-deoxy-glucose (FDG)-PET in the management of patients with non-small-cell lung cancer (NSCLC). Journal of Experimental & Clinical Cancer Research. 2008; 27: 52.

117. Mayer AT, Gambhir SS. The Immunoimaging Toolbox. J Nucl Med. 2018; 59: 1174-82.

118. Lau J, Rousseau E, Kwon D, Lin KS, Bénard F, Chen X. Insight into the Development of PET Radiopharmaceuticals for Oncology. Cancers (Basel). 2020; 12.

119. Iking J, Staniszewska M, Kessler L, Klose JM, Lückerath K, Fendler WP, et al. Imaging Inflammation with Positron Emission Tomography. Biomedicines. 2021; 9.

120. Mulero F. Editorial: ImmunoPET imaging in disease diagnosis and therapy assessment. Front Med (Lausanne). 2023; 10: 1231525.

121. Goldenberg DM, DeLand F, Kim E, Bennett S, Primus FJ, van Nagell JR, Jr., et al. Use of radiolabeled antibodies to carcinoembryonic antigen for the detection and localization of diverse cancers by external photoscanning. N Engl J Med. 1978; 298: 1384-6.

122. Manafi-Farid R, Ataeinia B, Ranjbar S, Jamshidi Araghi Z, Moradi MM, Pirich C, Beheshti M. ImmunoPET: Antibody-Based PET Imaging in Solid Tumors. Front Med (Lausanne). 2022; 9: 916693.

123. Hu S, Shively L, Raubitschek A, Sherman M, Williams LE, Wong JY, et al. Minibody: A novel engineered anti-carcinoembryonic antigen antibody fragment (single-chain Fv-CH3) which exhibits rapid, high-level targeting of xenografts. Cancer Res. 1996; 56: 3055-61.

124. Salvador JP, Vilaplana L, Marco MP. Nanobody: outstanding features for diagnostic and therapeutic applications. Anal Bioanal Chem. 2019; 411: 1703-13.

125. Kwon NY, Kim Y, Lee JO. Structural diversity and flexibility of diabodies. Methods. 2019; 154: 136-42.

126. Rodrigo G, Gruvegård M, Van Alstine JM. Antibody Fragments and Their Purification by Protein L Affinity Chromatography. Antibodies. 2015; 4: 259-77.

127. Li C, Han C, Duan S, Li P, Alam IS, Xiao Z. Visualizing T-Cell Responses: The T-Cell PET Imaging Toolbox. Journal of Nuclear Medicine. 2022; 63: 183-8.

128. Bouleau A, Lebon V, Truillet C. PET imaging of immune checkpoint proteins in oncology. Pharmacology & Therapeutics. 2021; 222.

129. Olafsen T, Torgov M, Zhang GG, Romero J, Zampila C, Marchioni F, et al. Pet imaging of cytotoxic human T cells using an 89Zr-labeled anti-CD8 minibody. Journal for ImmunoTherapy of Cancer. 2015; 3: P388.

130. Griessinger CM, Olafsen T, Mascioni A, Jiang ZK, Zamilpa C, Jia F, et al. The PET-Tracer 89Zr-Df-IAB22M2C Enables Monitoring of Intratumoral CD8 T-cell Infiltrates in Tumor-Bearing Humanized Mice after T-cell Bispecific Antibody Treatment. Cancer Research. 2020; 80: 2903-13.

131. Farwell MD, Gamache RF, Babazada H, Hellmann MD, Harding JJ, Korn R, et al. CD8-targeted PET Imaging of Tumor Infiltrating T cells in Patients with Cancer: A Phase I First-in-Human Study of 89Zr-Df-IAB22M2C, a Radiolabeled anti-CD8 Minibody. Journal of Nuclear Medicine. 2021: jnumed.121.2624.

132. Pandit-Taskar N, Postow MA, Hellmann MD, Harding JJ, Barker CA, O'Donoghue JA, et al. First-in-Humans Imaging with 89Zr-Df-IAB22M2C Anti-CD8 Minibody in Patients with Solid Malignancies: Preliminary Pharmacokinetics, Biodistribution, and Lesion Targeting. Journal of nuclear medicine : official publication, Society of Nuclear Medicine. 2020; 61: 512-9.

133. Schwenck J, Sonanini D, Seyfried D, Ehrlichmann W, Kienzle G, Reischl G, et al. In vivo imaging of CD8+ T cells in metastatic cancer patients: first clinical experience with simultaneous [89Zr]Zr-Df-IAB22M2C PET/MRI. Theranostics. 2023; 13: 2408-23.

134. Chakravarty R, Goel S, Cai W. Nanobody: The “Magic Bullet” for Molecular Imaging? Theranostics. 2014; 4: 386-98.

135. Ulaner GA, Lyashchenko SK, Riedl C, Ruan S, Zanzonico PB, Lake D, et al. First-in-Human Human Epidermal Growth Factor Receptor 2-Targeted Imaging Using (89)Zr-Pertuzumab PET/CT: Dosimetry and Clinical Application in Patients with Breast Cancer. J Nucl Med. 2018; 59: 900-6.

136. Laforest R, Lapi SE, Oyama R, Bose R, Tabchy A, Marquez-Nostra BV, et al. [89Zr]Trastuzumab: Evaluation of Radiation Dosimetry, Safety, and Optimal Imaging Parameters in Women with HER2-Positive Breast Cancer. Molecular Imaging and Biology. 2016; 18: 952-9.

137. Dijkers EC, Oude Munnink TH, Kosterink JG, Brouwers AH, Jager PL, De Jong JR, et al. Biodistribution of 89Zr-trastuzumab and PET Imaging of HER2-Positive Lesions in Patients With Metastatic Breast Cancer. Clinical Pharmacology & Therapeutics. 2010; 87: 586-92.

138. Laforest R, Lapi SE, Oyama R, Bose R, Tabchy A, Marquez-Nostra BV, et al. [(89)Zr]Trastuzumab: Evaluation of Radiation Dosimetry, Safety, and Optimal Imaging Parameters in Women with HER2-Positive Breast Cancer. Mol Imaging Biol. 2016; 18: 952-9.

139. Tamura K, Kurihara H, Yonemori K, Tsuda H, Suzuki J, Kono Y, et al. 64Cu-DOTA-trastuzumab PET imaging in patients with HER2-positive breast cancer. J Nucl Med. 2013; 54: 1869-75.

140. Li M, Ehlerding EB, Jiang D, Barnhart TE, Chen W, Cao T, et al. In vivo characterization of PD-L1 expression in breast cancer by immuno-PET with (89)Zr-labeled avelumab. Am J Transl Res. 2020; 12: 1862-72.

141. Jagoda EM, Vasalatiy O, Basuli F, Opina ACL, Williams MR, Wong K, et al. Immuno-PET Imaging of the Programmed Cell Death-1 Ligand (PD-L1) Using a Zirconium-89 Labeled Therapeutic Antibody, Avelumab. Mol Imaging. 2019; 18: 1536012119829986.

142. Bensch F, van der Veen EL, Lub-de Hooge MN, Jorritsma-Smit A, Boellaard R, Kok IC, et al. 89Zr-atezolizumab imaging as a non-invasive approach to assess clinical response to PD-L1 blockade in cancer. Nature Medicine. 2018; 24: 1852-8.

143. Wierstra P, Sandker G, Aarntzen E, Gotthardt M, Adema G, Bussink J, et al. Tracers for non-invasive radionuclide imaging of immune checkpoint expression in cancer. EJNMMI Radiopharmacy and Chemistry. 2019; 4.

144. Niemeijer AN, Leung D, Huisman MC, Bahce I, Hoekstra OS, van Dongen G, et al. Whole body PD-1 and PD-L1 positron emission tomography in patients with non-small-cell lung cancer. Nat Commun. 2018; 9: 4664.

145. Niemeijer AN, Oprea-Lager DE, Huisman MC, Hoekstra OS, Boellaard R, de Wit-van der Veen BJ, et al. Study of (89)Zr-Pembrolizumab PET/CT in Patients With Advanced-Stage Non-Small Cell Lung Cancer. J Nucl Med. 2022; 63: 362-7.

146. D'Huyvetter M, De Vos J, Xavier C, Pruszynski M, Sterckx YGJ, Massa S, et al. (131)I-labeled Anti-HER2 Camelid sdAb as a Theranostic Tool in Cancer Treatment. Clin Cancer Res. 2017; 23: 6616-28.

147. Keyaerts M, Xavier C, Heemskerk J, Devoogdt N, Everaert H, Ackaert C, et al. Phase I Study of 68Ga-HER2-Nanobody for PET/CT Assessment of HER2 Expression in Breast Carcinoma. J Nucl Med. 2016; 57: 27-33.

148. Chen Y-P, Kim HJ, Wu H, Price-Troska T, Villasboas JC, Jalali S, et al. SIRPα expression delineates subsets of intratumoral monocyte/macrophages with different functional and prognostic impact in follicular lymphoma. Blood Cancer Journal. 2019; 9: 84.

149. Parker CC, Bin Salam A, Song PN, Gallegos C, Hunt A, Yates C, et al. Evaluation of a CD206-Targeted Peptide for PET Imaging of Macrophages in Syngeneic Mouse Models of Cancer. Mol Pharm. 2023; 20: 2415-25.

150. Lauwers Y, De Groof TWM, Vincke C, Van Craenenbroeck J, Jumapili NA, Barthelmess RM, et al. Imaging of tumor-associated macrophage dynamics during immunotherapy using a CD163-specific nanobody-based immunotracer. Proc Natl Acad Sci U S A. 2024; 121: e2409668121.

151. Nguyen DH, Ball ED, Varki A. Myeloid precursors and acute myeloid leukemia cells express multiple CD33-related Siglecs. Experimental Hematology. 2006; 34: 728-35.

152. Tavaré R, Escuin-Ordinas H, Mok S, Mccracken MN, Zettlitz KA, Salazar FB, et al. An Effective Immuno-PET Imaging Method to Monitor CD8-Dependent Responses to Immunotherapy. Cancer Research. 2016; 76: 73-82.

153. Rashidian M, Lafleur MW, Verschoor VL, Dongre A, Zhang Y, Nguyen TH, et al. Immuno-PET identifies the myeloid compartment as a key contributor to the outcome of the antitumor response under PD-1 blockade. Proceedings of the National Academy of Sciences. 2019; 116: 16971-80.

154. Seo JW, Tavaré R, Mahakian LM, Silvestrini MT, Tam S, Ingham ES, et al. CD8+ T-cell density imaging with 64Cu-labeled cys-diabody informs immunotherapy protocols. Clinical Cancer Research. 2018.

155. Farwell MD, Gamache RF, Babazada H, Hellmann MD, Harding JJ, Korn R, et al. CD8-Targeted PET Imaging of Tumor-Infiltrating T Cells in Patients with Cancer: A Phase I First-in-Humans Study of (89)Zr-Df-IAB22M2C, a Radiolabeled Anti-CD8 Minibody. J Nucl Med. 2022; 63: 720-6.

156. Omidvari N, Jones T, Price PM, Ferre AL, Lu J, Abdelhafez YG, et al. First-in-human immunoPET imaging of COVID-19 convalescent patients using dynamic total-body PET and a CD8-targeted minibody. Sci Adv. 2023; 9: eadh7968.

157. De Pauw T, De Mey L, Debacker JM, Raes G, Van Ginderachter JA, De Groof TWM, Devoogdt N. Current status and future expectations of nanobodies in oncology trials. Expert Opin Investig Drugs. 2023; 32: 705-21.

158. Wang Y, Wang C, Huang M, Qin S, Zhao J, Sang S, et al. Pilot study of a novel nanobody (68) Ga-NODAGA-SNA006 for instant PET imaging of CD8(+) T cells. Eur J Nucl Med Mol Imaging. 2022; 49: 4394-405.

159. Blykers A, Schoonooghe S, Xavier C, D'Hoe K, Laoui D, D'Huyvetter M, et al. PET Imaging of Macrophage Mannose Receptor-Expressing Macrophages in Tumor Stroma Using 18F-Radiolabeled Camelid Single-Domain Antibody Fragments. J Nucl Med. 2015; 56: 1265-71.

160. Gondry O, Xavier C, Raes L, Heemskerk J, Devoogdt N, Everaert H, et al. Phase I Study of [(68)Ga]Ga-Anti-CD206-sdAb for PET/CT Assessment of Protumorigenic Macrophage Presence in Solid Tumors (MMR Phase I). J Nucl Med. 2023; 64: 1378-84.

161. Xavier C, Blykers A, Laoui D, Bolli E, Vaneyken I, Bridoux J, et al. Clinical Translation of [(68)Ga]Ga-NOTA-anti-MMR-sdAb for PET/CT Imaging of Protumorigenic Macrophages. Mol Imaging Biol. 2019; 21: 898-906.

162. Kristensen LK, Fröhlich C, Christensen C, Melander MC, Poulsen TT, Galler GR, et al. CD4(+) and CD8a(+) PET imaging predicts response to novel PD-1 checkpoint inhibitor: studies of Sym021 in syngeneic mouse cancer models. Theranostics. 2019; 9: 8221-38.

163. Clausen AS, Christensen C, Christensen E, Cold S, Kristensen LK, Hansen AE, Kjaer A. Development of a 64Cu-labeled CD4+ T cell targeting PET tracer: evaluation of CD4 specificity and its potential use in collagen-induced arthritis. EJNMMI Research. 2022; 12.

164. Kim I, Srinivasula S, DeGrange P, Long B, Jang H, Carrasquillo JA, et al. Quantitative PET imaging of the CD4 pool in nonhuman primates. European Journal of Nuclear Medicine and Molecular Imaging. 2022; 50: 14-26.

165. Tavaré R, McCracken MN, Zettlitz KA, Salazar FB, Olafsen T, Witte ON, Wu AM. Immuno-PET of Murine T Cell Reconstitution Postadoptive Stem Cell Transplantation Using Anti-CD4 and Anti-CD8 Cys-Diabodies. Journal of nuclear medicine : official publication, Society of Nuclear Medicine. 2015; 56: 1258-64.

166. Freise AC, Zettlitz KA, Salazar FB, Tavaré R, Tsai W-TK, Chatziioannou AF, et al. Immuno-PET in Inflammatory Bowel Disease: Imaging CD4-Positive T Cells in a Murine Model of Colitis. Journal of Nuclear Medicine. 2018; 59: 980-5.

167. Freise AC, Zettlitz KA, Salazar FB, Lu X, Tavaré R, Wu AM. ImmunoPET Imaging of Murine CD4+ T Cells Using Anti-CD4 Cys-Diabody: Effects of Protein Dose on T Cell Function and Imaging. Molecular Imaging and Biology. 2017; 19: 599-609.

168. Nagle VL, Hertz CAJ, Henry KE, Graham MS, Campos C, Pillarsetty N, et al. Noninvasive Imaging of CD4+ T Cells in Humanized Mice. Molecular Cancer Therapeutics. 2022; 21: 658-66.

169. Bruni D, Angell HK, Galon J. The immune contexture and Immunoscore in cancer prognosis and therapeutic efficacy. Nat Rev Cancer. 2020; 20: 662-80.

170. Hanahan D. Hallmarks of Cancer: New Dimensions. Cancer Discovery. 2022; 12: 31-46.

171. Jia Q, Wang A, Yuan Y, Zhu B, Long H. Heterogeneity of the tumor immune microenvironment and its clinical relevance. Exp Hematol Oncol. 2022; 11: 24.

172. Lin Z, Meng X, Wen J, Corral JM, Andreev D, Kachler K, et al. Intratumor Heterogeneity Correlates With Reduced Immune Activity and Worse Survival in Melanoma Patients. Front Oncol. 2020; 10: 596493.

173. Li J, Byrne KT, Yan F, Yamazoe T, Chen Z, Baslan T, et al. Tumor Cell-Intrinsic Factors Underlie Heterogeneity of Immune Cell Infiltration and Response to Immunotherapy. Immunity. 2018; 49: 178-93.e7.

174. Michaeli DT, Mills M, Michaeli T, Miracolo A, Kanavos P. Initial and supplementary indication approval of new targeted cancer drugs by the FDA, EMA, Health Canada, and TGA. Invest New Drugs. 2022; 40: 798-809.

175. Zhu S, Zhang T, Zheng L, Liu H, Song W, Liu D, et al. Combination strategies to maximize the benefits of cancer immunotherapy. J Hematol Oncol. 2021; 14: 156.

176. Dammes N, Peer D. Monoclonal antibody-based molecular imaging strategies and theranostic opportunities. Theranostics. 2020; 10: 938-55.

177. Mohr P, van Sluis J, Lub-de Hooge MN, Lammertsma AA, Brouwers AH, Tsoumpas C. Advances and challenges in immunoPET methodology. Front Nucl Med. 2024; 4: 1360710.

178. Rashidian M, Ingram JR, Dougan M, Dongre A, Whang KA, Legall C, et al. Predicting the response to CTLA-4 blockade by longitudinal noninvasive monitoring of CD8 T cells. Journal of Experimental Medicine. 2017; 214: 2243-55.

179. Huang L, Gainkam LO, Caveliers V, Vanhove C, Keyaerts M, De Baetselier P, et al. SPECT imaging with 99mTc-labeled EGFR-specific nanobody for in vivo monitoring of EGFR expression. Mol Imaging Biol. 2008; 10: 167-75.

180. Roovers RC, Laeremans T, Huang L, De Taeye S, Verkleij AJ, Revets H, et al. Efficient inhibition of EGFR signaling and of tumour growth by antagonistic anti-EFGR Nanobodies. Cancer Immunol Immunother. 2007; 56: 303-17.

181. Evazalipour M, D'Huyvetter M, Tehrani BS, Abolhassani M, Omidfar K, Abdoli S, et al. Generation and characterization of nanobodies targeting PSMA for molecular imaging of prostate cancer. Contrast Media Mol Imaging. 2014; 9: 211-20.

182. Bala G, Baudhuin H, Remory I, Gillis K, Debie P, Krasniqi A, et al. Evaluation of [(99m)Tc]Radiolabeled Macrophage Mannose Receptor-Specific Nanobodies for Targeting of Atherosclerotic Lesions in Mice. Mol Imaging Biol. 2018; 20: 260-7.

183. Jailkhani N, Ingram JR, Rashidian M, Rickelt S, Tian C, Mak H, et al. Noninvasive imaging of tumor progression, metastasis, and fibrosis using a nanobody targeting the extracellular matrix. Proc Natl Acad Sci U S A. 2019; 116: 14181-90.

184. Accogli T, Bruchard M, Végran F. Modulation of CD4 T Cell Response According to Tumor Cytokine Microenvironment. Cancers (Basel). 2021; 13.

185. Meyer JP, Adumeau P, Lewis JS, Zeglis BM. Click Chemistry and Radiochemistry: The First 10 Years. Bioconjug Chem. 2016; 27: 2791-807.

186. Bauer D, Cornejo MA, Hoang TT, Lewis JS, Zeglis BM. Click Chemistry and Radiochemistry: An Update. Bioconjug Chem. 2023; 34: 1925-50.

187. Haque S, Saizawa K, Rojo J, Janeway CA, Jr. The influence of valence on the functional activities of monoclonal anti-L3T4 antibodies. Discrimination of signaling from other effects. J Immunol. 1987; 139: 3207-12.

188. Lange G, Lewis SJ, Murshudov GN, Dodson GG, Moody PCE, Turkenburg JP, et al. Crystal structure of an extracellular fragment of the rat CD4 receptor containing domains 3 and 4. Structure. 1994; 2: 469-81.

189. Chabrol E, Fagnen C, Landron S, Marcheteau E, Stojko J, Guenin SP, et al. Biochemistry, structure, and cellular internalization of a four nanobody-bearing Fc dimer. Protein Sci. 2021; 30: 1946-57.

190. Ackaert C, Smiejkowska N, Xavier C, Sterckx YGJ, Denies S, Stijlemans B, et al. Immunogenicity Risk Profile of Nanobodies. Front Immunol. 2021; 12: 632687.

191. Muyldermans S, Baral TN, Retamozzo VC, De Baetselier P, De Genst E, Kinne J, et al. Camelid immunoglobulins and nanobody technology. Vet Immunol Immunopathol. 2009; 128: 178-83.

192. Vincke C, Loris R, Saerens D, Martinez-Rodriguez S, Muyldermans S, Conrath K. General strategy to humanize a camelid single-domain antibody and identification of a universal humanized nanobody scaffold. J Biol Chem. 2009; 284: 3273-84.

193. Tavaré R, McCracken MN, Zettlitz KA, Knowles SM, Salazar FB, Olafsen T, et al. Engineered antibody fragments for immuno-PET imaging of endogenous CD8+ T cells in vivo. Proc Natl Acad Sci U S A. 2014; 111: 1108-13.

194. De Groof TWM, Lauwers Y, De Pauw T, Saxena M, Vincke C, Van Craenenbroeck J, et al. Specific imaging of CD8 + T-Cell dynamics with a nanobody radiotracer against human CD8β. Eur J Nucl Med Mol Imaging. 2024; 52: 193-207.

195. Smit J, Borm FJ, Niemeijer A-LN, Huisman MC, Hoekstra OS, Boellaard R, et al. PD-L1 PET/CT imaging with radiolabeled durvalumab in patients with advanced stage non-small cell lung cancer. Journal of Nuclear Medicine. 2021: jnumed.121.2624.

196. Shultz LD, Schweitzer PA, Christianson SW, Gott B, Schweitzer IB, Tennent B, et al. Multiple defects in innate and adaptive immunological function in NOD/LTSZ-SCID mice. Journal of Immunology. 1995; 154: 180-91.

197. Serreze DV, Gaskins HR, Leiter EH. Defects in the differentiation and function of antigen presenting cells in NOD/Lt mice. J Immunol. 1993; 150: 2534-43.

198. Shultz LD, Lyons BL, Burzenski LM, Gott B, Chen XH, Chaleff S, et al. Human lymphoid and myeloid cell development in NOD/LtSz-scid IL2Rγnull mice engrafted with mobilized human hemopoietic stem cells. Journal of Immunology. 2005; 174: 6477-89.

199. Hegi-Johnson F, Rudd S, Hicks RJ, De Ruysscher D, Trapani JA, John T, et al. Imaging immunity in patients with cancer using positron emission tomography. npj Precision Oncology. 2022; 6.

200. Gainkam LO, Caveliers V, Devoogdt N, Vanhove C, Xavier C, Boerman O, et al. Localization, mechanism and reduction of renal retention of technetium-99m labeled epidermal growth factor receptor-specific nanobody in mice. Contrast Media Mol Imaging. 2011; 6: 85-92.

201. Babamohamadi M, Mohammadi N, Faryadi E, Haddadi M, Merati A, Ghobadinezhad F, et al. Anti-CTLA-4 nanobody as a promising approach in cancer immunotherapy. Cell Death Dis. 2024; 15: 17.

202. Debie P, Lafont C, Defrise M, Hansen I, van Willigen DM, van Leeuwen FWB, et al. Size and affinity kinetics of nanobodies influence targeting and penetration of solid tumours. Journal of Controlled Release. 2020; 317: 34-42.

203. Pan H, Liu J, Deng W, Xing J, Li Q, Wang Z. Site-specific PEGylation of an anti-CEA/CD3 bispecific antibody improves its antitumor efficacy. International Journal of Nanomedicine. 2018; Volume 13: 3189-201.

204. D'Huyvetter M, Vincke C, Xavier C, Aerts A, Impens N, Baatout S, et al. Targeted radionuclide therapy with A 177Lu-labeled anti-HER2 nanobody. Theranostics. 2014; 4: 708-20.

205. Rousseau E, Lau J, Kuo HT, Zhang Z, Merkens H, Hundal-Jabal N, et al. Monosodium Glutamate Reduces (68)Ga-PSMA-11 Uptake in Salivary Glands and Kidneys in a Preclinical Prostate Cancer Model. J Nucl Med. 2018; 59: 1865-8.

206. Vaidyanathan G, McDougald D, Choi J, Koumarianou E, Weitzel D, Osada T, et al. Preclinical Evaluation of 18F-Labeled Anti-HER2 Nanobody Conjugates for Imaging HER2 Receptor Expression by Immuno-PET. J Nucl Med. 2016; 57: 967-73.

207. Zhao L, Xing Y, Liu C, Ma S, Huang W, Cheng Z, Zhao J. Detection of HER2 expression using (99m)Tc-NM-02 nanobody in patients with breast cancer: a non-randomized, non-blinded clinical trial. Breast Cancer Res. 2024; 26: 40.

208. Demehri S, Cunningham TJ, Manivasagam S, Ngo KH, Moradi Tuchayi S, Reddy R, et al. Thymic stromal lymphopoietin blocks early stages of breast carcinogenesis. J Clin Invest. 2016; 126: 1458-70.

209. Shields NJ, Peyroux EM, Ferguson AL, Steain M, Neumann S, Young SL. Late-stage MC38 tumours recapitulate features of human colorectal cancer - implications for appropriate timepoint selection in preclinical studies. Frontiers in Immunology. 2023; 14.

210. Lau J, Cheung J, Navarro A, Lianoglou S, Haley B, Totpal K, et al. Tumour and host cell PD-L1 is required to mediate suppression of anti-tumour immunity in mice. Nature Communications. 2017; 8: 14572.

211. Scott EN, Gocher AM, Workman CJ, Vignali DAA. Regulatory T Cells: Barriers of Immune Infiltration Into the Tumor Microenvironment. Front Immunol. 2021; 12: 702726.

212. Jin Y, An X, Mao B, Sun R, Kumari R, Chen X, et al. Different syngeneic tumors show distinctive intrinsic tumor-immunity and mechanisms of actions (MOA) of anti-PD-1 treatment. Scientific Reports. 2022; 12.

213. Smith SE, Hoelzinger DB, Dominguez AL, Van Snick J, Lustgarten J. Signals through 4-1BB inhibit T regulatory cells by blocking IL-9 production enhancing antitumor responses. Cancer Immunol Immunother. 2011; 60: 1775-87.

214. Sulea T. Humanization of Camelid Single-Domain Antibodies. Methods Mol Biol. 2022; 2446: 299-312.

215. Fernández-Quintero ML, Guarnera E, Musil D, Pekar L, Sellmann C, Freire F, et al. On the humanization of VHHs: Prospective case studies, experimental and computational characterization of structural determinants for functionality. Protein Sci. 2024; 33: e5176.

216. De Feo MS, Pontico M, Frantellizzi V, Corica F, De Cristofaro F, De Vincentis G. 89Zr-PET imaging in humans: a systematic review. Clinical and Translational Imaging. 2022; 10: 23-36.

217. Braune A, Oehme L, Freudenberg R, Hofheinz F, van den Hoff J, Kotzerke J, Hoberück S. Comparison of image quality and spatial resolution between 18F, 68Ga, and 64Cu phantom measurements using a digital Biograph Vision PET/CT. EJNMMI Physics. 2022; 9: 58.

218. Cleeren F, Lecina J, Bridoux J, Devoogdt N, Tshibangu T, Xavier C, Bormans G. Direct fluorine-18 labeling of heat-sensitive biomolecules for positron emission tomography imaging using the Al(18)F-RESCA method. Nat Protoc. 2018; 13: 2330-47.

219. Xavier C, Blykers A, Vaneycken I, D'Huyvetter M, Heemskerk J, Lahoutte T, et al. (18)F-nanobody for PET imaging of HER2 overexpressing tumors. Nucl Med Biol. 2016; 43: 247-52.

220. Harmand TJ, Islam A, Pishesha N, Ploegh HL. Nanobodies as in vivo, non-invasive, imaging agents. RSC Chem Biol. 2021; 2: 685-701.